LBL-31125

Lawrence Berkeley Laboratory
UNIVERSITY OF CALIFORNIA

Materials & Chemical
Sciences Division

Dynamic-Angle Spinning and Double Rotation of Quadrupolar Nuclei

K.T. Mueller
(Ph.D. Thesis)

July 1991

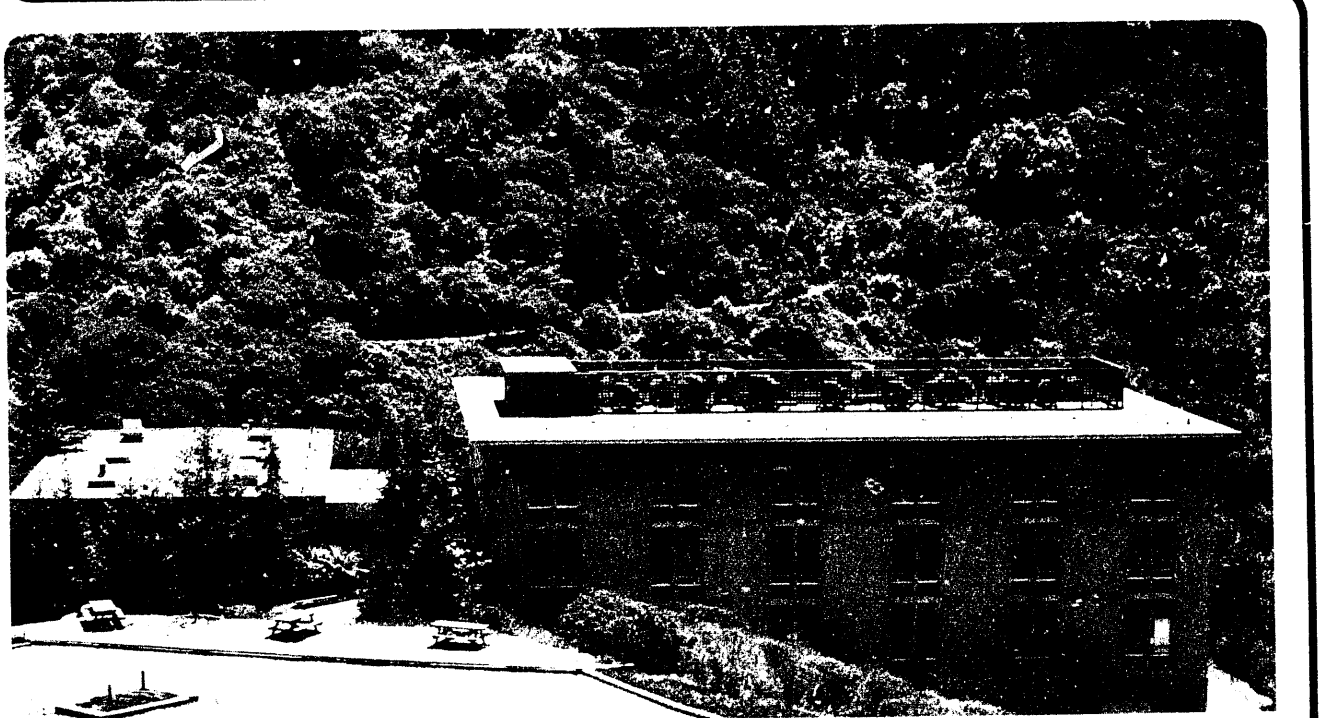

Prepared for the U.S. Department of Energy under Contract Number DE-AC03-76SF00098

LBL--31125

DE92 000837

Dynamic-Angle Spinning and Double Rotation of Quadrupolar Nuclei

Karl Todd Mueller

Department of Chemistry
University of California

and

Materials Sciences Division
Lawrence Berkeley Laboratory
University of California
Berkeley, California 94720

July 1991

This work was supported by the Director, Office of Energy Research, Office of Basic Energy Sciences, Materials Sciences Division, of the U.S. Department of Energy under Contract No. DE-AC03-76SF00098.

Dynamic-Angle Spinning and Double Rotation of Quadrupolar Nuclei

by

Karl Todd Mueller

Dynamic–Angle Spinning and Double Rotation of Quadrupolar Nuclei

by

Karl Todd Mueller

Abstract

Nuclear magnetic resonance (NMR) spectroscopy of quadrupolar nuclei is complicated by the coupling of the electric quadrupole moment of the nucleus to local variations in the electric field. The quadrupolar interaction is a useful source of information about local molecular structure in solids, but it tends to broaden resonance lines causing crowding and overlap in NMR spectra. Magic–angle spinning, which is routinely used to produce high resolution spectra of spin–$\frac{1}{2}$ nuclei like carbon–13 and silicon–29, is incapable of fully narrowing resonances from quadrupolar nuclei when anisotropic second–order quadrupolar interactions are present.

Two new sample–spinning techniques are introduced here that completely average the second–order quadrupolar coupling. Narrow resonance lines are obtained and individual resonances from distinct nuclear sites are identified. In dynamic–angle spinning (DAS) a rotor containing a powdered sample is reoriented between discrete angles with respect to a high magnetic field. Evolution under anisotropic interactions at the different angles cancels, leaving only the isotropic evolution of the spin system. In the second technique, double rotation (DOR), a small rotor spins within a larger rotor so that the sample traces out a complicated trajectory in space. The relative orientation of the rotors and the orientation of the larger rotor within the magnetic field are selected to average both first– and second–order anisotropic broadening.

The theory of quadrupolar interactions, coherent averaging theory, and motional

narrowing by sample reorientation are reviewed with emphasis on the chemical shift anisotropy and second–order quadrupolar interactions experienced by half–odd integer spin quadrupolar nuclei. The DAS and DOR techniques are introduced and illustrated with application to common quadrupolar systems such as sodium–23 and oxygen–17 nuclei in solids.

A more complete examination of a set of silicate minerals using oxygen–17 DAS and DOR reveals resolved resonance lines from up to nine crystallographically distinct oxygen sites in a solid. DAS experiments performed at two magnetic field strengths also exploit the different field dependence of the isotropic chemical and second–order quadrupolar shifts, and their contributions to the overall positions of the resonance lines are determined. Detailed analyses of the lineshapes in two–dimensional DAS experiments and the probehead used in a DAS experiment are also provided.

Contents

List of Figures

List of Tables

Acknowledgements

I have enjoyed my time in Berkeley and will treasure my memories from the past five years. In the beginning, graduate school appeared as a long journey into madness. At the other end, it seems but a brief visit with a horde of brilliant and talented associates.

The work presented here could not have been accomplished without the genius and encouragement of Professor Alex Pines. I am grateful for his teaching, guidance, and friendship. He has taught me to be concise and correct in my approach to science, from the formulation of ideas to the presentation of results. The remainder of my thesis committee, Professor Jeffrey Reimer and Professor Robert Harris, also influenced my approach to science. They have been constant sources of information and I have enjoyed my numerous conversations with them.

Inexperienced students profit immeasurably from their initial interactions within the Pines group. My early collaborations with Dr. Herman Cho, Dr. Dieter Suter, and Dr. A. J. Shaka provided me with firsthand knowledge of academic excellence. Other encounters have also contributed greatly to this work and further scientific endeavors. I especially thank Dr. Josef Zwanziger, Dr. E. Wrenn Wooten, Dr. Gerard Chingas, Dr. Bradley Chmelka, and Dr. Jonathan Stebbins (at Stanford) for help and instruction along the way. Briefer meetings and collaborations with Professor T. Terao and Dr. K. Takegoshi from Kyoto, Dr. Endel Lippmaa and Dr. Ago Samoson in Estonia, and Dr. Zbigniew Olejniczak, Dr. Philip Grandinetti, and Dr. Yue Wu at Berkeley have been enjoyable and fruitful.

My interactions with the rest of the Pines group have provided me with many friendships and a professional regard for a multitude of people. I wish to thank

Dr. Steven Rucker for his friendship and humor over these past years. His technical expertise and dynamic personality made him a powerful force in the group. Dr. John Pearson was the perfect hiking companion for me: his pace matched mine as we wandered the forested East Bay hills and the rocky ridges of the EBMUD lands. Scientific and non–scientific conversations with my friends Dr. Jeff Chang and Mark Rosen have also been appreciated. Other members of the Pines group including Jay Baltisberger, Boqin Sun, and Joe Sachleben have helped me along the way and I am deeply indebted to them and others for their time and effort. Dione Carmichael was the cause of the many pleasant departures from scientific endeavors, and Alex and the group are fortunate to have her there for support and assistance.

The support staff at Berkeley and at LBL have been instrumental in the success of the DAS and DOR projects. Dan Colomb and Anthony Tammer in the LBL machine shop, and Carl Gaskins, Hans Graetsch, and Dave Murai in the Chemistry Department shop, surmounted many technical obstacles to help produce a functional and robust DAS probehead which has taken all kinds of abuse and still performs incredibly.

Finally, I thank my parents, siblings, and other family members for being so supportive during the many years of my studies. Most of all, Lisa Mueller has been my best friend and constant source of strength. She has brought great happiness to my life, and I love her dearly.

To Lisa

Chapter 1

Spin Interactions in NMR

1.1 Introduction

Quadrupolar nuclei have nuclear spin angular momentum (I) greater than one–half, and this differentiates them from spin–$\frac{1}{2}$ nuclei which can never have a nuclear charge distribution with an electric quadrupole moment [1, 2]. Another major difference between spin–$\frac{1}{2}$ nuclei such as protons or carbon–13 and quadrupolar nuclei is that the quadrupolar spins have more magnetic substates associated with the nuclear spin angular momentum. While for isolated, non–quadrupolar species only two energy states are present, a quadrupolar nucleus has $2I + 1$ magnetic substates which separate in energy in a magnetic field. The high–field nuclear magnetic resonance (NMR) spectra obtained from quadrupolar nuclei probe the transitions made between the energy levels. Connections between nuclear spin states are routinely detected by either continuous–wave irradiation [3, 4, 5] or time–domain techniques [6]. While the largest interaction for spins is usually the nuclear Zeeman interaction, which provides the initial splitting of the magnetic substates, it is often

considered the least interesting. Importantly for chemists and chemical physicists, further variations in the energy levels arise from interactions of a nucleus with the surrounding microscopic environment. A detailed study of NMR spectra presents new insight into local bonding and structure in solids. Both spin–$\frac{1}{2}$ species and quadrupolar nuclei experience anisotropic magnetic shielding of the nucleus that provides clues to local magnetic fields. For quadrupolar nuclei alone the additional coupling of the electric quadrupole moment of the nucleus to local variations in the electric field provides another powerful tool for the investigation of local environments.

The objects studied are the magnetic resonances: transitions between the spin energy levels constitute the phenomena observed in the earliest continuous–wave nuclear magnetic resonance experiments. In time–domain NMR, coherences between energy levels are excited by resonant irradiation or other coherent processes. The coherences evolve in time, and some of them are detected as oscillations of voltage measured across an inductor surrounding the sample. A survey of the NMR of quadrupolar nuclei includes many experiments also common for spin–$\frac{1}{2}$ nuclei such as standard spectral acquisition by pulsed [7, 8] or continuous–wave [9] techniques, as well as relaxation studies [10], multiple–quantum spectroscopy [11], and sample spinning to narrow broad resonances [12, 13].

The experiments described in this thesis point in an exciting new direction for the NMR of quadrupolar nuclei. Two novel sample reorientation methods are introduced: dynamic–angle spinning (DAS) and double rotation (DOR) NMR. These techniques are especially applicable to half–odd integer spin quadrupolar nuclei where the relatively easy to observe central transition is broadened by second–order

quadrupolar interactions. Preliminary DAS and DOR experiments are presented on a variety of test compounds and significant resolution enhancement is demonstrated. Further experimental modifications and a detailed study of oxygen environments in a set of minerals are also presented.

First, however, the theory of quadrupolar interactions in NMR is discussed, leading up to the development of the DAS and DOR techniques. After a classical introduction of the nuclear electric quadrupole interaction, the quantum mechanical quadrupolar Hamiltonian is formulated. Coherent averaging theory is applied to half–odd integer spin nuclei which experience both chemical shift anisotropy (a magnetic interaction) and second–order quadrupolar broadening (an electric interaction). The truncation of the spin interactions by the large external magnetic field and the effect of rapid sample rotation are discussed and their impact on the observable spectra are calculated. The inability of simple sample spinning to sufficiently narrow the resonances leads to the main emphasis of this work. The theory of the two new techniques is presented, and in the subsequent chapter the first experimental realizations of these techniques are offered.

The remainder of this work deals with three topics: a detailed analysis of the proper phasing of lineshapes in two–dimensional dynamic–angle spinning experiments, a study of oxygen nuclei in silicate minerals employing both DAS and DOR, and finally the presentation of the DAS probehead designed and built for many of these experiments. The appendices include minor topics such as the actual DAS probehead mechanical drawings, a mechanical analysis of the effect of a rapid axis flip on a spinning sample container and its supporting air bearings, and computer programs used for calculations presented in the main text. The computer programs

showcase the *Mathematica*™ programming environment [14] where the programmer has the ability to solve complicated algebraic and trigonometric problems with symbolic manipulation.

Before any detailed descriptions or assumptions are made regarding the experiments to be carried out, it is instructive to study the spin energy levels of a nucleus in a magnetic field. Particularly interesting for quadrupolar nuclei is the coupling of the nuclear charge distribution to local electric fields: this is usually manifest in the electric quadrupolar interaction. After introducing the classical quadrupolar coupling, a correspondence may be made with the microscopic nature of the system and the quantum mechanical quadrupolar Hamiltonian is formulated. The remaining interactions and couplings of the nuclei are included as further contributions to the total spin Hamiltonian. Rotations of the spin system or the physical lattice containing the nuclei are also important for understanding the high–field NMR experiments introduced here, and these are dealt with formally at the end of this chapter.

1.2 The Quadrupolar Hamiltonian

A central point of this exposition of the spin interactions is the intimate connection between the physical and chemical properties of the system and the observables of NMR spectroscopy. It is therefore useful to follow the derivation of the quadrupolar coupling Hamiltonian from the basic physical arguments to its final representation as a quantum mechanical operator. Many equivalent forms of the quadrupolar Hamiltonian appear in the literature. Some are suited to specific phenomena such as relaxation [15] or coherent averaging [12, 16], while others are in a

more general form [17, 18].

The interaction energy of a charged nucleus with an external electric field is derived in detail in a large number of texts, especially those dealing with specific couplings such as the nuclear–electron hyperfine interactions [19]. This classical interaction energy equation is the starting point, after which the quantum mechanical analog of the nuclear charge density provides the quadrupolar Hamiltonian. Finally, the Wigner–Eckart theorem is introduced and discussed in order to present the Hamiltonian in a form which will be useful in NMR.

1.2.1 Classical Interaction

A nucleus, with atomic number Z and total charge Ze interacts with an electric potential $V(\mathbf{r})$ which is dependent on the spatial coordinates of the electric charges of the total system: the positions of the nucleus of interest, other nearby nuclei, and all associated electrons. This is the classical electrostatic interaction of a charged body with an external charge distribution. Although caused by small quantities of electric charge such as the electrons in their orbits surrounding a nucleus or the positive charges of nearby ions, the size of the potential could be considerable due to the proximity of the charges to the nucleus.

If the total nuclear charge is distributed over the volume of the nucleus ($\mathcal{V}$) with a charge density $\rho(\mathbf{r})$, the classical interaction energy is the integral over the nuclear volume of the product of the charge density and the potential:

$$E = \int_{\mathcal{V}} \rho(\mathbf{r}) V(\mathbf{r})\, d^3\mathbf{r}. \tag{1.1}$$

The nucleus is not being viewed simply as a point charge since the potential could still vary appreciably over the nuclear volume. The potential is expanded as a

Taylor series about the center of mass of the nucleus (which is also considered as the center of charge) and then it may be written

$$V(\mathbf{r}) = V(0) + \sum_{\alpha=1}^{3} x_\alpha \left(\frac{\partial V}{\partial x_\alpha}\right)_{\mathbf{r}=0} + \frac{1}{2}\sum_{\alpha=1}^{3}\sum_{\beta=1}^{3} x_\alpha x_\beta \left(\frac{\partial^2 V}{\partial x_\alpha \partial x_\beta}\right)_{\mathbf{r}=0} + \cdots \qquad (1.2)$$

where the variables x_α and x_β are the Cartesian coordinates: $x_1 = x$, $x_2 = y$, and $x_3 = z$. The subscript $\mathbf{r} = 0$ means that the derivatives of the potential are evaluated at the origin which is defined as the center of mass of the nucleus. Claims that the center of mass and the center of charge coincide for an atomic nucleus are based on the assumption that stationary nuclear states are of a definite parity [2, 18], and there is strong experimental evidence to support this postulate [20].

A direct relation to physical properties of the classical charged body is retained if the following substitutions are made:

$$\int_\nu \rho(\mathbf{r})\, d^3\mathbf{r} = Ze \qquad (1.3)$$

$$\int_\nu x_\alpha \rho(\mathbf{r})\, d^3\mathbf{r} = P_\alpha \qquad (1.4)$$

and

$$\int_\nu x_\alpha x_\beta \rho(\mathbf{r})\, d^3\mathbf{r} = Q'_{\alpha\beta}. \qquad (1.5)$$

The first integral is the total charge of the nucleus. The remaining two are higher moments of the electric charge distribution: the α component of the electric dipole moment P (a vector) and the $\alpha\beta$ component of the electric quadrupole moment Q' (a second–rank tensor). Keeping terms through those quadratic in the spatial coordinates in the expansion of the potential in Eq. 1.2, the electrostatic energy is

$$E = ZeV(0) + \sum_{\alpha=1}^{3} P_\alpha \left(\frac{\partial V}{\partial x_\alpha}\right)_{\mathbf{r}=0} + \frac{1}{2}\sum_{\alpha=1}^{3}\sum_{\beta=1}^{3} Q'_{\alpha\beta} \left(\frac{\partial^2 V}{\partial x_\alpha \partial x_\beta}\right)_{\mathbf{r}=0}. \qquad (1.6)$$

The first term in this equation is the classical interaction of a charged nucleus with a constant potential at the origin. It determines, for example, the packing of atoms in a solid and is independent of the nuclear orientation. Therefore, it will not affect the magnetic resonance spectrum and is dropped from further consideration. The second term, the classical electric dipole interaction, vanishes since the center of charge and the center of mass of the nucleus are assumed to coincide. In a classical picture the charges within the nucleus are in such rapid motion that the time averaged distribution of the electric charge density is an even function of position and the integral in Eq. 1.4 is identically zero. The remaining term is the nuclear electric quadrupole interaction. Higher–order terms are obtained by continuing the expansion, but the next parity allowed electric multipole is the hexadecapole and this is usually insignificant in size. See, however, the papers of Wang [21, 22] discussing the possibility of observing nuclear haxadecapole moments and how they may become important for the study of lattice defects, phase changes, and lattice dynamics in crystals.

Returning to the electric quadrupole interaction, the charge distribution external to the nucleus enters into the calculation as second derivatives of the potential. The tensor constructed from these second derivatives is called the electric field gradient (EFG) tensor to which the symbols

$$V_{\alpha\beta} \equiv \left(\frac{\partial^2 V}{\partial x_\alpha \partial x_\beta} \right)_{\mathbf{r}=0} \tag{1.7}$$

are assigned. By the equivalence of mixed partial derivatives, $V_{\alpha\beta}$ is a symmetric second–rank tensor and therefore has six independent components. It is also traceless, since by Laplace's equation

$$\nabla^2 V = 0, \tag{1.8}$$

and hence only five components are independent [1]. The appropriate modification of the theory if a source does exist at the origin involves replacing Eq. 1.8 with Poisson's equation [17].

It is always possible to transform the symmetric EFG tensor to a form in which it is diagonal by an orthogonal transformation to the principal axis system (PAS) of the EFG. The coordinate axes in the PAS are labelled with upper case letters X, Y, and Z and in this frame only the three diagonal components V_{XX}, V_{YY}, and V_{ZZ} are different from zero. These are still interrelated, since by Eq. 1.8

$$V_{XX} + V_{YY} + V_{ZZ} = 0, \tag{1.9}$$

and only two parameters are necessary to completely specify the electric field gradient. Further angular coordinates may enter the equations with rotation out of the principal axis system to a coordinate system defined by another frame such as the molecular axis system, the sample holder axis system, or possibly the laboratory (or magnet) axis system.

The parameters describing the EFG are usually chosen by first orienting the principal axis system so that the component of the tensor with the largest magnitude is along the Z–axis and the smallest along the X–axis, or

$$|V_{ZZ}| \geq |V_{YY}| \geq |V_{XX}|\,. \tag{1.10}$$

Then two convenient parameters are the *strength* of the EFG in units of electric charge

$$eq = V_{ZZ} \tag{1.11}$$

and the *asymmetry* parameter

$$\eta = \frac{(V_{XX} - V_{YY})}{V_{ZZ}}. \tag{1.12}$$

The asymmetry parameter is dimensionless and lies between 0 and 1. It essentially describes the deviation of the field gradient from axial symmetry. If the gradient is spherically symmetric, or has cubic or higher symmetry, then each component of the tensor is identically zero and the quadrupolar interaction vanishes completely [1].

As seen from Eq. 1.5 the quadrupole tensor Q' is also symmetric and second–rank but not traceless. It is more convenient for the calculations involved when a traceless quadrupolar tensor is introduced with components:

$$\begin{aligned} Q_{\alpha\beta} &= 3Q'_{\alpha\beta} - \delta_{\alpha\beta}\sum_{\gamma=1}^{3} Q'_{\gamma\gamma} \\ &= \int_{\nu} \rho(\mathbf{r})(3x_\alpha x_\beta - \delta_{\alpha\beta}r^2)\, d^3\mathbf{r}. \end{aligned} \tag{1.13}$$

The interaction energy is rewritten for the quadrupolar coupling as

$$E = \frac{1}{6}\sum_{\alpha=1}^{3}\sum_{\beta=1}^{3} Q_{\alpha\beta}V_{\alpha\beta} + \frac{1}{6}\sum_{\gamma=1}^{3} Q'_{\gamma\gamma}\sum_{\delta=1}^{3} V_{\delta\delta}. \tag{1.14}$$

The final term is identically zero since it contains the trace of the EFG tensor, which must be independent of orientation even under rotation out of the PAS. The remaining classical interaction is

$$E = \frac{1}{6}\sum_{\alpha=1}^{3}\sum_{\beta=1}^{3} Q_{\alpha\beta}V_{\alpha\beta} \tag{1.15}$$

which has the advantage of containing only traceless, second–rank tensors.

1.2.2 Quantum Mechanical Hamiltonian

Nuclear spin is a quantum mechanical property and, although the classical picture is a useful model providing excellent physical insight, the problem must be translated to the correct quantum mechanical language. This was first worked out by Casimir [19] in a prize essay on the nuclear–electric hyperfine interaction

published in 1936. To begin, the classical nuclear charge density is replaced with an operator containing products of the charges of the nucleons, q_k, with delta functions of their positions $\mathbf{r}_k$

$$\rho^{(op)}(\mathbf{r}) = \sum_k q_k \delta(\mathbf{r} - \mathbf{r}_k). \tag{1.16}$$

The neutrons are uncharged and only the protons enter the sum with $q_k = e$, the fundamental unit of electric charge. Substituting into the classical expression for $Q_{\alpha\beta}$ derived above, the $\alpha\beta$–component of the quantum mechanical quadrupole operator is

$$Q_{\alpha\beta}^{(op)} = e \sum_k (3x_{\alpha k} x_{\beta k} - \delta_{\alpha\beta} r_k^2). \tag{1.17}$$

The electric field gradient tensor is also a classical quantity and a corresponding quantum mechanical electron operator may be defined. Numerical values for the electric field gradient components are calculated by taking the expectation value over an appropriate electron wavefunction. In bulk matter it is usually the case that there is no orbital degeneracy for the electrons and the EFG operators may be replaced by their expectation values taken over the one predominant nondegenerate electron state describing the electron orbit [18]. The EFG tensor is then included in the Hamiltonian with an unknown numerical value and the understanding that the expectation value has been previously calculated or could be calculated if the charge distribution external to the nucleus were known. The same symbols as the classical EFG tensor are therefore used to denote the EFG in the quantum mechanical expression for the Hamiltonian. The components of the EFG tensor are ultimately provided by analysis of the NMR spectra of quadrupolar nuclei under ideal circumstances.

The quadrupolar Hamiltonian is obtained through substitution of the appro-

priate operators into the classical energy expression in Eq. 1.15, rewritten simply as

$$\mathcal{H}_Q = \frac{1}{6}\sum_{\alpha,\beta} Q_{\alpha\beta}^{(op)} V_{\alpha\beta} \tag{1.18}$$

with $V_{\alpha\beta}$ now the expectation value of an operator as described above.

Alternative Derivations

The preceding section has been only one of several analyses which would provide a correct quadrupolar Hamiltonian. Many authors [18, 23] begin from a different energy equation by writing the potential as a function of the positions of the charges external to the nucleus ($\mathbf{r}_m$) in a volume $\mathcal{V}_m$ and the distance from the charges to the nucleus ($|\mathbf{r}_m$ - $\mathbf{r}|$). Then the potential is

$$V(\mathbf{r}) = \int_{\mathcal{V}_m} \frac{\rho_m(\mathbf{r}_m)}{|\,\mathbf{r}_m - \mathbf{r}\,|}\, d^3 r_m. \tag{1.19}$$

The denominator is expanded in terms of Legendre polynomials and the Hamiltonian subsequently written as products of spherical harmonics in the coordinates of the nuclear and electronic variables by the spherical harmonic addition theorem. The detailed monograph of Cook and De Lucia [23] provides further details for the interested reader. One important result which comes out of this analysis is that the Hamiltonian may be expressed in spherical tensor rather then Cartesian tensor form. Cook and De Lucia provide the details of the conversion, especially useful if an interaction cannot be derived in spherical form directly. The quadrupolar Hamiltonian could have been initially expressed in spherical form, but here a closer connection with the definition of moments of the nuclear charge is retained using a Cartesian analysis. The spherical tensors are usually quoted in terms of the Cartesian coordinates when a final answer is presented However, spherical tensors do

possess useful properties under rotations of the system, so the next step is to use the proper rules to express the spherical tensors in terms of the quantities calculated above.

Spherical Tensor Components

The spherical quadrupolar tensor components are denoted by the operators $T^{(op)}_{2m}$ with m ranging from –2 to 2. The tensor operator $T^{(op)}$ is second–rank so it must have 5 components. In terms of the Cartesian coordinates

$$T^{(op)}_{20} = \frac{e}{2\sqrt{6}} \sum_k (3z_k^2 - r_k^2) \tag{1.20}$$

$$T^{(op)}_{2\pm1} = \mp \frac{e}{2} \sum_k z_k (x_k \pm i y_k) \tag{1.21}$$

and

$$T^{(op)}_{2\pm2} = \frac{e}{4} \sum_k (x_k \pm i y_k)^2. \tag{1.22}$$

The EFG tensor is also a second–rank tensor. The explicit components of the spherical EFG tensor (calling it $R^{(Q)}$) in a general coordinate system are related to the Cartesian components by

$$R^{(Q)}_{20} = \sqrt{\frac{3}{2}} V_{zz} \tag{1.23}$$

$$R^{(Q)}_{2\pm1} = \mp (V_{xz} \pm i V_{yz}) \tag{1.24}$$

$$R^{(Q)}_{2\pm2} = \frac{1}{2} (V_{xx} - V_{yy} \pm 2i V_{xy}). \tag{1.25}$$

In the principal axis system of the EFG the tensor components are referred to in the lower case ($r^{(Q)}$) and

$$r^{(Q)}_{20} = \sqrt{\frac{3}{2}} V_{ZZ} = \sqrt{\frac{3}{2}} eq \tag{1.26}$$

$$r^{(Q)}_{2\pm1} = 0 \tag{1.27}$$

$$r^{(Q)}_{2\pm2} = \frac{1}{2}(V_{XX} - V_{YY}) = \frac{1}{2}eq\eta. \tag{1.28}$$

The Hamiltonian in terms of the spherical tensors is written [15, 16]

$$\mathcal{H}_Q = \sum_{m=-2}^{2} (-1)^m T^{(op)}_{2m} R^{(Q)}_{2-m}. \tag{1.29}$$

It may be proven by direct calculation that Eqs. 1.18 and 1.29 are equivalent. The Hamiltonian in Eq. 1.29 is defined by the product of the positive m valued $T^{(op)}_{2m}$ and the negative m valued $R^{(Q)}_{2-m}$ since the scalar product of two tensors of rank k is

$$\mathbf{T^{(k)}} \cdot \mathbf{R^{(k)}} = \sum_{m=-k}^{k} (-1)^m T_{km} R_{k-m}. \tag{1.30}$$

At this point the Hamiltonian must be a scalar quantity: it is an energy operator which is independent of direction in space and invariant under rotations. This isotropy is subsequently broken upon application of large magnetic fields.

Use of the Wigner–Eckart Theorem

The expression for the Hamiltonian as it now stands is very complex, depending on the positions of all protons within the nucleus. To be useful in high–field NMR, this Hamiltonian must be transformed further into a spin Hamiltonian. Nuclear spin Hamiltonians are expressed in terms of spin angular momentum operators of the nucleus and matrix elements are calculated between eigenstates characterized by their associated eigenvalue of the I_z operator. This is a direct result of the Zeeman interaction being the dominant coupling for the spin system. The final transformation of the Hamiltonian comes from an important theorem on tensor operators, the Wigner–Eckart Theorem. Proofs of the Wigner–Eckart Theorem are found in texts on both angular momentum and quantum mechanics [24, 25] so will

not be included here. Sketched below are the essential rules and results of this important theorem.

An irreducible tensor operator of rank L has $2L + 1$ components, T_{LM}, which satisfy the following commutation relations with the *total* angular momentum of the system of interest:

$$[J_z, T_{LM}] = \hbar M T_{LM} \tag{1.31}$$

$$[J_+, T_{LM}] = \hbar\sqrt{L(L+1) - M(M+1)}\,T_{LM+1} \tag{1.32}$$

and

$$[J_-, T_{LM}] = \hbar\sqrt{L(L+1) - M(M-1)}\,T_{LM-1}. \tag{1.33}$$

The $J_\pm$ are the raising and lowering operators (or ladder operators) for the spin *plus* spatial angular momentum J and they are defined as

$$J_\pm = J_x \pm iJ_y. \tag{1.34}$$

A fully equivalent definition of an irreducible tensor of rank L is that it transforms under rotations in the same way as a spherical harmonic of rank L. Spherical harmonics ($Y_{LM}(\theta, \phi)$) will only be transformed into other spherical harmonics of the same rank upon rotation. By considering the commutation relations of an operator with the total angular momentum, or its behavior under rotations, its rank is discerned. A scalar operator is a tensor operator of rank zero, while a vector operator is of rank one. The electric quadrupole operator is of rank two, and so has five ($2L + 1$) independent components as noted above. For a nucleus which also has spin I, the electric quadrupole operator is an irreducible tensor with rank two in the tensor product space of the position state space (coordinate space) and the spin state space of the particle. Therefore, since total angular momentum is a

conserved quantity, rotations in the total space transform the components of the quadrupole operator only into linear combinations of themselves.

The Wigner–Eckart Theorem states that the matrix elements within this total state space of all irreducible tensor operators of rank L are proportional to one another. Nuclear states are described by the total spin quantum number (I), the projection of the total spin upon the z–axis (m), and possibly other quantum numbers denoted generically by α. Since the state of the nucleus is well–defined, only matrix elements diagonal in I and α must be considered. Essentially this is stating that I and α are good quantum numbers. In general it is necessary to compute matrix elements of the quadrupole operator in the form

$$\langle \alpha I m \mid Q^{(op)} \mid \alpha I m' \rangle \equiv \langle m \mid Q^{(op)} \mid m' \rangle. \tag{1.35}$$

The Wigner–Eckart Theorem is the essential link between irreducible spin operators of rank two and the quadrupole operator. When written in terms of spin operators, the matrix elements of the quadrupolar Hamiltonian are easily computed.

Second–rank irreducible spin operators are constructed in the same way that irreducible second–rank tensors in three–dimensional space are formed, as the direct product of two first–rank tensor operators (vectors) using the coupling of angular momenta and Clebsch–Gordon coefficients [15]. In terms of the vector spin operator components I_z and $I_{\pm 1}$ where

$$I_{\pm 1} = \mp \frac{1}{\sqrt{2}} (I_x \pm i I_y) \tag{1.36}$$

we obtain for the quadrupolar interaction:

$$T_{20}^{(Q)} = \frac{1}{\sqrt{6}} [3 I_z^2 - I^2] \tag{1.37}$$

$$T^{(Q)}_{2\pm1} = \frac{1}{\sqrt{2}}(I_z I_{\pm1} + I_{\pm1} I_z) \tag{1.38}$$

$$T^{(Q)}_{2\pm2} = I^2_{\pm1}. \tag{1.39}$$

The matrix elements of these operators are *proportional* to the matrix elements of the quadrupole operator and we need to compute the proportionality constant between the quadrupolar operators and the spin operators. First we note that all five independent components of the tensor operator $Q^{(op)}$ (or $T^{(op)}$) may be related to a single quantity. Assuming the spin to be quantized along the z or x_3 axis, the nuclear charges precess very rapidly about the direction of the nuclear spin and the external potential interacts with the time average of this charge distribution. In the Cartesian representation, the components of $Q^{(op)}_{\alpha\beta}$ for $\alpha \neq \beta$ are zero by symmetry. Further, $Q^{(op)}_{11} = Q^{(op)}_{22}$ by the cylindrical symmetry of the problem. Since the tensor is traceless, the sum of the diagonal components is zero and hence $Q^{(op)}_{11} = Q^{(op)}_{22} = -\frac{1}{2}Q^{(op)}_{33}$. In the spherical representation it becomes clear that only the difference between the charge distribution parallel and perpendicular to the z–axis is important.

The $m = I$ matrix element of the quadrupole operator with reference to the z–axis is traditionally defined to be equal to eQ, the electric quadrupole moment:

$$eQ = \langle I \mid Q^{(op)}_{33} \mid I \rangle \tag{1.40}$$

or

$$eQ = \langle I \mid e\sum_k \left(3z_k^2 - r_k^2\right) \mid I \rangle. \tag{1.41}$$

which by Eq. 1.20 is also the matrix element of $2\sqrt{6}T^{(op)}_{20}$. By the conclusions of the Wigner–Eckart Theorem, this must be proportional to $2\sqrt{6}T^{(Q)}_{20}$ from Eq. 1.37, or

$$
\begin{aligned}
eQ &= C\langle I \mid 2(3I_z^2 - I^2) \mid I\rangle \\
&= 2C(3I^2 - I(I+1))
\end{aligned} \tag{1.42}
$$

and the constant of proportionality is then

$$
C = \frac{eQ}{2I(2I-1)}. \tag{1.43}
$$

A popular measure of the strength of the quadrupole coupling is the quadrupolar coupling constant

$$
C_Q = \frac{e^2qQ}{h} \tag{1.44}
$$

which has the units of frequency. Note that this is a product of the electric quadrupole moment and the largest component of the electric field gradient tensor in the principal axis system.

In summary, we rewrite the derived form of the quadrupolar Hamiltonian as well as some equivalent forms which are often used in the literature. In the spherical tensor representation of the Hamiltonian:

$$
\mathcal{H}_Q = C \sum_{m=-2}^{2} (-1)^m T_{2m}^{(Q)} R_{2-m}^{(Q)} \tag{1.45}
$$

using Eqs. 1.37–1.39 and 1.23–1.25 for the definition of the "spin" and "space" parts of the Hamiltonian, respectively. Here again, the spatial part of the interaction is written in a general reference frame where the measurement is convenient, not necessarily the PAS of the quadrupolar interaction.

In Cartesian space the Hamiltonian is

$$
\mathcal{H}_Q = \frac{1}{6} \sum_{\alpha,\beta} Q_{\alpha\beta}^{(op)} V_{\alpha\beta} \tag{1.46}
$$

with components

$$
V_{\alpha\beta} = \left(\frac{\partial^2 V}{\partial x_\alpha \partial x_\beta} \right)_{\mathbf{r}=0} \tag{1.47}
$$

and from Eqs. 1.17 and further use of the Wigner–Eckart Theorem (see for example Slichter's text [17]):

$$Q_{\alpha\beta}^{(op)} = \frac{eQ}{6I(2I-1)}\left[\frac{3}{2}(I_\alpha I_\beta + I_\beta I_\alpha) - \delta_{\alpha\beta}I^2\right]. \tag{1.48}$$

This is often expressed in the more compact form

$$\mathcal{H}_Q = \mathbf{I}\mathcal{Q}\mathbf{I}, \tag{1.49}$$

where $\mathbf{I}$ is a vector of spin operators (I_x, I_y, I_z) and $\mathcal{Q}$ is a second rank tensor in Cartesian space [16].

Additional forms of the quadrupolar Hamiltonian appear in the literature for other physically interesting problems. As an example, Pettitt [26] shows that a simple quadratic form of the quadrupolar Hamiltonian may be written down in terms of the first–rank vector spin operators and one rotation from the frame of reference where the spin operators are defined to the principal axis system of the electric field gradient tensor. This would be useful in problems where the electric field gradients are complicated by fluctuations in charge density or orientation.

1.2.3 Matrix Elements of the Quadrupolar Hamiltonian

To complete this section the matrix elements of the quadrupolar Hamiltonian are calculated. Using the following matrix elements of the spin operators

$$\langle m \mid I_z \mid m\rangle = m \tag{1.50}$$

$$\langle m \mid I_{\pm 1} \mid m \pm 1\rangle = \mp\frac{1}{\sqrt{2}}\sqrt{(I \mp m)(I \pm m + 1)} \tag{1.51}$$

the matrix elements for $\mathcal{H}_Q$ are

$$\langle m \mid \mathcal{H}_Q \mid m\rangle = \frac{C}{\sqrt{6}}[3m^2 - I(I+1)]R_{20} \tag{1.52}$$

$$\langle m \pm 1 \mid \mathcal{H}_Q \mid m \rangle = \pm \frac{C}{2}(2m \pm 1)\sqrt{(I \mp m)(I \pm m + 1)}R_{2\mp 1} \tag{1.53}$$

$$\begin{aligned} \langle m \pm 2 \mid \mathcal{H}_Q \mid m \rangle &= \frac{C}{2}\sqrt{(I \mp m)(I \pm m + 1)} \times \\ &\quad \sqrt{(I \mp m - 1)(I \pm m + 2)}R_{2\mp 2} \end{aligned} \tag{1.54}$$

while

$$\langle m' \mid \mathcal{H}_Q \mid m \rangle = 0 \tag{1.55}$$

if $\mid m' - m \mid > 2$.

Explicit solutions for the eigenvalues of the quadrupolar Hamiltonian for a spin–k nucleus require diagonalizing a $(2k + 1) \times (2k + 1)$ matrix. This has been accomplished analytically only for spins up to $I = \frac{3}{2}$ [27].

1.3 Other Internal and External Hamiltonians

The NMR spectra of quadrupolar nuclei are determined not only by the quadrupolar interaction described above, but also by the other internal and external interactions of the spins. Among the important interactions for high–resolution NMR of solids are the Zeeman interaction, the isotropic chemical shift and the chemical shift anisotropy, the dipole–dipole coupling, and the effect of an external irradiating field. Radiofrequency pulses are dealt with in the next section (rotations of the system in spin space), while the other interactions are summarized below.

1.3.1 Zeeman Interaction

The interaction energy of a magnetic dipole with magnetic dipole moment $\boldsymbol{\mu}$ within a magnetic field ($\boldsymbol{B}$) is

$$E = -\boldsymbol{\mu} \cdot \boldsymbol{B}. \tag{1.56}$$

The magnetic dipole moment may be rewritten in terms of spin operators again using the Wigner–Eckart theorem, here for a vector operator. The result provides the Zeeman Hamiltonian. For a spin in a magnetic field of strength B_0 along a direction which we define as the laboratory z–axis,

$$\mathcal{H}_Z = -\gamma\hbar I_z B_0 \tag{1.57}$$

where the constant of proportionality is the magnetogyric ratio of the spin. The matrix elements of I_z are diagonal in the Zeeman basis (Eq. 1.50) and the characteristic frequency between neighboring ($\Delta m = 1$) levels is called the Larmor frequency:

$$\omega_0 = \gamma B_0. \tag{1.58}$$

The Zeeman interaction is usually the largest in magnitude in high–field NMR, and it has the effect of truncating the other spin Hamiltonians [28]. Therefore, to what will be a zero–order approximation, the states of the spin parallel or antiparallel to the z–axis (the Zeeman basis) characterize the system. Corrections to this rule are needed when interactions and couplings are no longer small compared to the magnitude of the Zeeman terms.

1.3.2 Isotropic and Anisotropic Chemical Shifts

The chemical shielding or chemical shift Hamiltonian in spherical tensor notation is

$$\mathcal{H}_{CS} = \gamma \sum_{\ell=0,2} \sum_{m=-\ell}^{\ell} (-1)^m T^{CS}_{\ell m} R^{CS}_{\ell -m}. \tag{1.59}$$

Here, the assumption has been made that only the symmetric part of the interaction is observable. The discussions of Haeberlen [28] and Ye [29] investigate this assumption further.

This interaction has two origins [30]. One is the coupling of the magnetic dipole of the spin to the magnetic fields arising from the motion of nearby electron clouds reacting to the applied magnetic field (a diamagnetic effect). The second is a paramagnetic effect due to the occupation of excited electron states.

The coupling tensor is called the chemical shift tensor (σ) which has a frame in which it is diagonal (the PAS for the chemical shift tensor). However, as opposed to the quadrupolar interaction, the trace of the CSA tensor is different from zero and is proportional to the isotropic chemical shift

$$\sigma_{iso}^{(CS)} = \frac{1}{3}(\sigma_{XX} + \sigma_{YY} + \sigma_{ZZ}). \tag{1.60}$$

The anisotropy and asymmetry of the chemical shift interaction are also important quantities and are defined by

$$\begin{aligned} \Delta\sigma &= \sigma_{ZZ} - \frac{1}{2}(\sigma_{XX} + \sigma_{YY}) \\ &= \frac{3}{2}(\sigma_{ZZ} - \sigma_{iso}^{(CS)}) \end{aligned} \tag{1.61}$$

and

$$\eta_\sigma = \frac{3}{2}\frac{(\sigma_{XX} - \sigma_{YY})}{\Delta\sigma}. \tag{1.62}$$

The useful components of the spherical tensors for the chemical shift interaction are

$$T_{00}^{(CS)} = I_z B_0 \tag{1.63}$$

$$T_{20}^{(CS)} = \sqrt{\frac{2}{3}} I_z B_0 \tag{1.64}$$

$$T_{2\pm1}^{(CS)} = \frac{1}{\sqrt{2}} I_{\pm1} B_0 \tag{1.65}$$

with all other $T_{mn}^{(CS)}$ zero or not important for our purposes, and

$$r_{00}^{(CS)} = \sigma_{iso}^{(CS)} \tag{1.66}$$

$$r_{20}^{(CS)} = \sqrt{\frac{2}{3}}\Delta\sigma \tag{1.67}$$

$$r_{2\pm1}^{(CS)} = 0 \tag{1.68}$$

$$r_{2\pm2}^{(CS)} = \frac{\Delta\sigma}{3}\eta_\sigma \tag{1.69}$$

with these final spatial tensors defined in the PAS of the chemical shift interaction.

1.3.3 Dipole–Dipole Coupling

The dipole–dipole coupling between two spins I_i and I_j is the final spin interaction which is considered here. It has a classical analogy in the interaction of two magnetic dipoles located a distance d away from each other. The magnetic dipoles here, however, are the nuclear spins themselves. The dipole–dipole Hamiltonian is represented in spherical tensor notation as

$$\mathcal{H}_D = -2\gamma_i\gamma_j \sum_{m=-2}^{2} (-1)^m T_{2m}^{(D)} R_{2-m}^{(D)}. \tag{1.70}$$

This is a two–spin operator, very similar to the quadrupolar interaction, but now the spatial tensor refers to a distance dependent interaction. The spin terms take the form

$$T_{20}^{(D)} = \frac{1}{\sqrt{6}}[3I_{zi}I_{zj} - \boldsymbol{I}_i \cdot \boldsymbol{I}_j] \tag{1.71}$$

$$T_{2\pm1}^{(D)} = \frac{1}{\sqrt{2}}(I_{zi}I_{\pm1j} + I_{\pm1i}I_{zj}) \tag{1.72}$$

$$T_{2\pm2}^{(D)} = I_{\pm1i}I_{\pm1j} \tag{1.73}$$

while the PAS spatial components are

$$r_{20}^{(D)} = \sqrt{\frac{3}{2}}d_{ij}^{-3} \tag{1.74}$$

$$r_{2\pm1}^{(D)} = 0 \tag{1.75}$$

$$r_{2\pm2}^{(D)} = 0 \tag{1.76}$$

where d_{ij} is the length of the internuclear vector between the two nuclei.

Even though dipolar interactions are important in NMR, this interaction will no longer be considered explicitly in any of the calculations that follow. Only the CSA and quadrupolar interactions in solids are considered in this thesis. The dipolar coupling between spins in solids is a complex multi–body problem and some empirical discussion will be in order when the dipolar interactions become important in the spectra obtained. References to important works will be provided at that point.

1.4 Rotations in NMR

Rotations in NMR take two distinct forms: rotations in spin space which affect the spin variables of the system only and rotations in coordinate space which transform the spatial tensors in the Hamiltonian. The sets of spherical tensors representing the spin and spatial parts of the Hamiltonian are basis sets for irreducible representations of rotations in their respective spaces, but not in the product space [31]. Therefore, rotations of the spatial coordinates does not affect the spin variables, while rotations in spin space have no affect on the spatial tensors. Tycko, in his work on the untruncation of NMR spectra in high magnetic field [31, 32, 33], treats these rotations together in a higher–dimensional space where irreducible tensors are defined by their transformation properties under *simultaneous* rotations of spin and spatial coordinates. Under simultaneous rotations, the dipolar Hamiltonian behaves as a scalar and *untruncated* spectra similar to isotropic zero–field dipolar spectra [34] may be recovered.

1.4.1 Rotations in Spin Space

To discuss rotations in spin space the concept of the density matrix [25, 35] is introduced. A quantum mechanical system is described by a wavefunction $\mid \psi \rangle$ and in this system the expectation value of an operator $\mathcal{A}$ is

$$\langle \mathcal{A} \rangle = \langle \psi \mid \mathcal{A} \mid \psi \rangle. \tag{1.77}$$

The wavefunction may be expanded in a complete set of orthonormal basis functions $\mid \phi_n \rangle$

$$\mid \psi \rangle = \sum_n c_n \mid \phi_n \rangle \tag{1.78}$$

so that

$$\langle \mathcal{A} \rangle = \sum_{n,m} c_m^* c_n \langle \phi_m \mid \mathcal{A} \mid \phi_n \rangle. \tag{1.79}$$

The matrix of values $c_m^* c_n$ with m and n running over the dimensionality of the vector space spanning the wavefunctions of the system may be considered to represent some Hermitian operator P with

$$\langle \phi_n \mid P \mid \phi_m \rangle = c_m^* c_n \tag{1.80}$$

and then

$$\langle \mathcal{A} \rangle = \sum_{n,m} \langle \phi_n \mid P \mid \phi_m \rangle \langle \phi_m \mid \mathcal{A} \mid \phi_n \rangle. \tag{1.81}$$

Since the set $\{\mid \phi_m \rangle\}$ forms a complete set of basis functions it obeys the closure theorem

$$\sum_m \mid \phi_m \rangle \langle \phi_m \mid = 1 \tag{1.82}$$

so that

$$\langle \mathcal{A} \rangle = \sum_n \langle \phi_n \mid P\mathcal{A} \mid \phi_n \rangle \tag{1.83}$$

$$= \mathrm{Tr}[P\mathcal{A}]. \tag{1.84}$$

In NMR we deal with a large ensemble of spins in a magnetic field, yet we still need to characterize the system and make meaningful measurements. The matrix elements $c_m^* c_n$ will vary over the ensemble but the matrix elements of the observable $\mathcal{A}$ in a fixed basis set will not change. An ensemble average is measured

$$\langle \mathcal{A} \rangle_{ens} = \sum_{n,m} \overline{c_m^* c_n} \langle \phi_m \mid \mathcal{A} \mid \phi_n \rangle \tag{1.85}$$

where the overbar in $\overline{c_m^* c_n}$ denotes an ensemble average.

The density matrix ρ of the system is defined as the matrix with elements

$$\langle \phi_n \mid \rho \mid \phi_m \rangle = \overline{c_m^* c_n} = \overline{\langle \phi_n \mid P \mid \phi_m \rangle}. \tag{1.86}$$

Then the ensemble average is calculated as

$$\begin{aligned} \langle \mathcal{A} \rangle_{ens} &= \sum_{n,m} \langle \phi_n \mid \rho \mid \phi_m \rangle \langle \phi_m \mid \mathcal{A} \mid \phi_n \rangle & (1.87) \\ &= \mathrm{Tr}[\rho \mathcal{A}]. & (1.88) \end{aligned}$$

The states within the full ensemble evolve in time under the action of the Hamiltonian for the system. The time evolution of the density operator is governed by the Liouville–von Neumann equation [36]

$$\frac{d\rho}{dt} = \frac{i}{\hbar} [\rho, \mathcal{H}]. \tag{1.89}$$

If $\mathcal{H}$ is time–independent the formal solution to Eq. 1.89 is

$$\rho(t) = e^{-\frac{i}{\hbar}\mathcal{H}t} \, \rho(0) \, e^{\frac{i}{\hbar}\mathcal{H}t}. \tag{1.90}$$

At thermal equilibrium, the usual state of the spin system before an NMR experiment begins, the density matrix is

$$\rho(0) = \frac{e^{-\mathcal{H}/kT}}{Z} \tag{1.91}$$

and the diagonal elements are

$$\overline{c_m^* c_m} = \frac{e^{-E_m/kT}}{Z} \tag{1.92}$$

where E_m is the energy associated with the state $\mid \phi_m \rangle$ and Z is the partition function

$$Z = \sum_n e^{-E_n/kT}. \tag{1.93}$$

The diagonal elements correspond to the probability distribution of the eigenstates. The off–diagonal terms are all considered to be zero at thermal equilibrium since the phases of the complex coefficients are assumed to be randomized (incoherent) over the ensemble. This is the hypothesis of random phases explained by Tolman [35].

The off–diagonal elements are referred to as coherences. If an off–diagonal element is not zero, then it specifies that there is a connection between the two energy levels. A coherent phase factor then exists in the density matrix elements. For a spin system at equilibrium there is no net component of magnetization in the plane tranverse to the large magnetic field and all coherences are zero.

In time–domain NMR, the measurements made are usually the components of transverse magnetization after a pulse or set of pulses of radiofrequency electromagnetic radiation is applied to the system:

$$\langle M_x \rangle = \mathrm{Tr}[\rho I_x] \tag{1.94}$$

and

$$\langle M_y \rangle = \mathrm{Tr}[\rho I_y]. \tag{1.95}$$

The operators I_x and I_y are the spin operators for the x and y components of the nuclear spin angular momentum. The initial density matrix of the system in high–field NMR is obtained by expanding the exponential in Eq. 1.91. If the Zeeman

Hamiltonian is assumed to be the dominant spin interaction then

$$\rho_r(0) = I_z \tag{1.96}$$

where the subscript r denotes a reduced density matrix [16]. In this form, all constants (additive and multiplicative) are dropped in order to focus on the dynamic part of the spin behavior. The initial state of the system is then said to be one of z–polarization.

RF Pulses on a Spin System

Radiofrequency pulses of a well–defined length (τ), amplitude (B_1), and phase (ϕ) are used to "rotate" nuclear spin states by creating and destroying coherences between nuclear spin energy levels or changing the relative populations of these levels. The action of a pulse of radiofrequency radiation at a frequency ω to a nucleus with magnetogyric ratio γ is to add another term to the Hamiltonian of the system:

$$\mathcal{H}_{\text{rf}} = \gamma B_1 \left[I_x \cos(\omega\tau + \phi) + I_y \sin(\omega\tau + \phi) \right]. \tag{1.97}$$

It is easiest to calculate the spin behavior by entering a frame of reference rotating about the laboratory z–axis at a frequency ω [37, 38]. In this frame the pulse appears as a static field applied in the transverse plane at an angle ϕ with respect to the x–axis. The Zeeman interaction still appears as a static field along the z–axis with an effective frequency of $(\omega - \omega_0)$. The effective Hamiltonian in the rotating frame for the Zeeman interaction and rf irradiation is

$$\mathcal{H}_{\text{eff}} = \hbar(\omega - \omega_0) I_z + \hbar\omega_1 (I_x \cos\phi + I_y \sin\phi) \tag{1.98}$$

where

$$\omega_1 = \gamma B_1. \tag{1.99}$$

Note that this effective Hamiltonian is now time–independent. The phase of the pulse, ϕ, determines whether the pulse is given along the x–axis (an x pulse where $\phi = 0°$), the y–axis (a y pulse where $\phi = 90°$), or any other axis in the xy–plane.

The density matrix must also be transformed into the rotating frame before the equations of motion may be solved. It may be easily calculated [17] that the density matrix in the rotating frame, ρ_R, obeys the following equations. If

$$\rho_R = e^{-i\omega t}\, \rho\, e^{i\omega t} \tag{1.100}$$

where ω is the frequency of the rotating reference frame with respect to the laboratory, then

$$\frac{d\rho_R}{dt} = \frac{i}{\hbar}\left[\rho_R, \mathcal{H}_{\text{eff}}\right]. \tag{1.101}$$

The actions of rf pulses are now readily discerned.

The initial density matrix for the system is described by the value of the reduced density matrix (the r subscript is now dropped) for the spins in equilibrium with the lattice

$$\rho(0) = I_z \tag{1.102}$$

and a *strong* (or on–resonance) pulse of length τ has the affect of rotating the initial density matrix

$$\rho(\tau) = e^{-i\omega_1 \tau I_\phi}\, \rho(0)\, e^{i\omega_1 \tau I_\phi}. \tag{1.103}$$

The spin operator

$$I_\phi = I_x \cos\phi + I_y \sin\phi \tag{1.104}$$

defines the rotation axis and the pulse flip angle, θ, is given by

$$\theta = \omega_1 \tau \tag{1.105}$$

and corresponds to the angle through which the "vector" I_z is rotated during a pulse. Spin space may be visualized (at least for uncoupled spin–$\frac{1}{2}$ nuclei) as a three dimensional space with axes x, y, and z corresponding to the spin operators I_x, I_y, and I_z. Rigorously, the 2×2 identity matrix is also needed for full definition of the state of the system, but this additive constant is usually disregarded. The net magnetization of the system corresponds to the polarization or magnetization vector whose components are traces of the density matrix with the spin operators. A 90 degree or $\pi/2$ pulse rotates the net magnetization from the z–axis through 90 degrees into the xy plane with the final angle between the x–axis and the magnetization vector equal to $(\phi - 90)$ degrees. This will occur irrespective of resonance offset (the difference between the irradiating frequency ω and the resonance frequency of the spins) if the radiofrequency power is sufficiently strong. Otherwise, the axis about which the magnetization is rotated will not lie in the xy plane and offset effects will be present. A useful equation for determining the fate of the density matrix after an on–resonance rf pulse with flip angle θ and phase ϕ is then

$$\rho = I_x \sin\theta \sin\phi - I_y \sin\theta \cos\phi + I_z \cos\theta. \tag{1.106}$$

Free Evolution of a Spin–$\frac{1}{2}$ System

Free evolution of the spin system occurs during the periods after or between strong rf pulses. It is governed by the total Hamiltonian for the system, although (as will be seen) some parts of the Hamiltonian are more important than others. Continuing with the example of an isolated spin–$\frac{1}{2}$ in a large magnetic field, the first step is to remain in the rotating frame where the pulses were analyzed. In this frame, the large Zeeman interaction does not exist and only occurs as an

offset term from the spectrometer irradiation frequency. In a sense, the frame of reference is spinning around the laboratory z–axis near to the Larmor frequency. As a technical interest, this is also the frame of reference where the detection takes place in most NMR spectrometers [39]. In this frame all other Hamiltonians gain a time dependence and are said to be in an interaction picture. Those parts of the Hamiltonians which commute with the Zeeman Hamiltonian are fully retained (the so–called secular parts) and this will be dealt with in the following chapter under the topic of secular or coherent averaging.

After a pulse, the effective Hamiltonian of the system in the rotating frame is

$$\mathcal{H}_{\text{eff}} = e^{-i\omega t I_z}\, \mathcal{H}\, e^{i\omega t I_z} \tag{1.107}$$

where this could be a sum of many interactions. The most interesting interaction here is that of an effective shift. In Chapter 2 it will become obvious that an inhomogeneous anisotropic interaction such as the chemical shift anisotropy or the second–order quadrupolar interaction will appear as an effective Hamiltonian proportional to the spin operator I_z with a shift frequency Ω.

The solution to the Liouville–von Neumann equation for a shift Hamiltonian is

$$\rho(t) = e^{-i\Omega I_z t}\, \rho(0)\, e^{i\Omega I_z t} \tag{1.108}$$

which is again a rotation in the spin space described above. The component of the density matrix (or polarization vector) along the z–axis will not evolve under a shift Hamiltonian: the I_z terms in the exponentials commute with the effective Hamiltonian. Any magnetization in the xy plane, however, will precess under the Hamiltonian with a frequency Ω for a time t. The phase angle accumulated by the density matrix or the magnetization vector in the xy–plane will be Ωt. After a

pulse, a density matrix of I_x (corresponding to x–magnetization) will evolve into a linear combination of I_x and I_y which will be detected as a signal oscillating in the transverse plane. The density matrix becomes

$$\rho(t) = I_x \cos \Omega t + I_y \sin \Omega t \tag{1.109}$$

and the measured signal is

$$\begin{aligned} \langle M_x \rangle &= \mathrm{Tr}[\rho(t) I_x] \\ &= \frac{1}{2} \cos \Omega t \end{aligned} \tag{1.110}$$

and

$$\begin{aligned} \langle M_y \rangle &= \mathrm{Tr}[\rho(t) I_y] \\ &= \frac{1}{2} \sin \Omega t. \end{aligned} \tag{1.111}$$

Depending on the initial phase of the rf pulse, the magnetization after 90 degree nutation could lie anywhere in the xy–plane and will always evolve into a linear combination of x and y polarization under the shift Hamiltonian.

Other Hamiltonians such as the dipolar Hamiltonian have similar effects in larger spin spaces where the density matrix is not simply a linear combination of the three spin operators for a single spin. The space is larger because more spins may be coupled together and the basis set for describing all states of the spin system expands. Still, the action of the Hamiltonians is described in terms of suitable rotations in spin space. The concept of coherences and spin operators has been treated at a very elementary level in this chapter and will be expanded upon in Chapter 5 where rotations in spin space become important for selection of pure–absorption–phase lineshapes in two–dimensional NMR.

1.4.2 Rotations in Coordinate Space

The Hamiltonian of interest in the spin system may not always be aligned so that the frame which is being used to measure the spectrum (usually the rotating frame described above) coincides with the frame of reference used to describe the interactions. Also, when samples such as powders or amorphous solids are under consideration, there are many crystallites or domains within a sample which have a random or pseudo–random distribution of the PAS frames with respect to a defined measurement frame. In the case of the quadrupolar interaction, the strength and the asymmetry parameter of the EFG tensor are defined in the PAS of the quadrupolar interaction: that frame where the EFG tensor is diagonal. The same is true for the chemical shielding parameters, except that the chemical shift has an isotropic component which is independent of orientation in space. The tensor nature of the interactions simplifies the transformations to other frames since the tensor components form an irreducible representation for rotation in space and must behave like second–rank spherical harmonics under rotations. The second–rank spherical harmonics will transform only into a linear combination of the five of themselves upon rotation of the axis system [25].

The spatial tensor components in the rotated frame (R) are related to the components in the initial frame (r) by

$$R_{2m} = \sum_{m'=-2}^{2} \mathcal{D}^{(2)}_{m'm}(\alpha, \beta, \gamma) r_{2m'} \tag{1.112}$$

where the $\mathcal{D}^{(2)}_{m'm}$ are the second–order Wigner rotation matrix elements

$$\mathcal{D}^{(2)}_{m'm}(\alpha, \beta, \gamma) = e^{-im'\alpha} d^{(2)}_{m'm}(\beta) e^{-im\gamma}. \tag{1.113}$$

The second–order reduced matrix elements $d^{(2)}_{m'm}(\beta)$ are found in Table 1.1. The

angles α, β, and γ are the Euler angles through which the original system must be rotated to bring the axes in line with the new axis system. A picture of these rotations will be presented in the upcoming theoretical discussion of the NMR spectra of quadrupolar spins.

Multiple rotations are often necessary depending on the complexity of the experiment under consideration. It will be seen that it is often beneficial to mechanically reorient a sample, with rotations performed in series to determine the components of the tensor in a frame where the measurement occurs. An important example is for a time–dependent rotation of the sample spinning at a frequency ω_r about the symmetry axis in a cylindrical rotor inclined at an angle θ with respect to the magnet (laboratory) reference frame. The transformation of the spatial tensor r from its PAS to the rotor frame (through the Euler angles α, β, and γ) and subsequently to the laboratory frame takes the form

$$R_{2m} = \sum_{m'=-2}^{2} \mathcal{D}^{(2)}_{m'm}(\omega_r t, \theta, 0) \sum_{m''=-2}^{2} \mathcal{D}^{(2)}_{m''m'}(\alpha, \beta, \gamma) r_{2m''}. \qquad (1.114)$$

This rotation equation, and variations of it that encompass more rotations, will be used extensively in subsequent discussions of sample reorientation techniques in NMR.

The preliminary theory has now been set forward for the NMR of quadrupolar nuclei and in the following chapters the effect of these spin Hamiltonians on the spectra is examined. The ability to rotate the density matrix of the system (the "direction" of the magnetization vector) with rf pulses or the spatial tensors by spinning a sample provide the NMR spectroscopist with external control of the spin system. By clever use of these external conditions it may be possible to provide greater insight into the properties of solids associated with the system–dependent

m'	m 2	1	0	-1	-2
2	$\left(\frac{1+\cos\beta}{2}\right)^2$	$-\frac{1+\cos\beta}{2}\sin\beta$	$\sqrt{\frac{3}{8}}\sin^2\beta$	$-\frac{1-\cos\beta}{2}\sin\beta$	$\left(\frac{1-\cos\beta}{2}\right)^2$
1	$\frac{1+\cos\beta}{2}\sin\beta$	$\cos^2\beta-\frac{1-\cos\beta}{2}$	$-\sqrt{\frac{3}{8}}\sin 2\beta$	$\frac{1+\cos\beta}{2}-\cos^2\beta$	$-\frac{1-\cos\beta}{2}\sin\beta$
0	$\sqrt{\frac{3}{8}}\sin^2\beta$	$\sqrt{\frac{3}{8}}\sin 2\beta$	$\frac{3\cos^2\beta-1}{2}$	$-\sqrt{\frac{3}{8}}\sin 2\beta$	$\sqrt{\frac{3}{8}}\sin^2\beta$
-1	$\frac{1-\cos\beta}{2}\sin\beta$	$\frac{1+\cos\beta}{2}-\cos^2\beta$	$\sqrt{\frac{3}{8}}\sin 2\beta$	$\cos^2\beta-\frac{1-\cos\beta}{2}$	$-\frac{1+\cos\beta}{2}\sin\beta$
-2	$\left(\frac{1-\cos\beta}{2}\right)^2$	$\frac{1-\cos\beta}{2}\sin\beta$	$\sqrt{\frac{3}{8}}\sin^2\beta$	$\frac{1+\cos\beta}{2}\sin\beta$	$\left(\frac{1+\cos\beta}{2}\right)^2$

Table 1.1: The reduced Wigner rotation matrix elements $d^{(2)}_{m'm}(\beta)$ in terms of the Eulerian angle β.

spatial tensors. One major goal is the explicit determination of the chemical shift and quadrupolar parameters leading to correlations of microscopic electromagnetic surroundings of a nucleus with macroscopic properties of materials.

Chapter 2

Coherent Averaging and Motional Narrowing

A formal theoretical analysis and treatment are needed to continue the study of quadrupolar nuclei in high–field NMR, specifically the case where half–odd integer nuclear spins are present in polycrystalline solids. The theory of an average Hamiltonian is reviewed and applied to both the chemical shift anisotropy and the quadrupolar interaction. Narrowing of broadened spectra from nuclei experiencing first–order chemical shift anisotropy is established for a polycrystalline solid undergoing rapid sample reorientation. It is also shown that spinning about a single spatial axis partially averages the quadrupolar interaction in the readily observed central transition resonance, yet this averaging is insufficient for complete narrowing of the broad anisotropies. Therefore a better, more efficient means of averaging is needed. The foundation is laid for a discussion of the new techniques of dynamic–angle spinning and double rotation NMR, introduced in the following chapter.

2.1 Average Hamiltonian Theory

The idea of an "average" Hamiltonian that describes the motion of a spin system was first introduced by Haeberlen and Waugh to explain the action of multiple–pulse NMR experiments [28, 40]. If the Hamiltonian is time–dependent and periodic, and observation of the spin system is performed stroboscopically (synchronized with the period of the Hamiltonian), the effective evolution of a spin system may be described by a somewhat simpler time–independent or average Hamiltonian. Many multiple–pulse sequences for scaling or suppressing selected interactions have been developed by these methods [16, 36].

At first it would appear that this theory is neither necessary nor compatible with the discussion of the time–independent quadrupolar Hamiltonian formulated in Chapter 1. Further manipulation of the quadrupolar interaction actually falls into the category of secular averaging, where a large time–independent Hamiltonian truncates smaller terms [28, 36]. This is an effective averaging in the interaction representation of the larger and dominant term in the Hamiltonian. The ideas and expressions from average Hamiltonian theory (AHT) are generally applicable in the high–field NMR of quadrupolar nuclei with quadrupolar coupling frequencies less than approximately one–tenth of the strength of the Zeeman interaction, a regime where a considerable amount of NMR is performed. The chemical shift Hamiltonian is also affected by the coherent averaging and this is introduced first as a simpler example of secular averaging.

2.1.1 General

The general principles of AHT and coherent averaging may be found in the papers of Haeberlen [40] and Rhim [41] and are also covered in detail in the books of Mehring [16] and Ernst [36]. The most important results are compiled here as they will be needed for reference in the calculations which follow. Many subtle points, such as time–ordering in the interaction transformation, are not needed here due to the simplicity of the system.

Consider a Hamiltonian which is the sum of two terms: a dominant interaction such as the Zeeman term in high–field NMR and a weaker interaction such as the chemical shift anisotropy or the quadrupolar coupling. The dominant term in the Hamiltonian is designated $\mathcal{H}_0$ and the weaker coupling $\mathcal{H}_1$. In the interaction representation of a static Hamiltonian $\mathcal{H}_0$, the weaker term becomes time–dependent and in this interaction frame is written

$$\widetilde{\mathcal{H}_1}(t) = e^{\frac{i}{\hbar}\mathcal{H}_0 t}\, \mathcal{H}_1\, e^{-\frac{i}{\hbar}\mathcal{H}_0 t}. \tag{2.1}$$

This is equivalent to entering the rotating reference frame where the large Zeeman Hamiltonian is absent. In this picture, the *average Hamiltonian* is a sum of time–independent, Hermitian Hamiltonians (called the Magnus expansion [42])

$$\overline{\mathcal{H}}_1 = \overline{\mathcal{H}}_1^{(0)} + \overline{\mathcal{H}}_1^{(1)} + \overline{\mathcal{H}}_1^{(2)} + \cdots \tag{2.2}$$

which approximates the time–dependent Hamiltonian of Eq. 2.1.

The "zero–order" term is especially simple: it is the time average of the interaction picture Hamiltonian over one correlation period (t_c) of the large interaction:

$$\overline{\mathcal{H}}_1^{(0)} = \frac{1}{t_c}\int_0^{t_c} dt_1 \widetilde{\mathcal{H}_1}(t_1). \tag{2.3}$$

This expression may be shown to be equivalent to first–order perturbation theory [28] and, though it is the zero–order term in AHT, it is commonly referred to as the *first–order correction.* If $\mathcal{H}_0$ is the Zeeman interaction (referred to as the zero–order perturbation), then the first–order correction of Eq. 2.3 is equivalent to keeping only the terms in the Hamiltonian which commute with the Zeeman interaction. These *secular* terms are invariant with respect to rotations about the z–axis defined by the magnetic field. This is analogous to standard perturbation theory where the first correction is the diagonal component of the Hamiltonian in the unperturbed basis.

The next term in the average Hamiltonian expansion is

$$\overline{\mathcal{H}}_1^{(1)} = \frac{-i}{2t_c}\int_0^{t_c} dt_2 \int_0^{t_2} dt_1 \left[\widetilde{\mathcal{H}_1}(t_2), \widetilde{\mathcal{H}_1}(t_1)\right], \tag{2.4}$$

referred to as the *second–order correction.* Here, if the time–dependent interaction Hamiltonian commutes with itself at all times, the second– and higher–order corrections will all be zero. The second–order correction will become especially important if the first–order correction vanishes for certain transitions.

Coherent averaging theory may now be applied to two of the interactions present in our spin system in the solid state: the chemical shift anisotropy and the nuclear electric quadrupolar interaction. These interactions provide the predominant line–broadening mechanisms in the spectroscopy of numerous quadrupolar species. One assumption which is implicit is that the dipolar interaction may be dismissed as small compared to these interactions. Since it is a multiple–body interaction where the coupling between all nearby spins must be considered, it is often regarded as a broadening mechanism which convolutes a Gaussian lineshape onto the frequency dimension data obtained in an NMR spectrum [43].

2.1.2 A Collection of Spins in a Large Magnetic Field

The spin system under consideration is a collection of half–odd integer quadrupolar nuclei in a large magnetic field such that the Zeeman Hamiltonian is much larger in magnitude than the quadrupolar or chemical shift interactions. The Hamiltonian is approximately

$$\mathcal{H} = \mathcal{H}_Z + \mathcal{H}_{CS} + \mathcal{H}_Q + \mathcal{H}_D, \tag{2.5}$$

a sum of Zeeman, chemical shift, quadrupolar, and dipolar terms. The complete forms of these Hamiltonians are presented in Chapter 1.

The starting point for calculation of the energy levels of the magnetic substates is the largest interaction, the Zeeman Hamiltonian. The Larmor frequencies for nuclear spin are on the order of tens to hundreds of MHz in conventional high–field superconducting magnets (5 to 12 Tesla magnetic fields). For example, the Larmor frequencies range from 29 to 69 MHz for the oxygen–17 nucleus ($I = \frac{5}{2}$) and 56 to 135 MHz for sodium–23 ($I = \frac{3}{2}$) at these field strengths. In comparison, proton resonance frequencies at the same field strengths will vary from 200 to over 500 MHz.

Oxygen–17 is an important nucleus in the solid–state and the focus of a large part of the experimental work in this thesis, so it will be used as a typical example of a quadrupolar nucleus. A spin–$\frac{5}{2}$ nucleus such as oxygen–17 has its magnetic substates split into six equally spaced levels by the Zeeman interaction (see Fig. 2.1) with the spacing between the energy levels equal to the Larmor frequency, ω_0. For oxygen–17 the gyromagnetic ratio is $\gamma = -3.6279 \times 10^7$ rad T^{-1} sec^{-1} and the magnitude of the Larmor frequency is about 14% that of protons. If only the Zeeman interaction is considered, all five $\Delta m = 1$ (magnetic dipole) transitions for

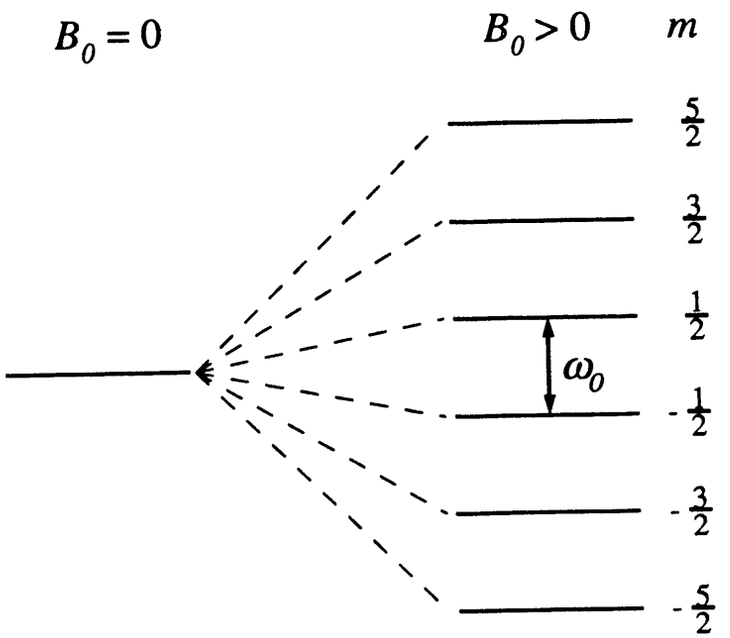

Figure 2.1: The six energy levels for a spin-$\frac{5}{2}$ nucleus under the influence of the Zeeman Hamiltonian. All $\Delta m = 1$ transitions have the same frequency difference which is the Larmor frequency ω_0.

oxygen-17 are degenerate and only one line at frequency ω_0 will appear in the NMR spectrum.

Chemical Shift Anisotropy in High Field

The chemical shift interaction is the first perturbation on the zero-order Zeeman Hamiltonian considered. Using the coherent averaging arguments of the previous section, the first-order perturbation to the Zeeman eigenvalues arise from those

terms in the Hamiltonian which commute with the Zeeman Hamiltonian. In other words, the averaging is accomplished over the Larmor period in spin space and only the $m = 0$ terms survive. Not surprisingly, these are the components containing only the spin operator I_z.

The first–order or *truncated* chemical shift Hamiltonian is

$$\begin{aligned} \overline{\mathcal{H}}_{CS}^{(0)} &= \gamma\hbar T_{00}^{(CS)} R_{00}^{(CS)} + \gamma\hbar T_{20}^{(CS)} R_{20}^{(CS)} \\ &= \hbar\omega_0 I_z \sigma_{iso}^{(CS)} + \hbar\omega_0 \sqrt{\frac{2}{3}} I_z R_{20}^{(CS)}. \end{aligned} \tag{2.6}$$

This is obtained using Eqs. 1.63, 1.64, and 1.66 for the spin and spatial tensors and the fact that the spatial tensor component $R_{00}^{(CS)}$ is the same in all axis systems. The first term contains the isotropic chemical shift and this is usually included with the Zeeman interaction, obtaining an effective Larmor frequency

$$\omega_0{}' = (1 - \sigma_{iso}^{(CS)})\omega_0. \tag{2.7}$$

Dispensing with the prime, it may always be assumed that the isotropic chemical shift is included with the Zeeman interaction. The Zeeman levels will still be separated by the same energy or frequency (see Fig. 2.2), although the spectrum will now be shifted compared to the pure Zeeman spectrum.

The second term on the right hand side of Eq. 2.6 contains the anisotropy of the chemical shift. The spatial tensor, $R_{20}^{(CS)}$, depends on the orientation of the chemical shift PAS relative to the Zeeman interaction reference frame. For a single crystal, where only one orientation of the PAS is present, the anisotropy will be the same for all equivalent nuclei and only one line will appear in the spectrum. It is more usually the case that many crystallites are present within the sample (such as in a powder or amorphous sample) and each crystallite will contribute to the observed spectrum. The result is called an anisotropic powder pattern.

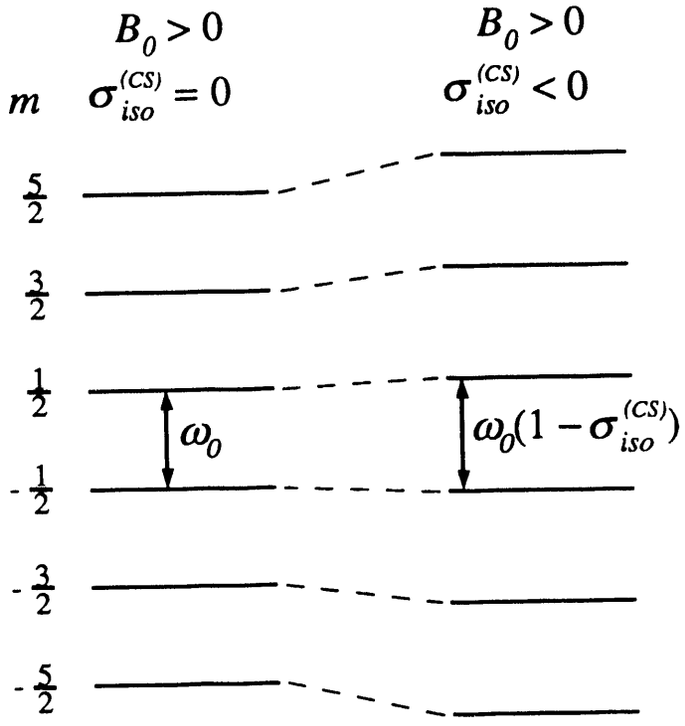

Figure 2.2: The energy levels for a spin-$\frac{5}{2}$ nucleus under the influence of the Zeeman Hamiltonian and an isotropic chemical shift.

To calculate the anisotropic frequency contributions from each possible orientation of a crystallite the energy difference between the m and $m+1$ Zeeman states is computed:

$$\begin{aligned}\omega_{aniso}^{(CS)} &= \frac{1}{\hbar}\left[\langle m+1 \mid \sqrt{\frac{2}{3}}\omega_0 I_z R_{20}^{(CS)} \mid m+1\rangle - \langle m \mid \sqrt{\frac{2}{3}}\omega_0 I_z R_{20}^{(CS)} \mid m\rangle\right] \\ &= \sqrt{\frac{2}{3}}\omega_0 R_{20}^{(CS)}. \end{aligned} \tag{2.8}$$

Following Eq. 1.112 the tensor component $R_{20}^{(CS)}$ in the laboratory frame is expressed as a sum of rotations of the principal components of the CSA tensor. The appropriate rotations defined by the Euler angles α, β, and γ are shown in Fig. 2.3. The tensor component expressed in terms of the Euler angles, the Larmor frequency, the chemical shift anisotropy ($\Delta\sigma$), and the asymmetry parameter (η_σ) is calculated using the Wigner rotation matrices of Eq. 1.113 and Table 1.1. The result is

$$\begin{aligned} R_{20}^{(CS)} &= \sum_{m=-2}^{2} \mathcal{D}_{m0}^{(2)}(\alpha,\beta,\gamma) r_{2m}^{(CS)} \\ &= \frac{1}{\sqrt{6}}\Delta\sigma\left[\left(3\cos^2\beta - 1\right) + \eta_\sigma \sin^2\beta\cos 2\alpha\right] \end{aligned} \tag{2.9}$$

so that

$$\omega_{aniso}^{(CS)} = \frac{\omega_0\Delta\sigma}{3}\left[\left(3\cos^2\beta - 1\right) + \eta_\sigma \sin^2\beta\cos 2\alpha\right]. \tag{2.10}$$

In a perfect powder the distribution of orientations for the chemical shift PAS lies isotropically on a sphere. A numerical sum over the orientations is performed to simulate the NMR spectrum. Equally spaced points in a grid on $(\alpha\beta)$–space are selected. The angle α runs from 0 to 2π while β is restricted to the angles between 0 and π. The intensity of the signal from each orientation is proportional to $\sin\beta$, and this weighting is included in the numerical sum. An alternative method [44] for calculating powder patterns is based on using triangles drawn on the faces

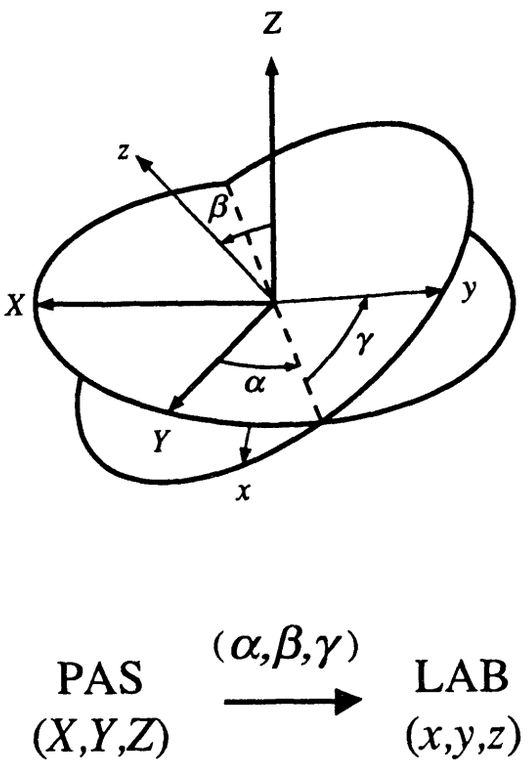

Figure 2.3: The rotations through the Euler angles α, β, and γ transform the tensor from the PAS of the interaction to the laboratory frame.

of an octahedron to define direction cosines which are calculated from indices of points, avoiding the time consuming calculation of sines and cosines by a computer. An efficient interpolation based on the triangles is also incorporated, leading to tremendous savings in computational time. Formulae for the CSA lineshapes have also been calculated analytically [28, 43] and involve the calculation or compilation of elliptic integrals. Numerical computation is usually preferred to allow a computer to vary the chemical shift parameters and obtain a best–fit to an experimental lineshape.

A sample simulation of a resonance broadened by chemical shift anisotropy is provided in Fig. 2.4. The isotropic chemical shift and the anisotropy ($\Delta\sigma$) used for the simulation are most generally written in units of ppm (parts per million) of the Larmor frequency, since in these units the spectrum is independent of the strength of the magnetic field. The simulation presented was calculated using $\sigma_{iso}^{(CS)} = 20$ ppm, $\Delta\sigma = 220.5$ ppm, and $\eta_\sigma = 0.51$. These are typical values for the chemical shift parameters found from phosphorus–31 nuclei in distorted tetrahedral sites in inorganic solids [45]. Note that the lineshape is quite broad, with a frequency width of 260 ppm. This frequency spread is much greater than the narrow lines observed in conventional NMR spectroscopy of, for example, protons in a liquid. Polycrystalline solid samples usually provide such broad lines due to the chemical shift or other coupling mechanisms that are anisotropic. After considering another important interaction in solids, the quadrupolar coupling, a method of line–narrowing in solids will be explored that will be able to average the anisotropy of the chemical shift.

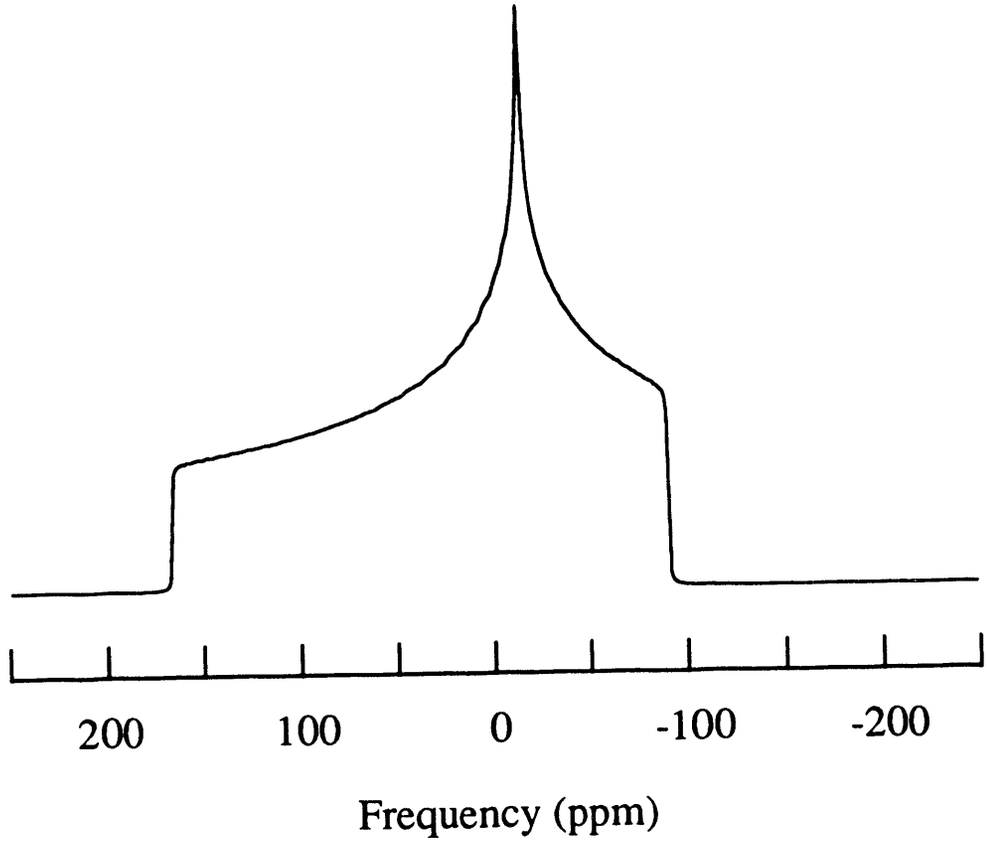

Figure 2.4: The NMR powder pattern from a nucleus with anisotropic chemical shielding. The chemical shift parameters used in the simulation are $\sigma_{iso}^{(CS)} = 20$ ppm, $\Delta\sigma = 220.5$ ppm, and $\eta_\sigma = 0.51$.

Quadrupolar Interaction in High Field

For quadrupolar nuclei in solids the quadrupolar coupling is often much larger then the chemical shift anisotropy, although this is not a definite rule. The relative magnitudes of these two interactions must be examined in the analysis of each spectrum of quadrupolar spins. At this point the chemical shift anisotropy will be ignored in the computation of the quadrupolar perturbation to the Zeeman Hamiltonian, although at a later point we will include it again.

The quadrupolar interaction in spherical tensor form is

$$\mathcal{H}_Q = C \sum_{m=-2}^{2} (-1)^m T_{2m}^{(Q)} R_{2-m}^{(Q)} \tag{2.11}$$

where Eq. 1.43 contains the spin–dependent constant C. Equations 1.37–1.39 and 1.23–1.25 provide the explicit forms of the quadrupolar spin operators and spatial tensors. In the interaction picture defined by the Zeeman Hamiltonian the quadrupolar Hamiltonian becomes time dependent,

$$\widetilde{\mathcal{H}_Q}(t) = e^{i\omega_0 I_z t}\, \mathcal{H}_Q\, e^{-i\omega_0 I_z t}. \tag{2.12}$$

Using the relation [18]

$$e^{i\omega_0 I_z t}\, T_{\ell m}\, e^{-i\omega_0 I_z t} = T_{\ell m}\, e^{i.n\omega_0 t} \tag{2.13}$$

with Eq. 2.11, the rotating frame quadrupolar Hamiltonian becomes

$$\widetilde{\mathcal{H}_Q}(t) = C \sum_{m=-2}^{2} (-1)^m e^{im\omega_0 t} T_{2m}^{(Q)} R_{2-m}^{(Q)}. \tag{2.14}$$

First–Order Calculation

The first–order average Hamiltonian is obtained using Eq. 2.3 and is the average of the interaction frame Hamiltonian:

$$\overline{\mathcal{H}}_Q^{(0)} = \frac{\omega_0}{2\pi}\int_0^{\frac{2\pi}{\omega_0}} dt_1 C \sum_{m=-2}^{2} (-1)^m e^{im\omega_0 t_1} T_{2m}^{(Q)} R_{2-m}^{(Q)}. \tag{2.15}$$

where the averaging period in this interaction picture is $t_c = 2\pi/\omega_0$, the Larmor period. The integral sign may be taken inside the summation and, since

$$\frac{\omega_0}{2\pi}\int_0^{\frac{2\pi}{\omega_0}} dt_1 e^{im\omega_0 t_1} = \delta_{m0}, \tag{2.16}$$

the first–order correction is

$$\begin{aligned} \overline{\mathcal{H}}_Q^{(0)} &= C T_{20}^{(Q)} R_{20}^{(Q)} \\ &= \frac{1}{\sqrt{6}}\left(\frac{eQ}{2I(2I-1)}\right)\left(3I_z^2 - I^2\right) R_{20}^{(Q)}. \end{aligned} \tag{2.17}$$

As with the chemical shift anisotropy, the spatial part of the interaction is explicitly written out for a nucleus in a PAS oriented by the Euler angles (α, β, γ) as

$$\begin{aligned} R_{20}^{(Q)} &= \sum_{m=-2}^{2} \mathcal{D}_{m'0}^{(2)}(\alpha,\beta,\gamma) r_{2m}^{(Q)} \\ &= \sqrt{\frac{3}{2}} eq \left[\left(3\cos^2\beta - 1\right) + \eta \sin^2\beta \cos 2\alpha\right]. \end{aligned} \tag{2.18}$$

The complete first–order quadrupolar Hamiltonian in the rotating frame is then

$$\overline{\mathcal{H}}_Q^{(0)} = \frac{e^2qQ}{8I(2I-1)}\left[\left(3\cos^2\beta - 1\right) + \eta\sin^2\beta\cos 2\alpha\right]\left(3I_z{}^2 - I^2\right), \tag{2.19}$$

and for each m substate the diagonal matrix element of the first–order quadrupolar interaction is

$$\langle m \mid \overline{\mathcal{H}}_Q^{(0)} \mid m\rangle = \frac{e^2qQ}{8I(2I-1)}\left[\left(3\cos^2\beta - 1\right) + \eta\sin^2\beta\cos 2\alpha\right]\left(3m^2 - I(I+1)\right). \tag{2.20}$$

The first-order quadrupolar frequency perturbation from the Larmor frequency between levels m and $m+1$ is

$$\begin{aligned}\omega^{(1Q)}_{m+1,m} &= \frac{1}{\hbar}\left[\langle m+1 \mid \overline{\mathcal{H}}^{(0)}_Q \mid m+1\rangle - \langle m \mid \overline{\mathcal{H}}^{(0)}_Q \mid m\rangle\right] \\ &= (2m+1)\frac{3e^2qQ}{8I(2I-1)\hbar}\left[\left(3\cos^2\beta - 1\right) + \eta\sin^2\beta\cos 2\alpha\right]. \quad (2.21)\end{aligned}$$

Several important points are worth mentioning. They are:

1. Each matrix element has an m^2 dependence. Therefore the energy levels with the same $|m|$ will be shifted by the same amount as shown in Fig. 2.5.

2. Because the absolute value of m is the same for both levels in the central $(\frac{1}{2} \leftrightarrow -\frac{1}{2})$ transition, the frequency difference for this transition only is unchanged from the zero–order Zeeman (plus chemical shift) frequency. Equivalently, in Eq. 2.21 $m = -\frac{1}{2}$ and the frequency change from the first–order quadrupolar interaction is zero.

3. For each transition other than the central transition the first–order quadrupolar frequencies are anisotropic. These are called the satellite transitions. The spectral frequencies depend on the orientation of the PAS of the electric field gradient tensor with respect to the laboratory frame. In the case of polycrystalline or amorphous solids, the contributions from all crystallites will add and an inhomogeneous powder pattern will be observed. However, the satellites may be hard to fully irradiate and detect due to their large spread in frequency as the angles are varied over the surface of a sphere. The discussion in Section 2.1.3 will address selective and non–selective irradiation of the quadrupolar transitions.

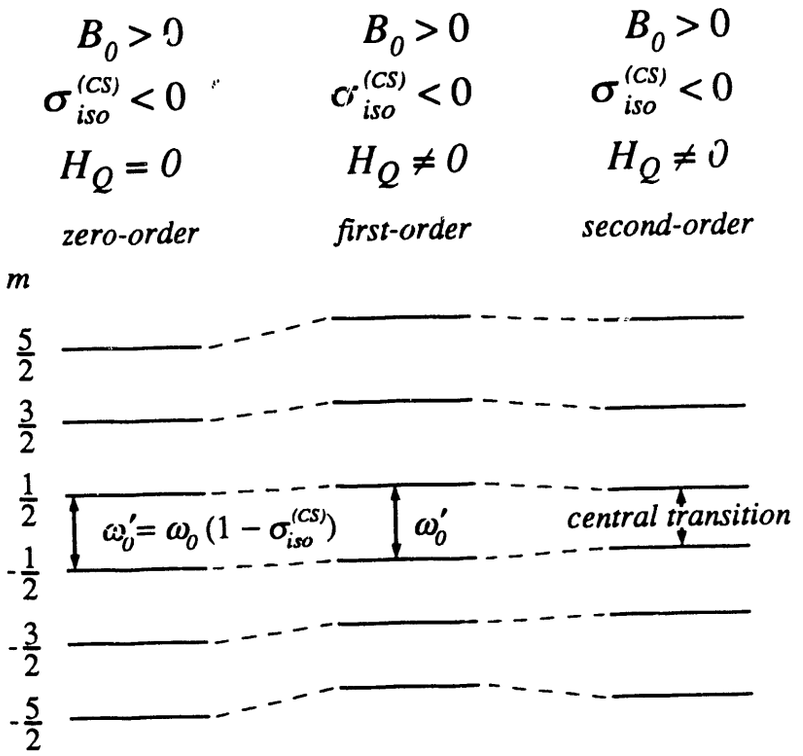

Figure 2.5: The energy levels for a spin-$\frac{5}{2}$ nucleus under the influence of the Zeeman Hamiltonian, isotropic chemical shift, and the first two orders of coherent averaging theory applied to the quadrupolar interaction. The energy level diagram is shown for the spins in a crystallite oriented in some particular direction within the magnet.

The estimated frequency spread of the first–order quadrupolar broadening of the satellite transitions in a powder is often many MHz which is much too broad to be seen in conventional solid–state NMR spectra.

Second–Order Calculation

Most importantly, in the case when only the central transition is detected, the NMR spectrum is unperturbed by first–order quadrupolar interactions. Second–order effects must then be considered to determine whether they are large enough to cause further observable perturbations to the energy levels. Extending the analysis to the next order of coherent averaging theory brings us to Eq. 2.4 which contains commutators of second–rank tensors in the spin variables and double integrals over the time variables t_1 and t_2. For the quadrupolar interaction

$$\begin{aligned}\overline{\mathcal{H}}_Q^{(1)} &= \frac{-i\omega_0}{4\pi}C^2\int_0^{\frac{2\pi}{\omega_0}}dt_2\int_0^{t_2}dt_1\sum_{m=-2}^{2}(-1)^m\sum_{m'=-2}^{2}(-1)^{m'}\times \\ &\quad \left[T_{2m}^{(Q)},T_{2m'}^{(Q)}\right]R_{2-m}^{(Q)}R_{2-m'}^{(Q)}e^{im\omega_0 t_1}e^{im'\omega_0 t_2}. \qquad (2.22)\end{aligned}$$

The result of this calculation has been published by Samoson, Kundla, and Lippmaa [12] in their study of the effects of magic–angle spinning on the NMR spectra of quadrupolar nuclei.

Results for the values of the quadrupolar spin commutators [15] provide the next set of substitutions. The useful results are

$$\left[T_{20}^{(Q)},T_{2\pm1}^{(Q)}\right] = \pm\frac{\sqrt{3}}{2}\left(4{I_z}^2\mp4I_z+1\right)I_{\pm1} \qquad (2.23)$$

$$\left[T_{20}^{(Q)},T_{2\pm2}^{(Q)}\right] = \pm\frac{12}{\sqrt{6}}\left(I_z\mp1\right)I_{\pm1}^2 \qquad (2.24)$$

$$\left[T_{21}^{(Q)},T_{2-1}^{(Q)}\right] = \frac{1}{2}\left(4I^2-8{I_z}^2-1\right)I_z \qquad (2.25)$$

$$\left[T_{22}^{(Q)},T_{2-2}^{(Q)}\right] = \left(2I^2-2{I_z}^2-1\right)I_z, \qquad (2.26)$$

where

$$I_{\pm 1} = \mp \frac{1}{\sqrt{2}} \left(I_x \pm i I_y \right). \tag{2.27}$$

The double integrals over the time variables are performed, keeping only the non-zero results. Expression 2.22 for the second-order quadrupolar Hamiltonian becomes

$$\begin{aligned}
\overline{\mathcal{H}}_Q^{(1)} &= \left(\frac{eQ}{4I(2I-1)} \right)^2 \frac{1}{\omega_0} \left\{ 2R_{21}^{(Q)} R_{2-1}^{(Q)} \left(4I^2 - 8{I_z}^2 - 1 \right) I_z + \right. \\
& 2R_{22}^{(Q)} R_{2-2}^{(Q)} \left(2I^2 - 2{I_z}^2 - 1 \right) I_z - \\
& \sqrt{12} R_{20}^{(Q)} R_{2-1}^{(Q)} \left(4{I_z}^2 - 4I_z + 1 \right) I_{+1} - \\
& \sqrt{12} R_{20}^{(Q)} R_{21}^{(Q)} \left(4{I_z}^2 + 4I_z + 1 \right) I_{-1} + \\
& 4\sqrt{6} R_{20}^{(Q)} R_{2-2}^{(Q)} \left(I_z - 1 \right) I_{+1}^2 + \\
& \left. 4\sqrt{6} R_{20}^{(Q)} R_{22}^{(Q)} \left(I_z + 1 \right) I_{-1}^2 \right\}.
\end{aligned} \tag{2.28}$$

The perturbation in the central transition eigenfrequencies is obtained from matrix elements of the second-order Hamiltonian in the Zeeman basis. The matrix elements are computed for the $m = \frac{1}{2}$ and $m = -\frac{1}{2}$ levels and the difference is the second-order quadrupolar energy (in frequency units):

$$\begin{aligned}
\omega_{\frac{1}{2},-\frac{1}{2}}^{(2Q)} &= \frac{1}{\hbar} \left[\langle \frac{1}{2} \mid \overline{\mathcal{H}}_Q^{(1)} \mid \frac{1}{2} \rangle - \langle -\frac{1}{2} \mid \overline{\mathcal{H}}_Q^{(1)} \mid -\frac{1}{2} \rangle \right] \\
&= \left(\frac{eQ}{4I(2I-1)\hbar} \right)^2 \frac{[4I(I+1)-3]}{\omega_0} \left\{ 2R_{21}^{(Q)} R_{2-1}^{(Q)} + R_{22}^{(Q)} R_{2-2}^{(Q)} \right\}.
\end{aligned} \tag{2.29}$$

The anisotropy of this frequency lies in the products of the spatial spherical tensors $R_{21}^{(Q)} R_{2-1}^{(Q)}$ and $R_{22}^{(Q)} R_{2-2}^{(Q)}$. There is also a shift of the center of gravity of the resonance line, which may be calculated by integrating the full equation over the surface of a sphere. This must wait, however, until the spatial dependence is obtained explicitly.

The spherical tensors must be expanded once again in terms of the Wigner rotation matrices :

$$\begin{aligned} R_{2m}^{(Q)} R_{2-m}^{(Q)} &= \sum_{m'=-2}^{2} \mathcal{D}_{m'm}^{(2)}(\alpha,\beta,\gamma) r_{2m'}^{(Q)} \sum_{m''=-2}^{2} \mathcal{D}_{m''-m}^{(2)}(\alpha,\beta,\gamma) r_{2m''}^{(Q)} \\ &= \sum_{m'=-2}^{2} \sum_{m''=-2}^{2} e^{i(m'+m'')\alpha} d_{m'm}^{(2)}(\beta) d_{m''-m}^{(2)}(\beta) r_{2m'}^{(Q)} r_{2m''}^{(Q)} \end{aligned} \tag{2.30}$$

for $m = 1$ and $m = 2$.

Due to symmetries of the reduced Wigner matrix elements with respect to switching of indices (see Table 1.1 again), and the form of the exponential terms in the summation, the expression for the second–order frequencies takes a simplified form as an expansion of cosines of even multiples of the angles α and β:

$$\omega_{\frac{1}{2},-\frac{1}{2}}^{(2Q)} = A \sum_{i=0}^{2} \sum_{j=0}^{2} a_{ij} \cos(2i\alpha) \cos(2j\beta) \tag{2.31}$$

with

$$A = \left(\frac{e^2 qQ}{4I(2I-1)\hbar} \right)^2 \frac{[4I(I+1)-3]}{8\omega_0}. \tag{2.32}$$

The angle γ fails to appear in the equation since the change in the sign of m in the products $R_{21}R_{2-1}$ and $R_{22}R_{2-2}$ always results in exponential terms containing γ which multiply to unity in the summation. The anisotropic expansion is calculated symbolically with a program (**static.m**) written in the *Mathematica*™ programming environment. The code for **static.m** and another program containing the definition of the Wigner rotations needed (**wigner.m**) appears in Appendix C. The values of the coefficients a_{ij} in Eq. 2.31 are compiled in Table 2.1

The second–order quadrupolar frequency of Eq. 2.31 has an isotropic component which is calculated by integration of this frequency expansion over the surface of a sphere. The isotropic frequency shift, $\omega_{\frac{1}{2},-\frac{1}{2}}^{(2Q,iso)}$, is

i	j	a_{ij}
0	0	$-\frac{5}{32}(18+\eta^2)$
0	1	$-\frac{9}{4}(1-\frac{5}{6}\eta^2)$
0	2	$\frac{9}{32}(18+\eta^2)$
1	0	$\frac{39}{8}\eta$
1	1	$-\frac{3}{2}\eta$
1	2	$-\frac{27}{8}\eta$
2	0	$\frac{27}{32}\eta^2$
2	1	$-\frac{9}{8}\eta^2$
2	2	$\frac{9}{32}\eta^2$

Table 2.1: Coefficients in the anisotropic frequency cosine expansion for the second–order energy difference in the central transition of a quadrupolar nucleus.

$$\begin{aligned}
\omega^{(2Q,iso)}_{\frac{1}{2},-\frac{1}{2}} &= \frac{1}{4\pi}\int_0^{\pi} d\beta \sin\beta \int_0^{2\pi} d\alpha \;\; \omega^{(2Q)}_{\frac{1}{2},-\frac{1}{2}} \\
&= \frac{1}{4\pi}\int_0^{\pi} d\beta \sin\beta \int_0^{2\pi} d\alpha A \sum_{i=0}^{2}\sum_{j=0}^{2} a_{ij}\cos(2i\alpha)\cos(2j\beta) \qquad (2.33)
\end{aligned}$$

which yields upon integration

$$\begin{aligned}
\omega^{(2Q,iso)}_{\frac{1}{2},-\frac{1}{2}} &= A\left(a_{00} - \frac{1}{3}a_{01} - \frac{1}{15}a_{02}\right) \\
&= -A\frac{12}{5}\left(1 + \frac{1}{3}\eta^2\right) \\
&= -\frac{3}{10}\left(\frac{e^2qQ}{4I(2I-1)\hbar}\right)^2 \frac{[4I(I+1)-3]}{\omega_0}\left(1 + \frac{1}{3}\eta^2\right). \qquad (2.34)
\end{aligned}$$

This result shows that the second–order quadrupolar interaction has an isotropic component which is independent of crystallite orientation and therefore the same for all equivalent spins in the sample. In frequency units it is inversely dependent on the strength of the magnetic field. It also contains a product of the quadrupolar parameters, usually separated into e^2qQ/h and η which determine the strength and the asymmetry of the local electric field gradient.

This analysis shows that the central transition lineshape from a second–order quadrupolar perturbation will be anisotropic. The PAS is tied to the crystal axis system or possibly modulated in time for a sample with internal motion present [15]. In any case, an ideal polycrystalline sample will yield a powder lineshape whose shape may be calculated numerically. One such simulation is presented in Fig. 2.6 for a spin–$\frac{5}{2}$ nucleus (oxygen–17) in a magnetic field of 9.4 T. The quadrupolar parameters are moderate values for EFG components (e^2qQ/h = 5.0 MHz and $\eta = 0$) which may appear, for example, in bridging oxygens in SiO_2 polymorphs [46]. Note that the center of gravity of the spectrum is shifted from the Larmor frequency (the zero of the frequency axis) and this shift is *not* an isotropic chemical shift but rather an isotropic second–order quadrupolar shift This isotropic shift may be

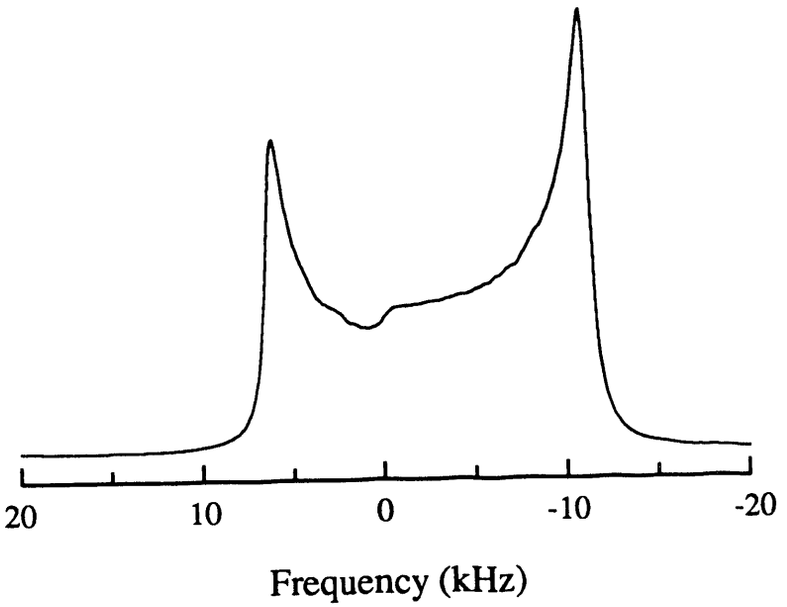

Figure 2.6: Simulation using a powder average over a sphere of the second–order quadrupolar frequencies in Eq. 2.31. The parameters used are for oxygen-17 nuclei in a 9.4 T magnetic field with $e^2qQ/h = 5.0$ MHz and $\eta = 0$. As described in the text, only the central transition is shown.

calculated using Eq. 2.34 and it is approximately 3 kHz at this field strength.

The spectrum in Fig. 2.6 reveals that the second–order lineshape is wide, with a spectral spread on the order of 20 kHz or 370 ppm at a Larmor frequency of 54.24 MHz. This is quite large and noticeable in high–field magnetic resonance. Resolution from a commercial or home–built NMR spectrometer is commonly on the order of 1 Hz or a fraction thereof, and the usual limitation on linewidth is the homogeneity of the large magnetic field. So the effects of the second–order contribution to the central transition lineshapes of quadrupolar nuclei must often be considered because very broad lines will be observed in the NMR spectra. The

lineshape is useful in that it provides a measure of the quadrupolar parameters. Once again, spectral simulations and computer best–fits may be used to determine the quadrupolar parameters and possibly the chemical shift parameters. Broad and overlapping spectral resonances, however, do not allow full interpretation in terms of shielding and quadrupolar effects for distinct nuclear sites, and only in the case of single or well–resolved resonances can a full analysis be undertaken.

Also of interest is the dependence of the isotropic and anisotropic second–order quadrupolar frequencies on the inverse of the Larmor frequency for the spins. For the same nucleus, changing magnetic fields will have the effect of changing both the width of the spectrum (the anisotropic spread is smaller at higher field) and the position of the center of gravity of the resonance (the isotropic second–order quadrupolar shift becomes less negative at higher field strengths). Conventional wisdom may then suggest that the best resolution may be obtained at higher field strengths and this is true for a purely quadrupolar resonance. However, the frequency spread due to the chemical shift anisotropy *increases* with an increase in Larmor frequency, and so further broadening of the spectrum may occur if the CSA is large.

2.1.3 The Effect of RF Pulses

The general effect of radiofrequency pulses on a spin–$\frac{1}{2}$ system was studied in Chapter 1. Further care must be taken when describing the excitation and detection of magnetic resonances in a quadrupolar system. Complete work on this subject was pursued by Schmidt [47] in the early 1970s, although selective excitation in fictitious spin–$\frac{1}{2}$ systems, including quadrupolar resonances, was discussed much earlier by Abragam [18]. A particularly illuminating paper by Man and cowork-

ers [48] calculates the spectral intensities and rotation angles from radiofrequency pulses for selective and non–selective excitation of all single–quantum ($\Delta m = 1$) transitions from nuclei with spins ranging from $I = \frac{1}{2}$ to $I = \frac{9}{2}$. The results are important for correctly performing quantitative NMR experiments and for the theory of nutation NMR experiments [49, 50, 51], where nuclear sites with different values of the quadrupolar coupling constant may be separated by their behavior during a series of strong radiofrequency pulses [52, 53, 54, 55]. The calculations performed by Man [48] only take into account the first–order quadrupolar interaction but this is sufficient for describing the excitation and detection behavior of the spins.

RF Pulses on a Quadrupolar System

Consider a collection of non–interacting quadrupolar spins with the spin angular momentum I being half odd–integral and greater than one. The central ($\frac{1}{2} \leftrightarrow -\frac{1}{2}$) transition is distinguished from the satellite ($m \leftrightarrow m-1$) transitions because it is not affected by first–order quadrupolar interactions. For any particular crystallite there will be a resonance from the central transition and each of the $(2I-1)$ satellite transitions. The frequency differences between the satellite resonances and the central transition will appear in the Hamiltonian as a fictitious chemical shift (as in Eq. 2.21)

$$\mathcal{H}^{\Delta}_{m+1,m} = \Omega_Q(2m+1)I_z \tag{2.35}$$

for the $m \leftrightarrow m+1$ transition. Writing this as an effective chemical shift is possible because the shifts of the satellite resonances are linear in m. The quantity Ω_Q depends on the quadrupole coupling constant, the asymmetry parameter, and the orientation of the crystallite within the magnetic field. A further second–order shift

takes place for both the central transition and the satellites, but this is smaller by a factor on the order of Ω_Q/ω_0 and will not disturb this analysis.

The important quantities to calculate are the initial value of the free induction decay (which will be maximized after a full 90° pulse) and the intensity of the spectral line from the $m+1 \leftrightarrow m$ transition. Two distinct regimes are present. The first is that of non–selective irradiation where the radiofrequency magnetic field is strong compared to both the quadrupolar interaction and the fictitious offset term of Eq. 2.35. The details of the calculation of the initial value of the FID and the spectral intensity are given in Ref. [48] and it is found that both quantities are proportional to the square of the $(m+1,\, m)$ matrix element of the spin operator I_x

$$\begin{aligned} (\xi_{m+1,m})^2 &= |\langle m+1\,|I_x|\,m\rangle|^2 \\ &= I(I+1) - m(m+1). \end{aligned} \tag{2.36}$$

Further, as long as the radiofrequency field is strong enough to irradiate and detect all transitions, the length of a 90° pulse for the different transitions will be independent of the value of $(\xi_{m+1,m})^2$ obtained from Eq. 2.36. This occurs because the radiofrequency Hamiltonian is considered as the only Hamiltonian operative during the pulse and thus the nutation frequencies for all of the transitions are equal. The integrated intensity will differ for each transition and it is found to follow a $(\xi_{m+1,m})^2$ dependence. For example, the satellite transitions for a spin–$\frac{3}{2}$ nucleus such as sodium–23 will have 25% less intensity than the central transition. In this case the 90° nutation time is the same as if *no* quadrupolar interaction were present.

Often it is impossible or undesirable to provide full non–selective excitation to the spin system. If the radiofrequency field strength is much less than the quadrupolar coupling strength, only selective excitation can be accomplished. The

effect of the pulse may now be neglected on all the transitions apart from the resonant transition which, for our purposes, will only be considered to be the central transition as the satellite transitions are spread over a larger frequency range than the central transition resonance. Only the two levels closest to the on–resonance frequency will be strongly perturbed under these conditions. It is calculated that the initial intensity of the FID and the relative line intensities are scaled down from the non–selective case by an additional factor of ξ. Further, the time for 90° nutation of the magnetization vector in the selective case is also decreased by a factor of ξ. Hence, for the central transition, 90° pulse times will be scaled by $I + \frac{1}{2}$ for a spin I nucleus. For nuclei such as sodium–23 ($I = \frac{3}{2}$) or oxygen–17 ($I = \frac{5}{2}$) we expect to find pulse widths for selective excitation of the central transition to be one–half and one–third as long as those found for non–selective irradiation.

A stern warning must be given here: *the selectivity of pulses must always be checked* when performing experiments in order to determine whether any assumption made in the theoretical development of the experiments has been violated. This may include the questions of treatment of other transitions in the time–development of the system or whether quantitative spectral intensities will be obtained. To check the selectivity, 90° pulse lengths in the sample under consideration should be compared to 90° pulse lengths in a sample where quadrupolar coupling is known to be negligible. This occurs, for example, in a cubic solid (such as NaCl) or a liquid (such as $H_2^{17}O$).

2.2 Motional Narrowing by Sample Reorientation

2.2.1 Introduction

One advantage an experimentalist has when using NMR spectroscopy is the ability, at least in principle, to distinguish individual resonances from distinct nuclear sites in a sample. A well–known example is the fact that the protons from an aromatic ring will resonate at a slightly different frequency (a few parts per million of the Larmor frequency) from those in a methyl group. The proton sites are magnetically inequivalent due to the difference in the local chemical shifts, which may then be correlated with local bonding and electronic environments. These differences are quite well established in the liquid state where resolved resonances with widths less than one Hz are observed. Other conditions which may cause changes in resonances are topological and geometrical effects (seen through the scalar couplings in liquids), as well as the dipolar and quadrupolar couplings which become important in the spectra of the solid state.

In order to better understand local bonding and electronic environments in solids, the optimal spectra would have full separation of resonances arising from magnetically inequivalent sites. The rapid, isotropic motions of molecules in a liquid occur on time scales much shorter than the Larmor period of the spins and therefore during one Larmor period the spins experience an average orientational environment. Interactions that have a scalar (or isotropic) component, such as the chemical shift and scalar coupling, are not averaged to zero but rather to their isotropic values. The isotropic chemical shift, as well as the scalar couplings which split lines into multiplet patterns, are used in high–resolution one– and two–dimensional

NMR to investigate molecular structure in liquids [56]. The dipolar and quadrupolar interactions are described by traceless tensors: they have no residual effect in the spectra usually observed. However, effects such as relaxation [10, 57] and the nuclear Overhauser effect [58, 59] are important in many cases and are caused by higher–order effects of these traceless interactions.

Early in the development of NMR, Andrew [60] and Lowe [61] realized that time–dependent motion could be imposed upon a solid to mimic or approximate the isotropic motion in liquids. In their experiments, the second–rank tensors describing the spatial interactions are modulated in time by the rotational motion of a cylindrical rotor containing the sample. The rotor is set spinning while inclined at an angle θ with respect to the direction of the large external magnetic field. It was found that at a certain angle, the "magic angle", the spinning averages the first–order interactions. An added criterion for complete averaging is that the rotor must spin quickly compared to the frequency spread of the interaction. The theoretical aspects of sample spinning are described below, first for the chemical shift anisotropy in polycrystalline solids and then for the quadrupolar interaction. The result of ultimate importance will be a calculation of the central transition frequencies from quadrupolar nuclei in solids while spinning the sample at an arbitrary angle with respect to the field.

2.2.2 Sample Spinning I: Chemical Shift Anisotropy

The theory developed above for the chemical shift anisotropy led to a truncated first–order Hamiltonian, after removing the isotropic shift, in the form

$$\overline{\mathcal{H}}_{CS}^{(0)} = \gamma T_{20}^{(CS)} R_{20}^{(CS)} \tag{2.37}$$

with the appropriate spherical tensors given by Eqs. 1.64 and 1.67–1.69, the spatial tensor components being defined in the principal axis system for the chemical shift interaction. The expression for $R_{20}^{(CS)}$ as a sum of rotations of the principal components of the CSA tensor revealed why this interaction is anisotropic: it depends upon the orientation in the laboratory of a crystallite containing the observed nuclei. The Hamiltonian for the system was a scalar (isotropic) quantity before the large magnetic field truncated the interaction by imposing a preferred spatial direction on the sample. The magnetic field also gives rise to the chemical shift interaction.

Now consider placing the entire sample within a cylindrical holder which will be rotated at a frequency ω_r about an axis inclined to the magnetic field at an angle θ. A helpful diagram of this is shown in Fig. 2.7. A time–dependent rotation is imposed upon the spatial tensor $R_{20}^{(CS)}$ and the spatial tensor in the laboratory frame is

$$\begin{aligned} R_{20}^{(CS)} &= \sum_{m'=-2}^{2} \mathcal{D}_{m'0}^{(2)}(\omega_r t, \theta, 0) \sum_{m''=-2}^{2} \mathcal{D}_{m''m'}^{(2)}(\alpha\beta\gamma) r_{2m''}^{(CS)} \\ &= \frac{\Delta\sigma}{2\sqrt{6}} \left(3\cos^2\theta - 1\right) \left[\left(3\cos^2\beta - 1\right) + \eta_\sigma \sin^2\beta \cos 2\alpha\right] \\ &\quad + C_1 \cos\omega_r t \\ &\quad + C_2 \cos 2\omega_r t \\ &\quad + S_1 \sin\omega_r t \\ &\quad + S_2 \sin 2\omega_r t \end{aligned} \tag{2.38}$$

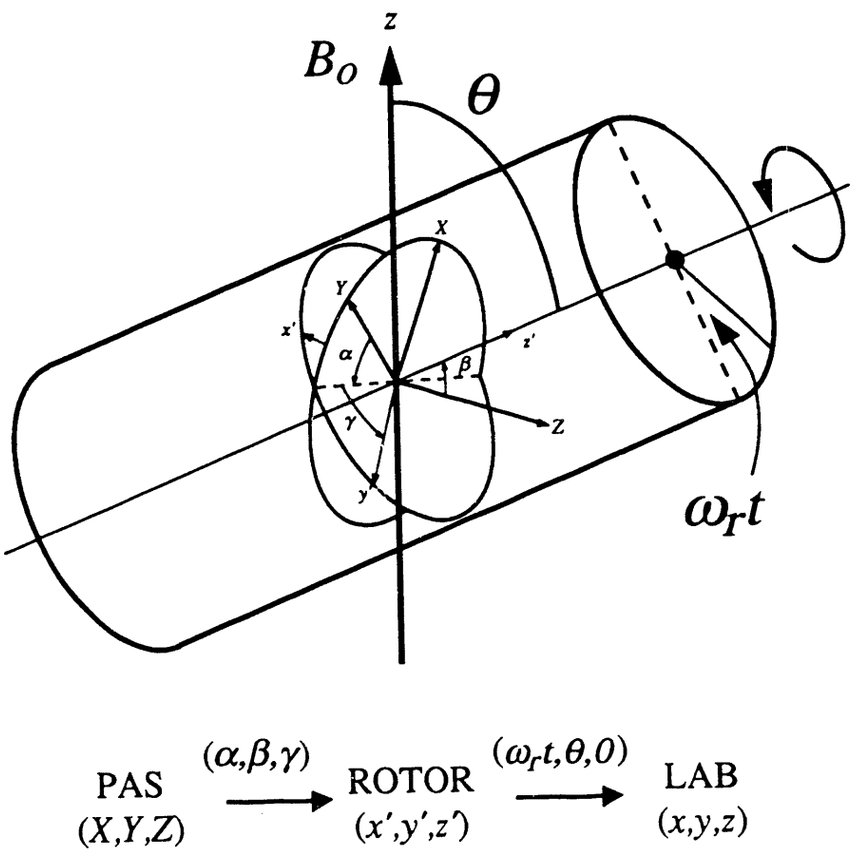

Figure 2.7: The rotations through the Euler angles α, β, and γ take the tensor from the PAS of the interaction to the rotor frame. The further rotations are determined by the product of the rotor frequency and time of rotation as well as the orientation of the rotor in the laboratory.

with

$$C_1 = -\frac{\Delta\sigma}{2\sqrt{6}} \sin 2\theta[3 - \eta_\sigma \cos 2\alpha] \sin 2\beta \tag{2.39}$$

$$C_2 = \frac{\Delta\sigma}{2\sqrt{6}} \sin^2\theta[3\sin^2\beta + \eta_\sigma \cos 2\alpha(1 + \cos^2\beta)] \tag{2.40}$$

$$S_1 = -\frac{\Delta\sigma}{\sqrt{6}} \sin 2\theta\eta_\sigma \sin 2\alpha \sin\beta \tag{2.41}$$

$$S_2 = -\frac{\Delta\sigma}{\sqrt{6}} \sin^2\theta\eta_\sigma \sin 2\alpha \cos\beta. \tag{2.42}$$

The time–independent and time–dependent parts of this tensor component may be considered separately.

The time–independent part of the chemical shift frequency remains anisotropic

$$\omega_{CS}^{aniso} = \frac{\omega_0\Delta\sigma}{6}\left(3\cos^2\theta - 1\right)\left[\left(3\cos^2\beta - 1\right) + \eta_\sigma \sin^2\beta \cos 2\alpha\right], \tag{2.43}$$

but now there is an additional angular factor when this expression is compared to the static case. This polynomial is the second Legendre polynomial of $\cos\theta$,

$$P_2(\cos\theta) = \frac{1}{2}\left(3\cos^2\theta - 1\right). \tag{2.44}$$

It has the same angular form as the d_{z^2}–orbitals encountered in the study of hydrogen–like atoms [2]. Since this polynomial has zeroes along the real axis, it is possible to completely average the chemical shift anisotropy by solving

$$P_2(\cos\theta) = 0 \tag{2.45}$$

and setting the rotor axis to this special angle.

The second Legendre polynomial is plotted in both linear and polar coordinates in Fig. 2.8, and in the first quadrant the solution is the magic angle, $\theta_m^{(2)} = 54.74°$, where the superscript is a reminder that this is a magic angle for second–rank tensor interactions. With the anisotropic term averaged to zero by magic–angle spinning

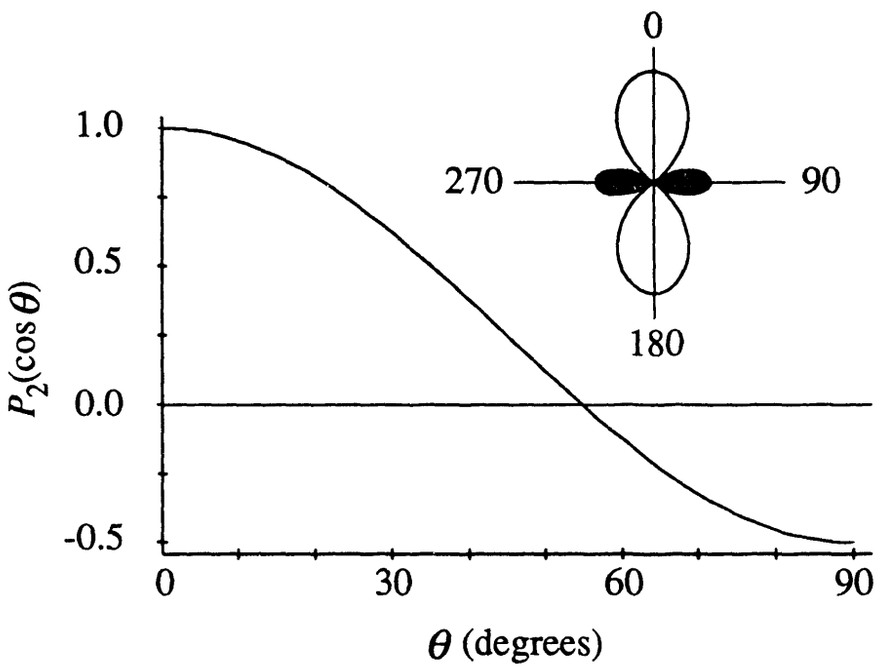

Figure 2.8: The second Legendre polynomial, $P_2(\cos\theta)$, as a function of angles in the first quadrant of a circle. The polar form is also shown at the upper right with shaded areas designating negative excursions of the function.

(MAS) only the isotropic chemical shift will cause inequivalent spins to appear at different spectral frequencies, thus providing resolution and spectral separation for solids approaching that available in NMR of the liquid–state [62, 63].

The time–dependent terms contain modulations at frequencies equal to and twice that of the spinning frequency. This leads to spinning sidebands [64, 65] at integer multiples of the spinning frequency for most spinning angles θ. If the rotation frequency is very fast so that ω_r is greater than the frequency spread in the

resonance from the static sample, these time–dependent terms become unimportant [64]. Discussion of any spinning sidebands present in the spectrum, however, necessitates retention of these terms. Information about the full anisotropy (averaged by magic–angle spinning) is retained in the sideband pattern [65] and an analysis of the sidebands can be useful in complete characterization of the local environment. If the ultimate goal is better resolution of the resonances from individual sites, then fast spinning at the magic angle is desired. Methods of suppressing spectral sidebands in MAS at slower spinning speeds have also been introduced [66, 67].

Other interesting angles for sample spinning besides the magic angle are $\theta = 0°$ and $\theta = 90°$. Spectra obtained while spinning parallel to the magnetic field (along the z–axis where $\theta = 0°$) are equivalent to the static spectrum as the full anisotropy is present: the second Legendre polynomial is unity and all time modulated terms disappear. A full powder pattern will appear from each inequivalent nuclear site in a polycrystalline solid. With the spinner axis perpendicular to the field ($\theta = 90°$) the value of $P_2(\cos\theta)$ is negative one–half and a scaled powder pattern of one–half the width of the static pattern is obtained, reversed along the frequency axis. Further, since $\sin\theta = 1$ and $\sin 2\theta = 0$ at $\theta = 90°$, the odd–order time–dependent terms will vanish and only even–order sidebands at multiples of twice the rotational frequency are present in the spectrum. Although the full chemical shift parameters could be determined from the powder patterns obtained at these angles, the widths of the patterns could cause overlap and distortion of other powder patterns rendering analysis difficult, if not impossible.

Many reviews of the NMR of solids include discussions of magic–angle sample spinning and the use of MAS to remove chemical shift anisotropy and other

first–order broadening [68, 69, 70]. While the ideas presented above introduce the methodology and utility of sample reorientation, the primary concern here is the behavior of quadrupolar spins under sample rotation. If similar line–narrowing could be achieved for the anisotropic resonances arising from the second–order quadrupolar interaction, high–resolution NMR would be applicable to a much wider group of nuclei in solids.

2.2.3 Quadrupolar vs. Chemical Shift Anisotropies

The second–order quadrupolar interaction is more complex than the chemical shift anisotropy and examination of the theory developed up to this point helps to explain both the similarities and the differences. When truncated to first–order, both interactions have the form

$$\overline{\mathcal{H}}_{\lambda}^{(0)} = C^{\lambda} T_{20}^{\lambda} R_{20}^{\lambda} \tag{2.46}$$

which is an anisotropic Hamiltonian due to the spatial anisotropy of the R_{20}^{λ} term. Expansions of R_{20}^{λ} in terms of the tensor components in the principal axis systems of both the quadrupolar and chemical shift interactions look similar as the angular rotations are the same. The only difference between the spatial tensors is the coupling parameters used in each case and the different constants in the C^{λ} terms. However, one can easily see the connection between the different coupling constants and asymmetry parameters. A major distinction is that the chemical shift interaction also has an isotropic term which shifts the frequency from each crystallite contributing to the powder pattern by an equal amount. Nonetheless, the first–order, static spectrum angular anisotropies have the same form in both Eqs. 2.10 and 2.21 and the NMR spectra from the quadrupolar satellite transitions will re-

semble those from the chemical shift anisotropy. The width of the pattern will be scaled by the order (m value) of the satellite transition. There will not be a single powder pattern for the quadrupolar satellites, but a total of $2I - 1$ overlapping, broad patterns.

The most distinct dissimilarity enters in the form of the spin operator T_{20}^{λ} for the two interactions. For the CSA, $T_{20}^{(CS)}$ is a single–spin operator, $I_z B_0$. Matrix elements of $T_{20}^{(CS)}$ are linear in m (the magnetic quantum number for the Zeeman level) and the matrix form of the operator is diagonal in the Zeeman basis. The energy differences for all $\Delta m = 1$ transitions are therefore the same. The quadrupolar spin operator $T_{20}^{(Q)}$ is a bilinear spin operator with no magnetic field dependence, $1/\sqrt{6}[3I_z^2 - I^2]$. The I^2 part of the operator is identical for all magnetic substates and is proportional to the unit operator: it can not affect spin evolution. As opposed to the CSA Hamiltonian, the matrix elements of the first–order quadrupolar Hamiltonian depend on m^2, and the central transition is unaffected by first–order quadrupolar coupling. The satellite transitions do have anisotropic quadrupolar shifts, resulting in powder patterns centered at the same frequency as the central transition (to first–order). The first–order width of the satellites is usually large enough to render them unobservable as it would be difficult to fully irradiate them, while their spectral intensity (reduced from that of the central transition according to Sec. 2.1.3) would be spread out over that entire frequency width.

In the case where the satellites are detected [71], full quadrupolar parameters and isotropic chemical shifts may be obtained. This is especially useful for nuclei with moderately large gyromagnetic ratios, high–spin values, and small quadrupolar coupling constants (such as some aluminum–27 nuclei in solids), as all of these

factors reduce the spectral width. With MAS, the quadrupolar satellite transitions should also be narrowed in first–order exactly like the chemical shift anisotropy. This has been observed in aluminum–27 [72], but the large spectral spread of the satellites necessitates careful analysis of the multitude of sidebands present in the spectrum.

2.2.4 Sample Spinning II: Quadrupolar Interactions

After the initial development of the magic–angle spinning technique, it was realized that if quadrupolar effects could not be accounted for by first–order perturbation theory then sample spinning would not be able to completely narrow these resonances [70]. Later, the subject was studied in more detail and the theory was developed for both magic–angle spinning of quadrupolar nuclei [12] and spinning at *any* angle with respect to the field [13]. The MAS results will be treated as a special case of sample spinning of quadrupolar nuclei in a rotor at an arbitrary angle with respect to the magnetic field.

The calculation for the effect of sample spinning on a quadrupolar central transition experiencing a prominent second–order contribution to the linewidth follows the same arguments as for the chemical shift anisotropy, but now includes a more complex spatial dependence because of the appearance of *products* of the spatial tensors for the second–order quadrupolar anisotropic frequencies (Eq. 2.29). The second–order frequency shift for the central transition of a quadrupolar nucleus was calculated above and is

$$\omega^{(2Q)}_{\frac{1}{2},-\frac{1}{2}} = \left(\frac{eQ}{4I(2I-1)\hbar}\right)^2 \frac{[4I(I+1)-3]}{\omega_0} \left\{2R^{(Q)}_{21}R^{(Q)}_{2-1} + R^{(Q)}_{22}R^{(Q)}_{2-2}\right\}. \qquad (2.47)$$

Under the conditions of sample spinning, the spatial tensors are expressed as a

product of a series of rotations from the quadrupolar PAS to the rotor frame, and finally to the laboratory (or interaction) frame (Fig. 2.7). Some may consider this a mathematical exercise which must be carried out by hand in order to fully understand the *physics* of the problem. The necessary tools are all available: the basic equation, the Wigner rotation matrices, and the spin and spatial tensors. However, the algebra becomes complicated due to the large number of terms present due to the multiple rotations. A *Mathematica*™ computer program has been written to accomplish these sums of products of rotations and is included in Appendix C under the name **vass.m**. The acronym VASS stands for variable–angle sample spinning as introduced by Oldfield and coworkers [73]. This code uses the program **wigner.m** to define the second–order Wigner rotation matrices, and goes on to define the principal components of the interaction in spherical tensor form. The calculation of the tensors in the laboratory frame after the two rotations allows the products $2R_{21}^{(Q)}R_{2-1}^{(Q)}$ and $R_{22}^{(Q)}R_{2-2}^{(Q)}$ to be calculated and summed. Once again, only the time–independent parts have been retained. In order to fully calculate the sidebands from the second–order quadrupolar interaction, all terms must be kept. See references [74] and [75] for further information on the full expressions including the time–modulated terms.

In concentrating on the time–independent frequencies, symmetry arguments point to a most useful and general form for the full expression. Beginning with the expression for the product of two tensor components under the rotations sketched in Fig. 2.7

$$
\begin{aligned}
R_{2m}^{(Q)} R_{2-m}^{(Q)} &= \sum_{m'=-2}^{2} \mathcal{D}^{(2)}_{m'm}(\omega_r t, \theta, 0) \sum_{n'=-2}^{2} \mathcal{D}^{(2)}_{n'm'}(\alpha, \beta, \gamma) r_{2n'}^{(Q)} \times \\
&\quad \sum_{m''=-2}^{2} \mathcal{D}^{(2)}_{m''-m}(\omega_r t, \theta, 0) \sum_{n''=-2}^{2} \mathcal{D}^{(2)}_{n''m''}(\alpha, \beta, \gamma) r_{2n''}^{(Q)} \\
&= \sum_{m'=-2}^{2} \sum_{n'=-2}^{2} \sum_{m''=-2}^{2} \sum_{n''=-2}^{2} e^{-i(m'+m'')(\omega_r t+\gamma)} e^{-i(n'+n'')\alpha} \times \\
&\quad d^{(2)}_{m'm}(\theta) d^{(2)}_{m''-m}(\theta) d^{(2)}_{n'm'}(\beta) d^{(2)}_{n''m''}(\beta) r_{2n'}^{(Q)} r_{2n''}^{(Q)}, \qquad (2.48)
\end{aligned}
$$

we need to remove the time–dependent terms. All terms which do not satisfy $m' + m'' = 0$ are dropped and the sum on m'' is eliminated by setting m'' always equal to $-m'$. The symmetries of the remaining terms are also important for the simplification of the result. First, the only non–zero components of the spherical tensor in the quadrupolar PAS are r_{20} and $r_{2\pm2}$, so the allowed values of n' and n'' in Eq. 2.48 are 0 and ±2. Therefore the sum $n' + n''$, which is the coefficient before the angle α, may only range between -4 and 4 in even steps. Further, $r_{22}^{(Q)}$ and $r_{2-2}^{(Q)}$ are equal in magnitude and sign. For the reduced Wigner matrices (see Table 1.1) many symmetries and antisymmetries are found upon interchanging the signs of the two indices. It seems prudent to search, then, for solutions similar to the expansion in terms of cosines of even multiples of the angles α and β as was found for the expansion of the second–order quadrupolar frequencies from a static sample. The computer program does this by making symbolic replacements with user defined trigonometric identities.

The trigonometric terms involving the angle θ are converted to powers of $\cos\theta$ to search for Legendre polynomials, now allowed to go as high as $P_4(\cos\theta)$ due to the products of the rotations containing squares of $\cos\theta$. The expansion desired is

in the form

$$\omega^{(2Q)}_{\frac{1}{2},-\frac{1}{2}} = A\sum_{i=0}^{2}\sum_{j=0}^{2} a'_{ij}\cos(2i\alpha)\cos(2j\beta) \tag{2.49}$$

where the prefactor A is the same as in the earlier static expansion of the anisotropic frequencies (see Eq. 2.32). Each coefficient a'_{ij} may now contain terms that depend on Legendre polynomials up to fourth–order:

$$a'_{ij} = a^{(0)}_{ij} + a^{(2)}_{ij}P_2(\cos\theta) + a^{(4)}_{ij}P_4(\cos\theta) \tag{2.50}$$

where $a^{(0)}_{ij}$ is independent of the spinning angle (it is actually proportional to $P_0(\cos\theta)$ which is unity for *all* angles), $P_2(\cos\theta)$ is the second Legendre polynomial of Eq. 2.44, and $P_4(\cos\theta)$ is the fourth Legendre polynomial

$$P_4(\cos\theta) = \frac{1}{8}\left(35\cos^4\theta - 30\cos^2\theta + 3\right). \tag{2.51}$$

The graphs in Fig. 2.9 display the fourth Legendre polynomial in Cartesian and polar coordinates.

The result of the calculation is a polynomial with 35 distinct terms. The *Mathematica*™ programming environment allows interactive examination of the complete polynomial or factors of particular arguments (say, the coefficient of the $\cos 4\alpha\cos 4\beta$ term) and the results are compiled in Table 2.2.

The only coefficient that has no angular dependence is $a^{(0)}_{00}$ and this leads to the correct isotropic second–order quadrupolar frequency shift (see Eq. 2.34). The remainder of the expansion depends on *both* the second and fourth Legendre polynomials.

The plot of the two Legendre polynomials together in Fig 2.10 now reveals the most striking difference between sample spinning experiments for first– and second–order interactions: there is no *single* angle at which all of the anisotropic second–order terms may be made to vanish as $P_2(\cos\theta)$ and $P_4(\cos\theta)$ have no common

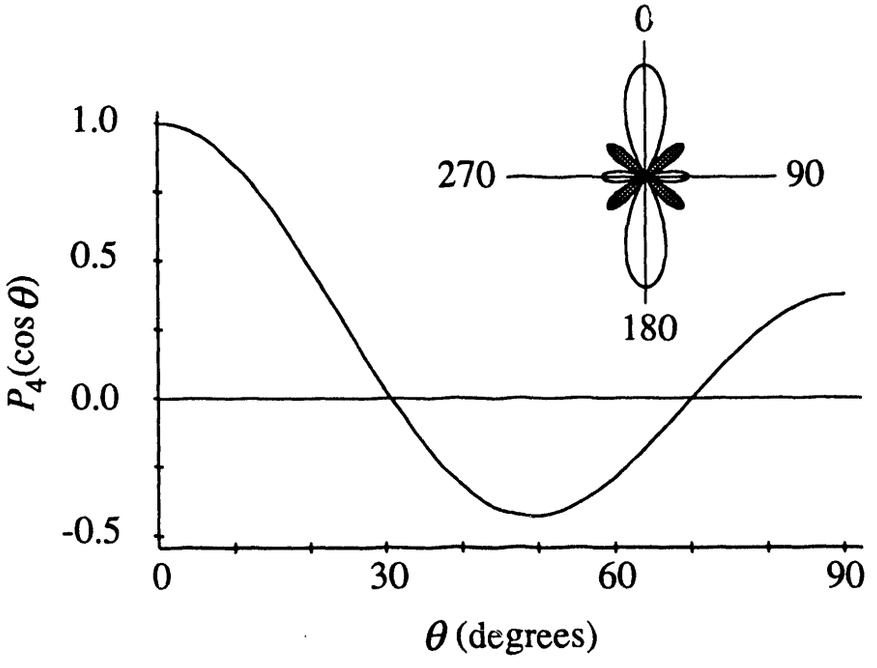

Figure 2.9: The fourth Legendre polynomial, $P_4(\cos\theta)$, as a function of angles in the first quadrant of a circle. The polar form is also shown at the upper right.

i	j	$a_{ij}^{(4)}$	$a_{ij}^{(2)}$	$a_{ij}^{(0)}$
0	0	$\frac{81}{1120}(18+\eta^2)$	$-\frac{12}{7}(1-\frac{1}{3}\eta^2)$	$-\frac{12}{5}(1+\frac{1}{3}\eta^2)$
0	1	$\frac{9}{56}(18+\eta^2)$	$-\frac{36}{7}(1-\frac{1}{3}\eta^2)$	0
0	2	$\frac{9}{32}(18+\eta^2)$	0	0
1	0	$\frac{81}{56}\eta$	$\frac{24}{7}\eta$	0
1	1	$\frac{27}{14}\eta$	$-\frac{24}{7}\eta$	0
1	2	$-\frac{27}{8}\eta$	0	0
2	0	$\frac{27}{32}\eta^2$	0	0
2	1	$-\frac{9}{8}\eta^2$	0	0
2	2	$\frac{9}{32}\eta^2$	0	0

Table 2.2: Coefficients in the anisotropic frequency cosine expansion (Eqs. 2.49 and 2.50) for the second–order energy difference in the central transition of a quadrupolar nucleus.

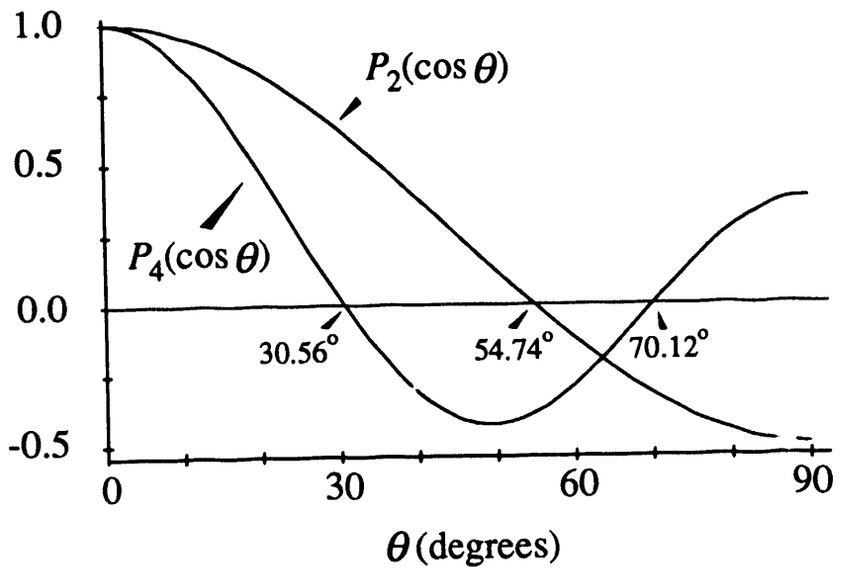

Figure 2.10: The second and fourth Legendre polynomial, $P_2(\cos\theta)$ and $P_4(\cos\theta)$, drawn together as a funtion of the angles in the first quadrant of a circle.

zero. The zero of $P_2(\cos\theta)$ is at the second–rank magic–angle $\theta_m^{(2)} = 54.74°$ while a zero for $P_4(\cos\theta)$ occurs at one of two fourth–rank magic angles, $\theta_m^{(4)} = 30.56°$ and $\theta_m^{(4)} = 70.12°$. Fourth–rank refers to the fact that the product of the two second–rank spatial tensors found in the second–order result contains a fourth–rank component which may be averaged at these angles.

Spectra obtained from spinning the sample at any one angle with respect to the magnetic field will be anisotropic no matter what angle is chosen. It is straightfor-

ward to calculate computer simulated spectra with the results compiled from this section. This is done at a variety of angles in Fig. 2.11 for a classic quadrupolar result: a single sodium–23 nucleus in a 9.4 T magnetic field with quadrupolar parameters $e^2qQ/h = 2.5$ MHz and $\eta = 0.7$. Several features of the sample spinning are presented in this figure.

First, the case of spinning about the z–axis ($\theta = 0°$) does not narrow the line at all from the static case (Fig. 2.4), but this is expected since the truncating Hamiltonian has cylindrical symmetry about this axis. When θ is set to 0° in the anisotropic frequency equation for a spinning sample the equation is identical to the static frequency expansion. In fact, this is an important check that the equations are correct. The magic–angle spinning spectrum ($\theta = 54.74°$) reveals that the line is not completely narrowed by MAS, as it would be if the interaction were first–order. Here there is a residual $P_4(\cos\theta)$ contribution to the lineshape. The spectra at the other (fourth–order) magic angles of $\theta = 30.56°$ and $\theta = 70.12°$ also show incomplete narrowing. At these angles the lineshape is governed purely by the magnitude of $P_2(\cos\theta)$.

In all cases, the anisotropic interaction may never be completely averaged. This is seldom a problem if the sample of interest contains only one resonance as shown in Fig. 2.11. It may then be compared to calculated lineshapes at any of a variety of angles and the quadrupolar parameters and isotropic shifts extracted. The problem arises in the chemically more interesting case of several inequivalent nuclear sites in a solid that contribute overlapping resonances. Of course when chemical shift anisotropy is also present the problem increases in complexity if spinning is undertaken at any angle other than the second–rank magic angle [74].

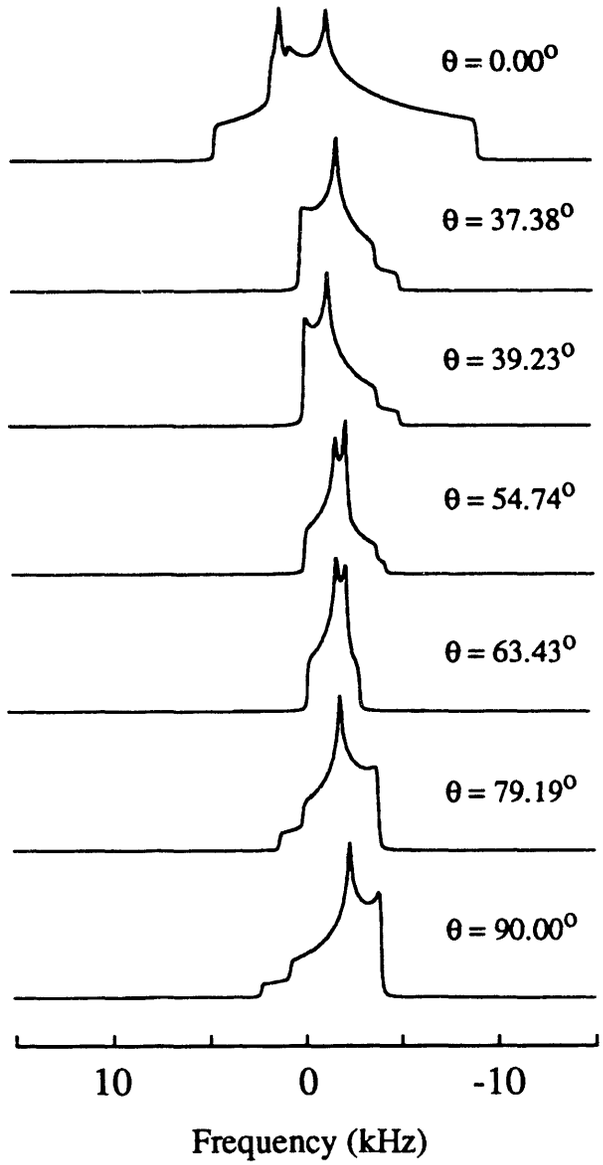

Figure 2.11: Simulations of the NMR spectra obtained as a function of the spinning angle, θ, from a polycrystalline sample with a single type of sodium–23 site in a 9.4 T magnetic field. The quadrupolar parameters are $e^2qQ/h = 2.5$ MHz and $\eta = 0.7$.

Chapter 3

Second–Order Averaging: Theory

3.1 Introduction

The analysis in Chapter 2 reveals a major problem to overcome in the NMR of half–odd integer spin quadrupolar nuclei. Even the central transition, which is readily observable and not broadened to first–order by the quadrupolar coupling, remains broad and anisotropic under sample spinning at any one angle. Possible causes of the broadening are the spatial anisotropy of the first–order chemical shielding interaction and the second–order quadrupolar coupling. Magic–angle spinning cancels the CSA component, but it does not completely average the second–order quadrupolar effects. Sample spinning does, however, narrow the resonances from those observed in the case of no spinning, which is also equivalent to spinning at an angle of 0° with respect to the magnetic field. Broad, overlapping central transition resonances appear throughout the NMR literature in spectra of important quadrupolar nuclei such as oxygen–17 [68, 76, 77, 78, 79, 80], sodium–23 [81, 82, 83], aluminum–27 [84, 85, 86, 87, 88, 89], and boron–11 [90, 91, 92, 93]. In many cases it

is the second–order quadrupolar coupling that must be averaged in order to simplify these spectra.

This chapter introduces the averaging of second–order quadrupolar effects. The solution lies in spinning about not just one, but *two* spatial axes during an NMR experiment. The two new experiments proposed are dynamic–angle spinning (DAS) and double rotation (DOR) NMR, and they may be viewed as the series and parallel versions of second–order averaging. The theoretical foundations for both techniques are a natural extension of those introduced in the previous chapter on coherent averaging and motional narrowing.

3.2 Dynamic–Angle Spinning

The NMR technique of magic–angle spinning (MAS) spatially averages interactions such as chemical shift anisotropy which have an angular dependence of $P_2(\cos\theta)$ under rapid sample spinning conditions. In dynamic–angle spinning (DAS) a sample spins around an axis inclined at an angle $\theta(t)$ such that the time averages of a set of $P_n(\cos\theta)$ are zero. The Legendre polynomials are an orthogonal set of functions which share few common zeroes, so the simplest case of DAS is when $\theta(t)$ assumes two discrete values θ_1 and θ_2 such that the time average of two Legendre polynomials are zero. Choosing angles such that the time averages of both $P_2(\cos\theta)$ and $P_4(\cos\theta)$ are zero will average the second–order quadrupolar broadening to its isotropic value, providing higher resolution in the spectra of half–odd integer spin quadrupolar nuclei.

DAS entails performing second–order averaging in series: spinning first at one angle during an experiment and then at another. The idea of changing rotor axis

orientation during an experiment is not a new one and has been introduced in NMR for a variety of reasons. These include correlations of narrow MAS lineshapes for spin–$\frac{1}{2}$ nuclei with CSA powder pattern lineshapes [94], retention of heteronuclear dipolar interactions or chemical shift anisotropy information under off–magic angle spinning conditions [95, 96], and more efficient cross–polarization away from the magic–angle for CPMAS experiments [97]. Workers in Professor Gary Maciel's lab at Colorado State University have also developed the technique of magic–angle hopping, correlating narrow isotropic and broad anisotropic spectra in a two–dimensional NMR experiment applicable to spin–$\frac{1}{2}$ nuclei [98]. Hopping a static sample to orientations corresponding to three of the six vertices of an octahedron allows separation of overlapping CSA powder patterns by their isotropic shifts in the second spectral dimension.

Using a time–dependent rotor axis orientation to address second–order quadrupolar effects was not proposed until 1988 when announcements were made independently by Llor and Virlet in Saclay [99, 100] and the Pines group in Berkeley [101, 102, 103]. The first experimental results came out of Berkeley [104, 105] and will be highlighted in the next chapter.

3.2.1 The DAS Concept

Conceptually, the general DAS experiment is more complicated than single–axis sample rotation. In MAS, a single pulse is usually applied to the sample and a free induction decay of the nuclear magnetization is observed. DAS is not this simple: a change in the axis orientation must be performed whose net effect during the experiment is to average the values of the selected $P_n(\cos\theta)$ to zero. We concentrate

here on the explicit calculations necessary to average first–order chemical shift and second–order quadrupolar interactions, although the analysis may be generalized to other couplings.

Calculations are always performed in the rotating frame of reference described in section 1.4.1 on rf pulses, where the effect of the pulses appear as rotations of the magnetization vector describing the net spin polarization. Only the central transition of the quadrupolar spin is considered, so the system is treated as a fictitious spin–$\frac{1}{2}$. The total Hamiltonian for spin evolution is the sum of isotropic and anisotropic contributions from each crystallite. A crystallite has a quadrupolar PAS related to the rotor axis frame by the Euler angles α, β, and γ. It also has a chemical shift anisotropy PAS described by another set of Euler angles α', β', and γ'. The rotor is spinning at an angle θ with respect to the external magnetic field. The form of the spin operators for the first–order chemical shift Hamiltonian (proportional to I_z) and those for the second–order quadrupolar interaction (proportional to I_z^3 and I_z) all appear proportional to I_z in the fictitious spin–$\frac{1}{2}$ representation of the operators, meaning that the frequencies of evolution for spins appear as an effective total shift with isotropic and anisotropic components. The phase factor accumulated under the evolution will be the product of the frequency and the evolution time.

If only the time–independent part of the Hamiltonian is considered for clarity (to eliminate the discussion of sidebands) the total shift is

$$\omega_{tot} = \omega_{iso} + \omega_{aniso} \tag{3.1}$$

where

$$\omega_{iso} = \omega_{iso}^{(CS)} + \omega_{iso}^{(2Q)} \tag{3.2}$$

which is independent of all angular arguments. Equation 2.34 contains the form of the second–order quadrupolar shift in the central transition.

The anisotropic frequency contributions depend on both the crystallite orientation and the rotor orientation:

$$\begin{aligned} \omega_{aniso} &= \omega_{aniso}^{(CS)}(\alpha', \beta', P_2(\cos\theta)) + \\ &\quad \omega_{aniso}^{(2Q)}(\alpha, \beta, P_2(\cos\theta), P_4(\cos\theta)) \end{aligned} \tag{3.3}$$

which is conveniently written as

$$\omega_{aniso} = A_2 P_2(\cos\theta) + A_4 P_4(\cos\theta). \tag{3.4}$$

The coefficients A_2 and A_4 may be determined from the calculations in the previous chapter, but for this discussion are not important. The sum is a combination of the CSA term (contributing to the $P_2(\cos\theta)$ coefficient) and the second–order quadrupolar effect (contained in both coefficients). The Euler angles γ and γ' do not appear in Eq. 3.3 since we are disregarding the sideband terms as discussed in Chapter 2.

The goal in second–order quadrupolar DAS is to find a time–dependent angular solution $\theta(t)$ which will average both Legendre polynomials to zero:

$$\int_0^\tau P_2(\cos\theta(t))dt = 0 \tag{3.5}$$

$$\int_0^\tau P_4(\cos\theta(t))dt = 0. \tag{3.6}$$

A variety of solutions are possible corresponding to monotonically increasing sweeps of the rotor axis from one angular endpoint to another [102]. A linear sweep between either $\theta_1 = 19.05°$ and $\theta_2 = 99.19°$ or $\theta_1 = 11.96°$ and $\theta_2 = 132.40°$ will accomplish this averaging, as will as a cosinusoidal sweep between $\theta_1 = 23.27°$ and $\theta_2 = 117.37°$

or $\theta_1 = 27.38°$ and $\theta_2 = 90.10°$. The experimental difficulties of such a sweep leading to sufficient averaging are extreme. The reorientation could not easily take place on a time scale where the spins would still be behaving coherently.

Another solution is to position the rotor axis at discrete orientations within the magnet. The goal is then to find two angles, θ_1 and θ_2, where spin evolution may take place retaining the isotropic terms of Eq. 3.2 while cancelling the anisotropic shift. Separating the experiment between the two angles allows for two evolution periods of length τ_1 and τ_2 at angles θ_1 and θ_2 respectively and two separate accumulations of a phase angle occur for the magnetization precessing under the influence of the shift Hamiltonian. To cancel the evolution from the anisotropic terms (Eq. 3.4) it is necessary that

$$P_2(\cos\theta_1)\tau_1 = -P_2(\cos\theta_2)\tau_2 \tag{3.7}$$

and

$$P_4(\cos\theta_1)\tau_1 = -P_4(\cos\theta_2)\tau_2 \tag{3.8}$$

simultaneously. A constant, k, is defined by

$$k = \frac{\tau_2}{\tau_1} \tag{3.9}$$

so that Eqs. 3.7 and 3.8 now read

$$P_2(\cos\theta_1) = -kP_2(\cos\theta_2) \tag{3.10}$$

$$P_4(\cos\theta_1) = -kP_4(\cos\theta_2). \tag{3.11}$$

This series of equations has an infinite, but bounded, set of solutions called *DAS complementary angles*. The solutions are shown graphically in Fig. 3.1 which was produced in the *Mathematica*™ programming environment (the code is included

in Appendix C). Only the first quadrant of angles need be considered due to the symmetry of the even–order Legendre polynomials.

The following restrictions apply to the solutions:

1. The value of k lies between 0.8 and 5.0.

2. Calling θ_1 the angle where the rotor axis is closer to the vertical (z–axis), θ_1 is constrained to lie between 0° and 39.23°. Then θ_2 must lie between 63.43° and 90°.

The appearance of these solutions on a graph of the Legendre polynomials is instructive. When $k = 1$, equal amounts of time are spent at the angles $\theta_1 = 37.38°$ and $\theta_2 = 79.19°$. The graph in Fig. 3.2 reveals that for these angles the values of both Legendre polynomials are equal and opposite, although neither is zero. Other interesting sets of angles are $\theta_1 = 0.00°$ and $\theta_2 = 63.43°$ where $k = 5$ and $\theta_1 = 39.23°$ and $\theta_2 = 90.00°$ where $k = 0.8$. In the first set, the relative amount of time spent at the first angle is a minimum. This set also maps onto an icosahedron revealing the power of group theory in the averaging of higher–order interactions [106]. For the second set of angles, the sensitivity of the rf detection in the experiment is a maximum for a receiver coil moving with the sample rotor. The two zeroes of $P_4(\cos\theta)$ are also a set of DAS complementary angles with k equal to approximately 1.87. Note that the second–rank magic angle, $\theta_m^{(2)} = 54.74°$, is *not* a permissible DAS angle in this simple two–angle experiment.

Pure second–order quadrupolar powder pattern shapes have been calculated for a variety of η values at sets of DAS angles and are presented in Fig. 3.3. For each pair of angles and each particular value of η the spectra are scaled mirror images about the isotropic shift. The scaling factor is the value of k for each pair.

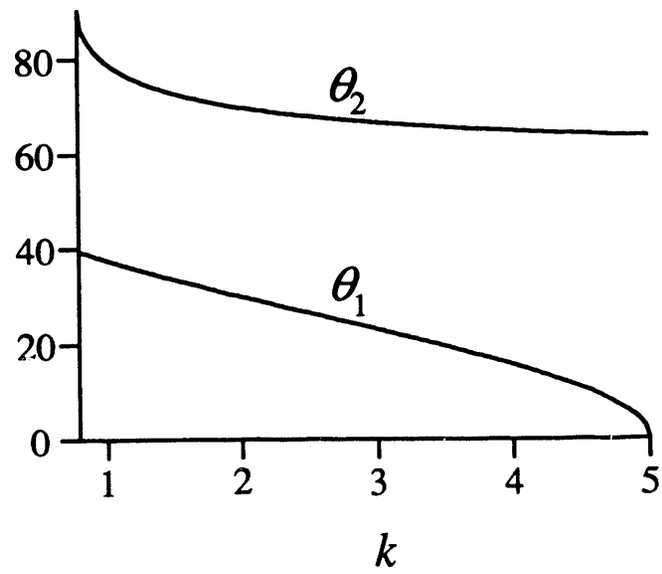

Figure 3.1: The solutions to Eqs. 3.10 and 3.11 as a function of k, the relative time spent at each DAS angle.

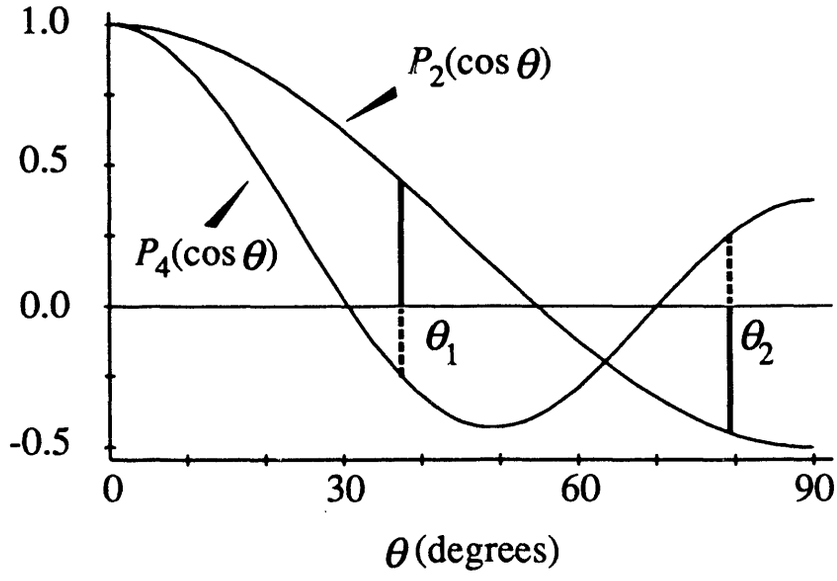

Figure 3.2: Contributions from the second and fourth Legendre polynomials cancel at the $k = 1$ set of DAS angles, $\theta_1 = 37.38°$ and $\theta_2 = 79.19°$.

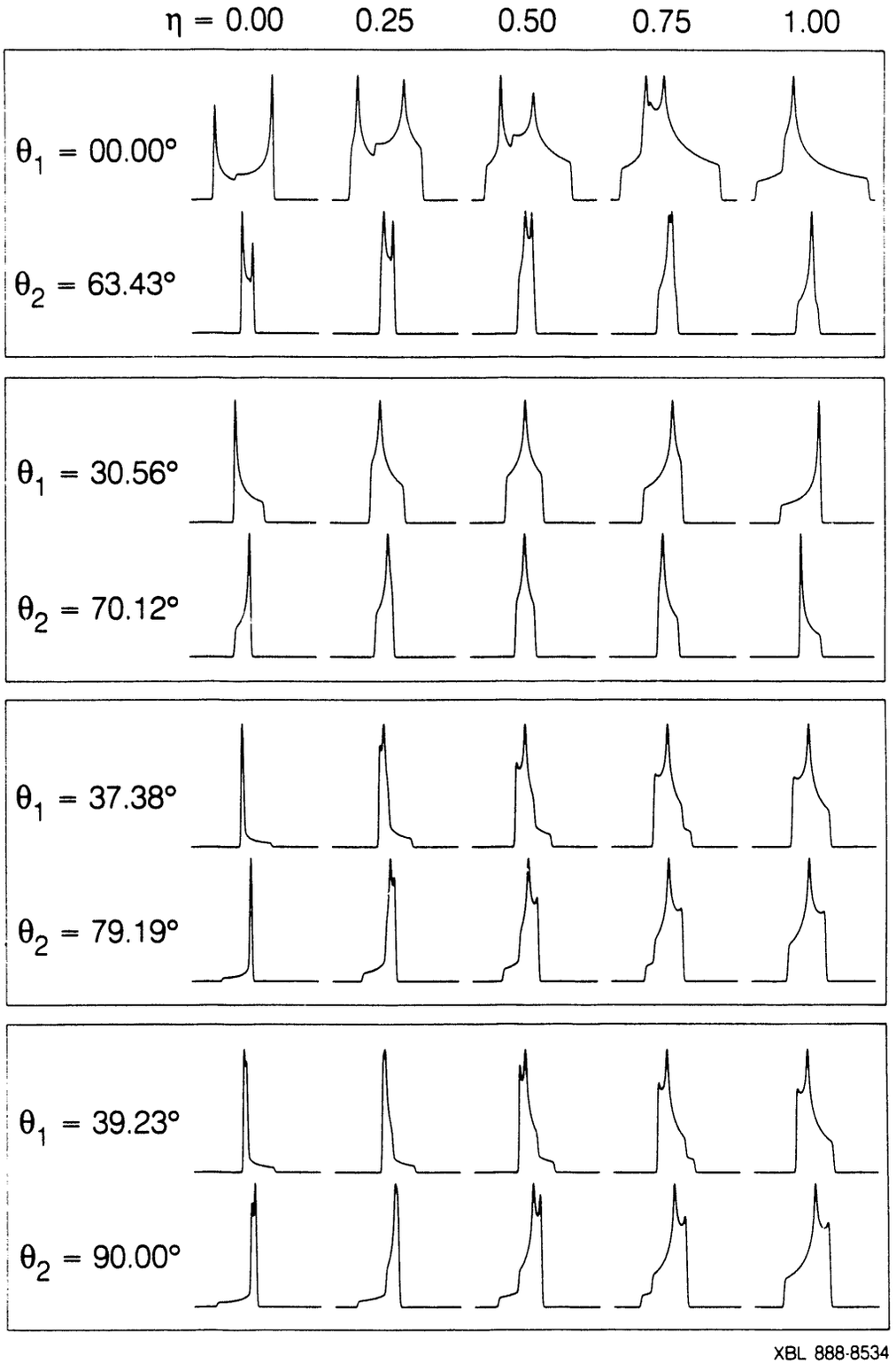

Figure 3.3: Simulated second–order powder patterns with rapid sample spinning for various values of the rotor axis angle and the asymmetry parameter (η) of the quadrupolar interaction. The spectra are grouped by pairs of DAS complementary angles.

3.2.2 The DAS Experiment

The DAS experiment can be accomplished as shown in Fig. 3.4. First, a set of DAS complementary angles is chosen. We define ω_1 as the evolution frequency at θ_1:

$$\omega_1 = \omega_{iso} + \omega_{aniso}(\theta_1). \tag{3.12}$$

The Euler angles have been dropped from these equations since only a single crystallite is considered. A sum over all crystallite orientations will be necessary to calculate the full signal and this is done after calculation of the angular dependence of the individual contribution from one crystallite.

The sample is first set spinning in a rotor inclined at an angle θ_1 with respect to the magnetic field direction (the laboratory z–axis). The initial 90° pulse along the x–axis rotates the magnetization down onto the negative y–axis where it evolves through an evolution angle $\omega_1\tau_1$. The density matrix becomes

$$I_z \longrightarrow -I_y \longrightarrow -I_y \cos\omega_1\tau_1 + I_x \sin\omega_1\tau_1 \tag{3.13}$$

The rotor is then hopped instantaneously to θ_2. The frequency ω_2 governs evolution at θ_2, and it is given by

$$\begin{aligned} \omega_2 &= \omega_{iso} + \omega_{aniso}(\theta_2) \\ &= \omega_{iso} - \frac{1}{k}\omega_{aniso}(\theta_1), \end{aligned} \tag{3.14}$$

since θ_1 and θ_2 are chosen as DAS angles where

$$\omega_{aniso}(\theta_2) = -\frac{1}{k}\omega_{aniso}(\theta_1). \tag{3.15}$$

This is verified by direct substitution of the set of equations for the Legendre polynomials (Eqs. 3.10 and 3.11) into Eq. 3.4. The evolution occurs for a further time

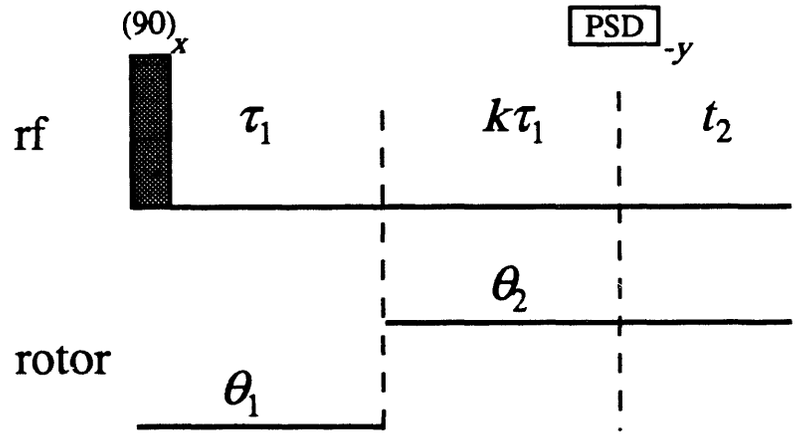

Figure 3.4: Radiofrequency pulse sequence and rotor axis orientation relative to the external magnetic field for a DAS experiment with an instantaneous hop between the two DAS angles. The rf pulse is a selective 90° pulse on the central transition.

τ_2 at θ_2 accumulating a further phase of $\omega_2\tau_2$. For the density matrix, evolution continues as

$$-I_y \cos\omega_1\tau_1 + I_x \sin\omega_1\tau_1 \rightarrow \quad -I_y \cos\omega_1\tau_1 \cos\omega_2\tau_2 + I_x \cos\omega_1\tau_1 \sin\omega_2\tau_2$$
$$+I_x \sin\omega_1\tau_1 \cos\omega_2\tau_2 + I_y \sin\omega_1\tau_1 \sin\omega_2\tau_2. \quad (3.16)$$

The total evolution time is called t_1. At time $t_1 = \tau_1 + \tau_2 = (1+k)\tau_1$ the *total* evolution phase is

$$\omega_1\tau_1 + \omega_2\tau_2 = \omega_{iso}t_1 \quad (3.17)$$

and the density matrix is

$$\begin{aligned}
\rho(t_1) &= -I_y(\cos\omega_1\tau_1 \cos\omega_2\tau_2 - \sin\omega_1\tau_1 \sin\omega_2\tau_2) \\
&\quad +I_x(\sin\omega_1\tau_1 \cos\omega_2\tau_2 + \cos\omega_1\tau_1 \sin\omega_2\tau_2) \\
&= -I_y \cos(\omega_1\tau_1 + \omega_2\tau_2) + I_x \sin(\omega_1\tau_1 + \omega_2\tau_2) \\
&= -I_y \cos(\omega_{iso}t_1) + I_x \sin(\omega_{iso}t_1). \quad (3.18)
\end{aligned}$$

As a function of t_1 the magnetization is only accumulating this *isotropic* phase: the net precession is governed by an isotropic frequency. This was calculated for a single crystallite orientation and, because equivalent magnetic nuclei in all crystallites have spins with the *same* isotropic frequency, the total signal from the entire sample is evolving as an isotropic shift. There is no longer a dependence of the frequency on any of the Euler angles α, β, α', or β'. Therefore, the averaging of the first– and second–order anisotropies is accomplished.

A problem with this scenario arises immediately. It is not mechanically feasible to hop instantaneously from one orientation to another. In fact, it may take on the order of tens of milliseconds to accomplish a move between appropriate angles.

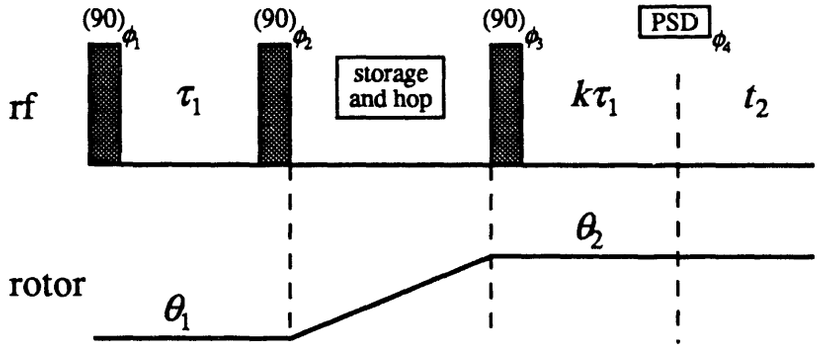

Experiment	ϕ_1	ϕ_2	ϕ_3	Real ϕ_4	Imag.
1	$+x$	$+x$	$+x$	$+y$	$-x$
2	$+y$	$+x$	$+x$	$-x$	$-y$

Figure 3.5: Radiofrequency pulse sequence, rotor axis orientation relative to the external magnetic field, and phase cycling used in a DAS experiment. All pulses are selective 90° pulses on the central transition.

During the hop, the magnetization must be stored [95, 98] along the z–axis or it will dephase (undergo irreversible decay) since the hop takes a long time compared to the spin–spin relaxation time constant, T_2. The necessary modification to the DAS experiment is outlined in Fig. 3.5.

The modified DAS experiment begins once again with a single 90° pulse on the central transition. This creates a coherence between the two spin energy levels which appears as an off–diagonal term in the reduced density matrix for the system.

expt.	$\rho(1^+)$	$\rho(\tau_1)$	$\rho(storage)$
1	$-I_y$	$-I_y\cos\omega_1\tau_1 + I_x\sin\omega_1\tau_1$	$-I_z\cos\omega_1\tau_1$
2	$+I_x$	$+I_x\cos\omega_1\tau_1 + I_y\sin\omega_1\tau_1$	$+I_z\sin\omega_1\tau_1$

expt.	$\rho(3^+)$	$\rho(t_1 = \tau_1 + \tau_2)$
1	$+I_y\cos\omega_1\tau_1$	$+I_y\cos\omega_1\tau_1\cos\omega_2\tau_2 - I_x\cos\omega_1\tau_1\sin\omega_2\tau_2$
2	$-I_y\sin\omega_1\tau_1$	$-I_y\sin\omega_1\tau_1\cos\omega_2\tau_2 + I_x\sin\omega_1\tau_1\sin\omega_2\tau_2$

Table 3.1: Time-development of the reduced density matrix during a DAS experiment in each of the two experiments of Fig. 3.5. The equilibrium state before each sequence is $\rho(0) = I_z$, and the notation $\rho(n^+)$ signifies the density matrix immediately following the n^{th} pulse.

As seen in Table 3.1 the original z–magnetization from the spins in equilibrium with the lattice, described by the density matrix I_z, is converted by the pulse to either x or y magnetization, described by I_x or I_y depending on the phase of the first pulse (ϕ_1 in Fig. 3.5). The magnetization then evolves in the first time domain of length τ_1 into a linear combination of x and y magnetization as above in the naive instantaneous experiment.

At this point the axis of the rotor must be hopped to angle θ_2. Before the hop, the magnetization must be stored along the z–axis where it will not evolve any further during the hop. This is accomplished with the second 90° pulse with phase ϕ_2. Only one component of the transverse magnetization may be stored at a time, so at least two experiments are necessary to fully reconstruct the desired signal. These two experiments are numbered 1 and 2 in Fig. 3.5, Table 3.1, and Table 3.2.

After the hop is completed, the stored component of the magnetization is returned to the transverse plane with the third pulse. The spin magnetization evolu-

expt.	x buffer	y buffer
1	$+\cos\omega_1\tau_1\cos\omega_2\tau_2$	$+\cos\omega_1\tau_1\sin\omega_2\tau_2$
2	$-\sin\omega_1\tau_1\sin\omega_2\tau_2$	$+\sin\omega_1\tau_1\cos\omega_2\tau_2$
sum	$\cos(\omega_1\tau_1+\omega_2\tau_2)$	$\sin(\omega_1\tau_1+\omega_2\tau_2)$

Table 3.2: The magnetization measured in each of the experiments of Fig. 3.5. The relative phase for addition to the data buffers is chosen by the detector (receiver) phase in the pulse program. Note that $\omega_1\tau_1 + \omega_2\tau_2 = \omega_{iso}t_1$ (see Eq. 3.17).

tion now continues at the second angle, θ_2, for an amount of time $\tau_2 = k\tau_1$. During this period, all of the anisotropic frequencies have changed sign and the net effect will be a refocussing of the transverse magnetization into a spin echo [107, 108] at the time $t_1 = \tau_1 + \tau_2$. For a single crystallite the echo would not be encountered. The decay of the initial magnetization from an anisotropic interaction in a powder is an interference effect of the signals from all crystallites, governed by the anisotropic frequency components. When these are reversed and cancelled, the rephasing appears as a spontaneous burst of magnetization returning along an axis in the transverse plane. The actual reconstruction of this echo takes place in the two parts in the DAS experiment due to finite hopping times, with appropriate cycling of the receiver phase to correctly add the signals into computer memory. The evolution of the magnetization at the echo point will have only evolved under the isotropic frequencies of the spins in the system. Table 3.2 shows how the refocussing occurs mathematically with the use of some simple trigonometric identities.

The magnetization is sampled at the point t_1. Then t_1 is incremented by Δt_1 and the two steps (both experiments 1 and 2) of the full DAS experiment are repeated.

Enough t_1 data points must be collected to obtain useful spectral resolution. The increment, Δt_1, determines the spectral width in the DAS experiment by the sampling theorem [109, 110]. Fourier transformation of the isotropic (t_1) data obtained in a DAS experiment yields a high–resolution isotropic DAS spectrum.

A second way to perform DAS is as a two–dimensional NMR experiment. Data is collected from the point of echo formation (t_1) in a second time domain (t_2) where the decay is again anisotropic. This anisotropic decay is equivalent to the decay observed after a single 90° pulse while spinning at the second DAS angle θ_2. By successively incrementing the t_1 time period from zero, a two–dimensional data set is obtained where evolution in the first time dimension is purely isotropic, while in the second dimension it is anisotropic as well. A two–dimensional Fourier transform of the data yields a correlation map of the isotropic DAS frequencies and their associated anisotropic powder patterns. This provides a method for separating overlapping powder patterns according to their isotropic resonances in the first frequency dimension. The low–resolution dimension powder pattern will always have a contribution from both quadrupolar and anisotropic chemical shift interactions, if present, because the magic angle for $P_2(\cos\theta)$ is not a DAS complementary angle (see Fig. 3.1).

The usefulness of DAS lies in the fact that the evolution is purely isotropic: each magnetically inequivalent spin species will have an isotropic resonance at the sum of the isotropic chemical shift and the isotropic second–order quadrupolar shift for that site. These parameters correlate well with structural and bonding parameters [68]. The isotropic resonances will not decay as quickly as the anisotropic resonances since the frequency spread is (ideally) homogeneous and therefore not spread over as

wide a frequency range. Narrow DAS resonances should result which are distinctly resolved for different nuclear sites.

3.3 Double Rotation

The second method proposed to average first– and second–order interactions is a parallel approach: spinning not around only one axis at a time, but around multiple axes. The conceptually straightforward but mechanically difficult solution is to place one rotor inside of another. This is the idea of double rotation (DOR), first described by Samoson, Lippmaa, and Pines [111]. While the inner rotor spins within the outer rotor, the motiou of the outer rotor causes the inner rotor spinning axis to sweep out a cone with respect to the external magnetic field as shown in Fig. 3.6. There are two time–independent angles which may be selected for the double rotation experiment: the angle which the inner rotor axis makes with resp ect to the outer rotor axis (θ_2) and the angle describing the orientation of the outer rotor with respect to the external magnetic field (θ_1). It is shown that by a prudent choice of angles, the second–order quadrupolar interaction (as well as the first–order chemical shift anisotropy) is averaged.

To describe the behavior of the spatial parts in the spin Hamiltonians (or equivalently the evolution frequencies), a further transformation is needed from the rotations that describes single–axis spinning at any arbitrary angle. The rotations needed are very similar to those for single–axis rotation shown in Fig. 2.7 with one further rotation betweer the inner rotor frame and a larger outer rotor containing the smaller. To summarize, the first transformation is from the PAS of the interaction (chemical shift or quadrupolar) to the inner rotor and is described by

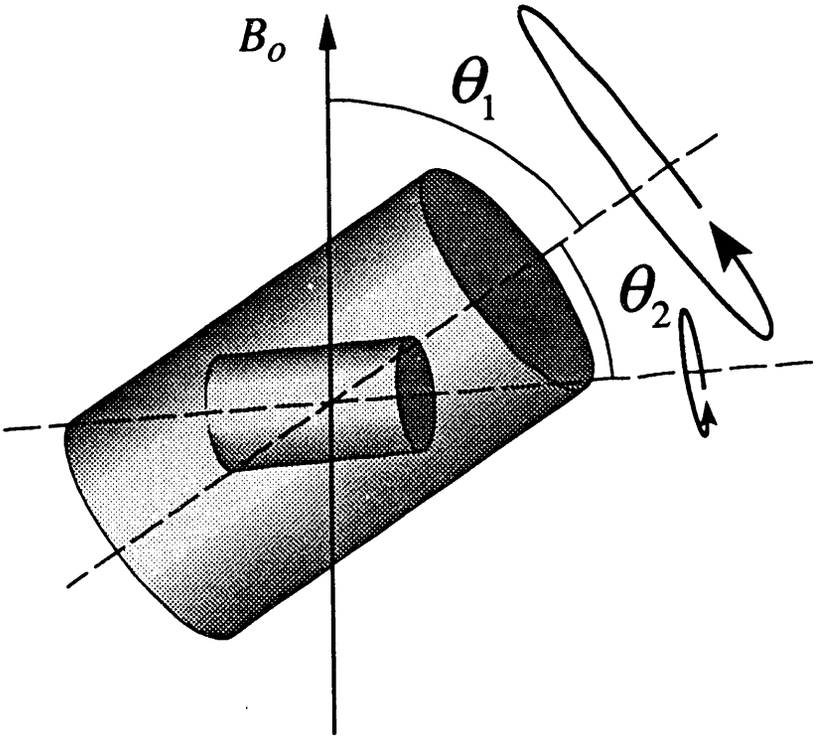

Figure 3.6: The double rotation experiment, where an inner rotor spins inside of an outer rotor which is itself spinning at an angle inclined to the magnetic field.

the Euler angles $\Omega = (\alpha, \beta, \gamma)$. The inner rotor is spinning at a frequency ω_{r2} around an axis inclined at θ_2 to the cylinder axis of the outer rotor. The Euler angles for the transformation from the inner rotor axis system to the outer rotor are $\Omega_2 = (\omega_{r2}t, \theta_2, \gamma_2)$. The outer rotor frequency is ω_{r1} and it is incli. ed at θ_1 to the magnetic field, so the final set of Euler angles are $\Omega_1 = (\omega_{r1}t, \theta_1, \gamma_1)$. Although only time–independent calculations will be considered explicitly, sidebands do become important in DOR experiments more often than in DAS experiments due to the slow speeds obtained experimentally for the outer rotor.

The Hamiltonians considered are the first–order chemical shift and the second–order quadrupolar Hamiltonians. The form of the full spatial tensor components under double rotation are

$$\begin{aligned} R_{2m} &= \sum_{m'=-2}^{2} \mathcal{D}^{(2)}_{m'm}(\omega_{r1}t, \theta_1, \gamma_1) \sum_{m''=-2}^{2} \mathcal{D}^{(2)}_{m''m'}(\omega_{r2}t, \theta_2, \gamma_2) \times \\ &\quad \sum_{m'''=-2}^{2} \mathcal{D}^{(2)}_{m'''m''}(\alpha, \beta, \gamma) r_{2m'''} \\ &= \sum_{m'=-2}^{2} \sum_{m''=-2}^{2} \sum_{m'''=-2}^{2} e^{-im\gamma_1} e^{-im'(\omega_{r1}t+\gamma_2)} e^{-im''(\omega_{r2}t+\gamma)} e^{-im'''\alpha} \times \\ &\quad d^{(2)}_{m'm}(\theta_1) d^{(2)}_{m''m'}(\theta_2) d^{(2)}_{m'''m''}(\beta) r_{2m'''}. \end{aligned} \tag{3.19}$$

First–Order Interactions under Double Rotation

The high–field NMR frequency for spins in an oriented crystallite with an anisotropic chemical shift has been stated generally in Eq. 2.8 and is

$$\omega^{(CS)}_{aniso} = \sqrt{\frac{2}{3}} \omega_0 R^{(CS)}_{20}. \tag{3.20}$$

Now, under double rotation, the time independent part of $R^{(CS)}_{20}$ is

$$R^{(CS)}_{20} = \sum_{m'''=-2}^{2} e^{-im'''\alpha} d^{(2)}_{00}(\theta_1) d^{(2)}_{00}(\theta_2) d^{(2)}_{m'''0}(\beta) r^{(CS)}_{2m'''} \tag{3.21}$$

since, for the time–independent terms, $m' = 0$ and $m'' = 0$. This is the same sum which appears in the static (non–spinning) calculation of the anisotropic frequencies with the addition of two factors, $d^{(2)}_{00}(\theta_1)$ and $d^{(2)}_{00}(\theta_2)$. These reduced Wigner matrices are the second Legendre polynomials of the cosine of their arguments, so

$$\omega^{(CS)}_{aniso} = \frac{\omega_0 \Delta\sigma}{3} P_2(\cos\theta_1) P_2(\cos\theta_2) \left[\left(3\cos^2\beta - 1 \right) + \eta_\sigma \sin^2\beta \cos 2\alpha \right]. \qquad (3.22)$$

If either θ_1 or θ_2 is chosen to be a zero of the second Legendre polynomial (the second–rank magic–angle of 54.74°) the anisotropic interaction will be averaged for every crystallite simultaneously.

Nothing is gained in the case of chemical shift anisotropy by using DOR instead of MAS. In this argument there is just a second angle which may be set arbitrarily. When ω_{r2} is set to zero and θ_2 is also zero, this is exactly equivalent to the case of spinning about a single axis.

Second–Order Interactions under Double Rotation

The more interesting interaction is, of course, the second–order quadrupolar interaction which is not averaged by single–axis reorientation. In this case, products of second–rank spherical tensors are encountered. Remembering Eq. 2.29 for the full (isotropic plus anisotropic) second–order quadrupolar frequencies,

$$\omega^{(2Q)}_{\frac{1}{2},-\frac{1}{2}} = \left(\frac{eQ}{4I(2I-1)\hbar} \right)^2 \frac{[4I(I+1)-3]}{\omega_0} \left\{ 2R^{(Q)}_{21} R^{(Q)}_{2-1} + R^{(Q)}_{22} R^{(Q)}_{2-2} \right\}, \qquad (3.23)$$

the products $R^{(Q)}_{2m} R^{(Q)}_{2-m}$ must be calculated under double rotation conditions. Before restriction to the time–independent terms, the product is

$$R^{(Q)}_{2m} R^{(Q)}_{2-m} = \sum_{m'=-2}^{2} \sum_{m''=-2}^{2} \sum_{m'''=-2}^{2} \sum_{n'=-2}^{2} \sum_{n''=-2}^{2} \sum_{n'''=-2}^{2}$$
$$e^{-i(m'+n')(\omega_{r1}t+\gamma_2)} e^{-i(m''+n'')(\omega_{r2}t+\gamma)} e^{-i(m'''+n''')\alpha} \times$$
$$d^{(2)}_{m'm}(\theta_1) d^{(2)}_{m''m'}(\theta_2) d^{(2)}_{m'''m''}(\beta) \times$$
$$d^{(2)}_{n'-m}(\theta_1) d^{(2)}_{n''n'}(\theta_2) d^{(2)}_{n'''n''}(\beta) r^{(Q)}_{2m'''} r^{(Q)}_{2n'''}. \tag{3.24}$$

Fortunately, restricting the analysis to the time–independent terms allows the following simplifications to be made: $n' = -m'$ and $n'' = -m''$. Since the ± 1 components of the spatial tensor for the quadrupolar interaction in the PAS of the electric field gradient tensor vanish, m''' and n''' take on three possible values each. The values in the sum for m' and m'' take on all five values from -2 to 2. Therefore the number of terms in one product of spatial tensors is 225, while for the full expression in Eq. 3.23 there would be 450 terms. Explicit calculation without a computer, while not impossible, is tedious. However, one possible way to approach this is to couple the spatial tensors into a larger (fourth–rank) tensor space as done by Samoson in his analysis of sideband patterns in double rotation [112].

The approach used here is to take advantage of a computer program which will manipulate the summation symbolically and produce the result in the most convenient form possible. Since an expansion of the frequency in a sum of cosines of even multiples of the Euler angles describing the orientation of the crystallite occurs for both the static and single–axis cases, that is the form sought. In particular,

$$\omega^{(2Q)}_{\frac{1}{2},-\frac{1}{2}} = A \sum_{i=0}^{2} \sum_{j=0}^{2} a''_{ij} \cos(2i\alpha) \cos(2j\beta) \tag{3.25}$$

where A has been defined before as

$$A = \left(\frac{e^2 qQ}{4I(2I-1)\hbar} \right)^2 \frac{[4I(I+1)-3]}{8\omega_0}. \tag{3.26}$$

As before, calculations were performed in the *Mathematica*™ programming environment with the code listed in Appendix C. The result calls for an expansion of the coefficients a''_{ij} as a sum of terms dependent upon Legendre polynomials, now with arguments related to the two angles θ_1 and θ_2. Then, for the expansion in Eq. 3.25, the coefficients are

$$a''_{ij} = a_{ij}^{(44)} P_4(\cos\theta_1) P_4(\cos\theta_2) + a_{ij}^{(22)} P_2(\cos\theta_1) P_2(\cos\theta_2) + a_{ij}^{(00)} \tag{3.27}$$

where $a_{ij}^{(00)}$ is an angular independent (isotropic) term.

The coefficients $a_{ij}^{(kk)}$ for $k = 0, 2, 4$ are compiled in Table 3.3. Comparison with Table 2.2, which provides the same expansion under single–axis rotation at an arbitrary angle, reveals that the coefficients match *exactly* for all polynomial orders. In effect, double rotation splits the $P_2(\cos\theta)$ and $P_4(\cos\theta)$ terms of the single–axis expansion into the products $P_2(\cos\theta_1)P_2(\cos\theta_2)$ and $P_4(\cos\theta_1)P_4(\cos\theta_2)$. The isotropic component remains the same, arising from only the angular independent term $a_{00}^{(00)}$. Explicitly,

$$\begin{aligned}
\omega_{\frac{1}{2},-\frac{1}{2}}^{(2Q,iso)} &= A\left(a_{00} - \frac{1}{3}a_{01} - \frac{1}{15}a_{02}\right) \\
&= -A\frac{12}{5}\left(1 + \frac{1}{3}\eta^2\right) \\
&= -\frac{3}{10}\left(\frac{e^2qQ}{4I(2I-1)\hbar}\right)^2 \frac{[4I(I+1)-3]}{\omega_0}\left(1 + \frac{1}{3}\eta^2\right)
\end{aligned} \tag{3.28}$$

since

$$a_{00}^{(44)} - \frac{1}{3}a_{01}^{(44)} - \frac{1}{15}a_{02}^{(44)} = 0 \tag{3.29}$$

and

$$a_{00}^{(22)} - \frac{1}{3}a_{01}^{(22)} - \frac{1}{15}a_{02}^{(22)} = 0. \tag{3.30}$$

As a further internal check on these equations, when either $\theta_1 = 0$ or $\theta_2 = 0$ the solution reduces to the single–axis spinning case. Further, if $\theta_1 = 0$ and $\theta_2 = 0$,

i	j	$a_{ij}^{(44)}$	$a_{ij}^{(22)}$	$a_{ij}^{(00)}$
0	0	$\frac{81}{1120}(18+\eta^2)$	$-\frac{12}{7}(1-\frac{1}{3}\eta^2)$	$-\frac{12}{5}(1+\frac{1}{3}\eta^2)$
0	1	$\frac{9}{56}(18+\eta^2)$	$-\frac{36}{7}(1-\frac{1}{3}\eta^2)$	0
0	2	$\frac{9}{32}(18+\eta^2)$	0	0
1	0	$\frac{81}{56}\eta$	$\frac{24}{7}\eta$	0
1	1	$\frac{27}{14}\eta$	$-\frac{24}{7}\eta$	0
1	2	$-\frac{27}{8}\eta$	0	0
2	0	$\frac{27}{32}\eta^2$	0	0
2	1	$-\frac{9}{8}\eta^2$	0	0
2	2	$\frac{9}{32}\eta^2$	0	0

Table 3.3: Coefficients in the anisotropic frequency cosine expansion (Eqs. 3.25 and 3.27) for the second–order energy difference in the central transition of a quadrupolar nucleus undergoing double rotation.

the static solution is obtained. Note that in the case of $\vartheta_1 = 0$ the axis of the inner rotor will still be sweeping out a cone in the laboratory frame. Since the magnet has cylindrical symmetry about this axis, the rotation is irrelevant.

A simplified expression for the first– and second–order anisotropic central transition frequencies in the system under double rotation is

$$\omega_{aniso}^{(CS)} + \omega_{aniso}^{(2Q)} = \sum_{\ell=2,4} A_\ell P_\ell(\cos\theta_1) P_\ell(\cos\theta_2). \tag{3.31}$$

The coefficients, A_ℓ, are functions of the spin quantum number of the nucleus, the quadrupolar coupling parameters, the chemical shift parameters, the resonance frequency for the nucleus, and the orientations of both the chemical shift PAS and the quadrupolar PAS. In order to completely average these anisotropies there are two choices of sets of angles (θ_1, θ_2). The first is

$$(\theta_1, \theta_2) = (\theta_m^{(2)}, \theta_m^{(4)}) \tag{3.32}$$

where $\theta_m^{(2)}$ and $\theta_m^{(4)}$ are second– and fourth–rank magic–angles: the zeroes of the functions $P_2(\cos\theta)$ and $P_4(\cos\theta)$. Numerically these are the usual magic angle, $\theta_m^{(2)} = 54.74°$, and the higher–order magic angles, $\theta_m^{(4)} = 30.56°$ or $\theta_m^{(4)} = 70.12°$ (see Fig. 2.10). An equally useful choice for complete averaging is

$$(\theta_1, \theta_2) = (\theta_m^{(4)}, \theta_m^{(2)}). \tag{3.33}$$

Of the four possibilities for the configuration of the double rotor apparatus, one provides the best sensitivity in an NMR experiment with the receiver coil coaxial with the outer rotor. The choice $(\theta_1, \theta_2) = (54.74°, 30.56°)$ provides the best combination of filling factor and relative NMR sensitivity [113] and has, so far, been used exclusively in DOR.

The theory of second–order averaging is now complete. Experimental proof that the second–order quadrupolar interactions may be averaged using these new methods is presented next.

Chapter 4

Second–Order Averaging: Experiments

4.1 Introduction

The narrowing of NMR resonances from quadrupolar nuclei occupying low symmetry sites in solids has been a dream of NMR spectroscopists for a long time. Two NMR experiments which will accomplish this goal were described in Chapter 3 and have now been carried out experimentally. The first results on full averaging of anisotropic second–order quadrupolar interactions in solids are described in this chapter. The goals of dynamic–angle spinning (DAS) and double rotation (DOR) are similar, but approach the narrowing of resonance lines using different philosophies. The experimental difficulties and accomplishments of each are important to a researcher who has a particular problem to solve and must weigh the use of either or both techniques. Therefore, a comparison of the expected benefits and difficulties of each type of experiment is essential.

Dynamic–angle spinning NMR is a new sample spinning experiment where a quick reorientation of the rotor must occur in order to accomplish the complete averaging of second–order quadrupolar interactions. The evolution is isotropic at only one time in each experiment, the time of the DAS echo. Therefore, DAS contains a second time dimension in a very natural way as the anisotropic decay after the echo also evolves in time. The more complex radiofrequency irradiation and the detection of the signal as an echo separates DAS from the single–pulse experiments used to acquire one–dimensional MAS or VASS spectra. The DAS experiment will first be traced out through its relation to single–axis spinning experiments. High–resolution spectra were obtained from sodium–23 nuclei in a sodium salt and these results are presented as the first experimental averaging of the second–order quadrupolar interaction. The two–dimensional nature of the DAS experiment is examined, and then the extension of this technique to oxygen–17 nuclei is presented.

In double rotation NMR, the difficulty in designing and fabricating a probehead to carry out the complex motion outweighs the actual NMR experimental procedure. A single rf pulse followed by quadrature acquisition of a signal is all that is necessary after a means of carrying out the double rotation motion is found. In DOR, the averaging is often much more efficient than in DAS. Whereas the signal in DAS may be attenuated due to incomplete refocussing of magnetization evolving under interactions other than the chemical shift anisotropy or quadrupolar interactions, the greatest deficiency in DOR spectra is the large number of spinning sidebands present due to modulation of the signal by the rotational motion of the slow outer rotor. These issues will be examined in DOR NMR spectra from sodium–23 and oxygen–17 nuclei in solids.

4.2 Dynamic–Angle Spinning

4.2.1 Experimental Preliminaries

The DAS experiments performed here are constructed from discrete hops of a spinner axis within a large magnetic field. Although a multiple number of axis hops may take place in a DAS experiment, the simplest DAS experiment consists of one hop with evolution time divided between the two DAS complementary angles. One experimental restriction is that these angles must lie within a disjoint set of angles which are a solution of Eqs. 3.7 and 3.8. If one angle lies between 0° and 39.23°, then the other is uniquely determined and must lie between 63.43° and 90.00°. Each of these solutions also has associated with it a single value of k, the parameter which determines the fraction of time spent at each angle during the experiment.

Both instrumental constraints and theoretical simplicity encourage the use of $k = 1$ in the DAS experiment. The evolution times at the two angles are equal and $\theta_1 = 37.38°$ while $\theta_2 = 79.19°$. The experiment is outlined in Fig. 4.1 and included in this figure is a more complicated phase cycle than the two experiments needed to fully reconstruct the second–order echo. The additional four–step phase cycle is introduced to remove experimental artifacts arising from longitudinal (T_1) relaxation during the hop between θ_1 and θ_2. It may be verified that in experiments 1 through 4 equivalent signals are obtained. The same is true for the last four permutations. The extra phase cycling will remove any magnetization which has relaxed during the hop and would cause additional intensity along the positive z–axis at the end of the hop. Extra peaks in the spectrum, called axial peaks, are shown to arise from such an experimental artifact [36]. To remove this undesirable

situation, the magnetization retained during the hop is stored for an equal number of experiments along the $+z$–axis and along the $-z$–axis. The phase cycling of the third pulse then alternately adds and subtracts any extra magnetization along the $+z$–axis only.

A commercially available or home–built MAS NMR probe is not adequate for performing a DAS experiment. It is necessary to quickly reorient the direction of the rotor axis while maintaining stable air flow to support and drive the rotor. Reliable electronic connections for the rf coil used to irradiate the sample and detect the net magnetization must also be present. A probehead to accomplish the hop of the rotor axis, designed by Professor T. Terao from Kyoto University in Japan, is sketched in Fig. 4.2. Initially, this type of probe was used for small hops away from the magic angle (a switched–angle sample spinning experiment) to study heteronuclear dipolar interactions [95] and to separate overlapping CSA patterns in solids [96].

The probehead was fabricated from Vespel, Delrin, and alumina parts. These materials were chosen based on their light weight, ease of machinability, and durability. They also have a history of excellent performance in MAS applications [114]. An important feature of this design is that the coil is wrapped around the stator and is moved along with the spinning axis. This increases the filling factor when compared to a coil which is static and must surround the complete spinning assembly. Filling factor is defined as the volume of the sample containing the spins divided by the total volume of the coil and the NMR sensitivity from a sample is proportional to the filling factor. Therefore, a coil wrapped around the stator provides a large filling factor which is desirable when working with low–abundance nuclei or those with small gyromagnetic ratios.

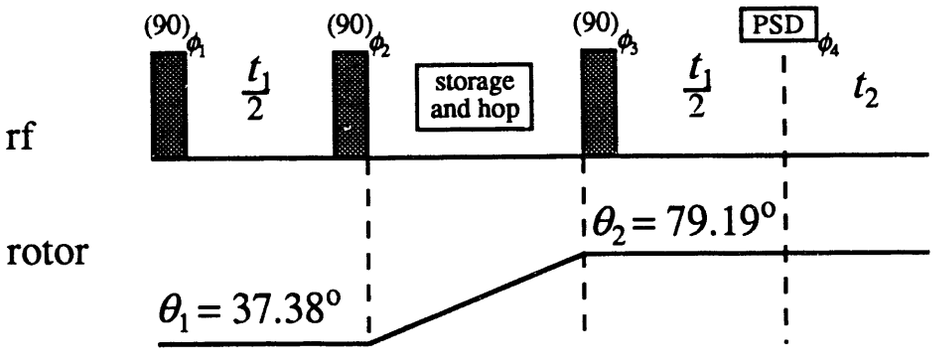

Experiment	ϕ_1	ϕ_2	ϕ_3	Real	ϕ_4	Imag.
1	+x	+x	+x	+y		-x
2	+x	+x	-x	-y		+x
3	-x	+x	+x	-y		+x
4	-x	+x	-x	+y		-x
5	+y	+x	+x	-x		-y
6	+y	+x	-x	+x		+y
7	-y	+x	+x	+x		+y
8	-y	+x	-x	-x		-y

Figure 4.1: The DAS experiment performed with $k = 1$ and therefore equal evolution times at the two DAS angles. Extra phase cycling is included to minimize experimental artifacts from relaxation during the storage and hop.

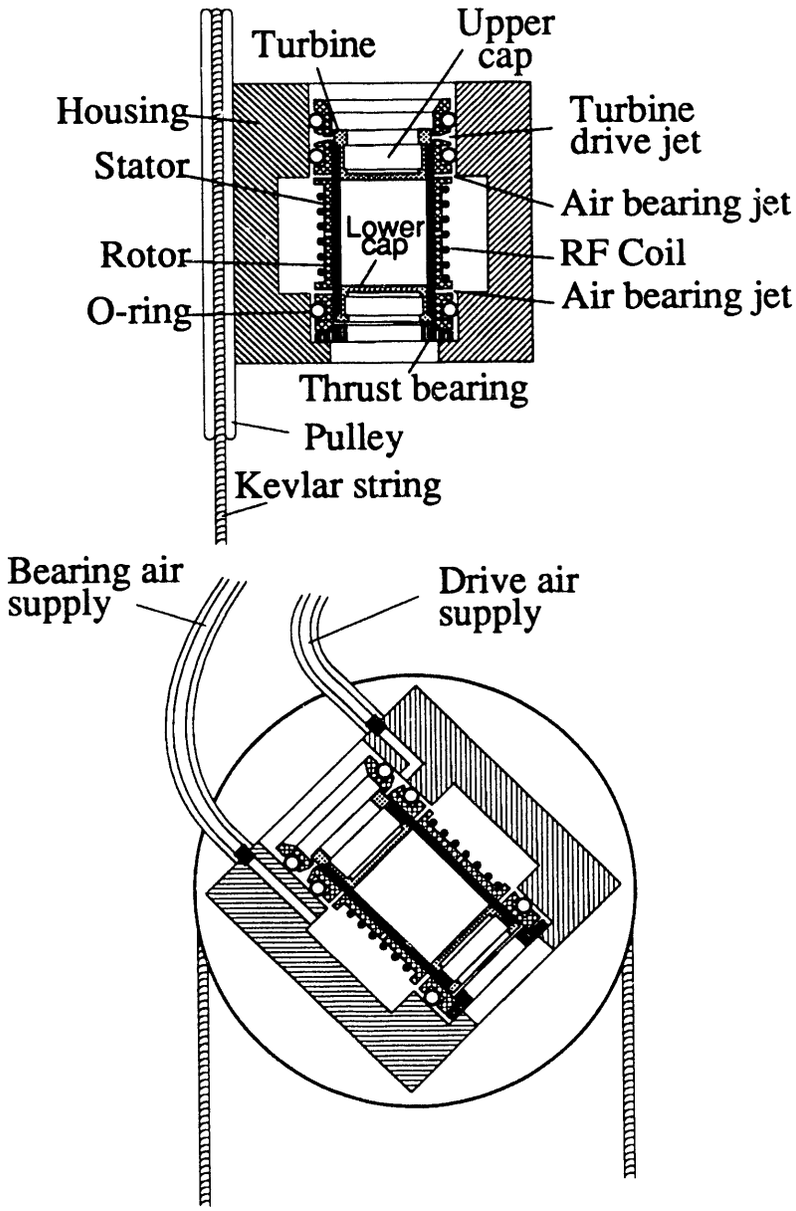

Figure 4.2: Cross–sectional views of the probehead used for the first DAS experiments. The rotor mechanism, dual air–delivery system, and mechanical axis flipping assembly are illustrated.

The variable–angle capability of this design is limited by the position of the coil with respect to the z–axis. The coil is used to irradiate the spins in the sample with short pulses of radiofrequency power and the irradiating field here is in the direction defined by the symmetry axis of the cylindrical coil. Only the component along the x–axis in the laboratory frame affects the spin angular momentum of the nuclei and this component depends on the cosine of the angle which the coil makes with the x–axis. This angle is the geometric complement of the angle θ describing the orientation of the rotor with respect to the z–axis. The irradiation efficiency obviously suffers as the angle θ approaches low angles. The length of time needed to cause 90° nutation of the magnetization, for full creation or mixing of spin coherences, will change when moving from one angle to the next and so must be calibrated at each angle used in the experiment. The detection efficiency also depends upon the direction of the coil, so that higher spinning angles (closer to 90°) provide the largest signal intensity. Therefore, the larger angle of 79.19° is chosen as the second angle in the $k = 1$ DAS experiment.

The probe is flipped between angles by a pulley/string arrangement coupled to an equivalent pulley on a high–torque, high–inertia stepper motor at the base of the magnet. Chapter 7 includes a further description of the laboratory setup for a DAS experiment and provides a detailed account of the testing procedure for probehead operation. The probe described here was optimized to perform a hop between $\theta_1 = 37.38°$ and $\theta_2 = 79.19°$ in 35 msec.

The air for the bearing and drive jets arrives through two hoses clamped to the top of the stator housing. This placement adds extra inertia to the probehead which may be avoided by supplying the air coaxial to the pulley axis. This is not possible

with the moving coil design since the connections for the rf coil are made along this axis. A fixed–coil probehead was designed as an improvement to the initial design and is described in a paper in the *Review of Scientific Instruments* [115] and in Chapter 7 of this work. The filling factor of a fixed coil probe will suffer as the coil volume must be expanded to fit around a larger portion of the hopping mechanism, but signal intensity is sacrificed in order to increase the electronic efficiency and reliability. The inertia of the assembly is also decreased in the new design with the goal of increasing the speed of the hop.

4.2.2 Sodium–23 NMR

The first nucleus considered in a DAS experiment was sodium–23. This choice was based on the high natural abundance (100%), moderate gyromagnetic ratio (about one–quarter that of protons), and moderate quadrupole coupling frequencies (C_Q values of approximately 2 to 3 MHz) of this nucleus. A simple sodium salt, sodium oxalate ($Na_2C_2O_4$) was the primary test compound and its crystal structure is known from x–ray diffraction studies [116]. It contains only one distinct type of sodium crystallographic site in its unit cell.

The NMR spectrum of a static sample of polycrystalline sodium oxalate is shown at the top of Fig. 4.3. This is the central transition powder pattern and it is approximately 15 kHz (140 ppm) wide due to the second–order quadrupolar interaction. The features are further broadened by chemical shift anisotropy and dipolar coupling of the spins. The field strength of 9.4 T corresponds to a sodium–23 resonance frequency of 105.84 MHz (and a proton resonance frequency of 400 MHz), so the field is already high enough to cause a considerable narrowing of the spectrum due

to the inverse square dependence (in ppm) of the quadrupolar anisotropy on the strength of the magnetic field (see Eq. 2.29).

Utilizing magic–angle spinning, the width of the pattern narrows to between 3 and 4 kHz and is almost five times narrower than the static spectrum. Spectral features associated with the second–order quadrupolar interaction are evident, but none of the singularities or shoulders in the pattern occur at the isotropic frequency (center of gravity) for the resonance. Computer simulations may be used to determine the isotropic chemical shift and quadrupolar parameters by either a best fit or visual matching and it is found that $\sigma_{iso}^{(CS)} = 1$ ppm, $C_Q = 2.5$ MHz and $\eta = 0.7$ yield the closest match. The center of gravity of the resonance occurs at −15 ppm which agrees with the isotropic second–order quadrupolar shift calculated from these parameters of −16 ppm. Overall, this is a well–characterized sample and yields an excellent, if somewhat chemically uninteresting, test for the new techniques.

The DAS probehead may be set to any orientation within the magnetic field, allowing acquisition of single–axis spinning spectra away from the usual magic–angle. In Fig. 4.4 the spectra at the two $k = 1$ DAS angles illustrate the reflection symmetry expected from Eqs. 3.7 and 3.8. Experimental observation of these resonances permits evaluation of the degree to which this mirroring is actually observed. The main anomaly is in the size of the first–order sidebands associated with each centerband resonance: those at the lower angle are larger. Theoretically, mirror symmetry should be observed only for the centerband. The modulation of the sidebands is also angle–dependent, but a dependence on the second and fourth Legendre polynomials is not found. The decrease in odd–order sideband intensity as θ increases

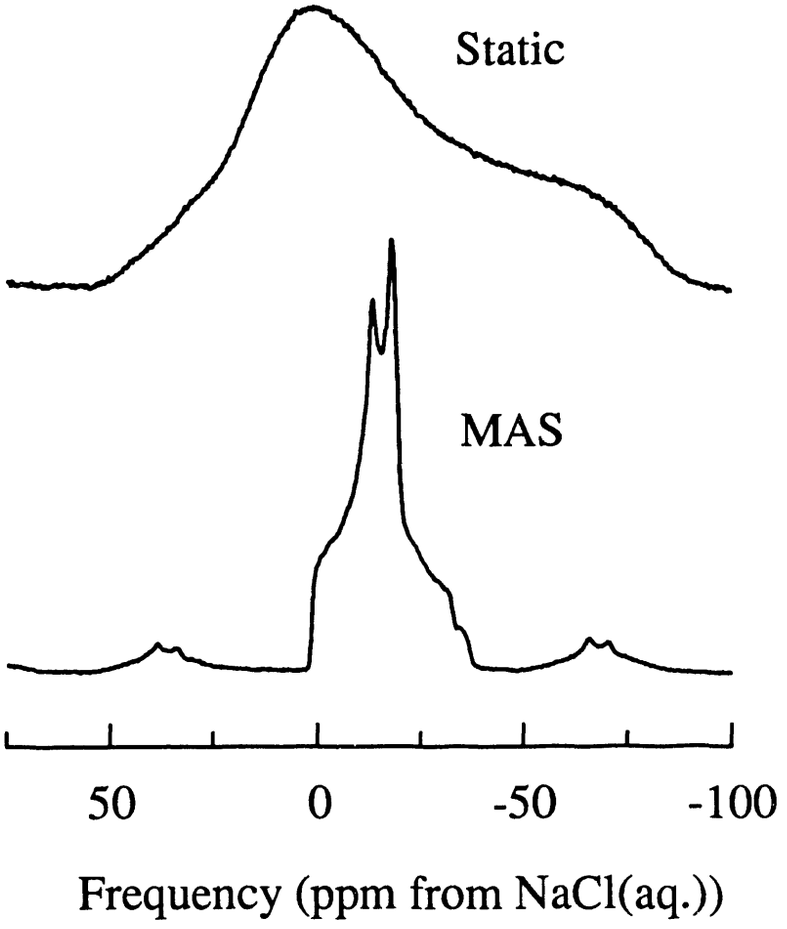

Figure 4.3: Static and magic-angle spinning (MAS) NMR spectra of sodium–23 in polycrystalline sodium oxalate ($Na_2C_2O_4$) at a field strength of 9.4 T. The zero of the frequency axis is the resonance frequency of sodium–23 in a saturated aqueous solution of sodium chloride.

is described in the equations of Lefebvre *et al.* in reference [74]. The centerband intensities do show the expected mirror symmetry about the isotropic frequency where they would intersect, here at around −15 ppm with respect to the sodium–23 resonance from a saturated aqueous solution of NaCl.

The reason that the DAS experiment works is closely related to the mirror symmetry. The resonance frequency for the spins in a particular crystallite, while the whole powder is spinning at $\theta_1 = 37.38°$, occurs at a definite position in the spectrum. The spins in this crystallite contribute independently to the spectrum: the lineshape is inhomogeneous and a hole could be burned into it by saturation of all spins resonant at one frequency. When the sample spins at $\theta_2 = 79.19°$, the same spins have their resonance at the same distance from the isotropic frequency, *but on the other side of the isotropic frequency.* This is true for all crystallites in the sample and so for the entire spectrum.

A standard $k = 1$ DAS experiment proceeds as follows. During the first half of the t_1 period, the spins are evolving under the frequencies in the $\theta_1 = 37.38°$ spectrum. This information is stored in Zeeman order (a component is saved along the z–axis), and then during the second half of t_1 the spins have an evolution governed by the frequencies at $\theta_2 = 79.19°$. The mirrored frequencies not only cancel, but the spectrum effectively collapses to the isotropic frequency and signal is seen from all spins in the sample, not just those which happen to be at the isotropic frequency at all times.

A similar description holds for a DAS experiment using any set of complementary angles. For the angles which are the zeroes of $P_4(\cos\theta)$ (the spectra are shown Fig. 4.5) the scaling factor is $k = 1.87$. Therefore, the evolution time at the second

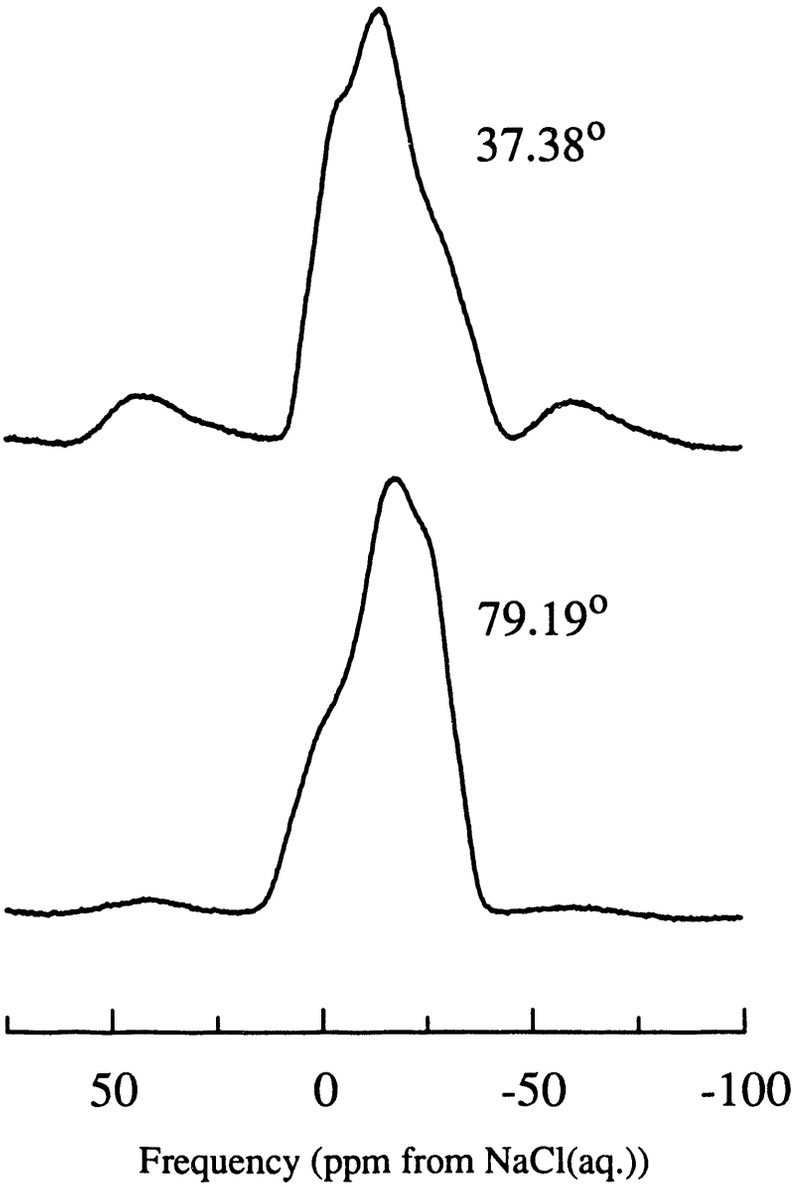

Figure 4.4: NMR spectra of sodium–23 in polycrystalline sodium oxalate ($Na_2C_2O_4$) at a field strength of 9.4 T while spinning the sample at the two $k = 1$ DAS angles 37.38° and 79.19°.

angle must be 1.87 times as long as at the first. This is also related to the shape of the spectra as they are mirror images about the isotropic frequency at −15 ppm and the width of the spectrum at the first angle is 1.87 times the width of the spectrum at the second angle. If spins in a particular crystallite resonate at a fixed frequency interval from the isotropic shift at the first angle, then at the second angle they will resonate on the other side of the isotropic shift but at a frequency closer to isotropic frequency. The ratio of the frequency differences from the isotropic shift is exactly k. For the anisotropic phase factors to cancel from the two evolution periods the product of the anisotropic frequency and the evolution time at the second angle must be equal and opposite in sign to that at the first. Since the anisotropic frequencies differ in sign and the frequency at the first angle is 1.87 times greater, the evolution time at the second angle must be 1.87 times as long.

4.2.3 Sodium–23 DAS

DAS Echoes

Consider the experiment illustrated in Fig. 4.1 with a sample of polycrystalline sodium oxalate in the rotor. After the initial pulse, the magnetization decays due to the interference from all of the frequencies in the spectrum at $\theta_1 = 37.38°$. The free induction decay (FID) of this signal is shown in Fig. 4.6(a) and the Fourier transform of this FID is the spectrum at the top of Fig. 4.4. After waiting a period of $t_1/2 = 500$ μsec the second pulse is applied and the magnetization is stored. The flip of the axis takes 35 msec from θ_1 to θ_2 and then another properly calibrated pulse returns the magnetization to the transverse plane. Proper phase cycling of the pulses (found in Fig. 4.1 and described in more detail in the text) produces the

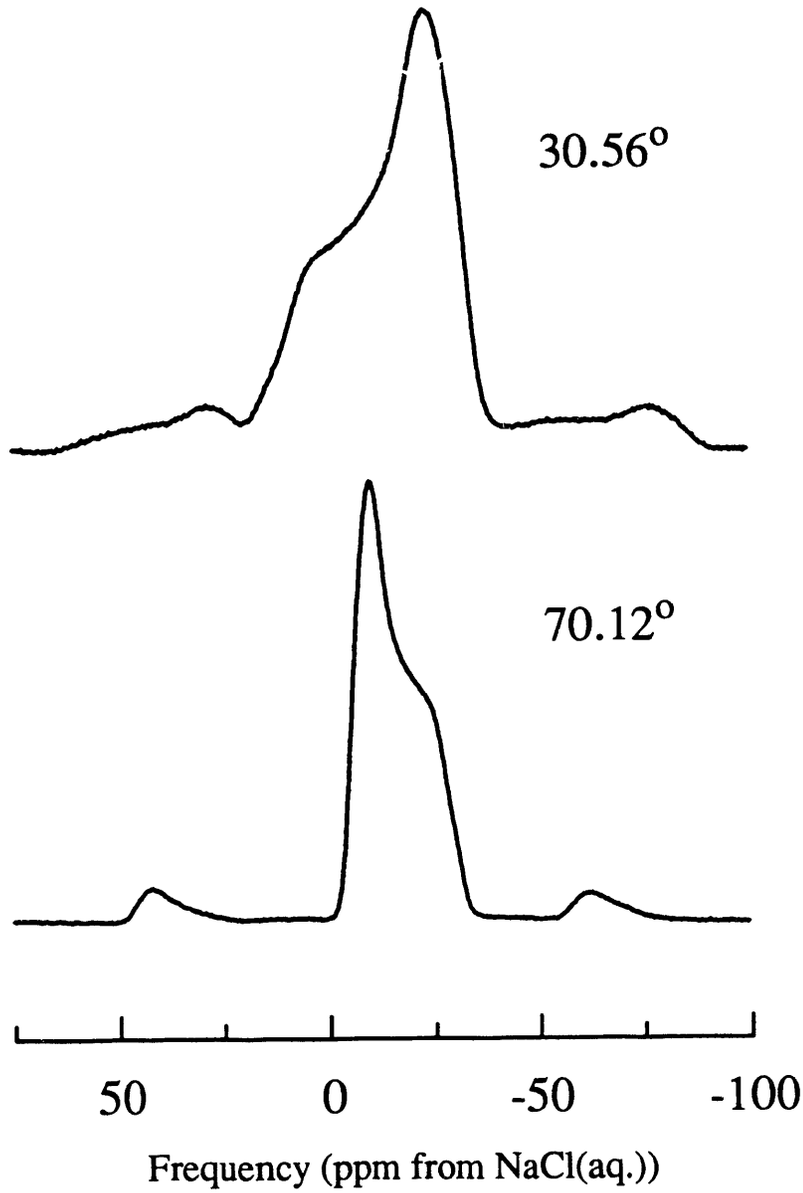

Figure 4.5: NMR spectra of sodium–23 in polycrystalline sodium oxalate ($Na_2C_2O_4$) at a field strength of 9.4 T while spinning the sample at the two DAS angles 30.56° and 70.12°. These two angles are the zeroes of the fourth Legendre polynomial and have an approximate scaling factor of $k = 1.87$

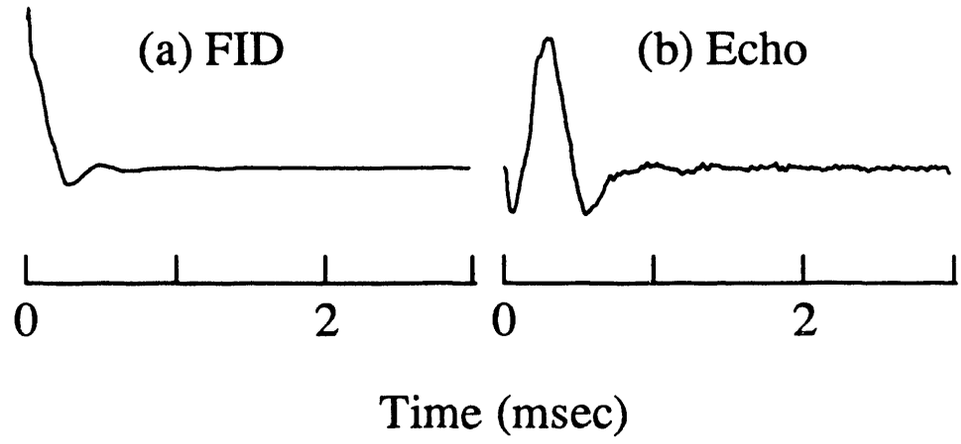

Figure 4.6: (a) The free induction decay (FID) from sodium oxalate while spinning at an angle of 37.38°. The Fourier transform of this signal is the spectrum while spinning at 37.38° shown in Fig. 4.4. (b) The second–order echo observed after performing the DAS experiment in Fig. 4.1. This echo corresponds to the refocussing of the anisotropic components of the second–order quadrupolar and chemical shift interactions.

second–order quadrupolar echo in Fig. 4.6(b). The echo maximum occurs when a further evolution period of $t_1/2 = 500$ μsec has passed after the third pulse. The magnetization at time t_1 (the echo top) has evolved for a total time of 1 msec under the isotropic frequency for the sodium–23 nuclei in this sample.

The data in the DAS experiment may be accumulated in a variety of ways. The usual way has been to begin data digitization at the point of echo formation and to continue acquisition in a second time domain, t_2. A two–dimensional data set is obtained containing both isotropic and correlated anisotropic frequency information for each distinct resonance resolved in the high–resolution (isotropic) domain.

Alternatively, the first data point in each t_2 domain (corresponding to the echo top) may be extracted and a one–dimensional isotropic interferogram constructed. Other data acquisition possibilities include accumulating the full echo after the third pulse (which may cause problems at short t_1 values unless another 180° pulse is used to form a full spin echo) or using a single–point detection method at each t_1 point with a pulsed spin–lock to obtain more efficient signal averaging.

One–Dimensional Sodium–23 DAS

The real and imaginary parts of the one–dimensional DAS interferogram from sodium oxalate are shown in Fig. 4.7. The t_1 time was varied in each of 128 experiments by $\Delta t_1 = 16$ μsec resulting in a spectral width of 62.5 kHz. Each data point is an average of four passes through the entire eight–pulse experiment. Pulse times for 90° nutation were 6.2 μsec at θ_1 and 4.1 μsec at θ_2 and the magnetic field strength was 9.4 T where the sodium–23 Larmor frequency is 105.84 MHz. The pulse lengths were calibrated for selective excitation of the central transition resonance by comparing the pulse lengths for maximization of the FID from the sodium oxalate sample and a sample of sodium chloride. The cubic symmetry of the sodium chloride produces a negligible EFG at the sodium lattice sites and therefore no quadrupolar broadening is observed in the central transition.

The Fourier transform of the decay in Fig. 4.7 is the high–resolution DAS spectrum shown in Fig. 4.8. The spectrum reveals only one isotropic line, at a frequency of –15 ppm. The linewidth is 575 Hz and spectral resolution is limited at this point by sodium dipole–dipole interactions.

The remaining lines are sidebands occurring at one–half of the rotor frequency of 3 kHz. The appearance of the sidebands at half of the rotor frequency is expected

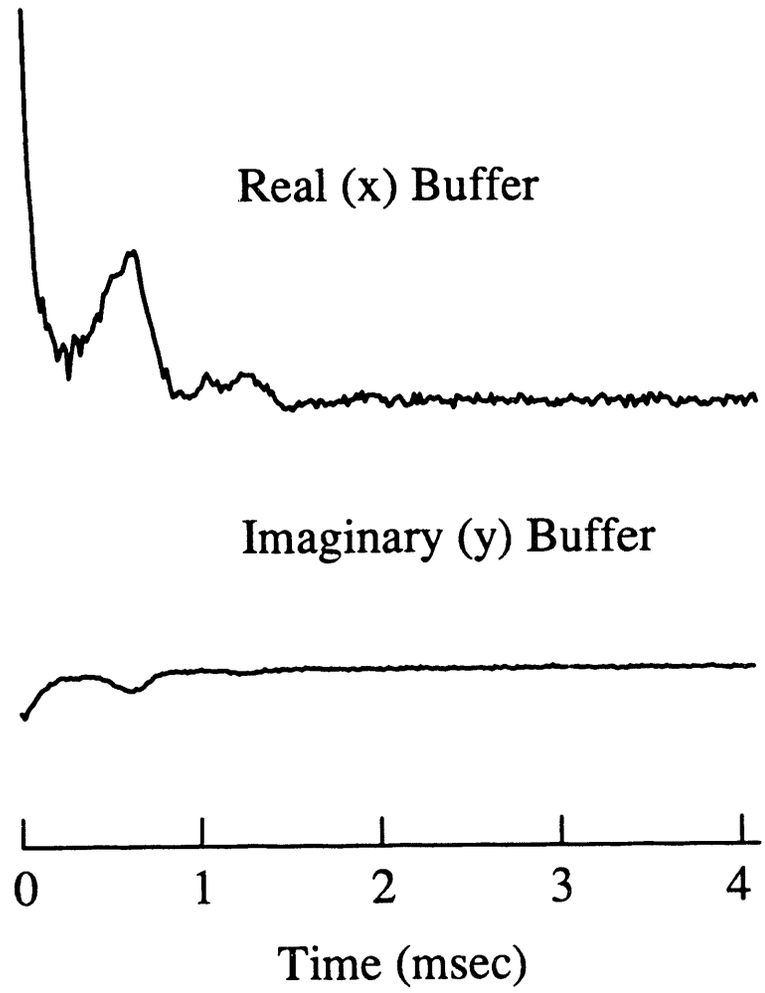

Figure 4.7: DAS free induction decay obtained from collecting the echo heights as a function of t_1 in a DAS experiment on sodium oxalate in a magnetic field of 9.4 T.

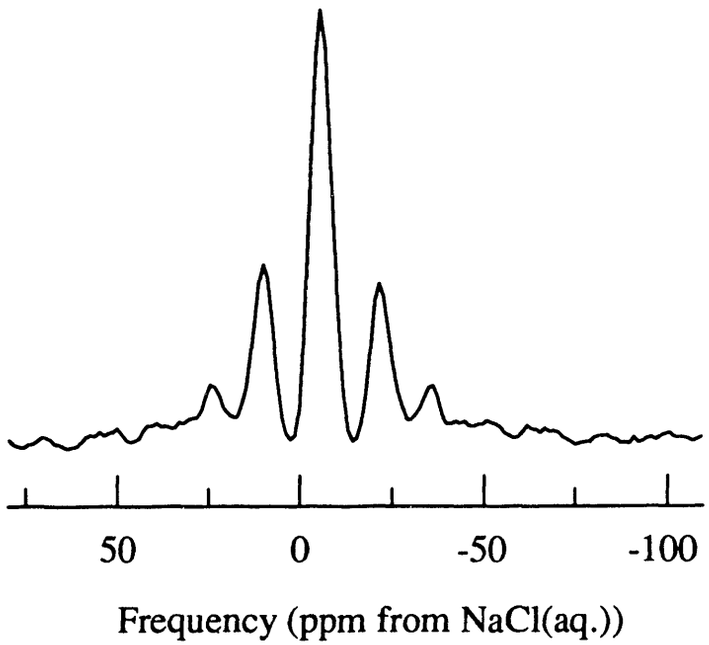

Figure 4.8: The DAS NMR spectrum of sodium–23 in sodium oxalate at 9.4 T reveals a narrower resonance line than the static and MAS spectra. The experimental conditions leading to this spectrum are described in the text and the frequency axis is expanded to show only the central 20 kHz of the spectrum.

since the evolution period is divided into two equal sections with a storage period between them. This effect is similar to that seen in two–dimensional spin–echo experiments [117]. For a physical picture of this phenomenon, the following argument is useful. The appearance of spinning sidebands in a spectrum corresponds to a modulation of the time domain signal which refocusses into a rotational echo once every rotor period [118]. The signal will die away in the FID and reappear at a time $\tau_r = 1/\nu_r$ where ν_r is the rotational frequency. In the first half of the DAS experiment, the maximum signal available for storage will be present when the evolution time equals the rotational period τ_r, and then at integer multiples of this time. After storage, the refocussed signal will also have a maximum when the second evolution time is equal to the same multiple of τ_r. The maximum signal (or the first dimension rotational echoes) in the one–dimensional DAS FID will occur when $t_1 = 2n\tau_r$ with n an integer. The rotational echoes occur only half as frequently in the first time domain and the Fourier transform of this corresponds to having a rotor spin at half of the rotation frequency. Therefore, sidebands are present at half of the rotor frequency in DAS. While the rotor in the probe described here spins at speeds between 3 and 3.5 kHz, newer versions achieve speeds up to 6 or 7 kHz and the sideband problem is generally reduced.

Two–Dimensional Sodium–23 DAS

The DAS data set from sodium oxalate may also be processed with a two–dimensional Fourier transform. The form of the signal as a function of t_1 and t_2 is

$$S(t_1, t_2) = \sum_{\text{all cryst.}} e^{i\omega_{iso}t_1} e^{i(\omega_{iso}+\omega_{aniso})t_2} \tag{4.1}$$

where the sum is over all crystallite orientations in the powder. A resonance at the isotropic frequency, ω_{iso}, appears in the high–resolution dimension of the spectrum while a broad powder pattern occurs in the second dimension due to the powder average of the anisotropic frequency. The powder pattern will be correlated with the high–resolution resonance at its isotropic frequency. However, since the data is accumulated to have the form in Eq. 4.1 in order to provide quadrature detection in both dimensions, a magnitude calculation must be performed on the final complex spectrum to obtain a two–dimensional map with all of its intensity positive. The problems associated with phase–twisted lineshapes (obtained from a Fourier transform of a signal such as that in Eq. 4.1) are addressed and resolved in the following chapter on pure–absorption–phase DAS.

A two–dimensional magnitude spectrum for sodium–23 in polycrystalline sodium oxalate is presented in Fig. 4.9. Since there is but a single distinct resonance from sodium in this sample, a single resonance is found in the contour map. The projections are the high–resolution DAS spectrum in the first frequency dimension and the low–resolution powder pattern in the second dimension, which is equivalent to the magnitude spectrum obtained from a sample spinning at $\theta_2 = 79.19°$. The resonance in the high–resolution dimension of the two–dimensional DAS spectrum is broader than that observed in the one–dimensional DAS spectrum since the magnitude calculation tends to broaden lines, especially adding intensity in the wings of a resonance.

In sodium–23 DAS, the width of the resonance lines are governed by dipole–dipole interactions such as those introduced in section 1.3.3. The strength of the dipolar interaction depends on the product of the gyromagnetic ratios for the two

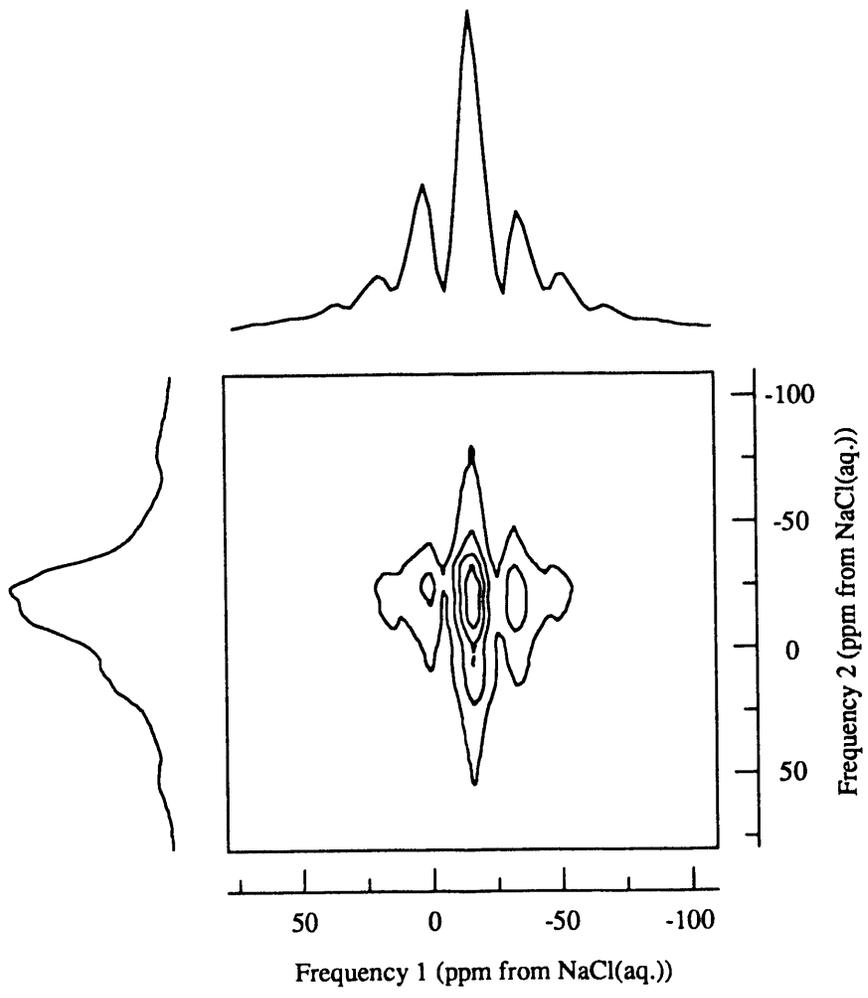

Figure 4.9: The two–dimensional DAS NMR spectra of sodium oxalate at a field strength of 9.4 T. The data are presented as a magnitude spectrum to avoid phase–twisted lineshapes.

spins involved. Homonuclear dipolar interactions are multi–body interactions which appear as bilinear spin terms and evolution due to these terms in the Hamiltonian are not stored efficiently by a DAS experiment. This irreversible loss of magnetization when strong dipolar couplings are present may also be related to the phenomena of spin–diffusion in solids [119] and the associated process of cross–relaxation in dipolar and quadrupolar systems [120, 121, 122].

4.2.4 Oxygen–17 DAS

Oxygen–17 is a quadrupolar nucleus ($I = \frac{5}{2}$) with a gyromagnetic ratio of approximately half that of sodium–23 and a much smaller natural abundance. Narrower DAS lines are expected for oxygen–17 due to overall weaker dipolar interactions. On the other hand, the quadrupolar couplings found experimentally [77, 78] and predicted theoretically [46] are often larger than in sodium–23. The first attempt at narrowing oxygen–17 resonances by DAS was performed on a sample of low cristobalite, a polymorph of SiO_2, enriched to 37% in oxygen–17. The natural abundance of oxygen–17 is 0.037% so enrichment is essential for obtaining reasonable signal intensity.

Experiments were performed in a 9.4 T magnetic field where the oxygen–17 Larmor frequency is 54.24 MHz. The 90° pulse times at θ_1 and θ_2 were 10.6 μsec and 6.0 μsec respectively compared to approximately 17 μsec with a sample $H_2{}^{17}O$. The spectra from a static sample and two separate DAS experiments are compiled in Fig. 4.10.

The isotropic frequency at –16.6 ppm (with respect to $H_2^{17}O$) is distinguished from the large set of sidebands present in both DAS spectra by comparing the

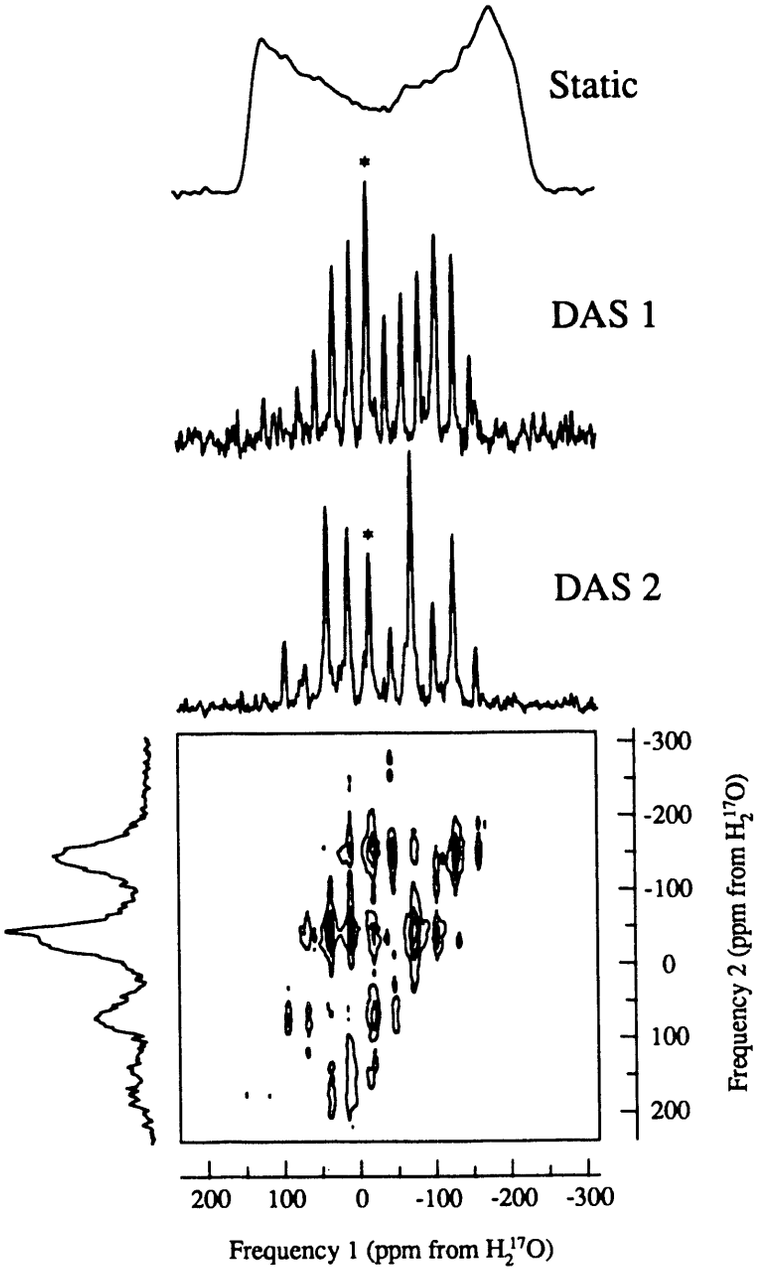

Figure 4.10: Static and DAS oxygen-17 NMR spectra of polycrystalline low cristobalite (a polymorph of SiO_2). The field strength is 9.4 T and the DAS spectra were obtained with spinning speeds of 2.46 and 3.04 kHz. This allows the isotropic peak (*) to be distinguished at -16.6 ppm. The contour map at the bottom is a magnitude spectrum of the full two-dimensional data set at the higher spinning speed.

spectra at two different spinning speeds. The isotropic peak does not shift and the sidebands move to integer multiples of one–half of the rotor frequency. The isotropic line has a residual linewidth of approximately 200 Hz, two orders of magnitude narrower than the resonance from a static sample. This is also nearly two and a half times narrower than the sodium–23 DAS resonance from sodium oxalate.

4.3 Double Rotation

4.3.1 Experimental Preliminaries

Once the double rotation motion is achieved in the laboratory, a DOR experiment is easier to accomplish than the DAS experiment because it is inherently one–dimensional. A single pulse and acquire NMR experiment is usually sufficient to obtain a high–resolution spectrum. See, however, the manuscript by Samoson regarding synchronized DOR for a more complicated DOR experiment aimed at suppression of odd–order sidebands in the spectrum [112].

The difficult task when performing DOR NMR is the design, building, and successful operation of a DOR probe. The first probehead was constructed by Dr. Ago Samoson, working closely with the Department of Chemistry machine shop at the University of California at Berkeley. It is described in reference [113] and has been honored by Research & Development Magazine as one of the 100 most significant new technological products of the year in 1989 [123]. Subsequent improvement of this design has been accomplished by Dr. Yue Wu, a postdoctoral researcher at Berkeley, and is also described in the literature [124]. This design is illustrated in Fig. 4.11.

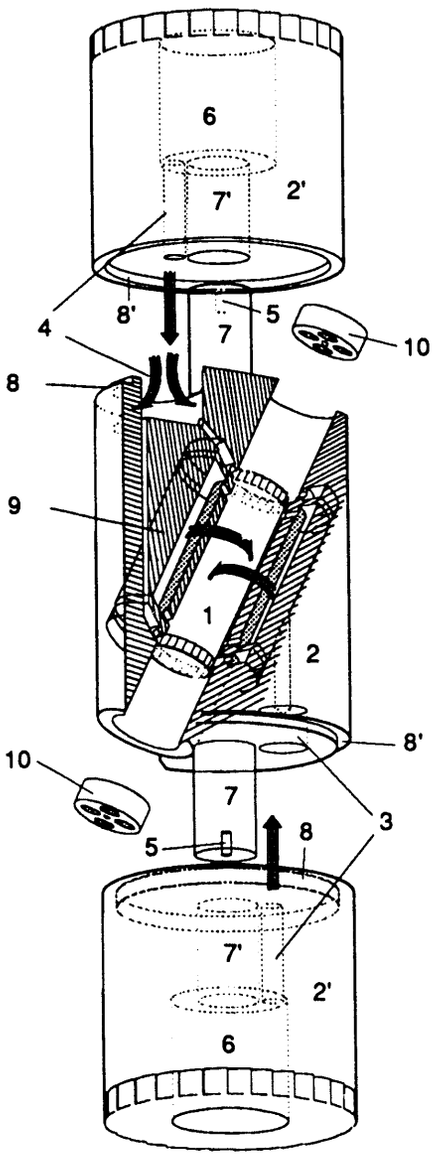

Figure 4.11: Schematic drawing of the NMR probehead for double rotation experiments.

The new double rotor has an inner rotor (1), with flutes at either end, which contains the sample. Its length is 13.3 mm and its diameter 4.6 mm. The outer rotor is machined in a variety of separate parts: the axles (7) and the step shoulders (8) hold the end pieces (2′) onto the center piece (2). The center piece contains the inner stator assembly (9), the inner rotor (1), and the inner stator endcaps (10). The overall length of the outer rotor assembly is 46 mm with a 13 mm diameter.

Air is brought into the inner rotor through the holes (3) and (4) in the end pieces. The air passes into drive and bearing mechanisms for the inner rotor from the top and bottom respectively. The inner rotor typically reaches rotation frequencies of 5 kHz. The outer rotor is placed in a conventional bearing/drive stator assembly fitted with two caps which direct air for the inner rotor into the holes (6). The outer rotor may reach speeds up to 2 kHz with no air flow supplied to the inner rotor. When the inner rotor is spinning, 1 kHz is the upper limit for steady performance.

The inner rotor is inclined at an angle of 30.56° with respect to the cylindrical axis of the outer rotor: this is a zero of $P_4(\cos\theta)$. The outer rotor is spun around an axis at the normal second–rank magic angle of 54.74° with respect to the large external magnetic field. As shown in Chapter 3, this will average first– and second–order anisotropies including those due to the chemical shift and the second–order quadrupolar interaction in the central transition of quadrupolar nuclei.

4.3.2 Sodium–23 DOR

As with DAS, the capabilities of the DOR experiment were first demonstrated on a well–characterized test compound. The sodium–23 resonance from polycrystalline sodium oxalate ($Na_2C_2O_4$) once again provides an excellent example.

The double rotation motion is begun by first bringing the smaller, inner rotor up to speed (approximately 5 kHz rotation frequency) and then beginning the motion of the outer rotor. It is crucial to keep the inner rotor from stopping during the spinning up to speed of the outer rotor. Crashes of the inner rotor were quite common in the first experimental tries, but eventually double rotation was achieved. The spectra of Figs. 4.12 and 4.13 illustrate early results for sodium oxalate.

Isotropic resonances in DOR NMR are distinguished from spinning sidebands by obtaining spectra at two outer rotor frequencies (Fig. 4.13). The resonance at −15 ppm is the isotropic shift for sodium−23 in sodium oxalate, as also measured in the DAS experiment. The sodium−23 resonance from DOR is noticeably narrower than that in the DAS spectrum: from DOR it is on the order of 150 Hz wide while it is almost four times as wide in the DAS spectrum. The difference in the two techniques is that in the serial DAS experiment there is a storage period where dipolar interactions could cause a decrease in the signal observed. Cross-relaxation to other energy levels not in the central transition or spectral spin diffusion are possible mechanisms for the observed broadening. Further investigation of this broadening is an important extension of this work.

4.3.3 Oxygen−17 DOR

A further example of DOR is its application to oxygen−17 nuclei in solids. A more complete study of oxygen−17 in minerals forms the basis of Chapter 6. Here, the first resolution of overlapping resonances from crystallographically inequivalent nuclei using these new techniques is presented [104].

Diopside is a polycrystalline silicate mineral belonging to the pyroxene fam-

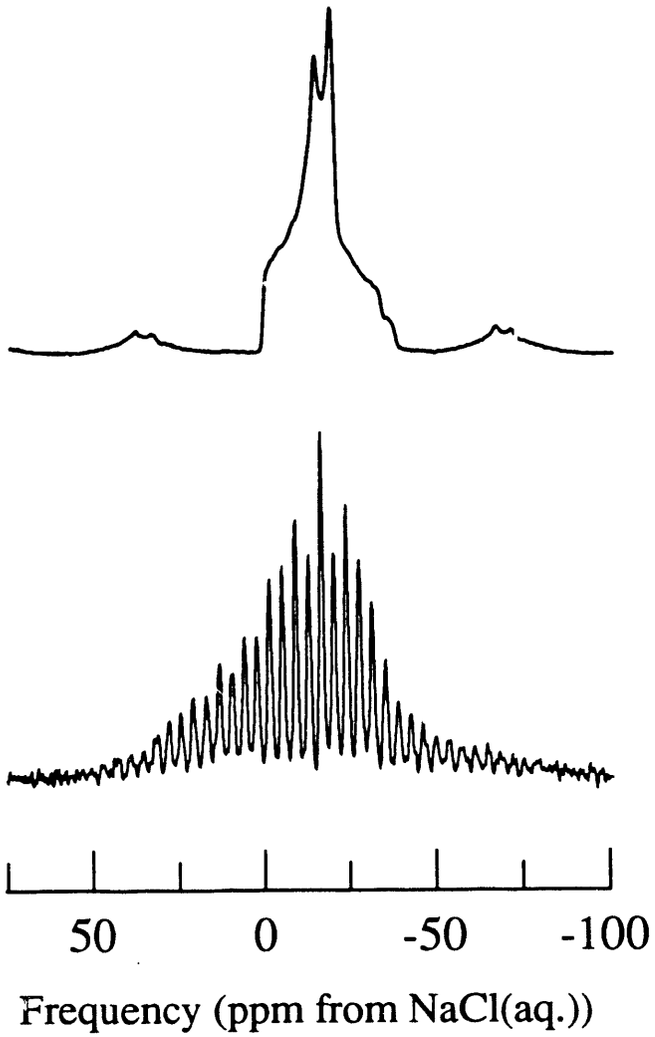

Figure 4.12: Top: MAS spectrum for sodium–23 in polycrystalline sodium oxalate ($Na_2C_2O_4$) at a field strength of 9.4 T. Bottom: Double rotation NMR spectrum of sodium–23 in sodium oxalate. In the DOR spectrum the sidebands occur at multiples of the outer rotor frequency (394 Hz). The frequency axis is given with respect to the sodium–23 resonance from a saturated aqueous solution of sodium chloride.

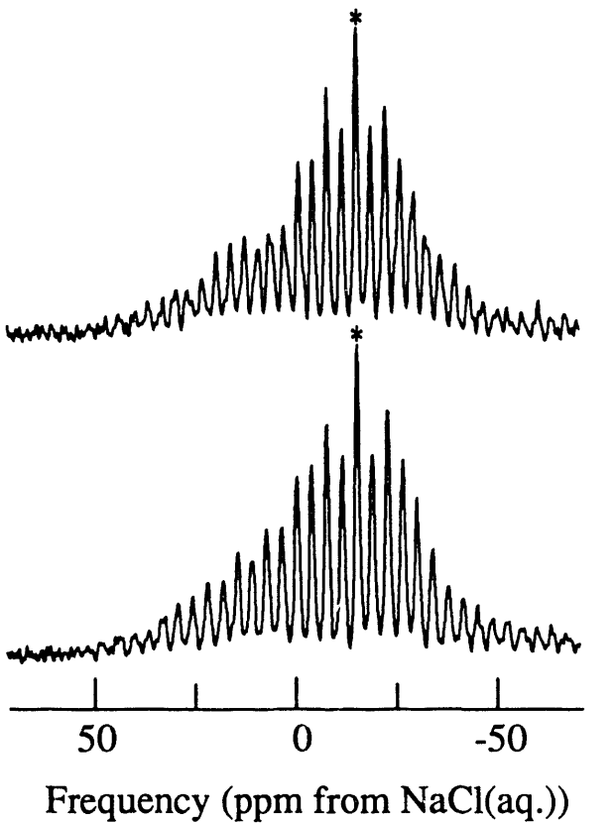

Figure 4.13: DOR spectra for sodium–23 in polycrystalline sodium oxalate ($Na_2C_2O_4$) at a field strength of 9.4 T. The rotational frequencies in the two experiments are 380 Hz (top) and 394 Hz (bottom) and the isotropic peak (*) occurs at –15 ppm.

ily [125]. Its molecular formula is $CaMgSi_2O_6$ and the unit cell contains three inequivalent oxygen–17 sites: two are terminal oxygens and one is a bridging species. These sites occur in a 1:1:1 ratio and we assume a random distribution of the 20% oxygen–17 enrichment in the sample. The oxygen–17 Larmor frequency is 54.24 MHz in a 9.4 T magnetic field. Pulse lengths of 4 μsec were used corresponding to tip angles of 30° from the z–axis for the central transition under selective irradiation conditions.

The spectra in Fig. 4.14 are MAS and DOR spectra of oxygen–17 in diopside. The two DOR spectra were obtained with different rotational frequencies of the outer rotor and the three isotropic resonances are discerned by comparison of the centerbands and spinning sidebands. These are the first spectra using these techniques in which crystallographically distinct nuclear sites which overlap in MAS spectra have been so clearly resolved.

4.4 A Comparison of DAS and DOR

The two techniques described and demonstrated above are both useful when second–order quadrupolar effects dominate the NMR spectra of half–odd integer quadrupolar nuclei. The differences and similarities of DAS and DOR are summarized in an attempt to distinguish which method may be more useful for a particular chemical problem.

The experiments themselves are undertaken in strikingly different ways: DAS is really a two–dimensional NMR technique whereas DOR is fundamentally one–dimensional. Two–dimensional NMR requires longer experimental times as one time dimension must be acquired pointwise by incrementing the time variable and

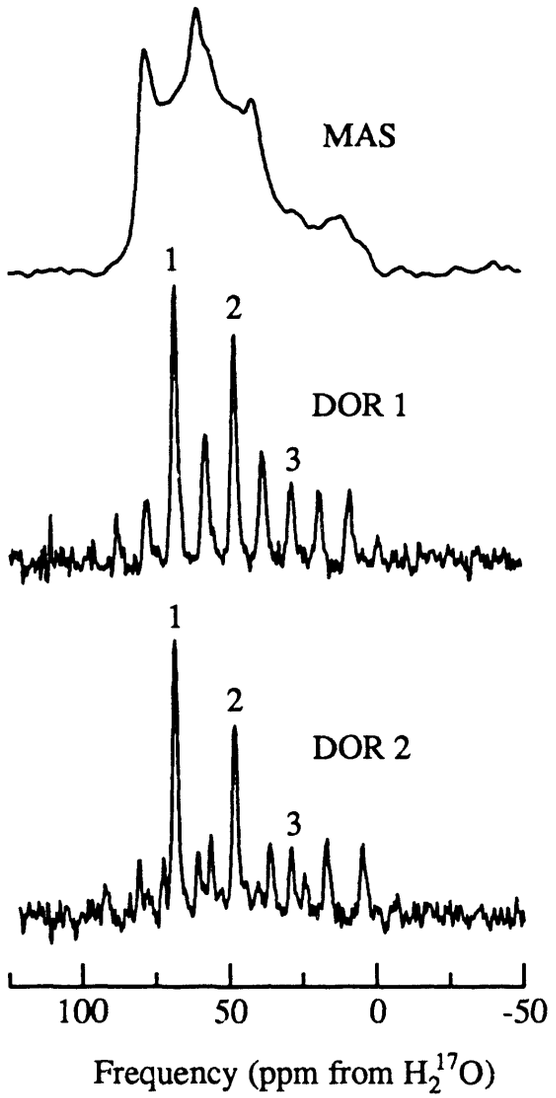

Figure 4.14: NMR spectra of oxygen–17 in the polycrystalline mineral diopside ($CaMgSi_2O_6$) at a field strength of 9.4 T. The top spectrum is the conventional MAS spectrum obtained while spinning at 5 kHz. Below are two DOR spectra obtained at different outer rotor spinning frequencies. The isotropic resonances are marked with numbers and sidebands occur at multiples of the outer rotor frequencies (540 and 680 kHz here). The frequency scale is referenced to the oxygen–17 resonance from $H_2^{17}O$.

running a whole set of one–dimensional experiments. The advantage of the two–dimensional method lies in the correlation of frequencies in the spectrum from the two time dimensions. The speed of obtaining a one–dimensional DOR spectra sacrifices the correlation of the isotropic and anisotropic resonances. This correlation is useful in full characterization of the chemical shift and quadrupolar parameters for the nuclei. Obtaining spectra at two or more field strengths is possible, however, with both techniques. This will also determine the isotropic chemical shift and the isotropic second–order quadrupolar shift, which contains a product of the quadrupolar parameters.

A correlation experiment with a double rotor could be accomplished in a manner similar to the MAS/powder pattern correlation experiments used for studying carbon–13 nuclei in solids [94]. While the outer rotor is inclined to the magnetic field at the second–rank magic angle, the second–order quadrupolar coupling is completely averaged. A hop of this axis to another angle (for example, to 90°) would provide a second time dimension where the anisotropies are again present. Once stable double rotation is accomplished, a hybrid DAS/DOR probe is a natural marriage of these two techniques. By having the inner rotor inclined to the larger rotor at the second–rank magic angle and beginning with the outer rotor at a fourth–rank magic angle, the chemical shift anisotropy would always be averaged at any orientation of the outer rotor.

The spinning speeds obtained in a DAS experiment provide efficient removal of sidebands compared to the slower outer rotor in the DOR technique. When quadrupolar coupling constants are large (greater than 2 MHz) the number of sidebands in a DOR spectrum can make spectral interpretation difficult, even when spectra

are obtained at two or more spinning speeds. Acquisition synchronized with the position of the outer rotor has been introduced to reduce the number of sidebands by a factor of two in a DOR spectrum [112, 124].

The need for a hop of the spinner axis during a DAS experiment places a restriction on the samples used to those with a sufficiently long relaxation times. During the experiment, magnetization along the magnetic field direction will decay with a time constant T_1, called the spin–lattice relaxation time. In samples studied by DAS, T_1 must be longer than the hopping time of 30 to 35 msec. This is often, but certainly not always, the case for quadrupolar species. The averaging in DOR is continuous, so there is no T_1 restriction. The need for a hop in a finite period of time is also thought to contribute to the widening of the resonance lines in the DAS spectra compared to the DOR spectra when dipole–dipole interactions become important.

Experimentally, DAS probes generally have a higher filling factor than DOR probes because the coil may be wound directly around the stator which is close to the rotor containing the sample. In DOR the coil is around the outer rotor stator assembly, although the sample fills the volume of only the inner rotor. Fixed–coil DAS probes also suffer similar degradation of filling factor. When high natural abundance nuclei such as sodium–23 and aluminum–27 are studied, the signal intensity is sufficiently strong in most experiments. When lower frequency, low abundance spins are considered the problems of signal–to–noise ratio become more acute and isotopic enrichment of the samples is often necessary..

In conclusion, both techniques have their own advantages and disadvantages. Empirically, it has been found that DAS works better for lower frequency, dilute

nuclei such as oxygen–17 where dipolar interactions are reduced and the large spread of frequencies produces a number of sidebands. Conversely, DOR has proven more effective in the study of sodium–23 and aluminum–27 where resonances appear close together and are too broad in the DAS spectra.

Chapter 5

Pure–Absorption–Phase DAS

5.1 Introduction

The first experimental realizations of second–order averaging (DAS and DOR) provide narrow isotropic resonances from quadrupolar nuclei. The overall shift of a resonance line observed in such a spectrum is the sum of two contributions, the chemical shift and the isotropic second–order quadrupolar shift, the latter depending on the strength and asymmetry of the local electric field gradients at the nucleus. The shielding and quadrupolar parameters correlate well with bond order and other structural properties, so that the narrowing of broad and often overlapping lines is useful for assigning resonances and extracting both qualitative and quantitative structural information.

In a conventional DAS experiment, momentarily dropping the extra phase cycling introduced in Chapter 4, the rf irradiation and rotor axis orientation schemes of Fig. 5.1 are necessary. For each t_1 increment, two experiments, labelled a and b, are summed in order to reconstruct a second–order DAS echo. In a second time

domain (t_2), a free induction decay containing information about the anisotropic part of the interaction may also be acquired. Two–dimensional Fourier transformation provides a correlation of anisotropic lineshapes in the ω_2 frequency domain with high resolution DAS lineshapes in ω_1. The early implementations of DAS employed phase modulation of the t_1 signal (the contribution to the signal from evolution during t_1 is a phase factor $e^{i\Omega_1 t_1}$) in order to obtain quadrature detection in the first time domain. This necessitates the display of the two–dimensional map as a magnitude spectrum [126]. Lineshapes in both dimensions are broadened by the magnitude calculation, and the inhomogeneous powder pattern lineshapes from second–order quadrupole interactions change markedly in this mode. A scheme for obtaining pure–absorption–phase lineshapes with quadrature detection in both dimensions of a DAS experiment has been developed [127], and is explained here in relation to coherence–transfer pathways and the theory of lineshapes in two–dimensional NMR. The immediate advantage of this new experimental strategy is narrower lineshapes in two–dimensional DAS correlation spectra.

5.2 Coherence Transfer

Coherences in magnetic resonance are a generalization of transverse magnetization [128, 129]: a state of the system where the net population difference between two spin eigenstates $\mid m\rangle$ and $\mid m-1\rangle$ may be zero but there is still a "connection" between the states. The order of a coherence, p, is the difference between the magnetic quantum numbers, and in the case of transverse magnetization $p = \pm 1$.

In high–field NMR, a coherent superposition of two eigenstates is a non–equi-

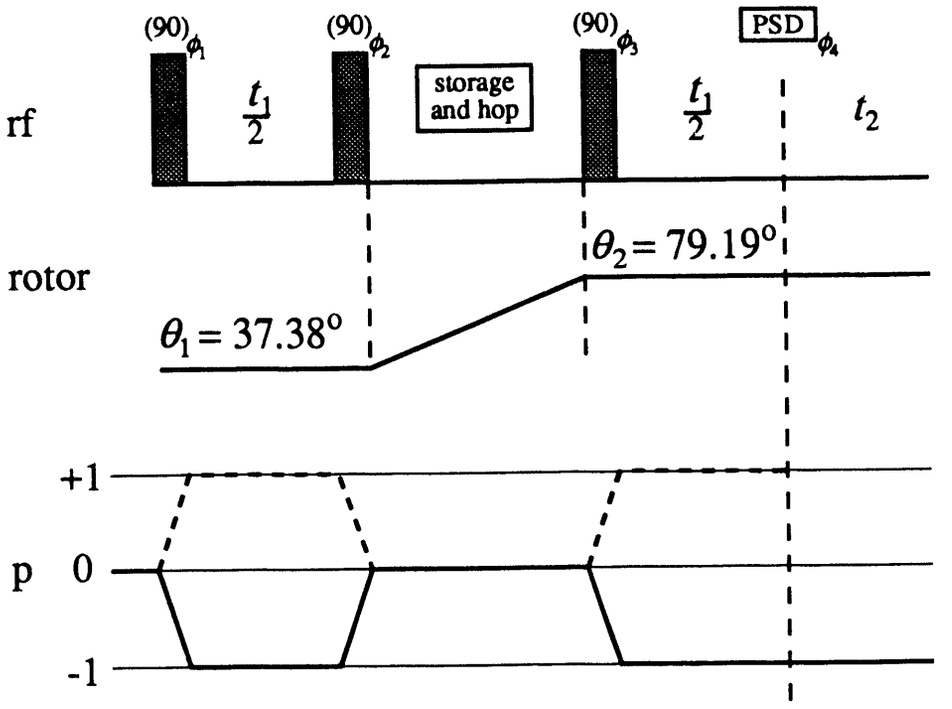

Experiment	ϕ_1	ϕ_2	ϕ_3	Real	ϕ_4	Imag.
a	+*x*	+*x*	+*x*	+*y*		-*x*
b	+*y*	+*x*	+*x*	-*x*		-*y*

Figure 5.1: The radiofrequency (rf) pulses, rotor position, and coherence order for a conventional (phase–modulated) DAS experiment.

librium state

$$| \Psi_{mn} \rangle = c_m \mid m \rangle + c_n \mid n \rangle \tag{5.1}$$

which evolves in time under the spin Hamiltonian for the system. A coherence between the states $\mid m \rangle$ and $\mid n \rangle$ corresponds to a non–zero off-diagonal term in the density matrix describing the system, $\rho_{mn} = \overline{c_m^* c_n}$, where the bar denotes an ensemble average. For each spin transition there are two associated coherences, ρ_{mn} and ρ_{nm}, with coherence orders of opposite sign. During free precession of the magnetization, the coherence order is preserved: $p = m - n$ is a good quantum number. The coherences are manipulated with radiofrequency pulses which *may* transfer coherence order depending on the flip angle, pulse power, resonance offset, and relative phase of the irradiation.

In earlier chapters the spin coherences were described in terms of Cartesian spin operators: I_x, I_y, and I_z. However, in the description of coherence–transfer pathways it becomes advantageous to use spherical tensor components of the spin angular momentum since a spherical component is uniquely associated with a particular coherence level [130]. Cartesian spin operators may be associated with two or more coherence levels as shown below. The transformation from Cartesian into normalized spherical components is

$$I_{+1} = -\frac{1}{\sqrt{2}}(I_x + iI_y) \tag{5.2}$$

$$I_0 = I_z \tag{5.3}$$

$$I_{-1} = \frac{1}{\sqrt{2}}(I_x - iI_y). \tag{5.4}$$

To return to the Cartesian basis, the non–trivial transformations are

$$I_x = -\frac{1}{\sqrt{2}}(I_{+1} - I_{-1}) \tag{5.5}$$

$$I_y = \frac{i}{\sqrt{2}}(I_{+1} + I_{-1}). \tag{5.6}$$

The density matrix at time t for a system of N spin-$\frac{1}{2}$ nuclei may be expanded in a set of 4^N spherical-basis product operators [131], each denoted by a particular $\mathbf{B}_s$ with expansion coefficients $b_s(t)$:

$$\rho(t) = \sum_{s=1}^{4^N} b_s(t)\mathbf{B}_s. \tag{5.7}$$

The orthogonality relations

$$\mathrm{Tr}[\mathbf{B}_r\mathbf{B}_s^*] = \delta_{rs}(2)^{N-2} \tag{5.8}$$

hold for these operators.

Quadrature detection is used almost exclusively in NMR spectroscopy in order to discriminate the signs of the spectral frequencies while allowing optimal use of pulse power and data storage capabilities. This corresponds to simultaneously digitizing the signal along two orthogonal axes in the xy plane. The complex signal is

$$S(t) = \mathrm{Tr}\left[\rho(t)\left(\sum_{\text{all nuclei}} I_x + iI_y\right)\right] \tag{5.9}$$

$$= \sqrt{2}(2)^{N-2} \sum_{\text{all nuclei}} b_{-1}(t) \tag{5.10}$$

and thus quadrature detection selects only one coherence level during the detection period (t_2 in Fig. 5.1). This coherence level is $p = -1$ since the only coefficient remaining in the expansion is $b_{-1}(t)$. Changing the phase of the receiver by an angle ϕ changes the signal acquired to

$$S(t,\phi) = \sqrt{2}(2)^{N-2}e^{-i\phi} \sum_{\text{all nuclei}} b_{-1}(t) \tag{5.11}$$

and phase cycling is useful for suppressing or retaining certain coherence orders during complex NMR experiments [129, 130]. Phase cycling is utilized in the DAS experiment to store separate components of the magnetization during the hop and then to form the proper DAS echo corresponding to refocussing of the anisotropic evolution frequencies.

In DAS, the system of quadrupolar spins is viewed as a collection of uncoupled fictitious spin-$\frac{1}{2}$ nuclei which simplifies all considerations of coherence transfer: in all of the preceeding equations, $N = 1$. Only four basis operators are needed: the identity operator, I_0, I_{+1}, and I_{-1}. The identity operator does not contribute to the NMR signal at any point, nor is it ever converted to observable signal, so may be disregarded in this analysis.

All of the necessary coherence-transfer pathways [129] needed to study the phase-modulated DAS experiment of Fig. 5.1 are found in Figs. 5.2 and 5.3. The simple rules used to construct these diagrams consider the change or evolution of coherences under (a) shifts whose average Hamiltonians are proportional to I_z with frequency Ω and evolution period t; and (b) radiofrequency pulses with tip angle β and irradiation phase ϕ. For free precession the $p = 0$ and $p = \pm 1$ coherences evolve as

$$I_p \xrightarrow{\Omega t I_z} I_p e^{-ip\Omega t} \tag{5.12}$$

while under radiofrequency pulses the coherence levels are changed according to

$$\begin{aligned} I_{\pm 1} \xrightarrow{-\phi I_z} \xrightarrow{\beta I_x} \xrightarrow{+\phi I_z} \quad & I_{\pm 1} \tfrac{(\cos\beta + 1)}{2} \\ & + I_0 \tfrac{-i \sin\beta}{\sqrt{2}} e^{\pm i\phi} \\ & + I_{\mp 1} \tfrac{(\cos\beta - 1)}{2} e^{\pm 2i\phi} \end{aligned} \tag{5.13}$$

$$I_0 \xrightarrow{-\phi I_z} \xrightarrow{\beta I_x} \xrightarrow{+\phi I_z} \quad I_{+1}\frac{-i\sin\beta}{\sqrt{2}}e^{-i\phi}$$
$$+I_0\cos\beta$$
$$+I_{-1}\frac{-i\sin\beta}{\sqrt{2}}e^{+i\phi}. \tag{5.14}$$

The phase shifts of the radiofrequency irradiation are taken into account in the above equations by first rotating around the z–axis by $-\phi$ degrees, performing the pulse along the new x–axis, and then reversing the rotation about the z–axis to bring the system back to its original reference frame. The rules for 90° x and y pulses may be found by setting $\beta = 90°$ and $\phi = 0°$ or 90° respectively.

For a fictitious spin–$\frac{1}{2}$ system, such as the central transition of quadrupolar nuclei, a selective 90° pulse will transform Zeeman order ($p = 0$) of the spin system in equilibrium into a linear combination of $p = +1$ and $p = -1$ (single–quantum) coherences. In other words, a 90° pulse creates transverse magnetization. Depending on the phase of the pulse, either $+x$– or $-y$–magnetization is produced. Evolution for time $t_1/2$ under the chemical shift and second–order quadrupolar Hamiltonians in the rotating frame allows accumulation of an exponential phase factor in each coherence. The frequency (called Ω_1) is the total frequency given in Eq. 3.1: a sum of isotropic and anisotropic terms depending on the crystallite orientation. The phase angle will be $\Omega_1 t_1/2$. A second 90° pulse on this system will mix the two coherences ($p = +1 \rightarrow p = -1$ and $p = -1 \rightarrow p = +1$) and also recombine the two single–quantum coherences into Zeeman order with a coefficient depending on the phase difference between the two pulses and the time of free precession. In experiment a of Fig. 5.1, where there is no phase change between the first two pulses, the negative cosine of the evolution phase at θ_1 is retained. In version b, the sine component is kept with a 90° phase shift between the two pulses.

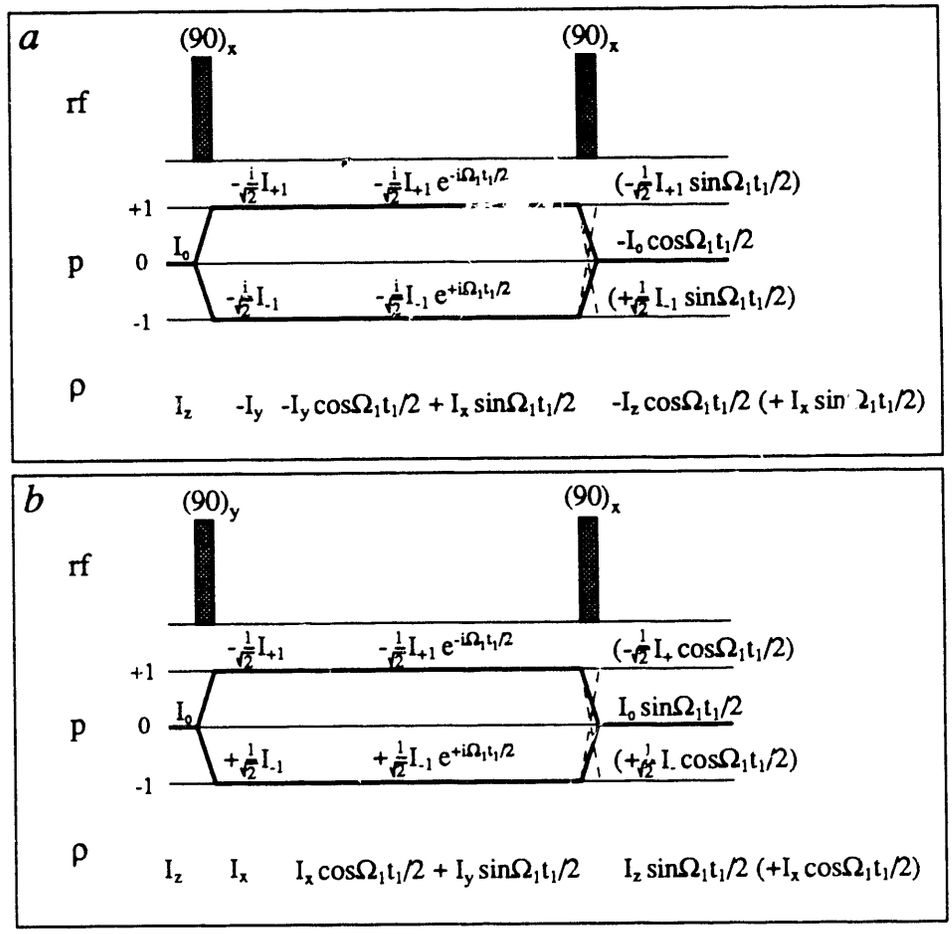

Figure 5.2: Simple coherence transfer mechanisms in the first part of the DAS experiment. The labels on each diagram correspond to the experiments labelled *a* and *b* in Fig. 5.1. The parentheses denote unobserved coherences that decay during the hop.

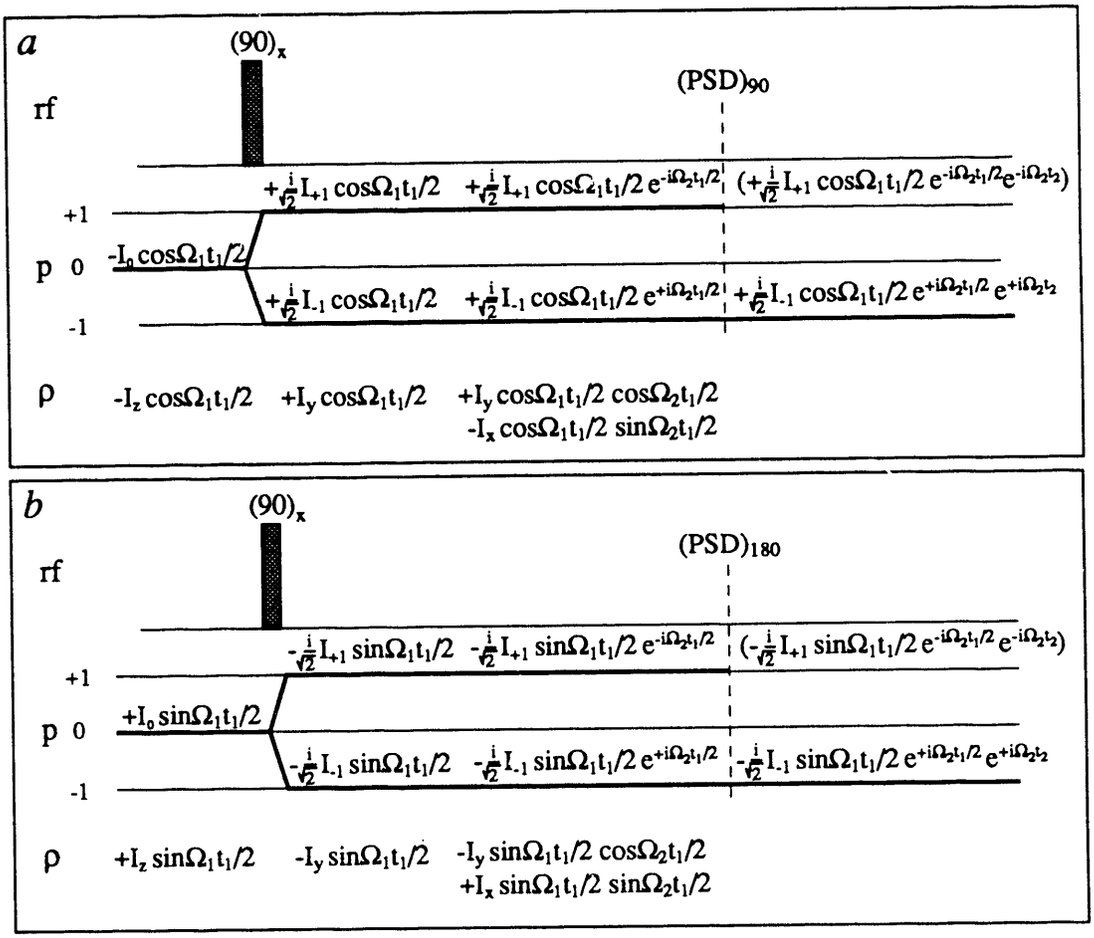

Figure 5.3: Simple coherence transfer mechanisms after the hop and during detection in the phase–modulated DAS experiment. Only the $p = -1$ coherence is detected, as explained in the text.

Since the remaining coherences in the transverse plane are still single–quantum coherences, they could also be detected at this time. In a DAS experiment, the transverse magnetization during the hop decays through irreversible processes and is dropped from consideration. The storage segment of the experiment selects populations (Zeeman order) and suppresses coherences and after the hop, only a component along the z–axis remains. The stored magnetization may be restored into the transverse plane by another pulse, and this collective process of storage and reinitiation of single–quantum coherences is called a z–filter [132]. The large Zeeman field along the z–axis is used to filter the transverse magnetization, essentially keeping a chosen component projected along either the x– or y–axis. Both $p = +1$ and $p = -1$ coherences are present after a z–filter and will evolve under another (or the same) Hamiltonian as during previous free precession.

In DAS, a second free precession must follow the hop to the second DAS angle (and z–filter) where anisotropic dephasing during the first period is refocussed. The evolution frequency is now Ω_2 and the evolution occurs for the same time period as before the hop. At time t_1 an echo has formed since the total phase is

$$(\Omega_1 + \Omega_2)\frac{t_1}{2} = \omega_{iso} t_1. \tag{5.15}$$

As described in Chapter 3 and Table 3.1, the state of the system in a DAS experiment at the point of refocussing (t_1) *before* detection and addition of the signals is

$$\rho_a(t_1) = +I_y \cos\Omega_1\frac{t_1}{2}\cos\Omega_2\frac{t_1}{2} - I_x \cos\Omega_1\frac{t_1}{2}\sin\Omega_2\frac{t_1}{2} \tag{5.16}$$

$$\rho_b(t_1) = -I_y \sin\Omega_1\frac{t_1}{2}\cos\Omega_2\frac{t_1}{2} + I_x \sin\Omega_1\frac{t_1}{2}\sin\Omega_2\frac{t_1}{2} \tag{5.17}$$

for the two experiments a and b respectively. If the signal is detected during t_2

according to phase ϕ_4 in Fig. 5.1 then (using Eq. 5.11)

$$S_a(t_1,t_2) = \frac{1}{2}\cos\Omega_1\frac{t_1}{2}e^{i\Omega_2(\frac{t_1}{2}+t_2)} \tag{5.18}$$

$$S_b(t_1,t_2) = \frac{i}{2}\sin\Omega_1\frac{t_1}{2}e^{i\Omega_2(\frac{t_1}{2}+t_2)} \tag{5.19}$$

Adding together the two signals from experiments a and b produces a signal

$$S(t_1,t_2) = \frac{1}{2}e^{i\omega_{iso}t_1}e^{i(\omega_{iso}+\omega_{aniso}(\theta_2))t_2}. \tag{5.20}$$

In this sort of echo experiment, both coherences have evolved up until the detection period yet only one ($p=-1$) is detected. Both coherence pathways were retained during the first evolution period since a second pulse mixed them to store a component of the evolving magnetization. The failure to again mix the coherences at the time of detection is the main problem here. As shown below, this complicates the phasing of two–dimensional spectra when only purely absorptive lineshapes are desired. A general rule for pure–absorption phase spectroscopy is that both positive and negative coherence orders (referred to as mirror–image pathways) must be retained until the time of detection [133]. In DAS, the further evolution in order to obtain the echo, coupled with the fact that only the $p=-1$ coherence is detected after time t_1, makes it impossible to use phase cycling alone to obtain pure–absorption–phase data.

5.3 Two–Dimensional NMR

A two–dimensional NMR experiment has at least two time periods of evolution during which the spin system evolves under separate effective Hamiltonians, and the characteristic frequencies of these Hamiltonians determine the frequencies observed

in the two–dimensional map or spectrum. Connections between frequencies in the two domains tell the experimenter about correlations in the two time domains for the same spins. Therefore, in DAS the isotropic resonances in the high–resolution isotropic dimension (ω_1) are correlated with their anisotropic resonances in the low–resolution (ω_2) dimension. The shape of the lines in the two–dimensional spectrum is an important consideration: often the lines are a mixture of absorption and dispersion lineshapes, a so–called phase–twisted lineshape [134]. The inseparability of the two components degrade the two–dimensional spectra since the dispersive contributions have broad tails and regions of negative intensity. Methods which circumvent this problem have been developed [135, 136], but are generally unsatisfactory for echo spectroscopy (such as DAS) without further modifications.

5.3.1 Lineshapes in Two–Dimensional NMR

The original two–dimensional NMR experiments such as Jeener's correlation spectroscopy (COSY) experiment [137] did not discriminate the sign of the frequencies in the first time dimension (t_1) of the experiment. Two–dimensional Fourier transformation of the time–domain matrix then leads to a spectrum folded about the transmitter frequency in ω_1. To overcome this, the transmitter frequency may be placed completely on one side of the spectrum. This has certain disadvantages: the transmitter power (symmetric about the carrier frequency) is distributed unevenly and the data storage overhead is severely penalized with empty space or noise. However, in this manner pure–absorption lineshapes are accessible. A problem arises when more efficient transmitter power distribution and data accumulation is desired.

In a one–dimensional NMR experiment, the signal is obtained in quadrature in order to discriminate the sign of the resonance frequency with respect to the carrier. The complex signal is distributed between a real (x) buffer and the orthogonal imaginary (y) buffer. A resonance with frequency Ω will produce a time–domain signal

$$S(t) = e^{i\Omega t} e^{-\frac{t}{T_2}} \tag{5.21}$$

where T_2 is a time constant describing irreversible decay of transverse magnetization (spin–spin relaxation). The signal is assumed to only be defined for $t \geq 0$. The Fourier transform of this signal is a sum of absorptive and dispersive components

$$\begin{aligned} F(\omega) &= \int_{-\infty}^{\infty} e^{i\omega t} S(t) dt \\ &= A + iD \end{aligned} \tag{5.22}$$

with

$$A = \frac{T_2}{1 + (\omega - \Omega)^2 {T_2}^2} \tag{5.23}$$

$$D = \frac{(\omega - \Omega){T_2}^2}{1 + (\omega - \Omega)^2 {T_2}^2}. \tag{5.24}$$

In two–dimensional NMR, we need to consider the signal from a spin whose frequency in the first (t_1) dimension is Ω_1, with a corresponding frequency in t_2 of Ω_2. Continuing the notation introduced above, A_2 and D_2 are the absorptive and dispersive components of the Lorentzian line at Ω_2 in the second frequency dimension. However, if the sign of the frequencies in the first dimension are not determined then lines will appear at $\pm\Omega_1$. The resonances at $\pm\Omega_1$ will have absorptive Lorentzian signals A_1^+ and A_1^- with corresponding dispersive components D_1^+ and D_1^-.

Experiments which correlate evolution frequencies from the same spin in two dimensions may be classified as either *amplitude* or *phase* modulated. The earliest two–dimensional experiments were amplitude modulated and did not discriminate in the sign of the frequencies in t_1. A complex signal is acquired in the second time domain with an initial amplitude proportional to the sine or cosine of the evolution angle in the first time period. Then

$$S_c(t_1, t_2) = \cos \Omega_1 t_1 e^{i\Omega_2 t_2} e^{-\frac{t_1}{T_{2,1}}} e^{-\frac{t_2}{T_{2,2}}} \tag{5.25}$$

is the cosine modulated signal. As above, $T_{2,1}$ and $T_{2,2}$ are time constants for exponential decay of the signals during t_1 and t_2 respectively. The two–dimensional Fourier transform of this signal is

$$\begin{aligned} F_c(\omega_1, \omega_2) &= \int_{-\infty}^{\infty}\int_{-\infty}^{\infty} e^{i\omega_1 t_1} e^{i\omega_2 t_2} S_c(t_1, t_2) dt_1 dt_2 \\ &= \frac{1}{2}(A_1^+ + iD_1^+ + A_1^- + iD_1^-)(A_2 + iD_2) \end{aligned} \tag{5.26}$$

which corresponds to a pair of phase–twisted lineshapes at Ω_2 in the second frequency dimension and at $\pm\Omega_1$ in the first. Folding the spectra about the carrier in ω_1 *will* provide a pure–absorption phase lineshape at the expense of placing the carrier totally on one side of the spectrum. Equivalently, the imaginary part of the t_2 decay may be zeroed and a real Fourier transform performed on the data. The preferred method, however, is to approach the problems of sign discrimination and pure–absorption lineshapes in a more elegant manner.

A correlation experiment may be modified to obtain data in a phase–modulated manner. To discriminate the sign of the coherences in the first time domain, the modulation of the signals during t_1 is converted from that of amplitude modulation to that of a complex phase modulation (a combination of sines and cosines). The

initial experiment is repeated with a relative phase change of 90° for all pulses preceeding the t_1 evolution period. A similar change of the detection (receiver) phase must also be made and the signals from the two experiments are summed together. The phase–modulated signal is

$$S_{pm}(t_1, t_2) = e^{i\Omega_1 t_1} e^{i\Omega_2 t_2} e^{-\frac{t_1}{T_{2,1}}} e^{-\frac{t_2}{T_{2,2}}} \tag{5.27}$$

and the two–dimensional Fourier transform of this signal is

$$\begin{aligned} F_{pm}(\omega_1, \omega_2) &= \int_{-\infty}^{\infty}\int_{-\infty}^{\infty} e^{i\omega_1 t_1} e^{i\omega_2 t_2} S_{pm}(t_1, t_2) dt_1 dt_2 & (5.28) \\ &= (A_1^+ + iD_1^+)(A_2 + iD_2) \\ &= (A_1^+ A_2 - D_1^+ D_2) + i(A_1^+ D_2 + A_2 D_1^+). & (5.29) \end{aligned}$$

This signal has both absorptive and dispersive components in the real part of the lineshape although it *has* discriminated the sign of the coherence in t_1. As discussed above this is not the most desirable signal. The pure–absorption–phase signal would have the form

$$F_{pp}(\omega_1, \omega_2) = A_1^+ A_2 + iD_1^+ D_2 \tag{5.30}$$

where all of the real components are in absorption mode. The observable differences between the pure–absorption signal (Eq. 5.30) and the phase–modulated signal (Eq. 5.29) are shown in Fig. 5.4. The broad dispersive wings in the lineshape from the phase–modulated signal are obviously undesirable and the pure–absorption lineshape is preferable if it can be obtained.

5.3.2 Two–Dimensional Pure–Absorption Experiments

There are two major methods described in the literature to obtain pure–absorption–phase two–dimensional NMR lineshapes [135, 136]. At first glance the

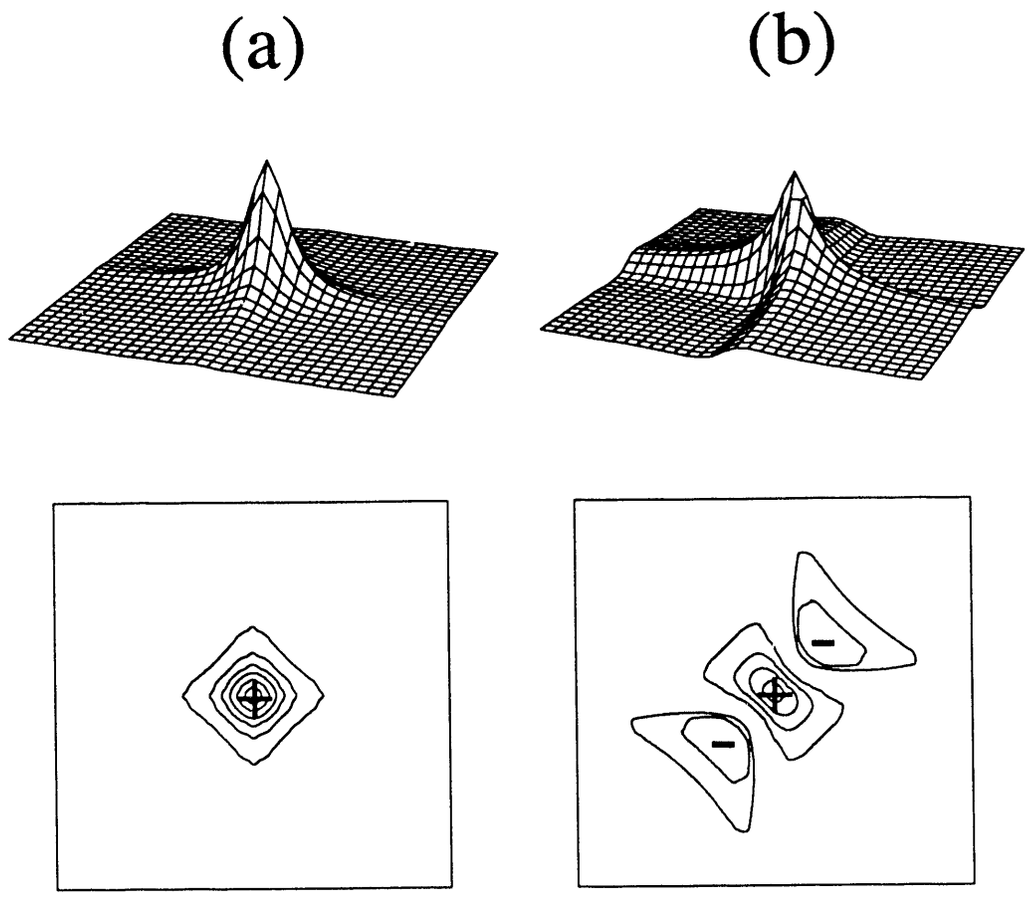

Figure 5.4: Mesh plots (top) and contour plots (bottom) of the two-dimensional NMR lineshapes corresponding to (a) pure-absorption-phase and (b) phase-modulated NMR experiments.

methods using TPPI [135] and what is called States method [136] seem to be very different, but on closer inspection are fully equivalent. The equivalency is not only in terms of signal–to–noise ratio or data accumulation time and storage necessary, but mathematically they are equivalent. This relation is studied in detail in the paper of Keeler and Neuhaus [126].

The discussion here is based on the States method [136] originally introduced for the accumulation of exchange NMR spectra. In this method, the cosine and sine modulated signals during t_1 are accumulated and stored separately. In the language of coherence–transfer pathways both the sum and the difference of both possible pathways in t_1 are retained. The two signals are then

$$S_c(t_1, t_2) = \cos \Omega_1 t_1 e^{i\Omega_2 t_2} e^{-\frac{t_1}{T_{2,1}}} e^{-\frac{t_2}{T_{2,2}}} \tag{5.31}$$

and

$$S_s(t_1, t_2) = \sin \Omega_1 t_1 e^{i\Omega_2 t_2} e^{-\frac{t_1}{T_{2,1}}} e^{-\frac{t_2}{T_{2,2}}} \tag{5.32}$$

The Fourier transforms of each time domain are performed separately, with the t_2 transform first. After the t_2 transform

$$F_c(t_1, \omega_2) = \cos \Omega_1 t_1 (A_2 + iD_2) \tag{5.33}$$

and

$$F_s(t_1, \omega_2) = \sin \Omega_1 t_1 (A_2 + iD_2). \tag{5.34}$$

The real part of F_s is swapped with the imaginary part of F_c to produce

$$F_c'(t_1, \omega_2) = (\cos \Omega_1 t_1 + i \sin \Omega_1 t_1) A_2 \tag{5.35}$$

and

$$F_s'(t_1, \omega_2) = (\cos \Omega_1 t_1 + i \sin \Omega_1 t_1) D_2. \tag{5.36}$$

The t_1 transform then yields

$$F_c''(\omega_1, \omega_2) = (A_1^+ + iD_1^+)A_2 \tag{5.37}$$

$$F_s''(\omega_1, \omega_2) = (A_1^+ + iD_1^+)D_2. \tag{5.38}$$

which provides a pure–absorption lineshape when the real part of F_c'' is displayed. This data processing is referred to as a hypercomplex Fourier transform [36] since there are two data sets in the complex plane (and hence two independent imaginary units) which may be manipulated separately.

5.4 Pure–Phase DAS: Theory

It should now appear more clear as to why the phase–modulated DAS experiment of Fig. 5.1 provides phase–twisted lineshapes. The coherence–transfer map for this experiment is also shown in the figure and has been carefully analyzed above. Evolution at $\theta_2 = 79.19°$ cancels anisotropic evolution at $\theta_1 = 37.38°$, but no additional coherence transfer occurs after echo formation at time t_1. Only one coherence–transfer pathway is retained at the end of t_1 in order to maintain frequency discrimination and phase–twisted lineshapes result. In order to obtain pure two–dimensional absorption lineshapes it is necessary to keep *both* halves of the coherence–transfer pathways, *i.e.* both $p = 0 \rightarrow -1 \rightarrow -1$ and $p = 0 \rightarrow +1 \rightarrow -1$ must be present, and this does not occur in conventional DAS since there is no coherence order change $p = +1 \rightarrow -1$ immediately before the beginning of the t_2 period. A related problem is encountered in liquid–state spin–echo correlated spectroscopy (SECSY) [138, 139], in which there is also no transfer of coherence after formation of a spin–echo. There is no possible way to phase cycle the pulses

so as to only obtain only sine or cosine modulation in t_1 as both $t_1/2$ periods are necessary in each experiment to refocus the anisotropic evolution. Further mixing of the coherences at the end of the t_1 period is needed. Two methods for doing this in a DAS experiment have been proposed [127].

5.4.1 Variation I: 90° Pulse

The conceptually simplest way to transfer coherence from $p = +1$ to $p = -1$ at the end of the t_1 evolution is suggested by the earlier discussion of coherence–transfer. Application of another 90° pulse before beginning t_2 acquisition will again mix the coherences. Figure 5.5 shows schematically how this can be accomplished in a DAS experiment with proper phase cycling. Note that the rotor continues to spin at the second DAS angle of 79.19°. The coherence–transfer pathways are also sketched in Fig. 5.5 and coherence pathways during the final two pulses of the experiment are examined in more detail in Fig. 5.6. The beginning of the experiment is identical to phase–modulated DAS: all pulses and phases are the same up until the end of the t_1 period. As before, two experiments a' and b' are necessary to reconstruct a full echo.

During the detection period only the $p = -1$ coherence is retained and the signals from the two experiments are

$$S_{a'}(t_1, t_2) = \frac{1}{2} \cos \Omega_1 \frac{t_1}{2} \cos \Omega_2 \frac{t_1}{2} e^{i\Omega_2 t_2} \tag{5.39}$$

$$S_{b'}(t_1, t_2) = -\frac{1}{2} \sin \Omega_1 \frac{t_1}{2} \sin \Omega_2 \frac{t_1}{2} e^{i\Omega_2 t_2} \tag{5.40}$$

The end result of summing experiments a' and b' is a signal which is amplitude modulated:

$$S(t_1, t_2) = \cos \omega_{iso} t_1 e^{i\Omega_2 t_2}. \tag{5.41}$$

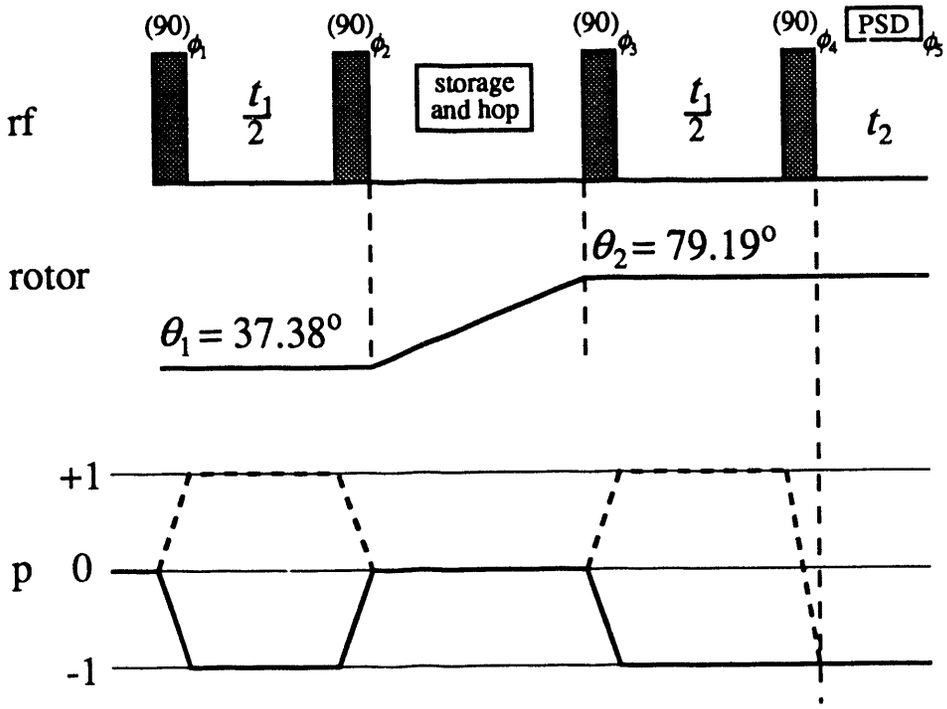

Experiment	ϕ_1	ϕ_2	ϕ_3	ϕ_4	Real ϕ_5	Imag.
a'	$+x$	$+x$	$+x$	$+y$	$+y$	$-x$
b'	$+y$	$+x$	$+x$	$+x$	$-x$	$-y$

Figure 5.5: One possible set of radiofrequency (rf) pulses, rotor positioning, and the related coherence orders for a pure–absorption–phase DAS experiment.

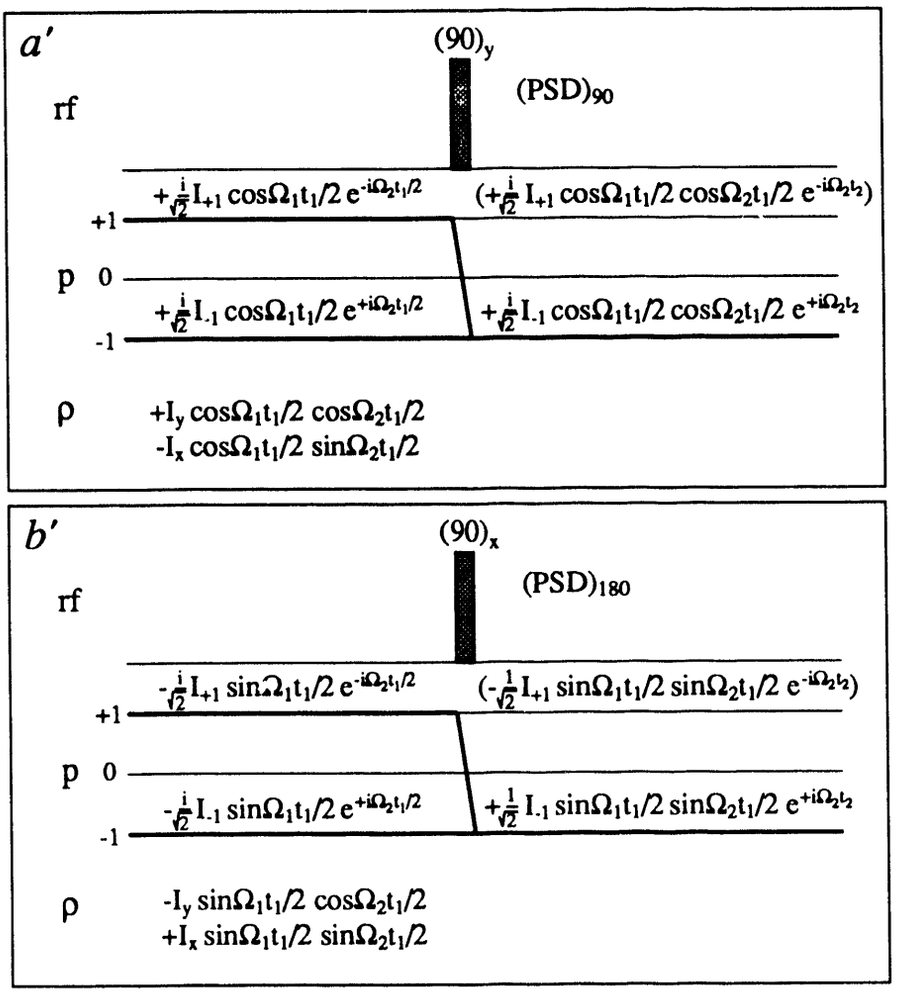

Figure 5.6: Detailed coherence–transfer pathways after the full t_1 evolution in the pure–absorption–phase DAS experiment of Fig. 5.5.

A second experiment must be undertaken to obtain the sine modulated signal. Experimentally, all pulse phases before the t_1 period (here, the first pulse only in each experiment a' and b') is changed by 90° with a similar change in the detection phase.

With this simple extension of the first DAS experiment, two–dimensional correlation with pure–absorption lineshapes is now possible with any allowable DAS angle in the second dimension. These include the angles between 0° and 39.23° or between 63.43° and 90°. The fraction of time t_1 spent at either angle will be different from one–half when using any set of angles other than 37.38° and 79.19°, depending on the relative magnitudes of the relevant Legendre polynomials at the two angles. The narrowing expected in a DAS experiment using the scheme in Fig. 5.5 is illustrated in Fig. 5.7 where simulations of phase–modulated, absolute value, and pure–absorption–phase DAS spectra are compared. The pure–phase spectrum contains a resonance which is noticeably narrower than the magnitude spectrum.

5.4.2 Variation II: Z–Filter

At any spinning angle other than the magic–angle of 54.74°, first–order interactions such as chemical shift anisotropy (CSA) may be large and contribute significantly to spectral broadening in the second frequency dimension of a DAS experiment. One goal of two–dimensional DAS is to extract shielding and quadrupolar parameters associated with distinct nuclear sites by fitting simulated powder patterns to single–site lineshapes extracted from slices through ω_1. Second–order quadrupolar lineshapes may be simulated at any spinning angle θ, neglecting CSA,

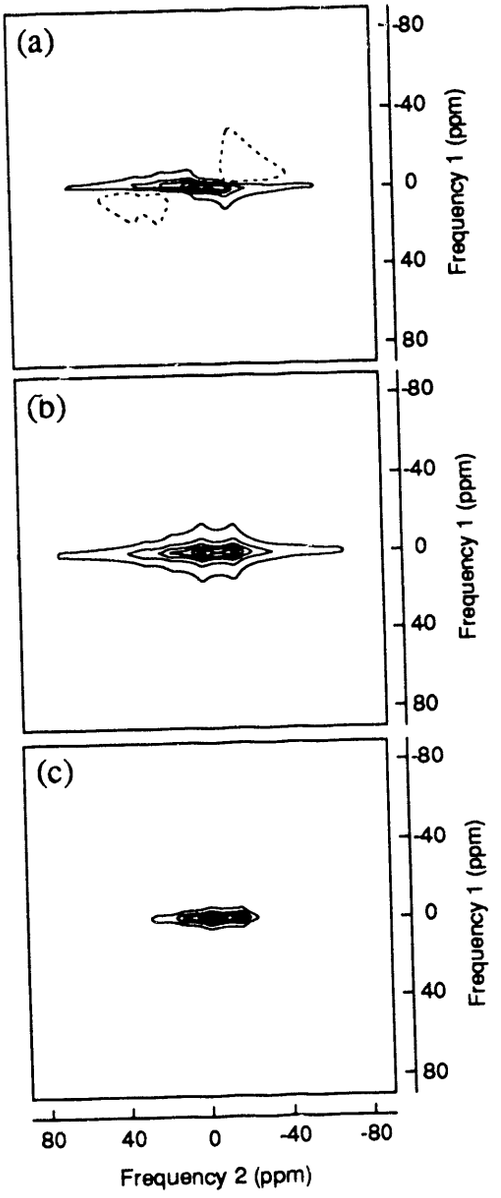

Figure 5.7: Computer simulations of two–dimensional DAS experiments. The system simulated contains isolated spin–$\frac{3}{2}$ nuclei with $C_Q = 2.5$ MHz and $\eta = 0.7$. (a) Phase–modulated detection following the scheme in Fig. 5.1. The dashed lines correspond to negative intensity contours. (b) Magnitude spectrum obtained from the phase–modulated data. (c) Pure–absorption–phase spectrum obtained using the scheme in Fig. 5.5 where the rotor continues to spin at $\theta_2 = 79.19°$.

and compared to experimental lineshapes in order to determine the quadrupolar coupling strength ($C_Q = e^2qQ/h$) and asymmetry parameter (η). However, the addition of three more parameters associated with the principal values of the CSA tensor, as well as the angles describing the relative orientations of the principal axis systems of the quadrupolar and shielding tensors, complicates analysis of the lineshapes. Hence, for optimal determination of the quadrupolar parameters and the isotropic chemical shift, especially in the presence of other anisotropic interactions, detection at the magic-angle (or possibly other non-DAS angles) in t_2 is desirable. Because 54.74° is not a DAS angle, an alternative scheme using a z-filter must be used in order to obtain pure-absorption lineshapes.

A z-filter is equivalent to the storage step of a DAS experiment where the magnetization is kept along the z-axis while the spinning angle is changed. This allows a single transverse magnetization component along either the x- or y-axis to be retained, while eliminating the other transverse component. Effectively, it produces an overall transfer and mixing of coherence from $p = +1 \rightarrow -1$, not by throwing one component away along the z-axis (as with a 90° pulse), but by storing and then reinitiating evolution of the chosen component by using two 90° pulses separated by a time delay. One advantage of a z-filter is that it should not be as sensitive to pulse imperfections as a single 90° pulse, since any magnetization remaining in the transverse plane after the first pulse should decay before the second pulse restores the evolution. In addition, and most importantly, we are able to flip the rotor axis to another orientation during the delay.

Using the scheme of Fig. 5.8, the axis of the rotor may be reoriented a second time, allowing detection to occur at *any* angle θ_3 with respect to the external field.

Figure 5.8 also details the necessary phase cycling and rotor positioning. As in the previous DAS experiments only two accumulations, a'' and b'', are necessary to reconstruct an echo even though more pulses are required to retain the coherence orders properly during t_1. The coherence–transfer pathways during the z–filter are examined in more detail in Fig. 5.9. Either method (States or TPPI) may then be used as above to obtain the correctly modulated signal and an appropriate two–dimensional Fourier transform provides the final result.

One powerful advantage gained by using the z–filter to accomplish pure–phase lineshapes is that the choice of the final angle θ_3 is free for the experimenter to determine. The choice $\theta_3 = 54.74°$ will produce lineshapes in ω_2 that are independent of CSA, which has a larger effect at higher magnetic field strengths and so may be the angle of choice when using DAS at higher fields. Other choices of θ_3 may include $\theta_3 = 0°$, thereby correlating the high resolution spectrum in the first frequency domain with static lineshapes for each distinct site, the static lineshapes being equivalent to lineshapes obtained while spinning along the z–axis. A final angle of 0° may also have been chosen with the 90° pulse version of the pure phase experiment (Fig. 5.5) because $\theta_2 = 0°$ is complementary to $\theta_1 = 63.44°$ with an evolution period five times longer at θ_2. Finally, the choice $\theta_3 = 43.5°$ is also interesting since at this angle the total second–order quadrupolar linewidth is independent of the asymmetry parameter of the electric field gradient [74], so that the width is determined by the quadrupolar coupling strength while only the shape of the line is determined by the asymmetry (η).

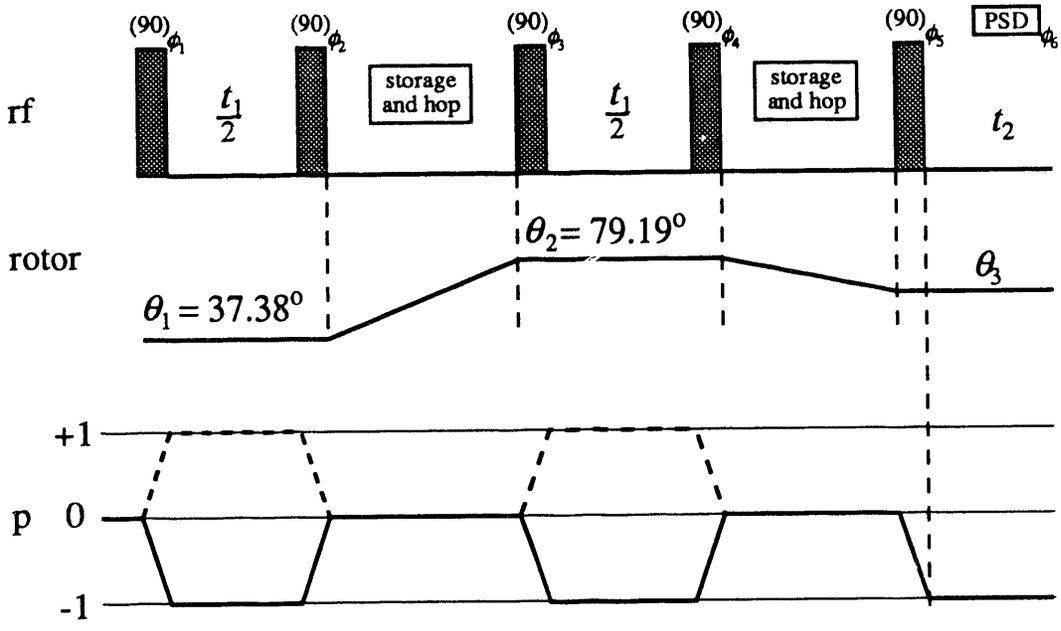

Experiment	ϕ_1	ϕ_2	ϕ_3	ϕ_4	ϕ_5	Real ϕ_6	Imag.
a'	$+x$	$+x$	$+x$	$+x$	$-x$	$+y$	$-x$
b'	$+y$	$+x$	$+x$	$+y$	$-y$	$-x$	$-y$

Figure 5.8: A second, more versatile alternative for a pure–absorption–phase DAS experiment using a z–filter.

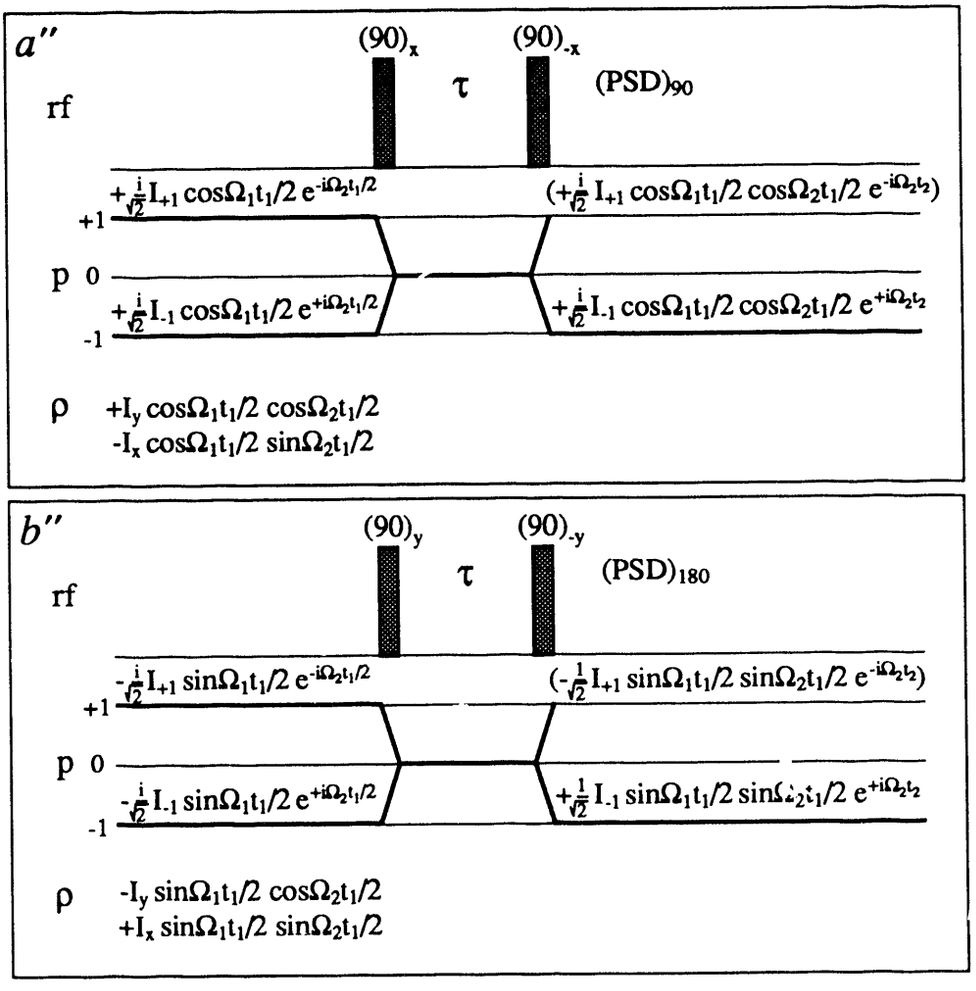

Figure 5.9: Detailed coherence–transfer pathways after the first hop in the pure–absorption–phase DAS experiment of Fig. 5.8 which utilizes a z–filter.

5.5 Experimental Results

The DAS experiments presented here were performed in a magnetic field of 9.4 T, corresponding to a resonance frequency of 105.84 MHz for sodium–23 ($I = \frac{3}{2}$). Phase–modulated experiments were performed as explained in the two previous chapters. Phase–sensitive experiments can be approached with two different data accumulation and processing methods: that of States *et al.* [136] where two separate data collections for each t_1 increment are performed followed by hypercomplex Fourier transformation [36]; or by time proportional phase incrementation (TPPI) [135, 140] where only one data set is used but the phases of the first pulses in both experiments a'' and b'' are incremented by 90° with each t_1. In either case at least two t_2 accumulations for each t_1 point must always be summed to give the reconstructed second–order echo. In the former method this number is therefore doubled as both collections for a distinct t_1 must also be run with a 90° phase shift of the first pulses to acquire the second of the two hypercomplex data sets. To achieve the same resolution and signal–to–noise by TPPI, twice as many t_1 increments must be used, thereby making equivalent the time and computer memory required for the two methods. We have tested both methods and find comparable results.

The experimental improvements are illustrated with a comparison of phase–modulated DAS and the z–filtered pure–phase experiment with an additional axis flip to $\theta_3 = 54.74°$. The latter experiment corresponds to a second dimension of magic–angle spinning correlated with high–resolution DAS. The sample is sodium oxalate ($Na_2C_2O_4$) and the nucleus studied is sodium–23. Pulse lengths for 90° nutation of the magnetization were on the order of 5 μsec for all experiments.

These were verified as selective pulses as explained in Chapter 2.

Figure 5.10 is a plot of the two-dimensional DAS spectrum of sodium oxalate obtained with conventional phase–modulated detection. The main difference between this spectrum and that shown in Fig. 4.9 is the spinning speed. This newer spectrum was obtained with an improved DAS probehead which is capable of obtaining rotational frequencies up to 6 kHz. Projections of the phase modulated spectrum appear in Fig. 5.11, along with the one–dimensional DAS spectrum of the same sample obtained from Fourier transformation of the echo heights as a function of the high–resolution time dimension, t_1. In the pure one–dimensional analysis, however, there is no immediate correlation of the high resolution line with the anisotropic lineshape, especially troublesome if two lines are very near to each other in the high resolution dimension. The projections reveal the extra broadening which accompanies the magnitude calculation, most notably in the wings of the narrowed resonance.

The spectrum in Fig. 5.12 was obtained with the z–filtered pure–absorption experiment of Fig. 5.8. Projections of this spectrum appear in Fig. 5.13. The high resolution DAS projection has a width of 600 Hz which is the same width as the one–dimensional DAS spectrum obtained from digitizing only the echo tops. The second–dimension is a MAS lineshape: computer simulations with the quadrupolar parameters $e^2qQ/h = 2.5$ MHz and $\eta = 0.7$ closely match both the MAS spectrum and the equivalent DAS projection as shown in Fig. 5.14. The DAS spectrum shows one isotropic peak at −15.0 ppm with respect to sodium–23 in aqueous NaCl, and thus the chemical shift may be calculated as 1.2 ppm or 127 Hz at 9.4 T.

In conclusion, the pure–phase results clearly show a narrower isotropic resonance

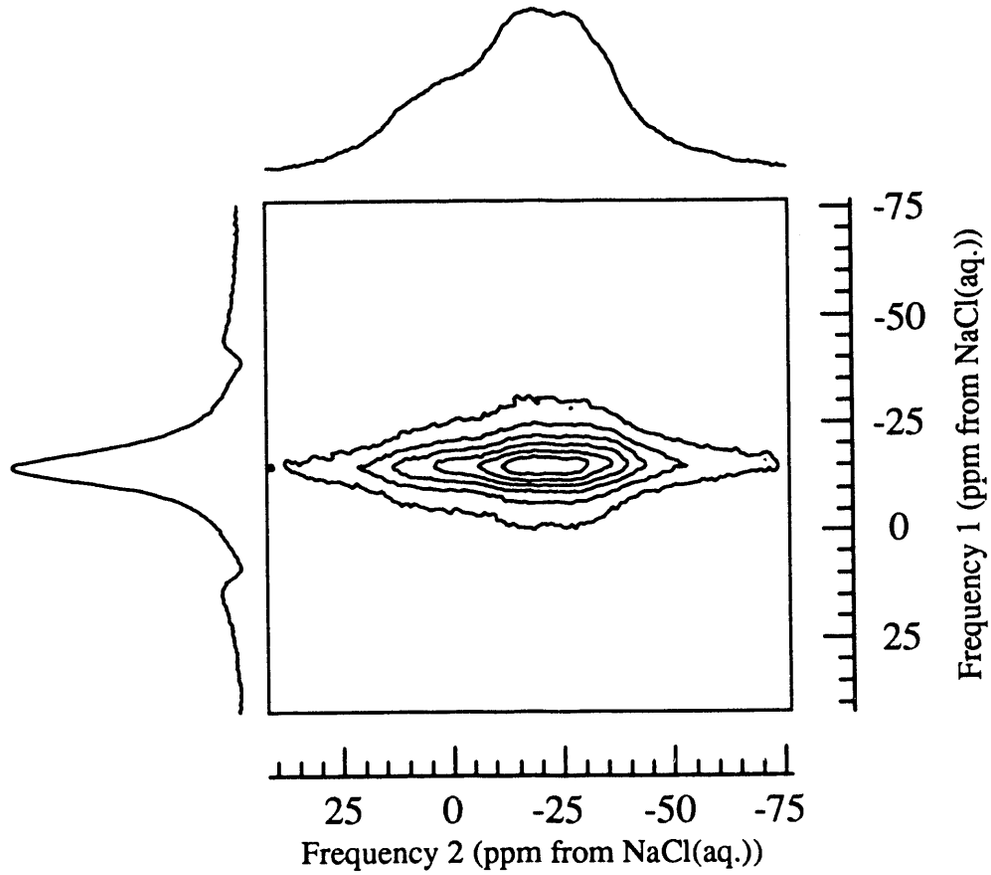

Figure 5.10: Phase–modulated DAS spectrum from sodium–23 in sodium oxalate ($Na_2C_2O_4$). The spectrum is displayed in magnitude mode as explained in the text.

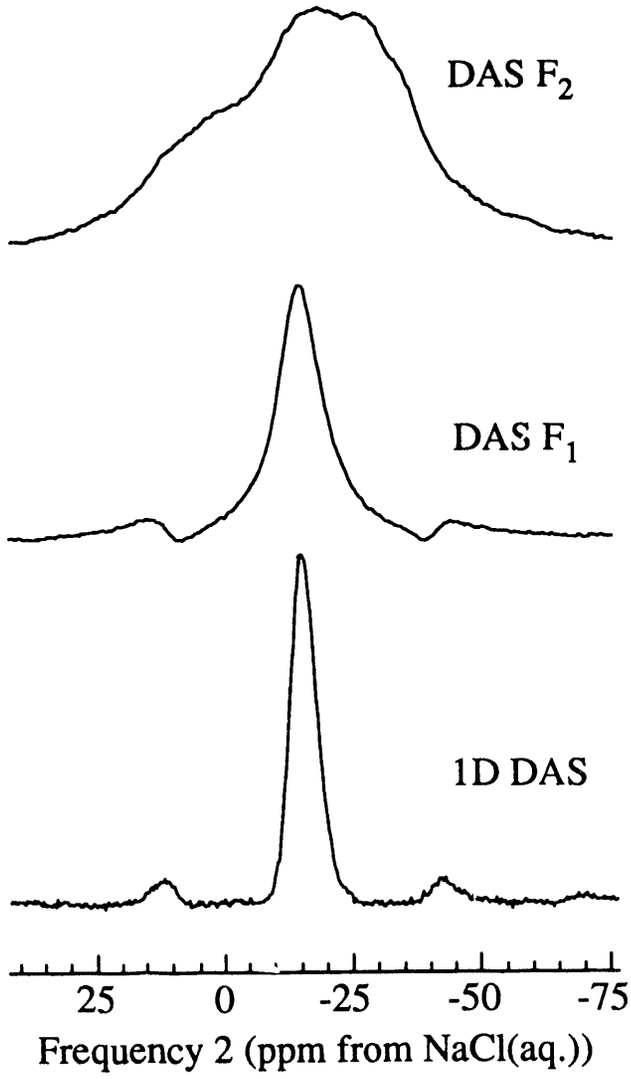

Figure 5.11: Projections along the two axes in the magnitude mode phase–modulated spectrum of Fig. 5.10. At the bottom is the one–dimensional DAS spectrum obtained from the echo maxima where no magnitude calculation is necessary and a narrowed resonance is obtained.

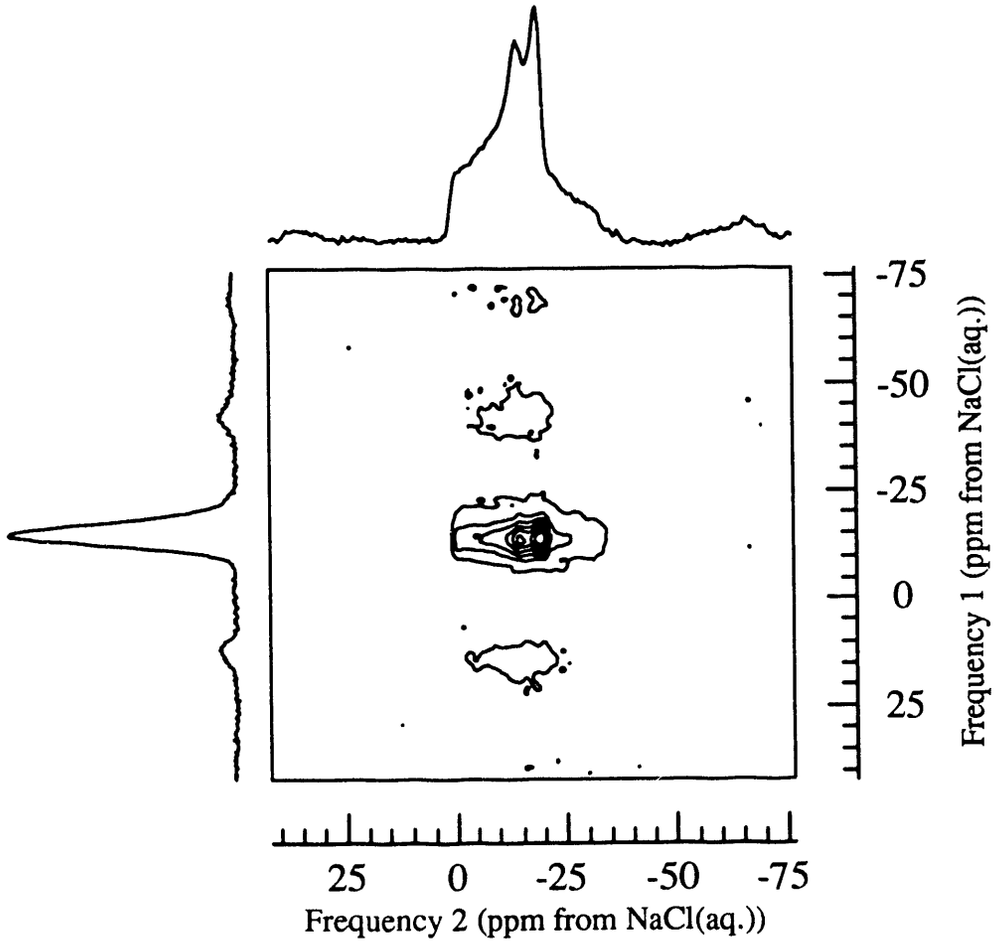

Figure 5.12: Pure–absorption–phase DAS spectrum from sodium–23 in sodium oxalate ($Na_2C_2O_4$), acquired with a z–filter and a final axis flip to 54.74°.

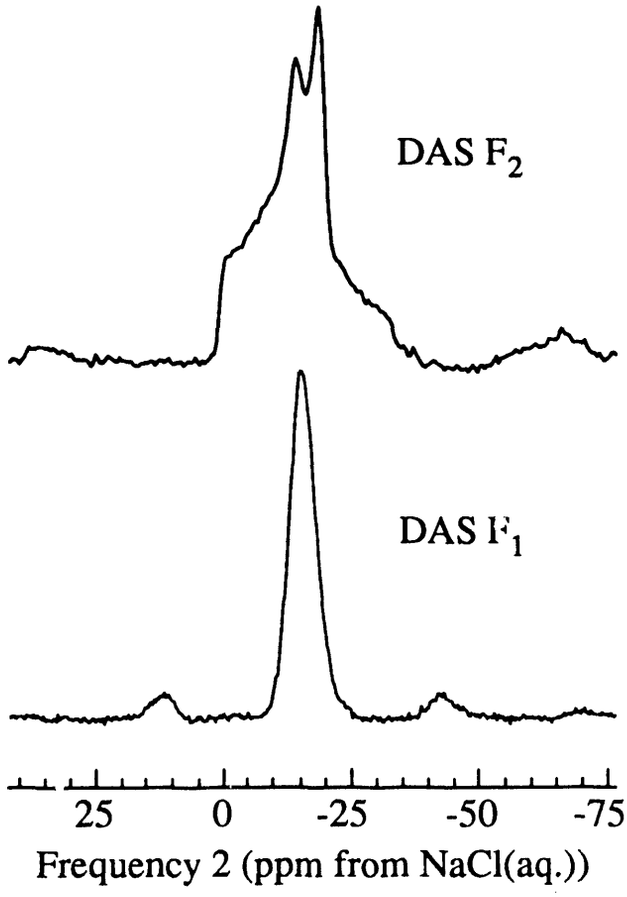

Figure 5.13: Projections along the two axes in the pure–absorption–phase DAS spectrum of Fig. 5.12. The top spectrum is equivalent to the one–dimensional MAS spectrum.

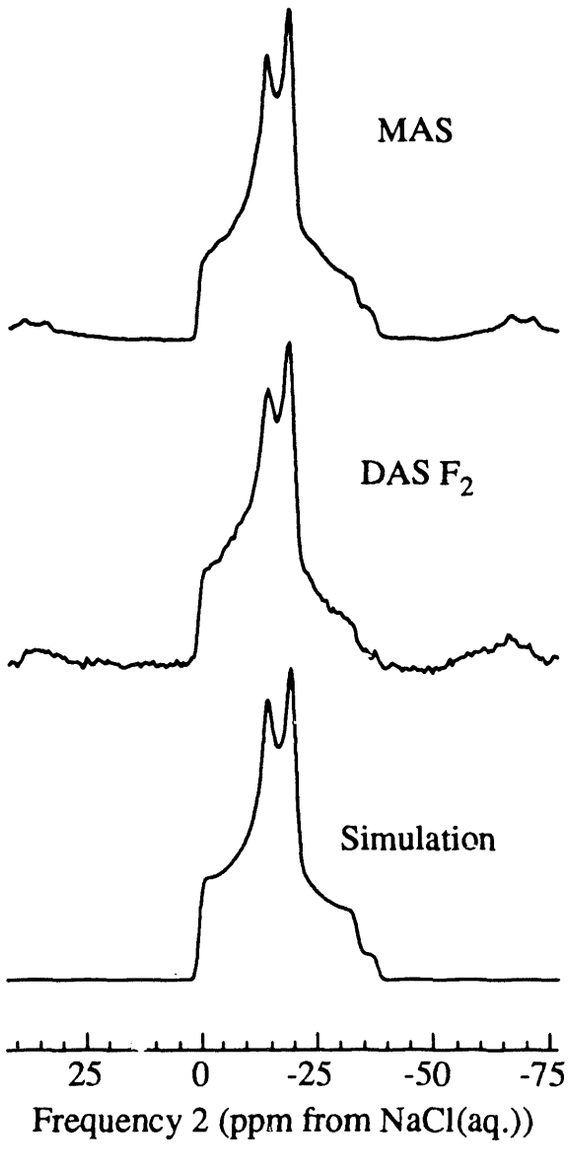

Figure 5.14: The MAS and pure-phase ω_2 projection closely match a simulated MAS spectrum with the parameters $\sigma_{iso}^{(CS)} = 1$ ppm, $e^2qQ/h = 2.5$ Mhz, and $\eta = 0.7$.

in the two–dimensional spectrum as well as the ability to obtain sharper spectral features in the second (anisotropic) dimension. Simple calculation of the isotropic chemical shift, the quadrupolar coupling constant, and the quadrupolar asymmetry parameter are also possible from the MAS lineshape obtained in the second DAS dimension. This will be especially critical when resonances overlap in the MAS spectra but may be separated in the first frequency dimension by their isotropic shifts in a DAS experiment.

Chapter 6

High–Resolution Oxygen–17 NMR of Silicates

Several oxygen–17 enriched silicates were studied using dynamic–angle spinning (DAS) and double rotation (DOR) nuclear magnetic resonance spectroscopy. In the spectra of a variety of silicate minerals, a narrow line is observed for each distinct oxygen site at the sum of the isotropic chemical shift and the field–dependent isotropic second–order quadrupolar shift. Resolution is increased by up to two orders of magnitude compared to conventional magic–angle spinning (MAS) spectra so that crystallographically inequivalent oxygens are now observable as distinct resonances in the spectra. The polycrystalline silicates investigated were diopside ($CaMgSi_2O_6$), wollastonite ($CaSiO_3$), clinoenstatite ($MgSiO_3$), larnite (Ca_2SiO_4), and forsterite (Mg_2SiO_4). Further, DAS experiments at two magnetic field strengths were performed to extract quadrupolar and chemical shift information. These parameters provide insight into the nature of the electronic environment surrounding the oxygen nuclei including the bond order and the oxygen coordination by neigh-

boring cations.

6.1 Introduction

Solid silicates display an array of structures and phases according to their composition and thermal treatment. As the molar percentage of cations increases, for example, the infinite three–dimensional framework of crystalline silica (SiO_2) gives way to more compact chains of Si–O atoms (pyroxenes and amphiboles) and discrete anionic species (orthosilicates and cyclosilicates). Such variations in microstructure can have significant impact on the macroscopic properties of silicate species [125]. Adsorption and reaction processes of porous aluminosilicates, such as zeolites, are tied closely to their local structure, influencing their use as catalysts, selective adsorbents, and ion–exchange media in a variety of important industrial processes [141]. Furthermore, the abundance of silicon and oxygen in the Earth's crust [142] makes physicochemical studies of solid silicates important for understanding many natural geochemical processes.

The microstructure of silicates can be probed by examining the electromagnetic environment of their nuclei using NMR spectroscopy. Nearby electrons influence the local magnetic field at the nucleus by both paramagnetic and diamagnetic mechanisms, so that measurement of the shielding (chemical shift) tensor at a specific site is a sensitive probe of the local bonding [68]. A nucleus with a non–spherical charge distribution couples additionally to local electric field gradients through the electric quadrupole interaction [1, 9, 143, 144]. Determination of the strength of the quadrupolar coupling and the deviation of the electric field gradient from axial symmetry provides additional structural insight, because the interaction is also

dependent upon bonding and symmetry of the local atomic environment.

High–field NMR has been used to study silicates, focussing primarily on the silicon–29 nucleus [145, 146, 147] which, like carbon–13, is a low abundance spin–$\frac{1}{2}$ isotope. Line broadening in silicon spectra is caused predominantly by anisotropy of the chemical shift and may be removed using magic–angle spinning (MAS) NMR [63, 64, 148]. High resolution results can be obtained in this way [149], often yielding quantitative structural information from experimental spectra. High resolution oxygen–17 NMR studies of silicates, however, are much more difficult as a result of quadrupolar couplings of the oxygen–17 nuclei. In a polycrystalline or amorphous sample NMR resonances are broadened by the spatial anisotropy of the second–order interaction, which cannot be fully averaged by MAS methods [12, 150]. Individual spectral lines from distinct oxygen–17 nuclear sites typically overlap, and the separation and identification of different oxygens is difficult.

The developments described in this thesis allow an increase in NMR spectral resolution by up to two orders of magnitude for quadrupolar nuclei and DAS and DOR have therefore been applied to a number of silicate minerals. The resolution of oxygen sites in these samples bodes well for the study of other oxygen–containing materials such as biologically important systems (amino acids and proteins), polymers, and ceramic superconductors.

In both DAS and DOR, the isotropic frequency shift measured (δ_{iso}^{obs}) is the sum of an isotropic chemical shift and a field–dependent isotropic second–order shift. The theoretical analysis of Chapter 2 provides the useful equations, rewritten here in terms of isotropic *shifts* rather than frequencies.

$$\delta_{iso}^{obs} = \delta_{iso}^{(CS)} + \delta_{iso}^{(2Q)} \tag{6.1}$$

where $\delta_{iso}^{(CS)}$ is the isotropic chemical shift and $\delta_{iso}^{(2Q)}$ is the isotropic second order quadrupolar shift for a nucleus with spin I:

$$\delta_{iso}^{(2)} = -\frac{3}{40}\left(\frac{C_Q^2}{\nu_0^2}\right)\frac{\left(I(I+1)-\frac{3}{4}\right)}{I^2(2I-1)^2}\left(1+\frac{1}{3}\eta^2\right)\times 10^6 \tag{6.2}$$

where

$$C_Q = \frac{e^2qQ}{h} \tag{6.3}$$

and

$$\nu_0 = \frac{\omega_0}{2\pi}, \tag{6.4}$$

the Larmor frequency in Hz. It is useful to separate these two contributions in order to determine the values of $\delta_{iso}^{(CS)}$, C_Q, and η. Since the quadrupolar shift is proportional to the inverse of the square of the magnetic field strength, while the isotropic chemical shift is frequency independent, performing an experiment at two or more field strengths determines the isotropic chemical shift and a product of the quadrupolar parameters (C_Q and η) for each site. Alternatively, the quadrupolar parameters may be determined from the second dimension in a DAS experiment by simulations of resolved powder patterns at isotropic positions in the first dimension. The pure–absorption–phase DAS experiment described in Chapter 5 could prove especially useful for spectral simulation purposes when a final hop to the magic–angle is used. In such a situation the powder pattern is no longer influenced by the first–order chemical shift anisotropy and the number of parameters in the simulation decreases by six.

6.2 Experimental

6.2.1 Sample Preparation

All silicate compounds were synthesized from oxygen–17 enriched SiO_2, CaO, and MgO precursor compounds prepared from reaction of $H_2^{17}O$ with the proper inorganic starting materials [151]. $Si^{17}O_2$ was produced by reacting liquid $H_2^{17}O$ with $SiCl_4$ vapor at ambient temperature and pressure, followed by dehydration of the product at 1473 K. $Ca(^{17}OH)_2$ was synthesized by direct oxidation of calcium metal with $H_2^{17}O$ under ambient conditions in an argon glove box, with $Ca^{17}O$ produced by drying the hydroxide at 853 K. Reacting saturated solutions of $K^{17}OH$ and $MgCl_2$ at 298 K precipitated $Mg(^{17}OH)_2$, which yielded $Mg^{17}O$ upon decomposition at 653 K.

The simple oxide products were mixed together in proper stoichiometric amounts, heated to elevated temperatures in sealed platinum tubes or in a nitrogen atmosphere, and cooled to ambient conditions to produce homogeneous crystalline phases of diopside ($CaMgSi_2{}^{17}O_6$), forsterite ($Mg_2Si^{17}O_4$), larnite ($Ca_2Si^{17}O_4$), clinoenstatite ($MgSi^{17}O_3$), and wollastonite ($CaSi^{17}O_3$). Enrichments of oxygen–17 were 20% in the diopside, 41% in the wollastonite and clinoenstatite, and 43% in the larnite and forsterite. Phase identity was checked by powder x–ray diffraction and silicon–29 NMR. The forsterite sample was slightly off stoichiometry and contained approximately 25% clinoenstatite.

6.2.2 NMR Experiments

Experiments were performed in magnetic fields of 9.4 T and 11.8 T, corresponding to oxygen–17 resonance frequencies of 54.25 MHz and 67.81 MHz respectively. The probeheads for the sample reorientation were machined from commercially available Delrin and Vespel polymers. The DOR probehead has been described in detail elsewhere [124] and was mentioned briefly in Chapter 4. The DAS probehead is a new version, improved from that used in previous experiments [105], and it is described in Chapter 7. It is the same probehead used for the pure–absorption–phase experiments in Chapter 5.

The DAS experiments were performed with axis flips from $\theta_1 = 37.38°$ to $\theta_2 = 79.19°$ and appropriate phase cycling of the radiofrequency pulses. For these angles, the evolution times at the two angles must be equal ($k = 1$) in order to cancel the anisotropic frequency contributions. Eight experiments are necessary to reconstruct a full second–order quadrupolar echo (with a minimization of experimental artifacts) which is digitized starting from the point of refocussing. The second time dimension (t_2) contains the digitized data after refocussing of first and second–order anisotropic interactions, and its Fourier transform provides the spectrum of the sample while spinning at θ_2. The first time dimension (t_1) is the sum of the two evolution times leading to the anisotropic refocussing. This first dimension is incremented by a time Δt_1 (typically tens of microseconds) and the anisotropic decay during t_2 is recorded for each t_1 delay. The spectral width in the second frequency dimension is the inverse of the sampling period between data points in the second time dimension, while the spectral width in the first frequency dimension is $1/\Delta t_1$.

One–dimensional DAS spectra are obtained by a Fourier transformation of the echo heights as a function of the first time dimension. This yields resolved lines with quantitative peak intensities after assignment and integration of all spinning sidebands. The two–dimensional DAS spectra are presented in absolute–value mode to avoid phase–twisted lineshapes [126]. Projections along the first frequency axis also provide high resolution results, although some additional line broadening occurs owing to the absolute value calculation. Pure–absorption–mode DAS experiments are also possible, reducing linewidths in the two–dimensional spectra and allowing correlation with magic–angle spinning powder patterns in the second dimension. Preliminary oxygen–17 pure–phase spectra suffered from poor signal–to–noise ratios and have therefore not been included here.

A DOR spectrum, while technically more demanding to obtain, is acquired in a one–pulse NMR experiment, which provides high resolution spectra with fewer total signal acquisitions than in the DAS experiment. Fourier transformation of a one–dimensional FID provides the high resolution spectrum immediately. Comparison of spectra obtained at a variety of spinning speeds can help in the assignment of sidebands arising from the larger (outer) rotor. DAS spectra also contain sidebands (at integer multiples of one–half of the rotor frequency), but since the spinning speeds used here are on the order of many kHz this rarely hinders analysis of the data. Used together, these two techniques provide unambiguous peak assignments for all of the samples studied here.

6.3 Results

The MAS spectra of oxygen–17 in the minerals studied are shown in Fig. 6.1: powder patterns from distinct oxygen sites overlap at this field strength of 9.4 T. Diopside, forsterite, and clinoenstatite have been investigated previously [77, 78] with analyses assuming the presence of three inequivalent oxygen sites. Spectra were simulated in these previous investigations by fitting the experimental NMR lineshapes to computer generated powder patterns, and the isotropic chemical shifts and quadrupolar parameters obtained are compiled in Table 6.1. A difference in the magnitude of the quadrupolar coupling constant, C_Q, for bridging versus non-bridging oxygen sites is observed, and this is attributed to the difference in ionicity of cation–oxygen bonds in the two arrangements. The more ionic bonds associated with the terminal oxygens result in less p–orbital contribution to the electric field gradient [78] and thus a lower quadrupolar coupling frequency. Equations 6.1 and 6.2 allow calculation of the total isotropic shifts expected at both 9.4 T and 11.8 T and these are included in Table 6.1.

6.3.1 One–Dimensional DAS and DOR Experiments

DAS and DOR spectra of the same silicate minerals are shown in Fig. 6.2. Isotropic shifts are distinguished from spinning sidebands by performing experiments at two or more spinning speeds, and by comparison of the DAS and DOR spectra. Due to the presence of many peaks in some of the spectra, labelling of the isotropic peaks and sidebands would add confusion to the presentation of the results, so the isotropic values are compiled in Table 6.2.

The DAS and DOR results for diopside ($CaMgSi_2{}^{17}O_6$) and forsterite ($Mg_2Si^{17}O_4$)

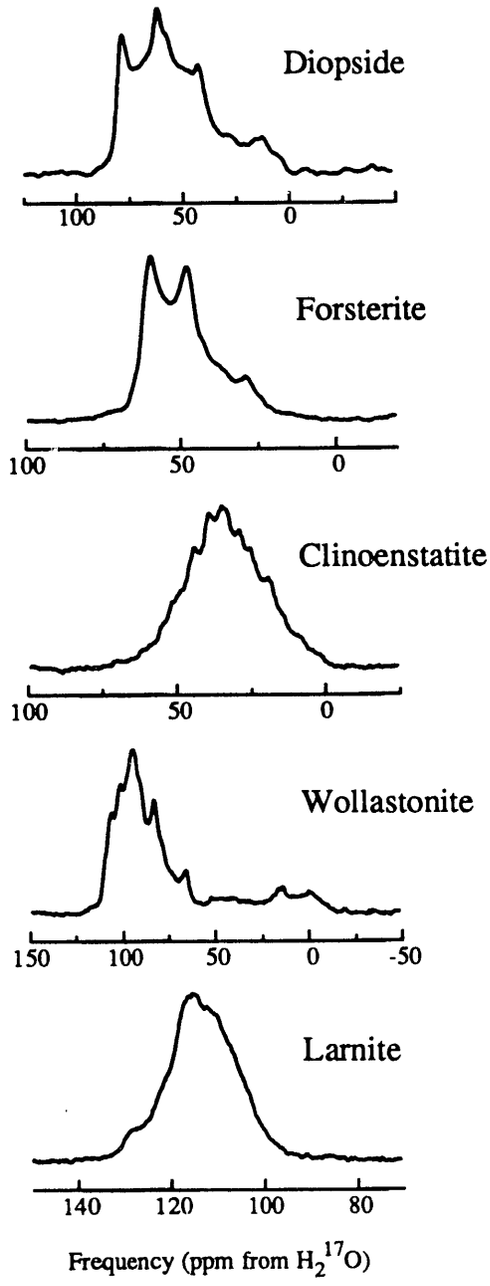

Figure 6.1: Magic–angle spinning spectra of oxygen–17 in a collection of silicates at a magnetic field strength of 9.4 T. The rotor frequency is approximately 5.4 kHz and the frequency axes are referenced to oxygen–17 in $H_2^{17}O$.

compound	ref.	site	occ.	$\delta_{iso}^{(CS)}$(ppm)	C_Q (MHz)	η	$\delta_{iso}^{9.4T}$(ppm)	$\delta_{iso}^{11.8T}$(ppm)
diopside	[78]	*nb*	1	84	2.7	0.0	69	74
$CaMgSi_2O_6$		*nb*	1	63	2.7	0.1	48	53
		br	1	69	4.4	0.3	28	43
forsterite	[77]	*a*	2	61	2.35	0.2	50	54
Mg_2SiO_4		*b*	1	62	2.35	1.0	47	52
		c	1	47	2.7	0.3	32	37
clinoenstatite	[78]	*nb*	1	60	3.2	0.0	39	47
$MgSiO_3$		*nb*	1	42	3.2	0.0	21	29
		br	1	62	5.1	0.3	7	27

Table 6.1: Previously determined oxygen-17 chemical shift ($\delta_{iso}^{(CS)}$) and quadrupolar parameters (C_Q and η) for three silicates, based on three-site models. The designations *nb* and *br* signify nonbridging and bridging oxygen sites, respectively. For forsterite, all three sites are nonbridging. The total isotropic shifts one should observe (δ_{iso}^{obs}) at 9.4 T and 11.8 T are also calculated (see Eqs. 6.1 and 6.2).

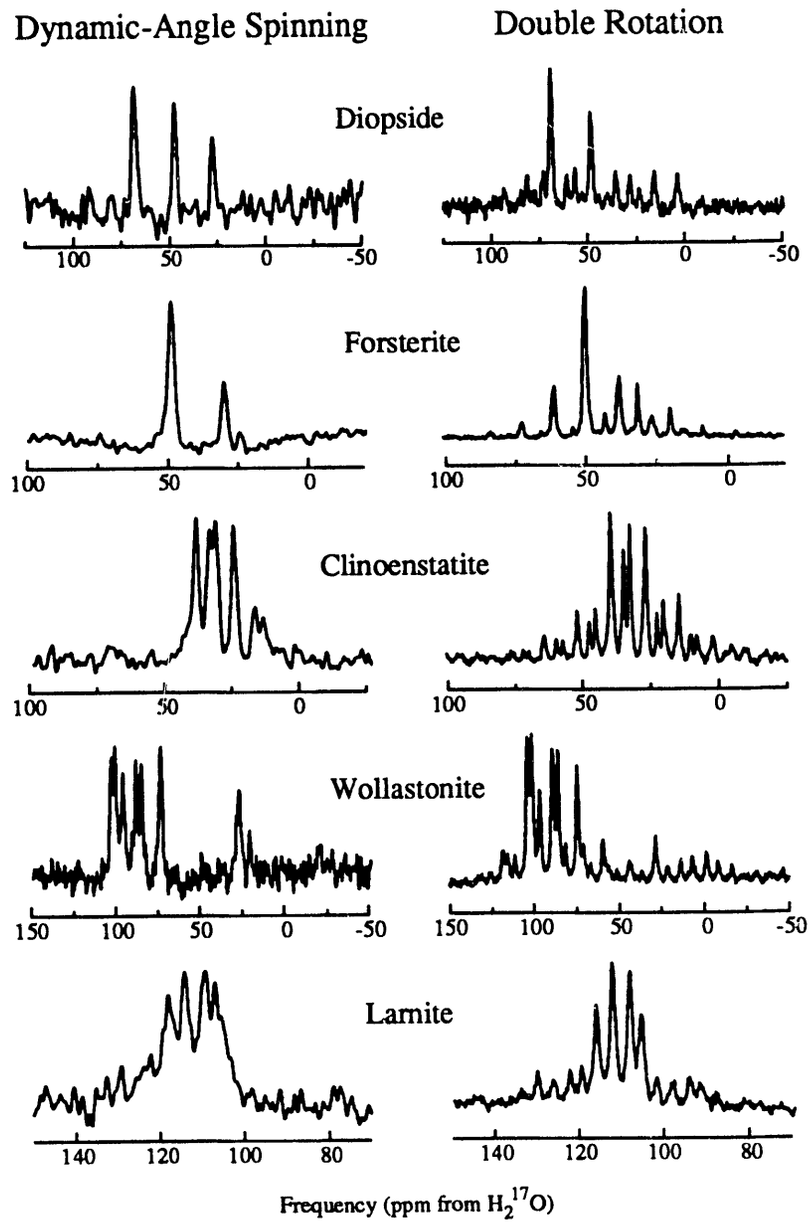

Figure 6.2: Dynamic–angle spinning and double rotation spectra of oxygen–17 in a variety of silicates at a magnetic field strength of 9.4 T. The rotor frequency is approximately 5.4 kHz in the DAS experiments, while in the double rotation experiments the inner rotor spins at approximately 5 kHz and the outer rotates at about 800 Hz.

compound	$\delta_{iso}^{9.4T}$(ppm)	compound	$\delta_{iso}^{9.4T}$(ppm)
diopside	69.2	wollastonite	103.4
$CaMgSi_2O_6$	48.5	$CaSiO_3$	100.1
	28.6		96.5
forsterite	49.0		89.0
Mg_2SiO_4	49.0		85.8
	30.8		74.3
clinoenstatite	39.3		28.2
$MgSiO_3$	34.5		28.2
	32.3		21.6
	26.3	larnite	117.3
	18.0	Ca_2SiO_4	113.3
	15.0		108.8
			106.3

Table 6.2: Experimentally determined oxygen-17 isotropic shifts. All reported values are ppm from the oxygen-17 resonance in $H_2^{17}O$. Errors in all measurements are approximately ± 0.5 ppm.

agree with models having three distinct oxygen sites. This is consistent with their reported crystal structures [152, 153] shown in Figs. 6.3(a) and 6.3(b). The quadrupolar parameters and isotropic chemical shifts, determined from previous MAS experiments [77, 78], predict isotropic shifts in excellent quantitative agreement with the new experimental values. The three resonances are fully resolved in the diopside spectra, with their integrated intensities reflecting a 1:1:1 oxygen site occupancy. Analysis of the forsterite data is less straightforward due to partial overlap of the narrowed peaks from two oxygen–17 sites. Expansion of the region around the most intense peak in the DOR spectrum (Fig. 6.4) reveals a shoulder on the resonance from a third oxygen site. Comparison with the MAS spectra at 11.8 T (ref. [77]) strengthens the conclusion that three main sites are present. Moreover, the enhanced resolution of the new techniques permits impurity phases to be detected, as evidenced by the small peak at 26 ppm in both DAS and DOR spectra. We attribute this to an impurity in the polycrystalline forsterite, also detected by x–ray diffraction and silicon–29 NMR [154]. Its identification as clinoenstatite is also consistent with the position of the peak in the oxygen–17 spectra.

The DAS and DOR spectra of clinoenstatite ($MgSi^{17}O_3$) are consistent with a crystal structure having six inequivalent oxygens in the unit cell [155], four which are terminal sites and two which bridge adjacent silicate tetrahedra (see Fig. 6.3(c)). The sidebands in the DOR spectrum, arising from the motion of the larger rotor, make identification of the upfield resonances difficult; the higher spinning speeds in the DAS experiment permit an unambiguous assignment. Previous interpretations [78], based solely on static spectra, allowed for only three inequivalent oxygens. The small spread in the total isotropic shifts, and similar quadrupolar parameters,

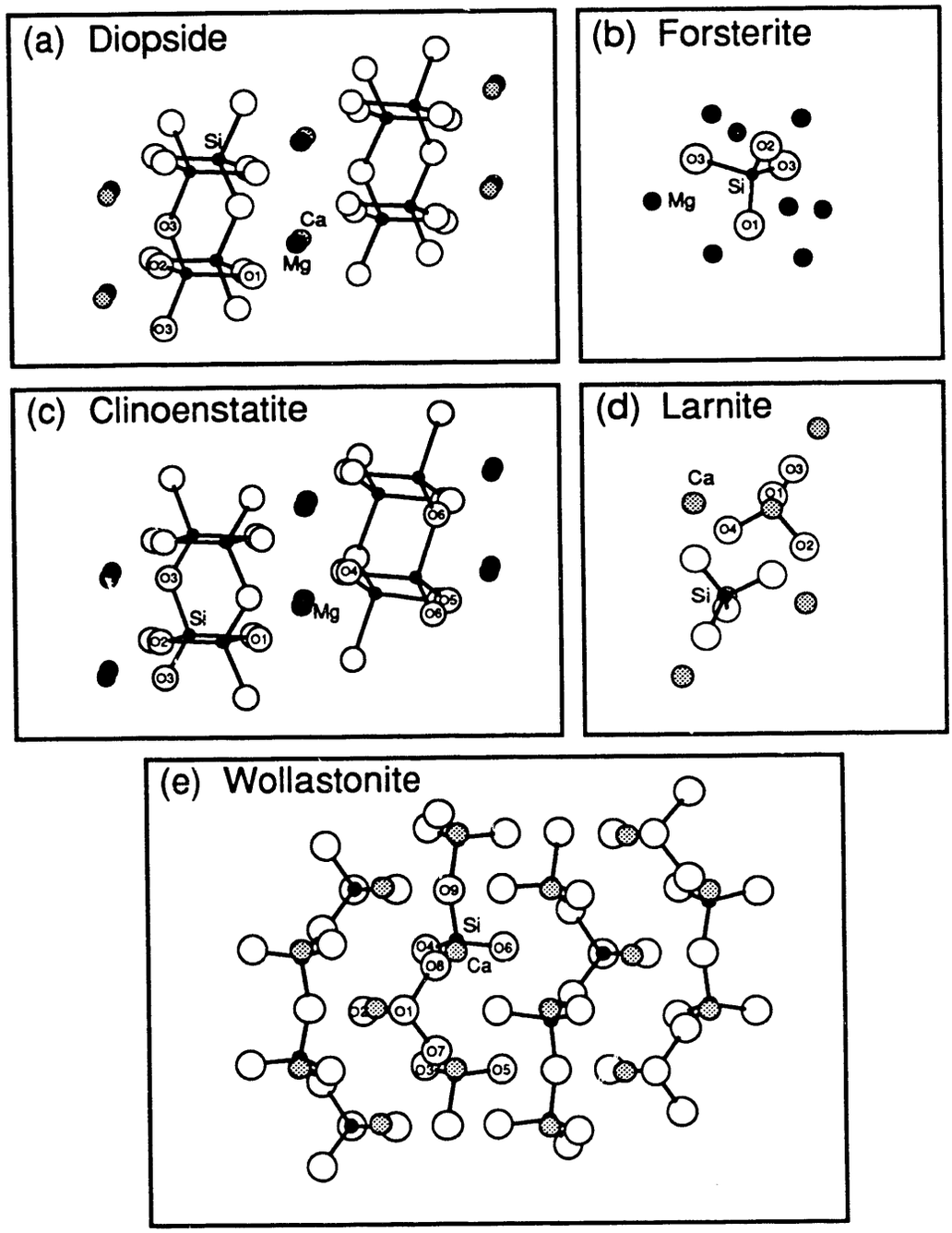

Figure 6.3: Crystal structures of the silicate minerals studied.

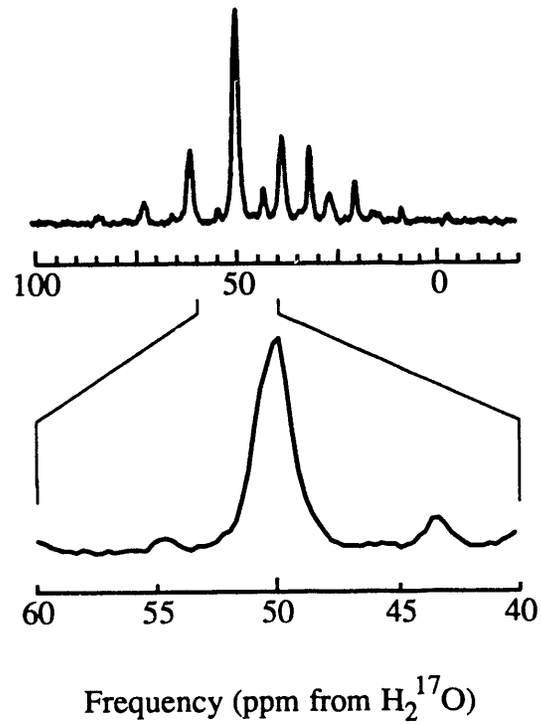

Figure 6.4: Expansion of the DOR spectrum of forsterite around 50 ppm. The shoulder on the left hand side of the largest peak indicates the presence of the third resonance.

cause similar sites to be indistinguishable in lower resolution techniques, and this can also cause errors in the assignment of simulations to the spectra used to extract chemical shift and quadrupolar parameters. We assign the two less intense resonances at 18 and 15 ppm to bridging oxygen species O3 and O6 in Fig. 6.3(c), as the spread of the signal into more sidebands and less isotropic peak intensity is a signature of a larger quadrupolar coupling constant.

For more complicated silicate species, such as the wollastonite ($CaSi^{17}O_3$), structural characterization using MAS alone is essentially impossible. The polytype parawollastonite, shown in Fig. 6.3(e), contains nine distinct oxygen sites [156]. One–dimensional DAS and DOR results show eight assignable oxygen–17 resonances for this particular silicate. As explained below, two–dimensional data analysis helps to locate the ninth spectral line which overlaps with another resonance at 28.2 ppm, as well as allowing preliminary assignment of the upfield resonances to the three bridging oxygens (O7, O8, and O9 in Fig. 6.3(e)).

Finally, the larnite (β–$Ca_2Si^{17}O_4$) structure in Fig. 6.3(d) contains four distinct oxygen nuclei surrounding a central silicon atom with slightly different cation coordinations at each site [157]. The MAS spectrum is much narrower for larnite than for the other minerals, and the isotropic shifts for the distinct oxygens are much closer together. Four resonances are seen in the high resolution DAS and DOR spectra of larnite in Fig. 6.2. Additional broadening of the DAS lines compared to the DOR resonances is noticeable in all of the spectra presented, but it is most evident in the narrow spread of oxygen–17 resonance frequencies from larnite. Relaxation to other magnetic sublevels ($m \neq \pm\frac{1}{2}$) during the rather long flipping time between the two DAS angles can lead to additional broadening in the DAS

spectrum compared to the continuous DOR experiment. It is also possible that spin evolution under residual dipolar interactions present at angles other than the magic–angle during both periods in the high–resolution (t_1) time domain is not refocussed and this may contribute to additional broadening.

6.3.2 Two–Dimensional DAS Experiments

The DAS experiments involve two time dimensions in a natural way, and two–dimensional Fourier transformation of the data can correlate the isotropic peaks along the high resolution frequency axis with the spectra obtained while spinning at the second angle ($\theta_2 = 79.19°$). Results for diopside, wollastonite, and clinoenstatite are presented in Figs. 6.5–6.7. Patterns which overlap in conventional one–dimensional spectra are now separated in a two–dimensional display. With diopside, for example, slices integrated over the lineshape at the isotropic frequencies in the first dimension projected onto the second frequency axis are shown in Fig. 6.8. Simulations of lineshapes with the quadrupolar parameters and isotropic shifts from Table 6.1 match these patterns closely. It must be stressed that these spectra represent absolute value lineshapes obtained while spinning the sample at an angle of 79.19°. The chemical shift anisotropy and dipolar interactions present under these conditions lead to additional line broadening which has been taken into consideration here only through additional exponential broadening of the signals calculated for each particular site.

Similar examination of the wollastonite two–dimensional DAS spectrum reveals the power of using the second dimension to make spectral assignments. The resonance at 28.2 ppm in the first frequency dimension appears to arise from two

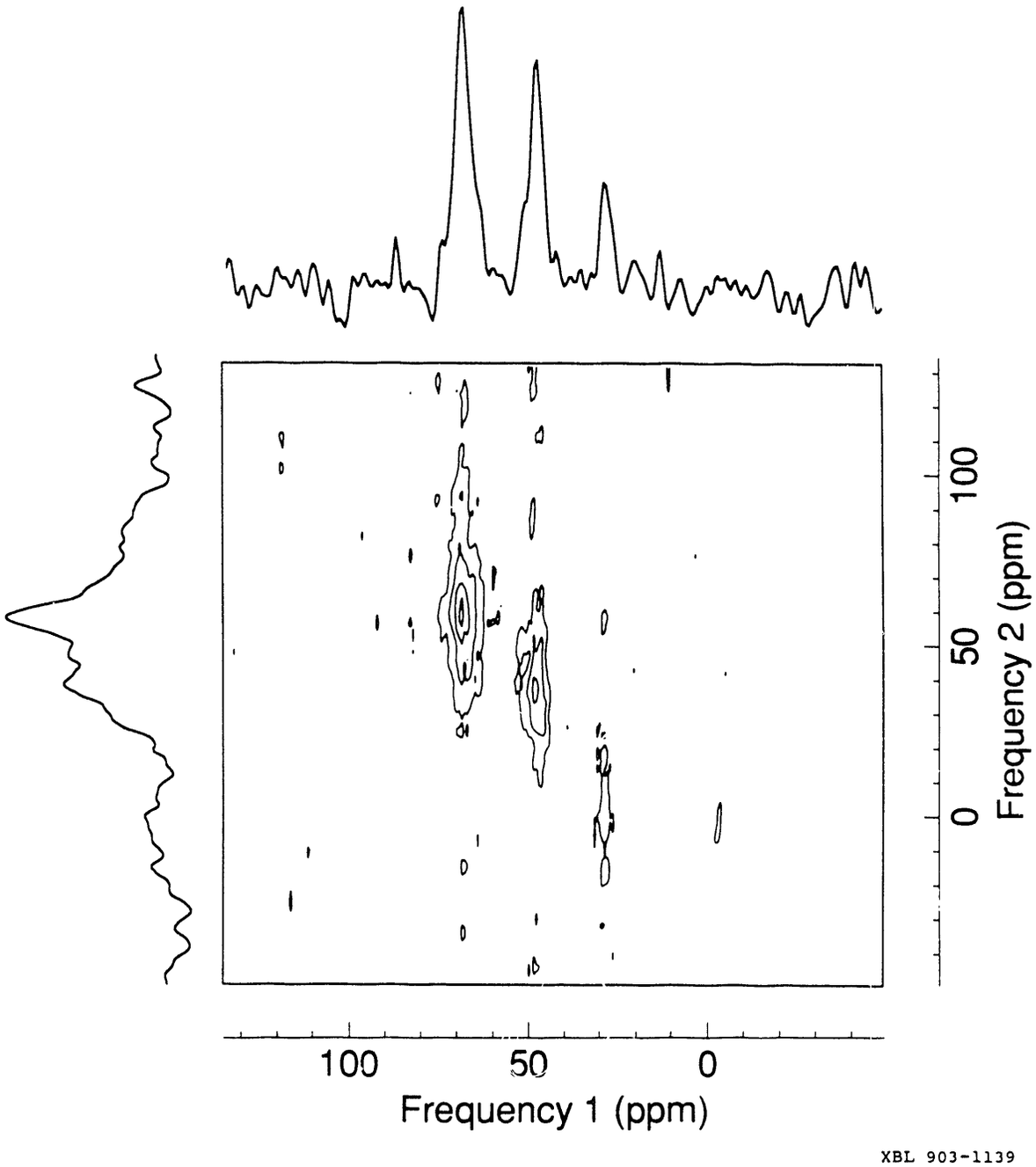

Figure 6.5: Two–dimensional DAS spectrum of diopside.

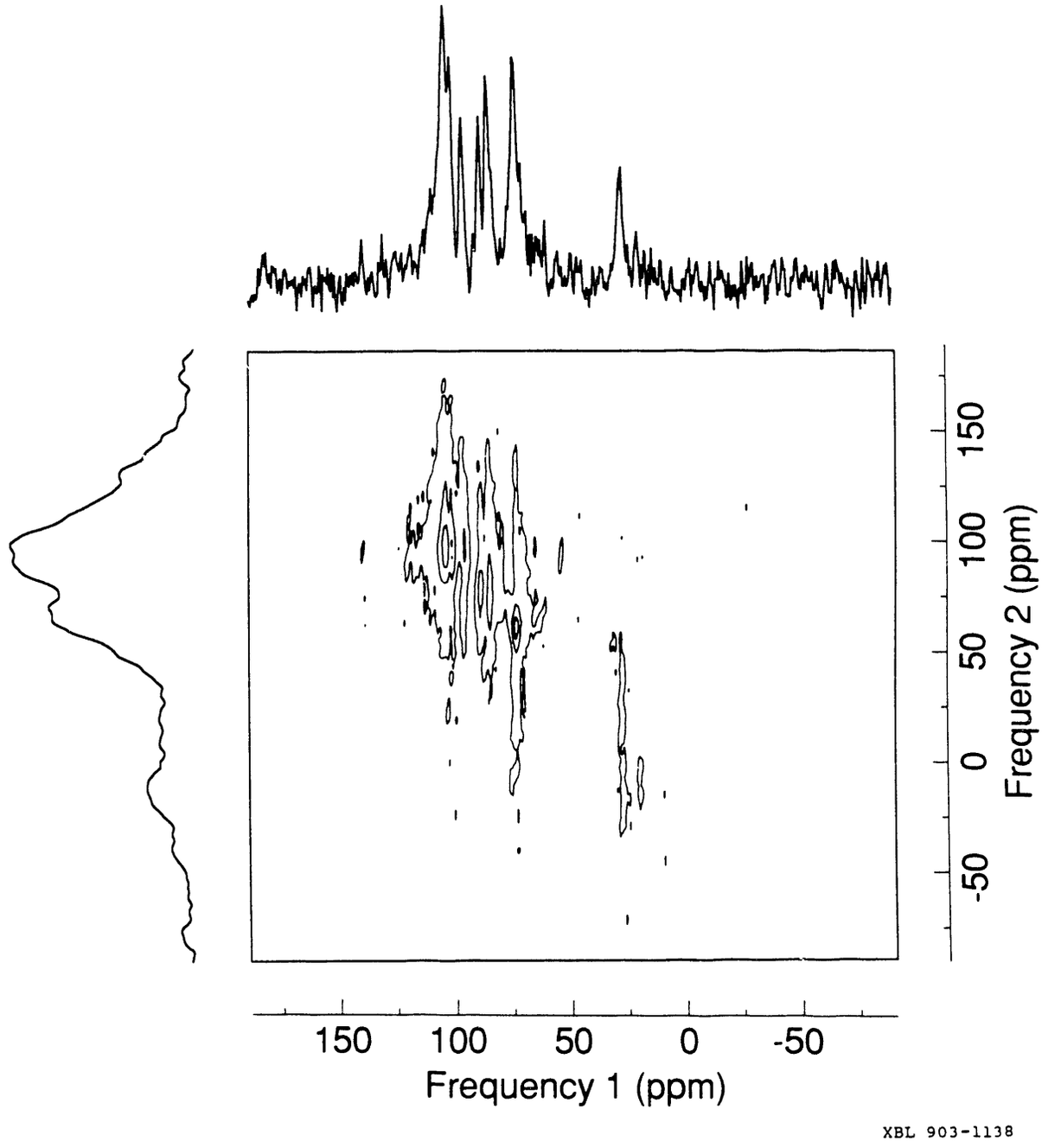

Figure 6.6: Two–dimensional DAS spectrum of wollastonite.

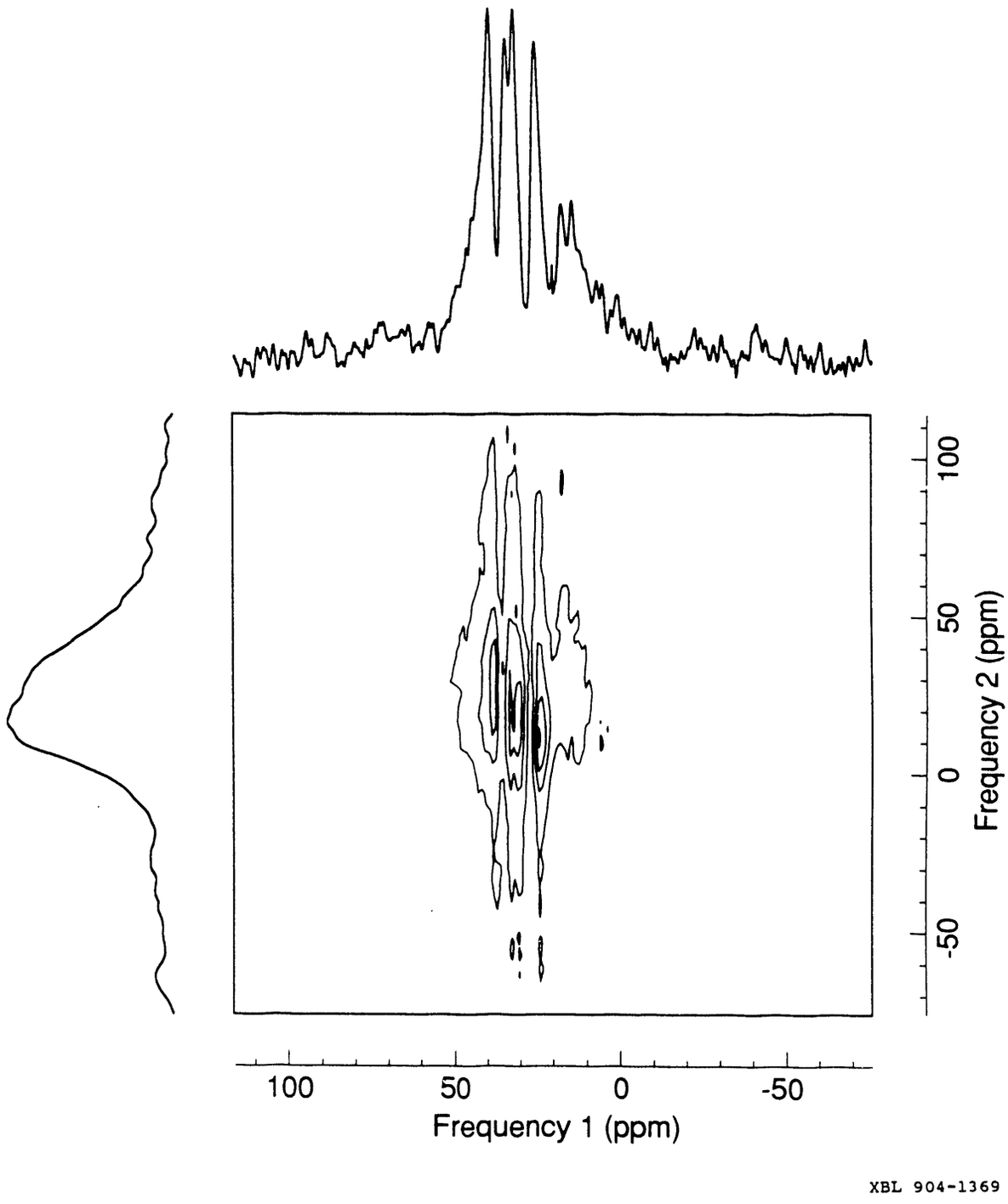

Figure 6.7: Two–dimensional DAS spectrum of clinoenstatite.

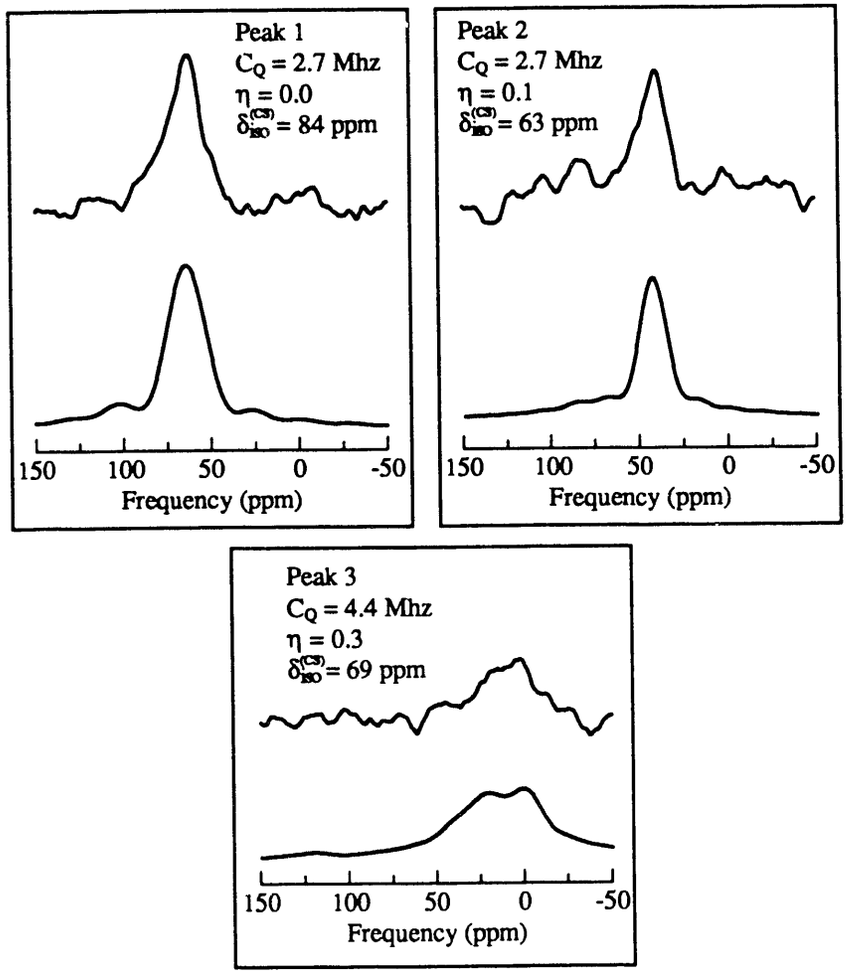

Figure 6.8: Slices taken parallel to the low resolution (powder pattern) dimension of the diopside two–dimensional DAS spectrum in Fig. 6.5.

resonances in the second dimension, which would occur as an overlap of two powder patterns in the 28.2 ppm slice. The number of spectral features present indicate two resonances with quadrupolar coupling constants in the range of 4 to 5 MHz, indicative of bridging sites. The integrated intensity is also twice that of the isotropic resonance at 21.6 ppm, which we assign to the third distinct bridging oxygen in the structure. With these assignments, the resonances from all nine crystallographically distinct oxygens can be identified.

More complicated structures, such as those found in larnite, clinoenstatite and wollastonite, require careful analysis of the two–dimensional DAS data to extract the quadrupolar and chemical shift parameters. Preliminary fits using the second frequency dimension in the two–dimensional spectra of clinoenstatite and wollastonite provide approximate parameters (see reference [158]), but more precise fits are still difficult. In particular, the broad lines from the bridging oxygen resonances in both species suffer from a poor signal–to–noise ratio. DAS at two field strengths allows separation of the chemical shift and quadrupolar shifts and sheds more light onto the differences in local structure present in these materials.

6.3.3 DAS at Two Field Strengths

Dynamic–angle spinning spectra obtained at two field strengths will provide enough information to solve a set of equations (in the form of Eqs. 6.1 and 6.2) for the isotropic chemical shift and the isotropic second–order quadrupolar shift. The isotropic chemical shift provides information regarding the local electronic structure, especially bond order and oxygen coordination. The size of the isotropic second–order quadrupolar shift is weakly dependent on the asymmetry parameter of the

electric field gradient at the nucleus and more strongly dependent on the size of the largest component (V_{ZZ}). This correlates strongly with local bonding parameters such as p–orbital occupancy and charge transfer from oxygen lone pairs to silicon in d–p π–bonding models [46].

According to the analysis above and the development of the theory in Chapters 1 and 2, the isotropic chemical shift is field–independent while the quadrupolar shift depends on the inverse of the square of the magnetic field. Therefore, at a higher field strength the second–order shift, and hence the overall shift, will move to a higher frequency. Care must be taken to minimize the possibility that resonances will unexpectedly "cross" as the field strength is changed and in this case the second (anisotropic) dimension of a DAS experiment is especially useful.

As an example of the effect observed, Fig. 6.9 shows the two oxygen–17 DAS spectra obtained for diopside at magnetic field strengths of 9.4 T and 11.8 T. As the field strength is increased the resonances shift to higher frequency as expected. The two equations to be solved are

$$\delta_{obs}^{9.4\mathrm{T}} = \delta_{iso}^{(CS)} - 2.03691 C_Q^2 (1 + \frac{\eta^2}{3}) \tag{6.5}$$

$$\delta_{obs}^{11.8\mathrm{T}} = \delta_{iso}^{(CS)} - 1.30476 C_Q^2 (1 + \frac{\eta^2}{3}) \tag{6.6}$$

and the calculated isotropic chemical shifts are 86, 64, and 69 ppm for the three resonances. The corresponding products of the quadrupolar parameters $C_Q(1 + \eta^2/3)^{\frac{1}{2}}$ are 2.9, 2.7 and 4.4 MHz respectively. Once again, these agree very well with the previously determined values. The full results for the five silicates studied here are found in Tables 6.3 and 6.4.

To summarize, in the past sharp NMR spectra from spin–$\frac{1}{2}$ nuclei such as silicon–29 have been useful in studying local bonding parameters in solids. Equally

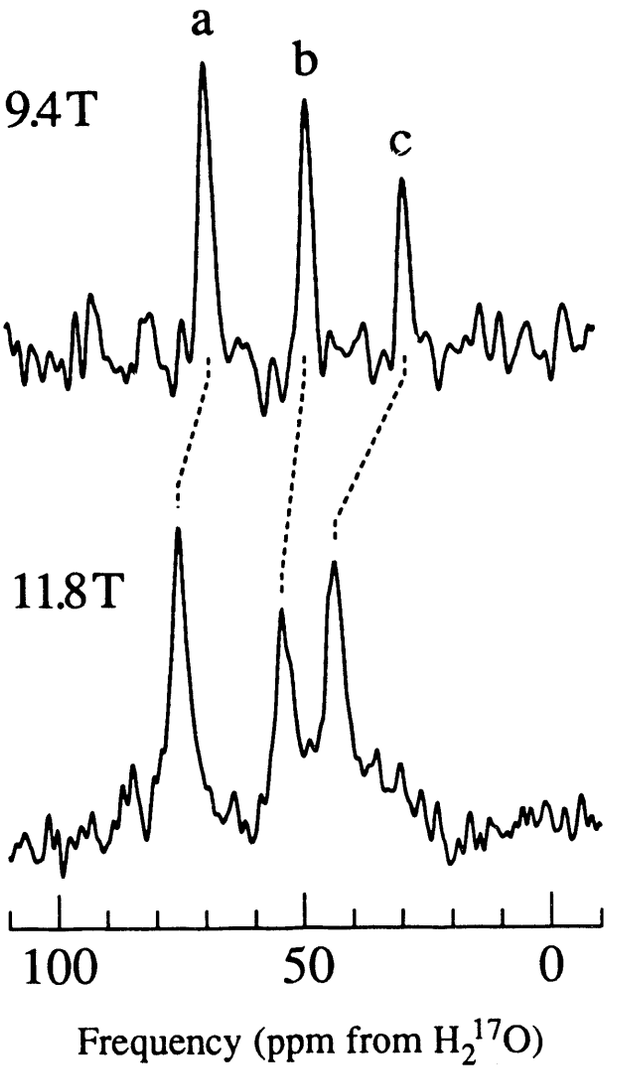

Figure 6.9: DAS spectra of diopside ($CaMgSi_2O_6$) at 9.4 T and 11.8 T.

compound	$\delta_{obs}^{9.4T}$ (ppm)	$\delta_{obs}^{11.8T}$ (ppm)	$\delta_{iso}^{(CS)}$ (ppm)	$C_Q(1+\frac{\eta^2}{3})^{\frac{1}{2}}$ (MHz)
diopside	69.2	75.1	86	2.8
$CaMgSi_2O_6$	48.5	54.0	64	2.7
	28.6	43.3	69	4.5
forsterite	49.0	57.1	72	3.3
Mg_2SiO_4	49.0	54.8	65	2.7
	30.8	37.5	49	3.0
clinoenstatite	39.3	45.5	57	2.9
$MgSiO_3$	34.5	44.1	61	3.6
	32.3	42.0	59	3.6
	26.3	39.0	62	4.2
	18.0	36.8	70	5.1
	15.0	34.7	70	5.2

Table 6.3: Results from performing DAS experiments at 9.4 T and 11.8 T. The isotropic chemical shift and product of quadrupolar parameters were calculated from Eqs. 6.5 and 6.6.

compound	$\delta_{obs}^{9.4T}$ (ppm)	$\delta_{obs}^{11.8T}$ (ppm)	$\delta_{iso}^{(CS)}$ (ppm)	$C_Q(1+\frac{\eta^2}{3})^{\frac{1}{2}}$ (MHz)
wollastonite	103.4	107.4	115	2.3
$CaSiO_3$	100.1	105.1	114	2.6
	96.5	100.2	107	2.2
	89.0	91.9	97	2.0
	85.8	91.9	103	2.9
	74.3	79.3	88	2.6
	28.2	44.9	75	4.8
	28.2	44.9	75	4.8
	21.6	37.8	67	4.7
larnite	117.3	123.3	134	2.9
Ca_2SiO_4	113.3	118.5	128	2.7
	108.8	113.4	122	2.5
	106.3	112.0	122	2.8

Table 6.4: Results from performing DAS experiments at 9.4 T and 11.8 T. The isotropic chemical shift and product of quadrupolar parameters were calculated from Eqs. 6.5 and 6.6.

useful resolution is now available from quadrupolar nuclei including oxygen–17 as illustrated here for a class of oxygen–17 enriched minerals. Resolved resonances have been observed from samples with up to nine crystallographically distinct oxygen sites. In DAS, two–dimensional spectral analysis is used for correlating isotropic chemical shifts with quadrupolar parameters (C_Q and η) at each oxygen site. In DOR, a technically more demanding experiment, one–dimensional spectra can be accumulated directly. Performing DAS or DOR experiments at two field strengths allows quantitative determination of the isotropic chemical shift and the quadrupolar shift. It is anticipated that pure–absorption–phase DAS will ultimately allow complete determination of the quadrupolar parameters, rather than a product of the coupling constant and asymmetry parameter, once acceptable signal strengths are achieved.

Chapter 7

A Dynamic–Angle Spinning NMR Probe

A probe for dynamic–angle spinning (DAS) NMR experiments comprises a spinning cylindrical sample holder whose axis may be reoriented rapidly between discrete directions within the bore of a superconducting magnet. This allows the refocussing of nuclear spin magnetization that evolves under anisotropic interactions such as chemical shift anisotropy and quadrupolar coupling. The probe includes an axial air delivery system to bearing and drive jets which support and spin a rotor containing the sample. Axis reorientation is accomplished with a pulley attached to the probehead and coupled to a stepping motor outside of the magnet. The choice of motor and gear ratio is based on an analysis of the moments of inertia of the motor and load, the desired angular resolution, and simplicity of design. Control of angular accuracy and precision is essential, and the determination of the performance of this probe is illustrated with testing procedures used routinely in experimental setup. The need for quick reorientation of the axis is dictated

by the relaxation of magnetization to thermal equilibrium (spin-lattice relaxation) and dipolar relaxation of spins in the energy levels of the central transition to other magnetic energy levels (cross-relaxation and spectral diffusion). Angular accuracy is also necessary to sufficiently cancel the anisotropic evolution at the two angles, while reproducibility of the angles is essential due to the use of signal averaging and the two-dimensional nature of these experiments.

7.1 Apparatus

The experimental apparatus for dynamic–angle spinning is, to a first approximation, similar to that used in a conventional MAS experiment. However in DAS the spinning angle of the rotor with respect to the laboratory reference frame (or magnet reference frame) is dynamic or time–dependent. For these experiments a mechanical device is required to rapidly reorient a spinning sample axis between two or more angles, synchronized with radiofrequency pulses to manipulate the nuclear spin magnetization. The general goals for probe performance were short reorientation time, accurate and precise angular control, and radiofrequency efficiency, in that order. The following analysis led to this particular design.

Assume that the motor used to drive the body through a hop has an essentially constant torque N_M over the required speed range. Neglecting friction, the power delivered by the motor during reorientation generates or absorbs rotational kinetic energy according to

$$\begin{aligned} N_M\omega_M &= \frac{d}{dt}\left(\frac{1}{2}I_M\omega_M^2 + \frac{1}{2}I_B\omega_B^2\right) \\ &= I_M\omega_M\alpha_M + I_B\omega_B\alpha_B \ , \end{aligned} \tag{7.1}$$

where $\omega_{M,B}$ and $\alpha_{M,B}$ are the magnitudes of the angular velocities and accelerations of the motor (M) and the body (B) housing the rotor. Also assume that a transmission links the motor and body angles $\theta_{M,B}$ by a ratio

$$\beta = \frac{\theta_B}{\theta_M} = \frac{\omega_B}{\omega_M} = \frac{\alpha_B}{\alpha_M}, \tag{7.2}$$

and that the inertia of the linkage is either incorporated or negligible. By eliminating the motor variables in Eq. 7.1 using Eq. 7.2 the body acceleration is expressed as:

$$\alpha_B = \frac{\beta N_M}{(I_M + \beta^2 I_B)}. \tag{7.3}$$

As a function of β this expression has a maximum value

$$\alpha_{max} = \frac{N_M}{2\sqrt{I_M I_B}} = \frac{\alpha_0 \beta_0}{2} \tag{7.4}$$

where $\alpha_0 = N_M/I_M$ is the free–motor acceleration and β_0 is the optimum transmission coupling factor, $\sqrt{I_M/I_B}$. This demonstrates that a massive motor having a large free acceleration will provide optimal speed performance although, as shown next, this optimum is very insensitive to changes in mechanical parameters.

The parameter of direct interest is the reorientation time τ_r required to move the rotor through an angle $\Delta\theta = \theta_2 - \theta_1$. Assuming ideal control, where the motor can be operated at any acceleration consistent with its torque, the rotor may be accelerated during the first half of the motion and decelerated during the second half, so

$$\frac{\Delta\theta}{2} = \frac{1}{2}\alpha_B \left(\frac{\tau_r}{2}\right)^2, \tag{7.5}$$

and

$$\tau_r = 2\sqrt{\frac{\Delta\theta}{\alpha_B}}. \tag{7.6}$$

Combining this with Eqs. 7.3 and 7.4 the reorientation time is

$$\tau_r = \tau_{min}\sqrt{\cosh\left(\ln\left(\frac{\beta}{\beta_0}\right)\right)}\ , \tag{7.7}$$

where

$$\tau_{min} = 2\sqrt{\Delta\theta/\alpha_{max}}\ . \tag{7.8}$$

The appearance of hyperbolic functions is characteristic of impedance matching problems, of which this is a mechanical example.

The result in Eq. 7.7 shows a weak dependence of the reorientation time on almost all mechanical parameters, and the consequent difficulty of making substantial time reductions by mechanical improvements. The strongest dependences are upon the hop angle and motor torque/acceleration: these enter under square roots, and are the first parameters to optimize. Also note that τ_{min} depends upon the fourth root of the moments of inertia. The square root expression in Eq. 7.7, which we call the time inflation factor, has a very weak dependence upon the optimal coupling condition, as the plot in Fig. 7.1 indicates. This is beneficial in the sense that it leaves the choice of the coupling parameter β relatively free.

Current technology offers fast motors have free accelerations in the range of 10^5 to 10^6 rad/sec^2. Motor moments of inertia span the range from 10^{-5} to 10^{-6} kg m^2 and the stator assemblies built to hold the rotor in our experiments have inertias which fall at the low end of this range. Given these ranges, and that $\Delta\theta \approx \pi/4$, τ_{min} spans the relatively narrow range from 1 to 4 msec, despite a variation of two orders of magnitude in the independent parameters. As seen below, however, such short times have not been achieved: the primary limiting factor is obtaining sufficiently subtle motion control for the motor performance to approach these theoretical limits.

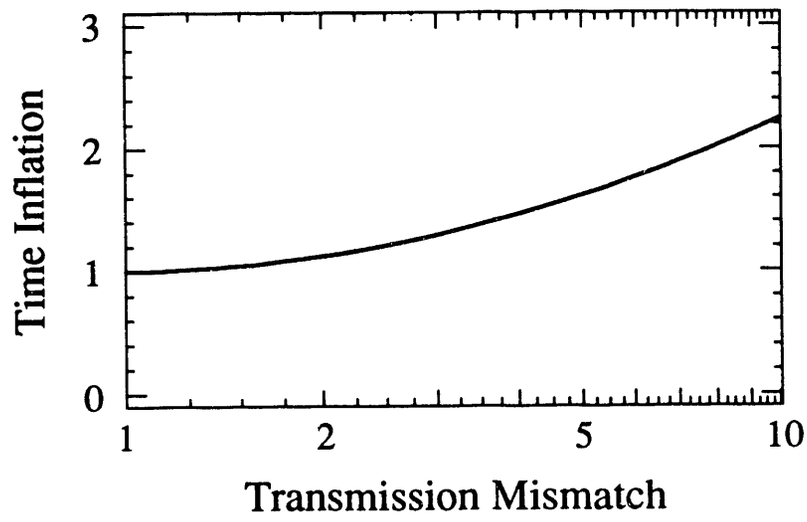

Figure 7.1: Time inflation factor as a function of β/β_0.

Motor selection in our laboratory was based largely on intrinsic acceleration. Because performance is such a weak function of β, while motor and body inertias are comparable, direct drive ($\beta = 1$) was chosen for control convenience. Although a variety of gear and belt options are possible, a simple string/pulley linkage seemed to be the lightest and simplest alternative. We have used PMI (model USS–52M–006) and Sigma (model 803–D2220–F04) motors; Portescap P–series motors are also suitable for this type of design. All motors have comparable free accelerations, but the Sigma motors are preferable because of their larger torque and inertia.

A Whedco model IMC–1151–1–A controller drives the motors. The IMC accepts commands and allows preprogramming of movement profiles using a PC as a dummy terminal. There are also external profile enable and trigger lines available which allow TTL level signals to trigger execution of profiles and commands within

individual profiles. Movement commands, acceleration and deceleration rates, maximum speed, and start/stop pulse rates are loaded before an experiment is begun, and final control of the motor is through TTL level pulses sent to the IMC from the NMR spectrometer pulse programmer. Synchronization of movement with the radiofrequency pulses in the experiment is then easily accomplished with the spectrometer software. The basic laboratory setup for a DAS experiment is sketched in Fig. 7.2.

A schematic of the DAS probehead is shown in Fig. 7.3. The stator body and endcaps are shown placed on an aluminum platform, and the radiofrequency coil and $\frac{1}{8}$-inch diameter copper tubes for air delivery to the endcaps are also visible in this view. The coil is wound from copper magnet wire, but here it is shown as transparent to enhance the view of otherwise obscured components of the probehead. The assembly is built to fit within the 70 mm room temperature shims of a widebore superconducting magnet. The stator body and its internal parts (the stator sleeve and the rotor, discussed below) are machined from Vespel, a polyimide chosen for its high strength and ease of machinability. The endcaps and pulley are made of Delrin (polyacetal), a commercially available, less costly, high modulus plastic. A full set of technical drawings for the probehead, used by the machinists in the Department of Chemistry machine shop to fabricate this probe, are included in Appendix A.

The cylindrical stator body (diameter 15.9 mm) is located by glass ball bearings (Microminiature Bearings Co.) in polyacetal races held in place by the endcaps. The bearings allow smooth, low friction reorientation. High pressure air is delivered through the endcaps and bearings to channels in the stator body. This axial flow of

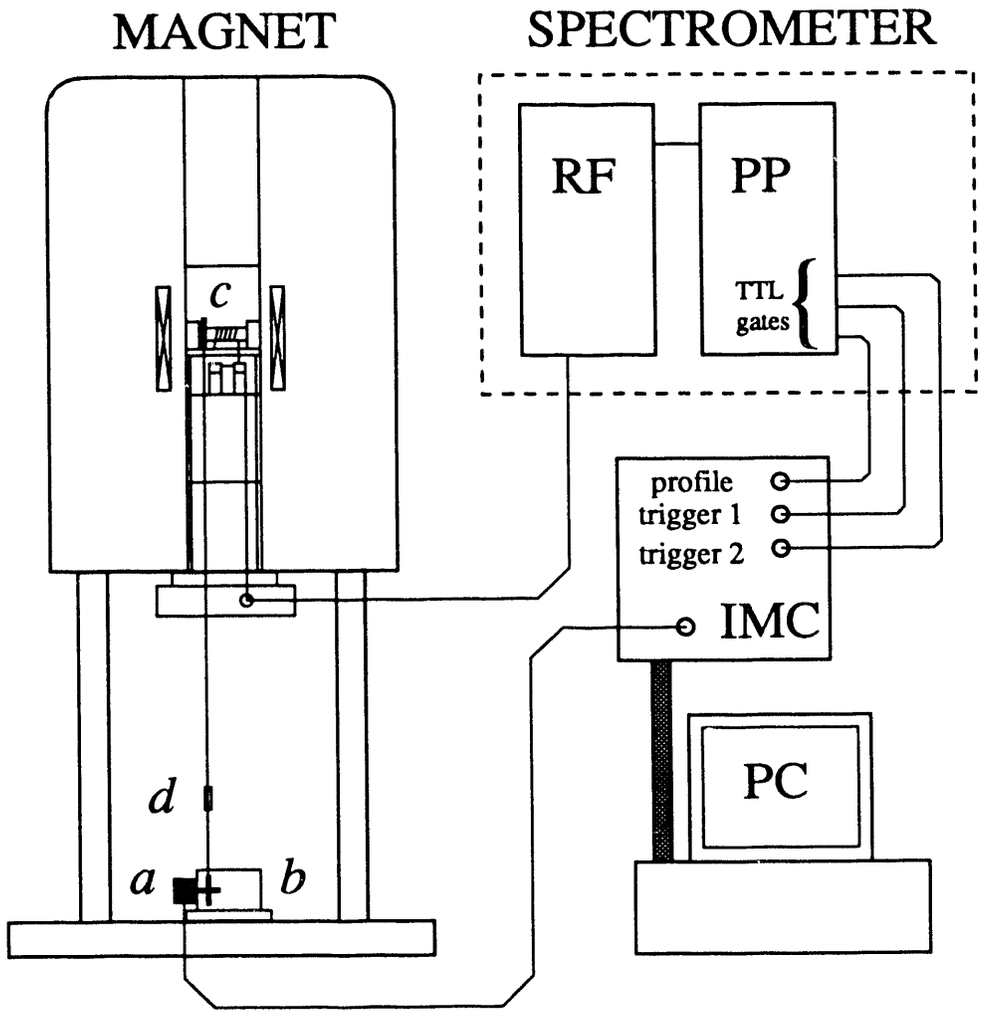

Figure 7.2: Schematic of the laboratory setup for a DAS experiment. The spectrometer pulse programmer (PP) controls the radiofrequency (RF) irradiation and the triggering of the Intelligent Motor Controller (IMC). The personal computer (PC) allows loading of predefined hop profiles into the IMC. The motor (*a*) sits at the base of the magnet in the motor housing (*b*) and is coupled to the DAS probehead (*c*) with a string tightened by nylon turnbuckles (*d*).

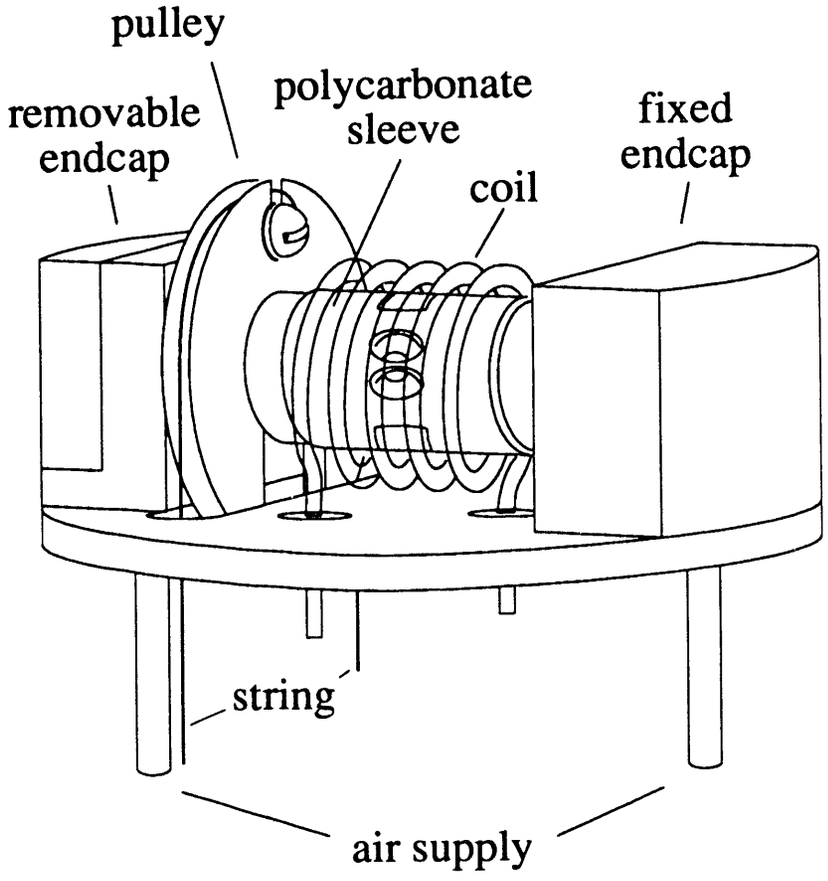

Figure 7.3: Schematic of the probehead for a DAS experiment.

air is undisturbed by the hopping motion, and no external hoses are needed which would add excess inertia to the assembly. A lightweight polycarbonate sleeve is positioned around the center of the stator body to keep the rotor in place.

Since a stationary rf coil surrounds the assembly, the stator body must be removed in order to change the sample. Removal of the pulley and unfastening of the side of one endcap (two screws) allows the stator body to slide out of the assembly, keeping one bearing set pressed around the end of the stator body while leaving the second pressed inside the fixed endcap. The former bearing outer race diameter is of slightly greater diameter than the stator body to allow removal.

The stator sleeve and sample holder are shown in the expanded drawing of Fig. 7.4. The sleeve is machined separately, press fitted into the stator body, and the whole assembly is turned on a lathe to preserve the cylindrical symmetry of the stator body. From one end of the stator body a single air hole feeds the center drive channel. The two outer bearing channels are also filled with pressurized air by splitting the axial channel from the other endcap into two channels which meet the stator cavity near the circumference of the stator body. Air forced through the 12 radial bearing holes (0.3 mm diameter) at each end of the stator supports the rotor. Each circle of bearing holes are at a 45° angle with respect to the cylindrical axis of the stator sleeve to keep their exit ports as near the ends of the rotor as possible. This maximizes support, allowing use of the longest (and therefore most stable) rotors. The bearing air escapes through the top and bottom of the spinner chamber.

Approximately 30 psi of bearing pressure is required to prevent rotor touchdown during hops. The effect of the hop on a rapidly spinning rotor is discussed in Ap-

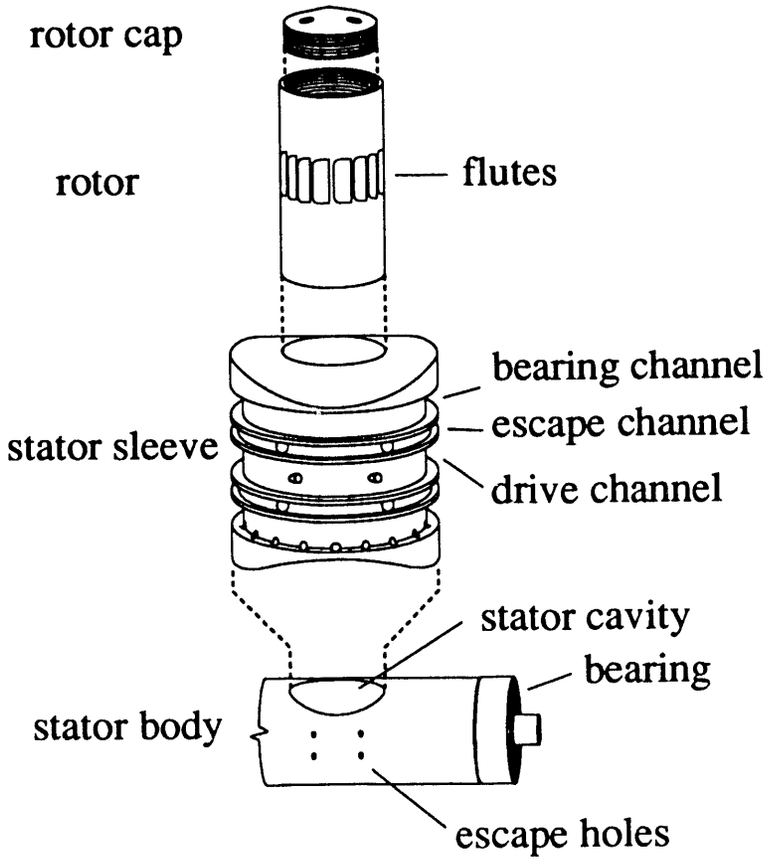

Figure 7.4: Expanded view of the stator, stator body, and sample holder.

pendix B. The conclusion is that crashes associated with hops are due to dynamic disturbances that disrupt ordinarily stable equilibrium air patterns, and not failure of the bearings to support the excess load caused by moving the rotor.

The six drive holes (1.0 mm diameter) are in the plane orthogonal to the spinning axis and are directed tangentially to give the air a rotary flow component when impinging upon the wide rotor flutes. The air provides torque to the rotor, moving up and down the flutes to then be released quickly to the laboratory through the escape holes. The escape holes are also drilled tangentially, but in a direction opposite to that of the drive holes and offset by one-sixth of the distance around the circumference of the stator. This presumes an impulse rather than reaction drive, which is consistent with improved performance obtained by lengthening the rotor flutes. Decoupling of the two air delivery and escape paths in this way minimizes the turbulent flow of air within the vicinity of the rotor, with the intent of increasing spinning stability and reliability. Drive pressures of 60 to 70 psi are necessary to provide routine rotor spinning frequencies of 5 to 6 kHz using 6.3 mm diameter rotors.

The rotors themselves are 15.9 mm long with conical screw caps on either end. Twelve flutes are centered along the body, having a length of 4.0 mm and a depth of 0.3 mm. The total sample volume is 0.15 cubic centimeters in a standard rotor with 1.0 mm wall thickness. Flat spacers within the rotors separate the powdered sample material from an angular standard (usually potassium bromide, deuterated 1,4-dimethoxybenzene, or deuterated hexamethylbenzene) used to set the magic angle. The rotor is held in place longitudinally with a thin polycarbonate sleeve rather than more conventional fixed endcaps to optimize the rotor length while

minimizing both the coil volume and stator body moment of inertia. Holes are cut in the ends and the sides of this sleeve to allow free discharge of the bearing and drive air. The conical ends of the rotors slowly wear away at the bearing points on the sleeve and this piece typically needs replacement after approximately 500 hours of operation.

The pulley has a diameter at the bottom of the string guide of 31.8 mm. It slides onto a square slot on the stator body, and has a notch cut into one side of the string guide for passage of the string to a fastening screw. The string is a length of Kevlar (Dupont aramid fiber) with a diameter of approximately 0.8 mm. At the base of the magnet, the string is also attached to a second pulley mounted on the shaft of the stepping motor. A similar notch and fastening screw are present on the lower pulley, providing an efficient coupling of angular position with negligible mechanical backlash. The string is tightened with turnbuckles located approximately halfway between the bottom pulley and the point of entry of the string into the magnet bore (see Fig. 7.2).

An external, fixed-coil arrangement is used for irradiation with the radiofrequency (B_1) field. This sacrifices electrical efficiency, but surmounts problems experienced with an earlier moving coil design [105]. The earlier design, sketched in Fig. 4.2, was used for the first DAS experiments. Specifically, tuning changes associated with axis motion and difficulty with sliding contacts or moving leads are avoided with this new design. A major advantage of this arrangement is equivalent performance at all angles: pulse lengths for 90° nutation of the magnetization are independent of the axis orientation, and it is possible to perform NMR experiments at any axis angle, including 0°. This latter axis orientation results in a

signal which is equivalent to that obtained from a static sample, and allows two-dimensional NMR spectroscopy correlating the powder pattern lineshapes observed from a static sample with the high resolution lines provided by DAS (or MAS) narrowing.

Another inconvenience with the original probe design was the use of an alumina stator. The observation of aluminum nuclei is compromised due to the background signal obtained from the stator which is inside of the coil. This new design uses only aluminum-free parts inside of the coil and therefore observation of aluminum nuclei is now possible.

7.2 Experimental Results

7.2.1 Hopping Performance

To investigate the performance of the probe, the strong time-domain free induction decay (FID) signal is observed after a 90° pulse is applied to the deuterium nuclei in a rotating sample of deuterated 1,4-dimethoxybenzene. The deuterium nucleus (spin-1) is affected by first-order quadrupolar interactions, which are motionally averaged while spinning at the magic angle [159, 160]. Since the distribution of resonance frequencies is large (on the order of 75 kHz at 9.4 T) the inhomogeneous static lineshape in the frequency domain is broken up into spinning sidebands, symmetrically displaced about a central (isotropic) peak and occuring at integer multiples of the rotor frequency. Away from the magic angle, the two $\Delta m = 1$ transitions obtain different isotropic frequencies and the resonance splits into a doublet. When exactly at the magic angle the inverse Fourier transform of

the isotropic signal and its envelope of sidebands, a time domain FID composed of a train of rotational echoes occurring once every rotor cycle, is observed. The sensitivity of the time and frequency domain signals to the angle of the spinning axis with respect to the external field is demonstrated in Fig. 7.5. Under typical experimental conditions, the step size used is obtained from one-sixteenth stepping of a 200 step per revolution motor, or 0.1125°/step. Moving through the magic angle in one step increments verifies the suitability of the magic–angle condition as a mark for determining absolute axis orientation.

The hop in a DAS experiment is made between $\theta_1 = 37.38°$ and $\theta_2 = 79.19°$, a difference of 41.81°. The nearest angles obtainable with the magic angle of 54.74° as a fixed reference and 0.1125° angular resolution are $\theta_1 = 37.41°$ and $\theta_2 = 79.15°$, a difference of 41.74° or 371 steps. When the spinning axis is set 371 steps off of the magic angle, the time necessary to complete a hop of 41.74° is determined by initiating the return hop to the magic angle and waiting for a delay time before applying a pulse to the system. The FID is then recorded, and the delay varied until an FID matching that of Fig. 7.5(c) is observed. The decays in Fig. 7.6 show the effect of changing the time allowed for the hop. Undistorted signals are observed 28 msec after the initiation of an axis hop, corresponding to measured motor drive current pulses of 25 msec, and an inferred settling time of 3 msec. This is much less than the 100 msec or longer longitudinal relaxation times (T_1) of many quadrupolar nuclei in solids, and is therefore sufficiently short to allow storage of the signal during the reorientation with negligible loss in signal intensity.

Attempts to increase the speed of the hop by increasing the acceleration of the motor through its triangular speed profile led to decreased performance because of

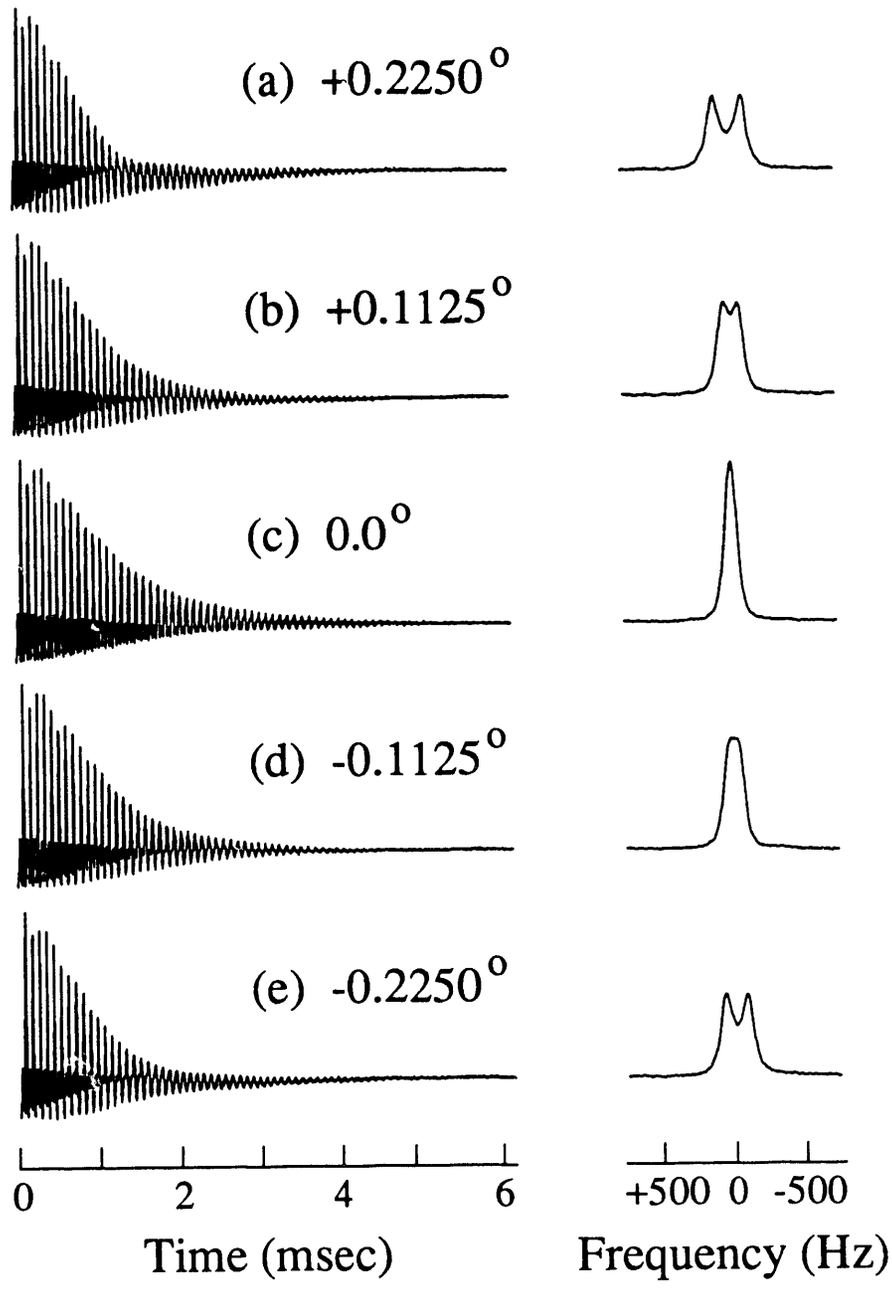

Figure 7.5: Time–domain magnetization decays and the resulting NMR spectral lines for deuterium in an angular standard as a function of offset from the magic angle.

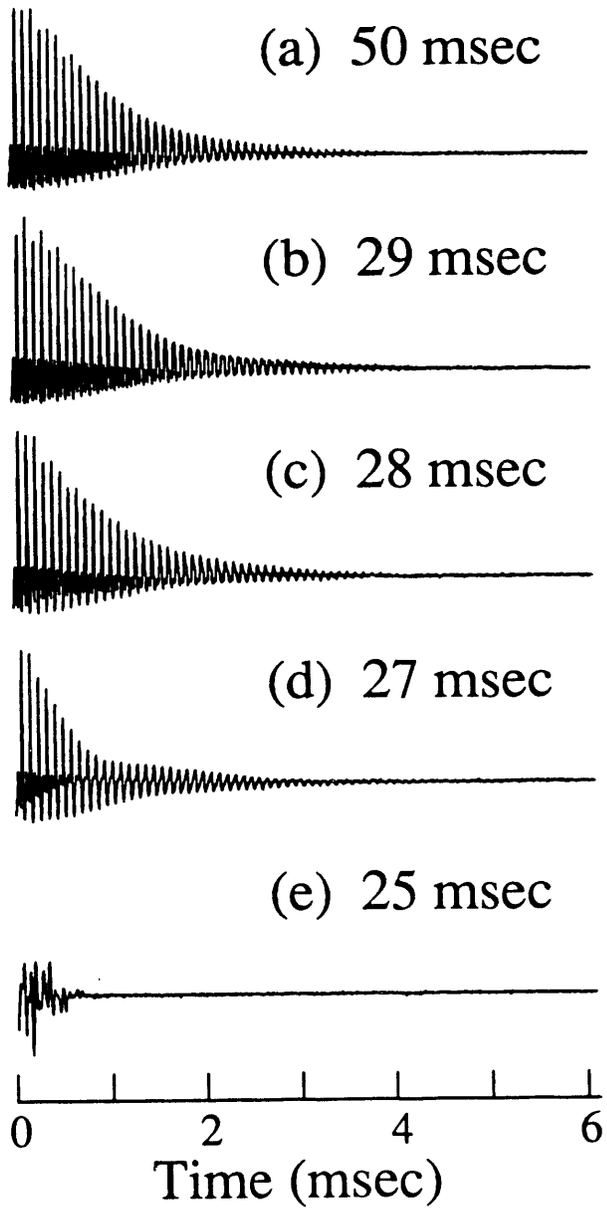

Figure 7.6: Time–domain magnetization decays from the deuterium nuclei in an angular standard as a function of the time allowed in a test hop through 41.74° to the magic angle.

angular overshoot. A smaller start/stop pulse rate was then necessary, leading to overall slower performance. The use of optical encoder feedback could not compensate completely for the overshoot as a finite time (on the order of a few msec) is required to search for the desired final angle. Similar hopping performance is now routinely achieved using a 1024 step optical encoder which provides 0.1756° angular resolution using a position pulse multiplier of two (set in the IMC).

7.2.2 Aluminum–27 DAS

The ability to observe aluminum–27 with this probehead is important as aluminum–27 is a major constituent of advanced materials such as zeolites, other molecular sieves and catalytic supports, clays, and ceramics. The capabilities of this probe are demonstrated with the DAS spectrum of the single aluminum–27 species present in petalite ($LiAlSi_4O_{10}$), a polycrystalline lithium ore. The pure–absorption–phase DAS experiment of Chapter 5 was performed with a second hop to the magic-angle of 54.74°. The two–dimensional spectrum at 9.4 T (aluminum–27 Larmor frequency of 104.26 MHz) appears in Fig. 7.7.

The single peak in the high–resolution DAS dimension appears at a total isotropic shift of 46 ppm with respect to aluminum–27 in a saturated $Al(NO_3)_3$ solution. The second dimension corresponds to the MAS spectrum for this sample and it may be simulated and the quadrupolar parameters extracted. We find e^2qQ/h = 4.62±0.05 MHz with an asymmetry parameter η of 0.48±0.03 and these results are in excellent agreement with those calculated from recent dc SQUID measurements on the same sample [161]. The isotropic chemical shift is then calculated to be 59 ppm with respect to the standard $Al(NO_3)_3$ solution. This result bodes

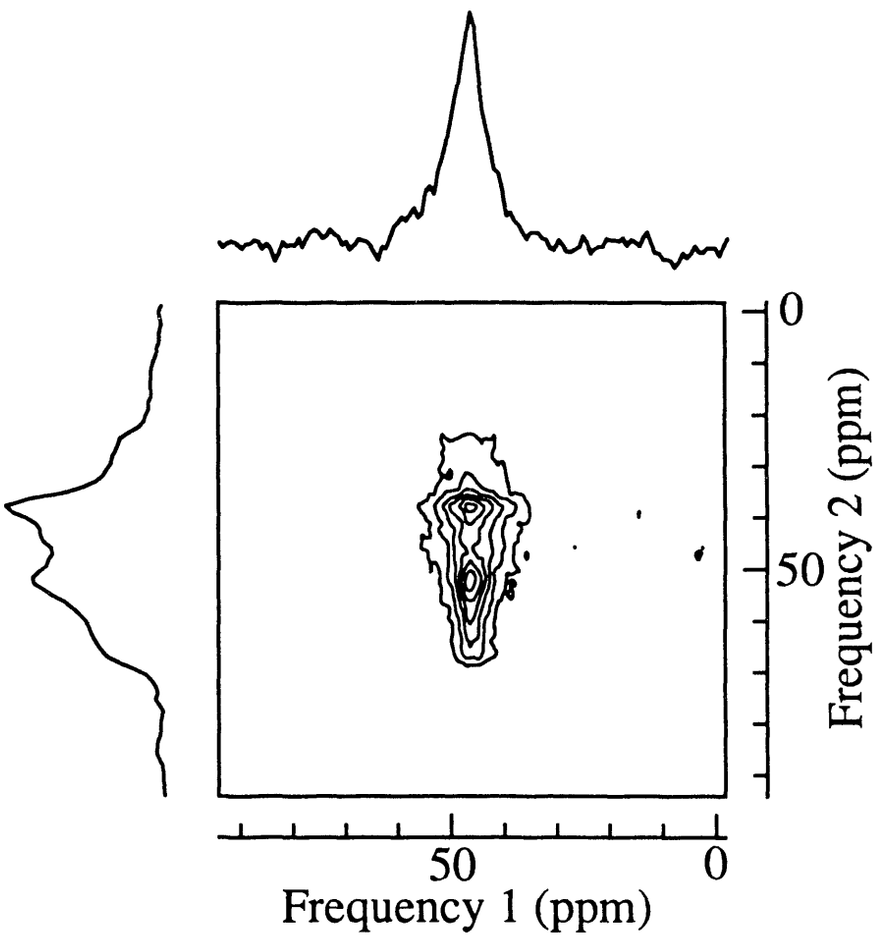

Figure 7.7: Two–dimensional pure–phase DAS spectrum of aluminum–27 in petalite ($LiAlSi_4O_{10}$).

well for the separation and complete determination of quadrupolar parameters from overlapping aluminum resonances like those in more complex aluminosilicate samples, using the DAS dimension to separate lineshapes in the powder pattern (low resolution) dimension which may then be simulated individually.

This discussion has provided an analysis of the design and examples of real laboratory performance of a dynamic–angle spinning probe suitable for narrowing resonance lines in spectra of quadrupolar nuclei. The experimental results obtainable with this design are illustrated here and in previous chapters. This design offers several advantages in its present form. Relatively simple mechanical construction has provided reliable operation and reasonable hopping times using commercially available mechanical drives. The stationary rf coil eliminates potential difficulties associated with moving rf circuit components and complications due to changing the irradiation direction, and permits use of all axis angles with equal efficiency. The observation frequency is also easy to change, often accomplished with a simple change of irradiation coil. Overall, this probe is well suited for homonuclear dynamic–angle correlation studies of nuclei with moderate sensitivity and reasonable relaxation rates. It is clear that there is room for improvement in several areas: we expect that attention to controller electronics could reduce hopping times below 10 msec, and that a more compact coil design could improve the filling factor and overall rf performance, as well as allowing higher frequency operation. It would likewise be useful to extend probe versatility by incorporating features such as heteronuclear decoupling and variable temperature capability.

Bibliography

[1] M. H. Cohen and F. Reif, *Sol. State Phys.* **5**, 321 (1957).

[2] C. Cohen-Tannoudji, B. Diu, and F. Laloë, *Quantum Mechanics* (J. Wiley, New York, 1977).

[3] E. M. Purcell, H. C. Torrey, and R. V. Pound, *Phys. Rev.* **69**, 37 (1946).

[4] F. Bloch, W. W. Hansen, and M. Packard, *Phys. Rev.* **69**, 127 (1946).

[5] F. Bloch, W. W. Hansen, and M. Packard, *Phys. Rev.* **70**, 474 (1946).

[6] R. R. Ernst, *Adv. Mag. Reson.* **2**, 1 (1966).

[7] I. Solomon, *Phys. Rev.* **110**, 61 (1958).

[8] P. Mansfield, *Phys. Rev.* **137**, A961 (1965).

[9] R. V. Pound, *Phys. Rev.* **79**, 685 (1950).

[10] P. S. Hubbard, *J. Chem. Phys.* **53**, 985 (1970).

[11] S. Vega, *Phys. Rev.* **A 23**, 3152 (1981).

[12] A. Samoson, E. Kundla, and E. Lippmaa, *J. Magn. Reson.* **49**, 350 (1982).

[13] H.-J. Behrens and B. Schnabel, *Physica* **114B**, 185 (1982).

[14] S. Wolfram, *Mathematica*^{TM}*: A System for Doing Mathematics by Computer* (Addison–Wesley, Redwood City, CA, 1988).

[15] H. W. Spiess, in *NMR: Basic Principles and Progress,* vol. 15, P. Diehl, E. Fluck, and R. Kosfeld, Eds. (Springer–Verlag, Berlin, 1978).

[16] M. Mehring, *Principles of High Resolution NMR in Solids*, 2nd edition (Springer–Verlag, Berlin, 1983).

[17] C. P. Slichter, *Principles of Magnetic Resonance*, 3rd edition (Springer–Verlag, Berlin, 1990).

[18] A. Abragam, *The Principles of Nuclear Magnetism* (Clarendon, Oxford, 1961).

[19] H. B. G. Casimir, *On the Interaction Between Atomic Nuclei and Electrons* (Teyler's Tweede Genootschap, Haarlem, 1936).

[20] J. H. Smith, E. M. Purcell, and N. F. Ramsey, *Phys. Rev.* **108**, 120 (1957).

[21] T.-C. Wang, *Phys. Rev.* **99**, 566 (1955).

[22] T.-J. Wang, *J. Magn. Reson.* **64**, 194 (1985).

[23] R. L. Cook and F. C. De Lucia, *Am. J. Phys.* **39**, 1433 (1971).

[24] A. R. Edmonds, *Angular Momentum in Quantum Mechanics* (Princeton University Press, Princeton, NJ, 1960).

[25] J. J. Sakurai, *Modern Quantum Mechanics* (Benjamin/Cummings, Menlo Park, CA, 1985).

[26] B. A. Pettitt, *J. Magn. Reson.* **48**, 309 (1982).

[27] G. M. Muha, *J. Magn. Reson.* **53**, 85 (1983).

[28] U. Haeberlen, *High Resolution NMR in Solids: Selective Averaging* in *Advances in Magnetic Resonance, Suppl. 1,* J. S. Waugh, Ed. (Academic Press, New York, 1976).

[29] S. Ding and C. Ye, *Chem. Phys. Lett.* **170**, 277 (1990).

[30] J. A. Tossell, *Phys. Chem. Mineral.* **10**, 137 (1984).

[31] R. Tycko, *J. Chem. Phys.* **92**, 5776 (1990).

[32] R. Tycko, *J. Magn. Reson.* **75**, 193 (1987).

[33] R. Tycko, *Phys. Rev. Lett.* **60**, 2734 (1988).

[34] D. P. Weitekamp, A. Bielecki, D. B. Zax, K. W. Zilm, and A. Pines, *Phys. Rev. Lett.* **50**, 1807 (1983).

[35] R. C. Tolman, *The Principles of Statistical Mechanics* (Oxford University Press, New York, 1946).

[36] R. R. Ernst, G. Bodenhausen, and A. Wokaun, *Principles of Nuclear Magnetic Resonance in One and Two Dimensions* (Clarendon Press, Oxford, 1987).

[37] I. I. Rabi, N. F. Ramsey, and J. Schwinger, *Rev. Mod. Phys.* **26**, 167 (1954).

[38] T. C. Farrar and E. D. Becker, *Pulse and Fourier Transform NMR: Introduction to Theory and Methods* (Academic Press, New York, 1971).

[39] E. Fukushima and S. B. W. Roeder, *Experimental Pulse NMR: A Nuts and Bolts Approach* (Addison–Wesley, Reading, MA, 1981).

[40] U. Haeberlen and J. S. Waugh, *Phys. Rev.* **175**, 453 (1968).

[41] W.-K. Rhim, D. D. Elleman, and R. W. Vaughan, *J. Chem. Phys.* **59**, 3740 (1973).

[42] W. Magnus, *Com. Pure Appl. Math.* **7**, 649 (1954).

[43] P. C. Taylor, J. F. Baugher, and H. M. Kriz, *Chem. Rev.* **75**, 203 (1975).

[44] D. W. Alderman, M. S. Solum, and D. M. Grant, *J. Chem. Phys.* **84**, 3717 (1986).

[45] T. M. Duncan and D. C. Douglass, *Chem. Phys.* **87**, 339 (1984).

[46] N. Janes and E. Oldfield, *J. Am. Chem. Soc.* **108**, 5743 (1986).

[47] V. H. Schmidt, *Proc. Ampère Intl. Summer School II,* Basko Polje, Yugoslavia (1971).

[48] P. P. Man, J. Klinowski, A. Trokiner, H. Zanni, and P. Papon, *Chem. Phys. Lett.* **151**, 143 (1988).

[49] A. Samoson and E. Lippmaa, *Phys. Rev.* **B 28**, 6567 (1983).

[50] A. Samoson and E. Lippmaa, *Chem. Phys. Lett.* **100**, 205 (1983).

[51] D. Fenzke, D. Freude, T. Fröhlich, and J. Haase, *Chem. Phys. Lett.* **111**, 171 (1984).

[52] P. P. Man, *J. Magn. Reson.* **67**, 78 (1986).

[53] A. P. M. Kentgens, J. J. M. Lemmens, F. M. M. Geurts, and W. S. Veeman, *J. Magn. Reson.* **71**, 62 (1987).

[54] P. P. Man, *J. Magn. Reson.* **77**, 148 (1988).

[55] A. Samoson and E. Lippmaa, *J. Magn. Reson.* **79**, 255 (1988).

[56] N. Chandrakumar and S. Subramanian, *Modern Techniques in High-Resolution FT-NMR* (Springer-Verlag, New York, 1987).

[57] T. E. Bull, S. Forsén, and D. L. Turner, *J. Chem. Phys.* **70**, 3106 (1979).

[58] A. W. Overhauser, *Phys. Rev.* **91**, 476 (1953).

[59] A. W. Overhauser, *Phys. Rev.* **92**, 411 (1953).

[60] E. R. Andrew, A. Bradbury, and R. G. Eades, *Nature (London)* **182**, 1659 (1958).

[61] I. J. Lowe, *Phys. Rev. Lett.* **2**, 285 (1959).

[62] J. Schaefer, E. O. Stejskal, and R. Buchdahl, *Macromolecules* **8**, 291 (1975).

[63] J. Schaefer and E. O. Stejskal, *J. Am. Chem. Soc.* **98**, 1031 (1976).

[64] M. M. Maricq and J. S. Waugh, *J. Chem. Phys.* **70**, 3300 (1979).

[65] J. Herzfeld and A. E. Berger, *J. Chem. Phys.* **73**, 6021 (1980).

[66] W. T. Dixon, *J. Magn. Reson.* **44**, 220 (1981).

[67] W. T. Dixon, *J. Chem. Phys.* **77**, 1800 (1982).

[68] R. J. Kirkpatrick, in *Spectroscopic Methods in Mineralogy and Geology, Reviews in Minerology,* vol. 18, F. C. Hawthorne, Ed. (Mineralogical Society of America) 341 (1988).

[69] G. E. Maciel, *Science* **226**, 282 (1984).

[70] E. R. Andrew, *Phil. Trans. Roy. Soc. Lond. A* **299**, 505 (1981).

[71] A. Samoson, *Chem. Phys. Lett.* **119**, 29 (1985).

[72] H. J. Jakobsen, J. Skibsted, H. Bildsøe, and N. C. Nielsen, *J. Magn. Reson.* **85**, 173 (1989).

[73] S. Ganapathy, S. Schramm, and E. Oldfield, *J. Chem. Phys.* **77**, 4360 (1982).

[74] F. Lefebvre, J.-P. Amoureux, C. Fernandez, and E. G. Derouane, *J. Chem. Phys.* **86**, 6070 (1987).

[75] J. P. Amoureux, C. Fernandez, and F. Lefebvre, *Mag. Reson. Chem.* **28**, 5 (1990).

[76] S. Schramm, R. J. Kirkpatrick, and E. Oldfield, *J. Am. Chem. Soc.* **105**, 2483 (1983).

[77] S. Schramm and E. Oldfield, *J. Am. Chem. Soc.* **106**, 2502 (1984).

[78] H. K. C. Timken, S. E. Schramm, R. J. Kirkpatrick, and E. Oldfield, *J. Phys. Chem.* **91**, 1054 (1987).

[79] H. K. C. Timken, G. L. Turner, J.-P. Gilson, L. B. Welsh, and E. Oldfield, *J. Am. Chem. Soc.* **108**, 7231 (1986).

[80] H. K. C. Timken, N. Janes, G. L. Turner, S. L. Lambert, L. B. Welsh, and E. Oldfield, *J. Am. Chem. Soc.* **108**, 7236 (1986).

[81] E. Oldfield, S. Schramm, M. D. Meadows, K. A. Smith, R. A. Kinsey, and J. Ackerman, *J. Am. Chem. Soc.* **104**, 919 (1982).

[82] R. K. Harris and G. J. Nesbitt, *J. Magn. Reson.* **78**, 245 (1988).

[83] C. Jäger, S. Barth, and A. Feltz, *Chem. Phys. Lett.* **154**, 45 (1989).

[84] L. B. Alemany, H. K. C. Timken, and I. D. Johnson, *J. Magn. Reson.* **80**, 427 (1988).

[85] R. J. Kirkpatrick, K. A. Smith, S. Schramm, G. Turner, and W.-H. Yang, *Ann. Rev. Earth Planet. Sci.* **13**, 29 (1985).

[86] L. B. Alemany and G. W. Kirker, *J. Am. Chem. Soc.* **108**, 6158 (1986).

[87] E. Lippmaa, A. Samoson, and M. Mägi, *J. Am. Chem. Soc.* **108**, 1730 (1986).

[88] C. S. Blackwell and R. L. Patton, *J. Phys. Chem.* **92**, 3965 (1988).

[89] P. J. Grobet, J. A. Martens, I. Balakrishnan, M. Mertens, and P. A. Jacobs, *Appl. Catal.* **56**, L21 (1989).

[90] G. L. Turner, K. A. Smith, R. J. Kirkpatrick, and E. Oldfield, *J. Magn. Reson.* **67**, 544 (1986).

[91] J. F. Baugher, H. M. Kriz, P. C. Taylor, and P. J. Bray, *J. Magn. Reson.* **3**, 415 (1970).

[92] S. E. Svanson and B. Johansson, *Acta Chem. Scand.* **23**, 628 (1969).

[93] D. E. Woessner, *Zeit. Phys. Chem. Neue Folge* **152**, 309 (1987).

[94] A. Bax, N. M. Szeverenyi, and G. E. Maciel, *J. Magn. Reson.* **55**, 494 (1983).

[95] T. Terao, H. Miura, and A. Saika, *J. Chem. Phys.* **85**, 3816 (1986).

[96] T. Terao, T. Fujii, T. Onodera, and A. Saika, *Chem. Phys. Lett.* **107**, 145 (1984).

[97] M. Sardashti and G. E. Maciel, *J. Magn. Reson.* **72**, 467 (1987).

[98] A. Bax, N. M. Szeverenyi, and G. E. Maciel, *J. Magn. Reson.* **52**, 147 (1983).

[99] A. Llor and J. Virlet, at *Ninth Experimental NMR Conference* Bad Aussee, Austria (May 1988).

[100] A. Llor and J. Virlet, *Chem. Phys. Lett.* **152**, 248 (1988).

[101] A. Pines, at *Ninth Experimental NMR Conference* Bad Aussee, Austria (May 1988).

[102] G. C. Chingas, C. J. Lee, E. Lippmaa, K. T. Mueller, A. Pines, A. Samoson, B. Q. Sun, D. Suter, and T. Terao, in *Proc. XXIV Congress Ampère,* Poznań, Poland 1988 J. Stankowski, N. Pisłewski, and S. Idziak, Eds., D62.

[103] C. J. Lee, *NMR with Generalized Dynamics of Spin and Spatial Coordinates,* PhD. Thesis (University of California, Berkeley, CA, 1988).

[104] B. F. Chmelka, K. T. Mueller, A. Pines, J. Stebbins, Y. Wu, and J. W. Zwanziger, *Nature (London)* **339**, 42 (1989).

[105] K. T. Mueller, B. Q. Sun, G. C. Chingas, J. W. Zwanziger, T. Terao, and A. Pines, *J. Magn. Reson.* **86**, 470 (1990).

[106] A. Samoson, B. Q. Sun, and A. Pines, to be published in *Pulsed Magnetic Resonance: NMR, ESR, and Optics (a recognition of E. L. Hahn),* D. M. S. Bagguley, Ed. (Clarendon, Oxford, 1992).

[107] E. L. Hahn, *Phys. Rev.* **80**, 580 (1950).

[108] H. Y. Carr and E. M. Purcell, *Phys. Rev.* **94**, 630 (1954).

[109] S. Goldman, *Information Theory* (Prentice Hall, Englewood Cliffs, New Jersey, 1953).

[110] R. M. Bracewell, *The Fourier Transform and its Applications* (McGraw-Hill, New York, 1965).

[111] A. Samoson, E. Lippmaa, and A. Pines, *Mol. Phys.* **65**, 1013 (1988).

[112] A. Samoson and E. Lippmaa, *J. Magn. Reson.* **84**, 410 (1989).

[113] A. Samoson and A. Pines, *Rev. Sci. Instrum.* **60**, 3239 (1989).

[114] F. D. Doty and P. D. Ellis, *Rev. Sci. Instrum.* **52**, 1868 (1981).

[115] K. T. Mueller, G. C. Chingas, and A. Pines, *Rev. Sci. Instrum.* **62**, 1445 (1991).

[116] G. A. Jeffrey and G. S. Parry, *J. Am. Chem. Soc.* **76**, 5283 (1954).

[117] G. Bodenhausen, S. P. Kempsell, R. Freeman, and H. D. W. Hill, *J. Magn. Reson.* **35**, 337 (1979).

[118] J. S. Waugh, M. M. Maricq, and R. Cantor, *J. Magn. Reson.* **29**, 183 (1978).

[119] D. Suter and R. R. Ernst, *Phys. Rev.* **B 25**, 6038 (1982).

[120] I. Solomon, *Phys. Rev.* **99**, 559 (1955).

[121] N. Bloembergen, S. Shapiro, P. S. Pershan, and J. O. Artman, *Phys. Rev.* **114**, 445 (1959).

[122] P. S. Pershan, *Phys. Rev.* **117**, 109 (1960).

[123] *Research & Development,* October 1989, 58 (1989).

[124] Y. Wu, B. Q. Sun, A. Pines, A. Samoson, and E. Lippmaa, *J. Magn. Reson.* **89**, 297 (1990).

[125] W. A. Deer, R. A. Howie, and J. Zussman, *Rock-Forming Minerals* (Halsted Press, New York, 1978).

[126] J. Keeler and D. Neuhaus, *J. Magn. Reson.* **63**, 454 (1985).

[127] K. T. Mueller, E. W. Wooten, and A. Pines, *J. Magn. Reson.* **92**, 620 (1991).

[128] A. D. Bain, *J. Magn. Reson.* **56**, 418 (1984).

[129] G. Bodenhausen, H. Kogler, and R. R. Ernst, *J. Magn. Reson.* **58**, 370 (1984).

[130] T. T. Nakashima and R. E. D. McClung, *J. Magn. Reson.* **70**, 187 (1986).

[131] A. D. Bain and S. Brownstein, *J. Magn. Reson.* **47**, 409 (1982).

[132] O. W. Sørensen, M. Rance, and R. R. Ernst, *J. Magn. Reson.* **56**, 527 (1984).

[133] H. Kessler, M. Gehrke, and C. Griesinger, *Angew. Chem. Int. Ed. Engl.* **27**, 490 (1988).

[134] G. Bodenhausen, R. Freeman, R. Niedermeyer, and D. L. Turner, *J. Magn. Reson.* **26**, 133 (1977).

[135] D. Marion and K. Wüthrich, *Biochem. Biophys. Res. Commun.* **113**, 967 (1983).

[136] D. J. States, R. A. Haberkorn, and D. J. Ruben, *J. Magn. Reson.* **48**, 286 (1982).

[137] J. Jeener, *Proc. Ampère Intl. Summer School II,* Basko Polje, Yugoslavia (1971).

[138] K. Nagayama, K. Wüthrich, and R. R. Ernst, *Biochem. Biophys. Res. Commun.* **90**, 305 (1979).

[139] K. Nagayama, A. Kumar, K. Wüthrich, and R. R. Ernst, *J. Magn. Reson.* **40**, 321 (1980).

[140] G. Drobny, A. Pines, S. Sinton, D. Weitekamp, and D. Wemmer, *Symp. Farad. Soc.* **13**, 49 (1979).

[141] D. W. Breck, *Zeolite Molecular Sieves: Structure, Chemistry, and Use* (J. Wiley, New York, 1974).

[142] B. Douglas, D. H. McDaniel, and J. J. Alexander, *Concepts and Models of Inorganic Chemistry*, 2nd edition (J. Wiley, New York, 1983).

[143] K. Narita, J.-I. Umeda, and H. Kusumoto, *J. Chem. Phys.* **44**, 2719 (1966).

[144] G. M. Volkoff, *Can. J. Phys.* **31**, 820 (1953).

[145] A.-R. Grimmer, F. von Lampe, and M. Mägi, *Chem. Phys. Lett.* **132**, 549 (1986).

[146] E. Lippmaa, M. Mägi, A. Samoson, G. J. Engelhardt, and A.-R. Grimmer, *J. Am. Chem. Soc.* **102**, 4889 (1980).

[147] M. Mägi, E. Lippmaa, A. Samoson, G. Engelhardt, and A.-R. Grimmer, *J. Phys. Chem.* **88**, 1518 (1984).

[148] C. A. Fyfe, *Solid State NMR for Chemists* (CFC Press, Guelph, 1983).

[149] C. A. Fyfe, J. H. O'Brien, and H. Strobl, *Nature (London)* **326**, 281 (1987).

[150] E. Kundla, A. Samoson, and E. Lippmaa, *Chem. Phys. Lett.* **83**, 229 (1981).

[151] B. F. Chmelka, *Distribution of Metal and Adsorbed Guest Species in Zeolites,* PhD. Thesis (University of California, Berkeley, CA, 1989).

[152] B. Warren and W. L. Bragg, *Z. Kristallogr.* **69**, 168 (1928).

[153] R. W. G. Wyckoff, *Crystal Structures*, volume 3 (Interscience, New York, 1948).

[154] J. Stebbins, unpublished results.

[155] N. Morimoto, D. E. Appleman, and H. T. Evans Jr., *Z. Kristallogr.* **114**, 120 (1960).

[156] F. J. Troger, *Z. Kristallogr.* **127**, 291 (1968).

[157] C. M. Midgely, *Acta Crystallogr.* **5**, 307 (1952).

[158] K. T. Mueller, Y. Wu, B. F. Chmelka, J. Stebbins, and A. Pines, *J. Am. Chem. Soc.* **113**, 32 (1991).

[159] E. R. Andrews and R. G. Eades, *Disc. Far. Soc.* **34**, 38 (1963).

[160] C. Ye, B. Sun, and G. E. Maciel, *J. Magn. Reson.* **70**, 241 (1986).

[161] C. Connor, J. Chang, and A. Pines, *J. Chem. Phys.* **93**, 7639 (1990).

Appendix A

Probe Designs

This appendix contains the full set of technical drawings for a DAS probehead as used by the machine shop in the Department of Chemistry at the University of California at Berkeley. The original probe was fabricated at the Materials and Chemicals Sciences Division machine shop at Lawrence Berkeley Laboratory. A full description of the probe is contained in Chapter 7 and Ref. [115].

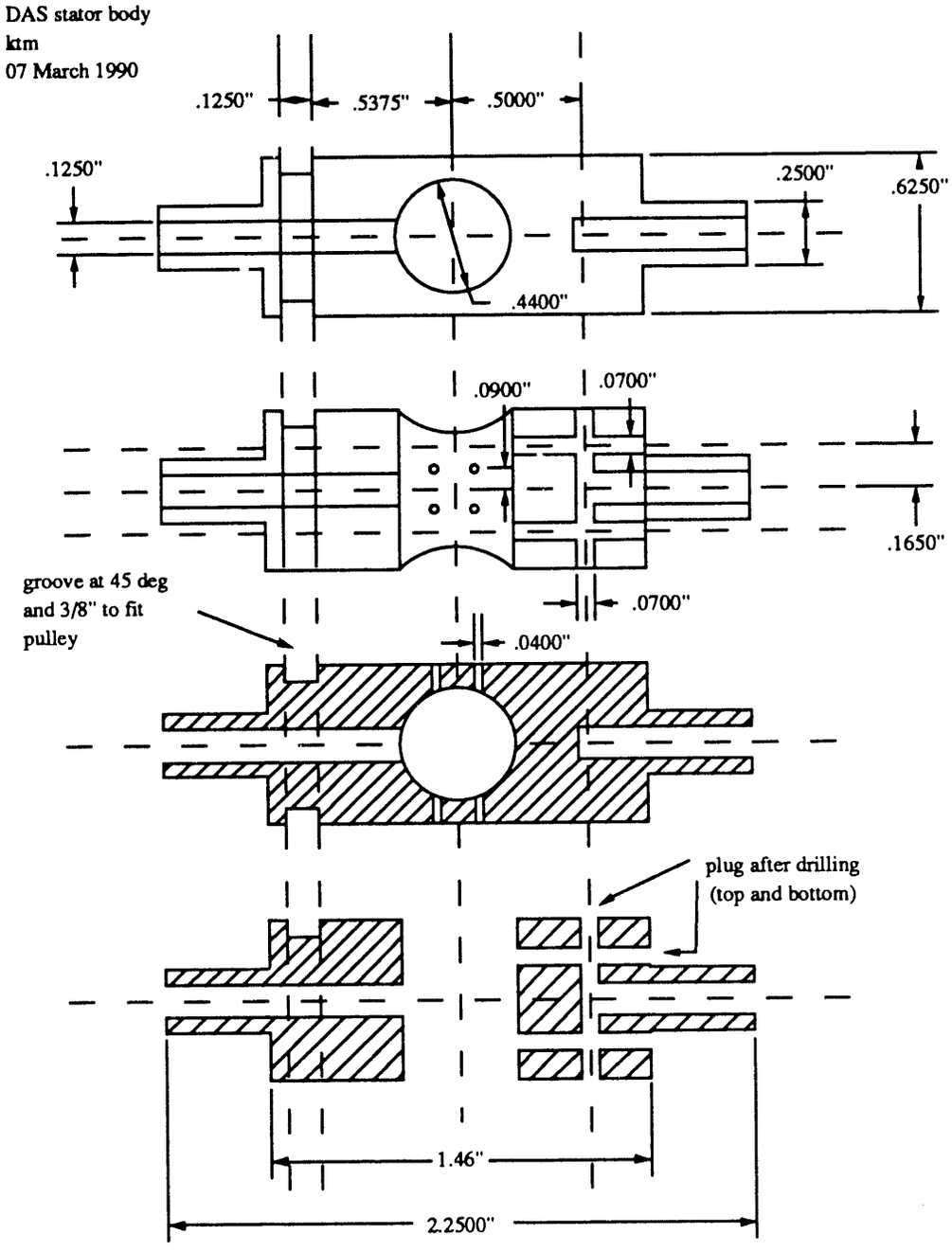

Figure A.1: Stator body for DAS probehead.

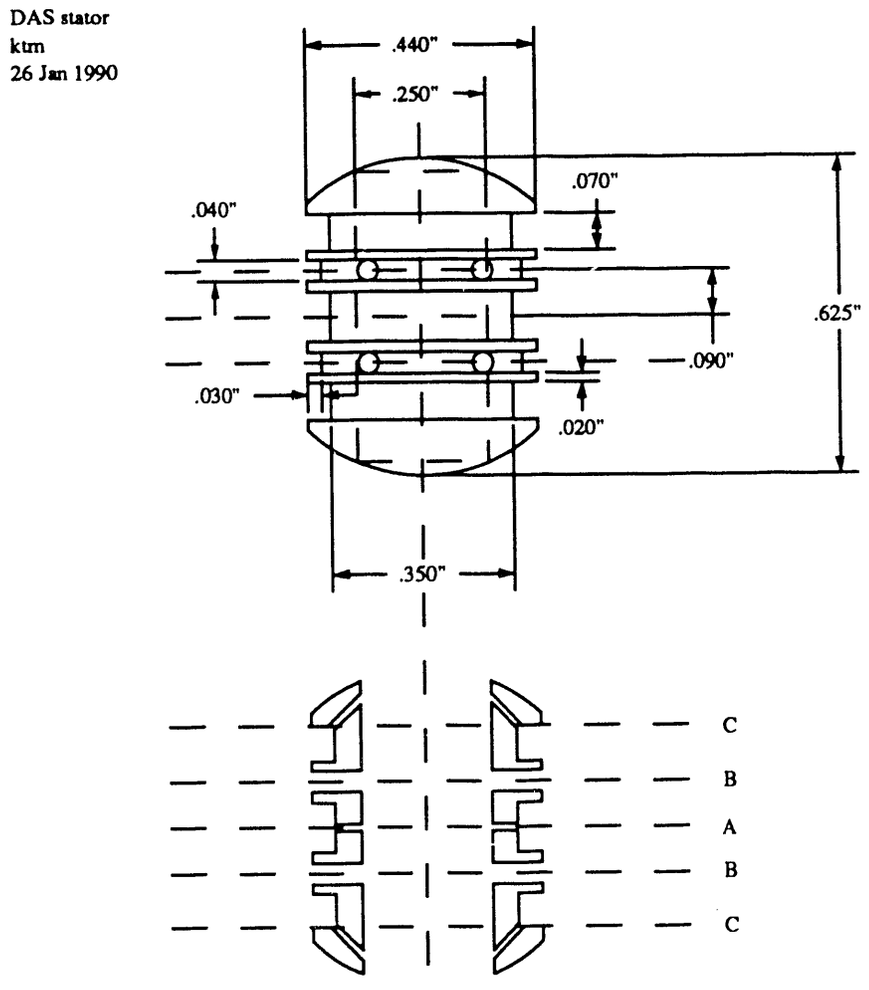

Figure A.2: Stator for DAS probehead. The letters to the right in the bottom sketch refer to the sections in Fig. A.3.

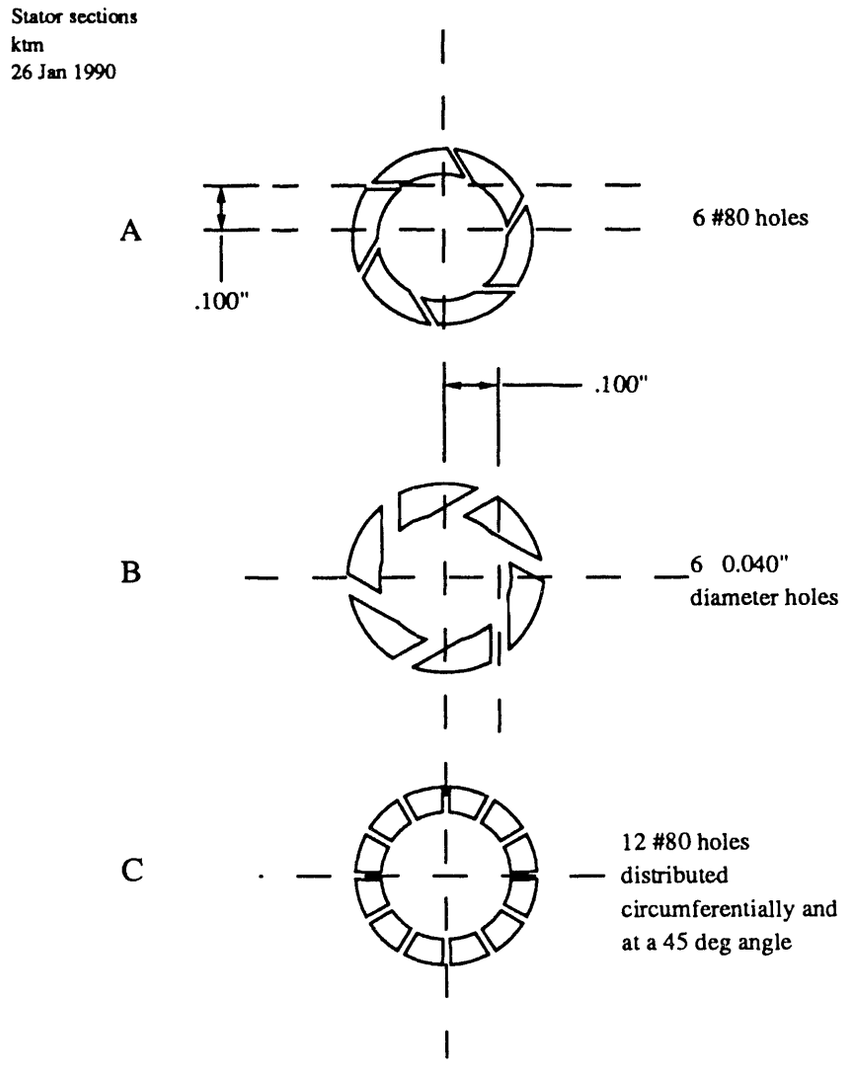

Figure A.3: Configuration of holes in stator for DAS probehead (sections marked in reference to Fig. A.2).

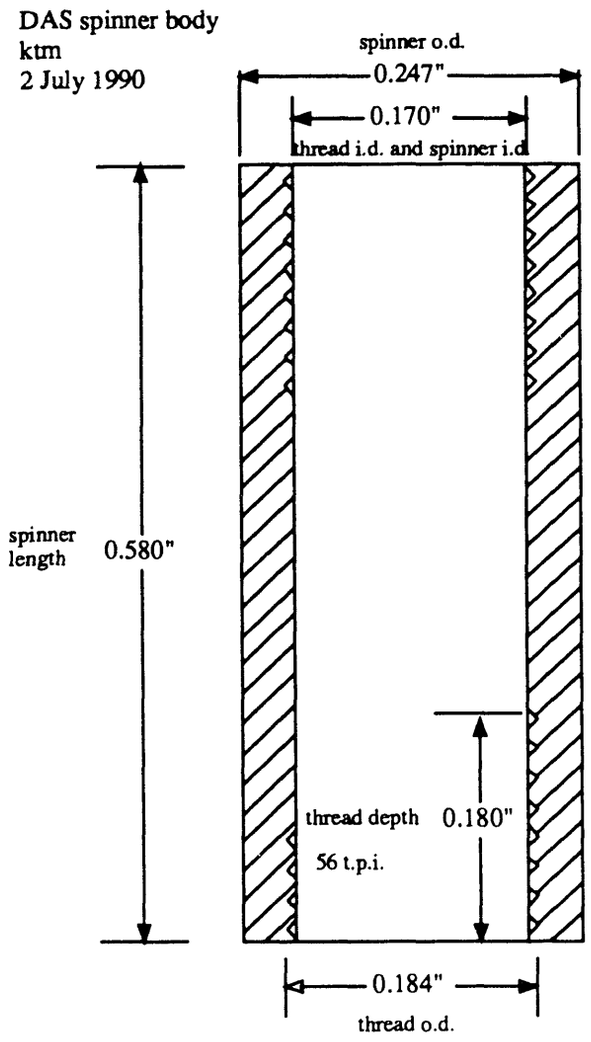

Figure A.4: Spinner for DAS. The flutes are cut as described in the text of chapter 7.

DAS spinner caps
ktm
2 July 1990

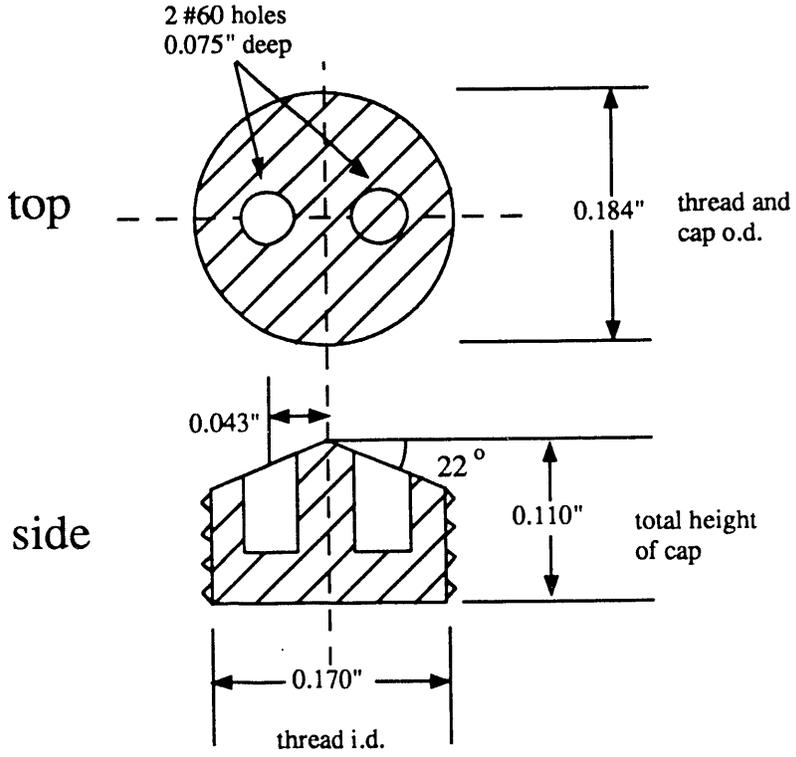

Figure A.5: Caps for DAS spinner.

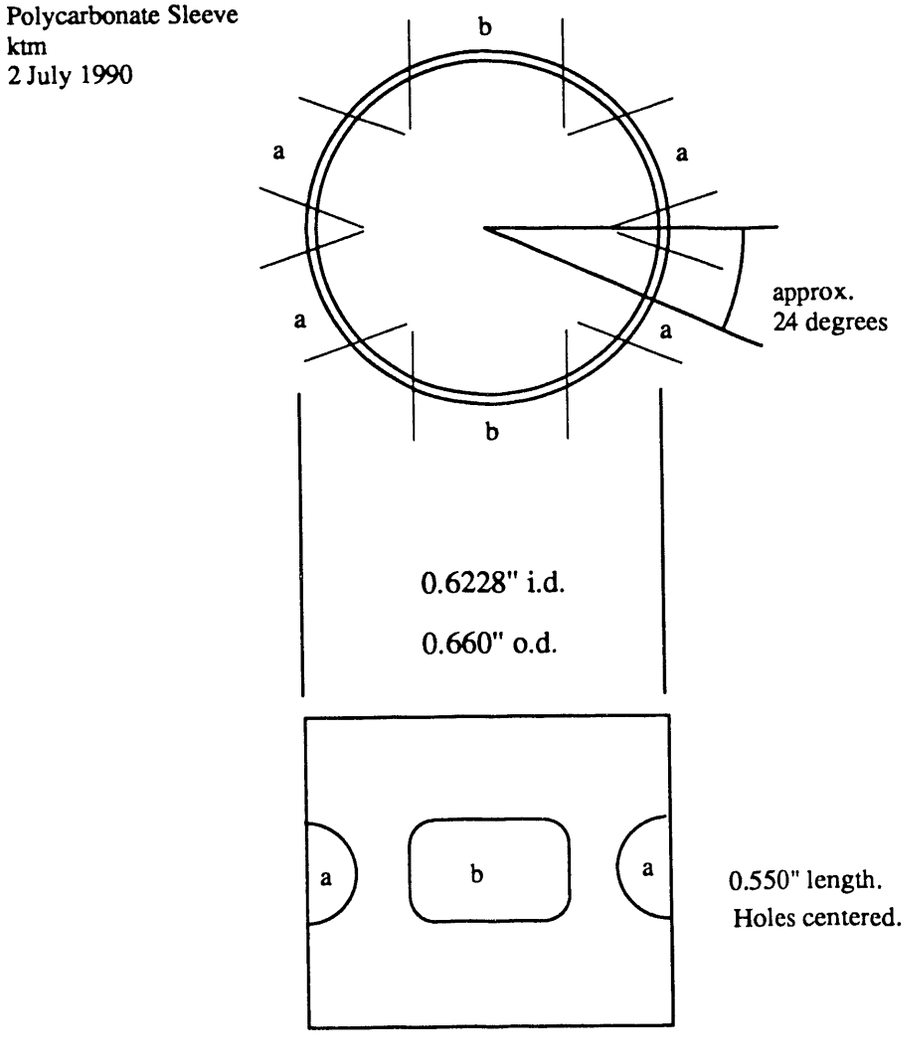

Figure A.6: Polycarbonate sleeve for DAS probehead.

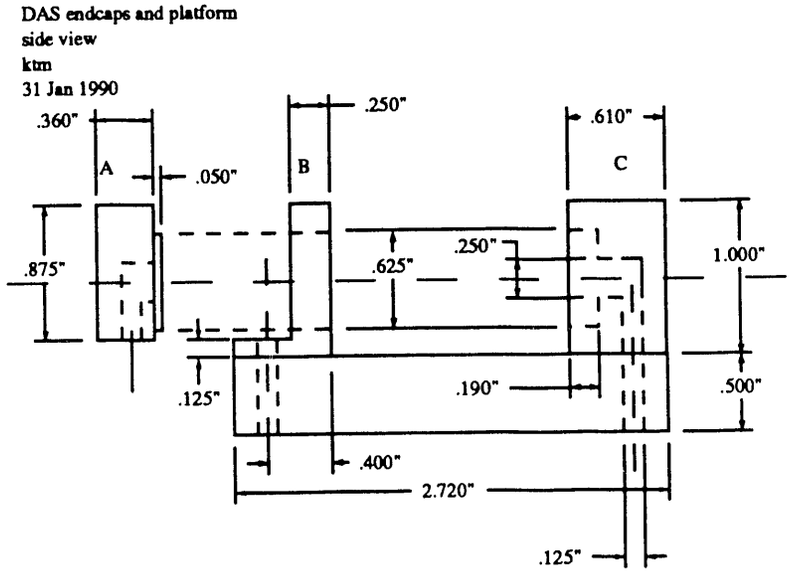

Figure A.7: Side view of endcaps for DAS probehead. The letters A, B, and C distingish the distinct parts in this drawing and Figs. A.8 and A.9.

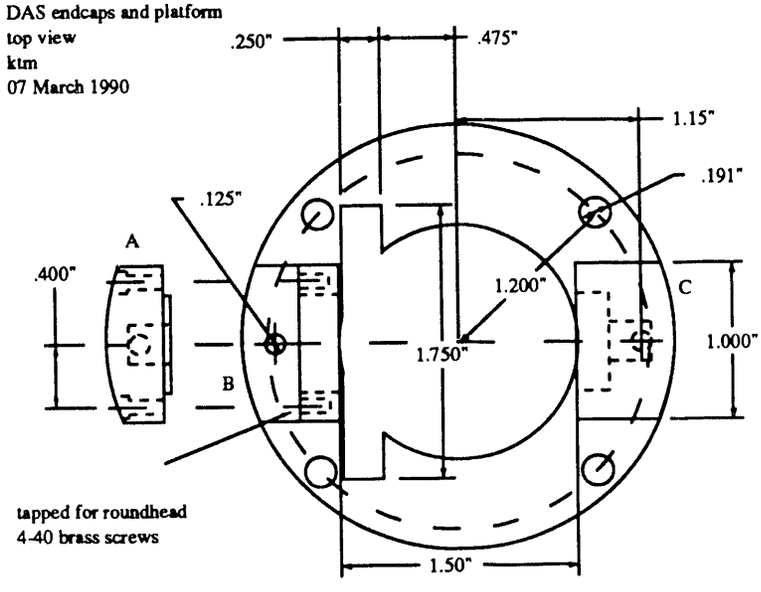

Figure A.8: Top view of endcaps for DAS probehead.

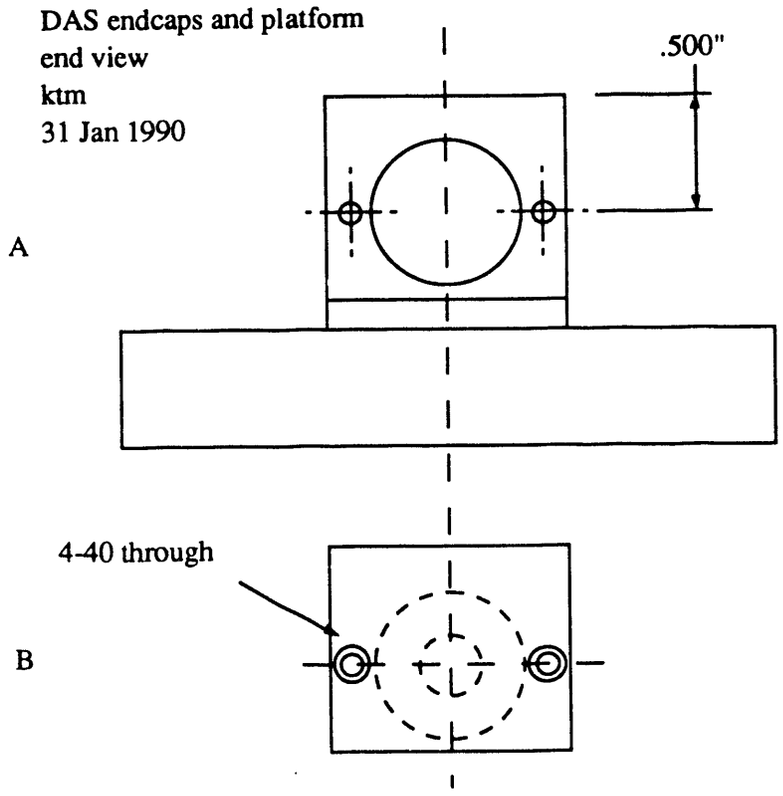

Figure A.9: End view of endcaps for DAS probehead.

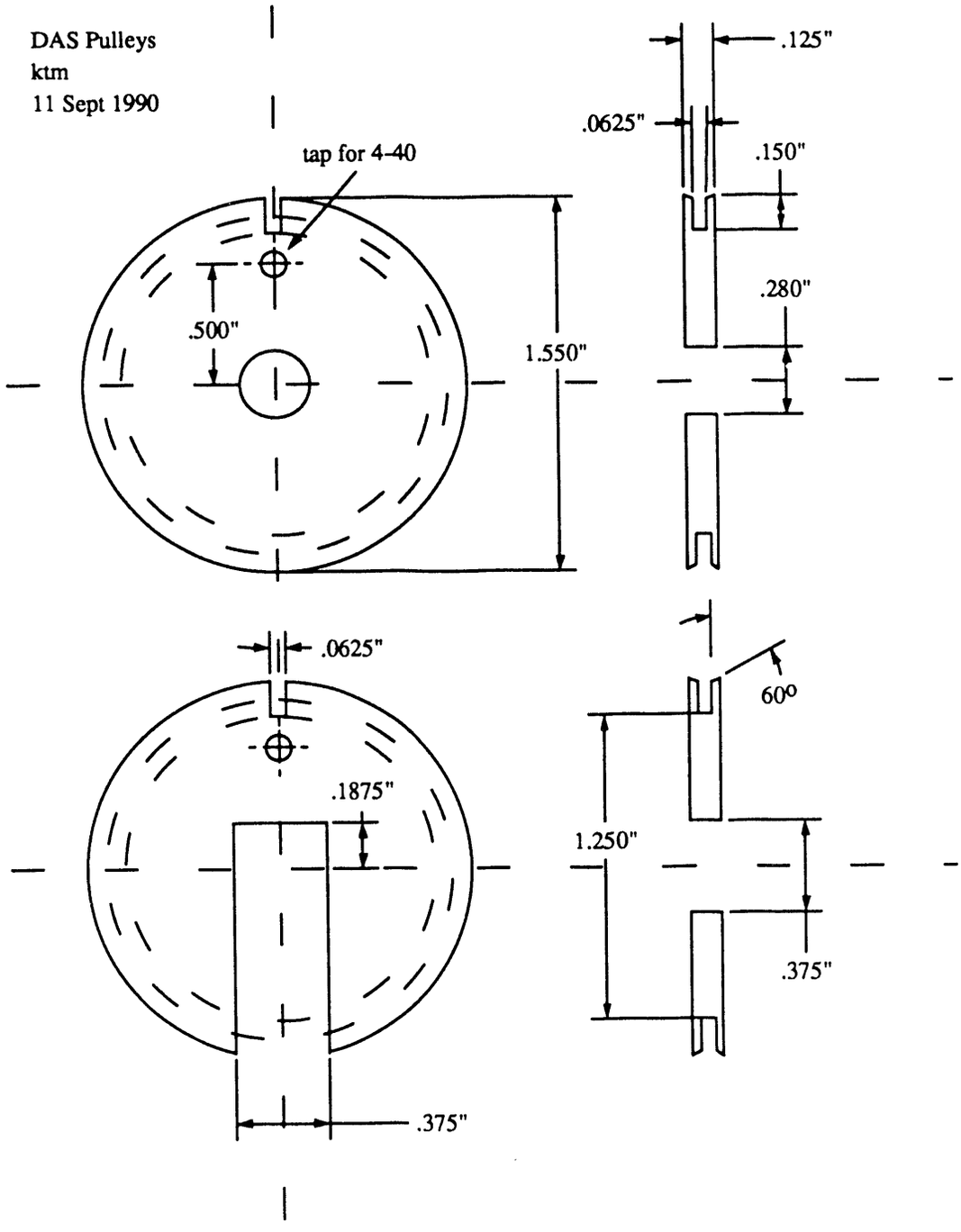

Figure A.10: Pulleys for DAS motor (top) and probehead (bottom).

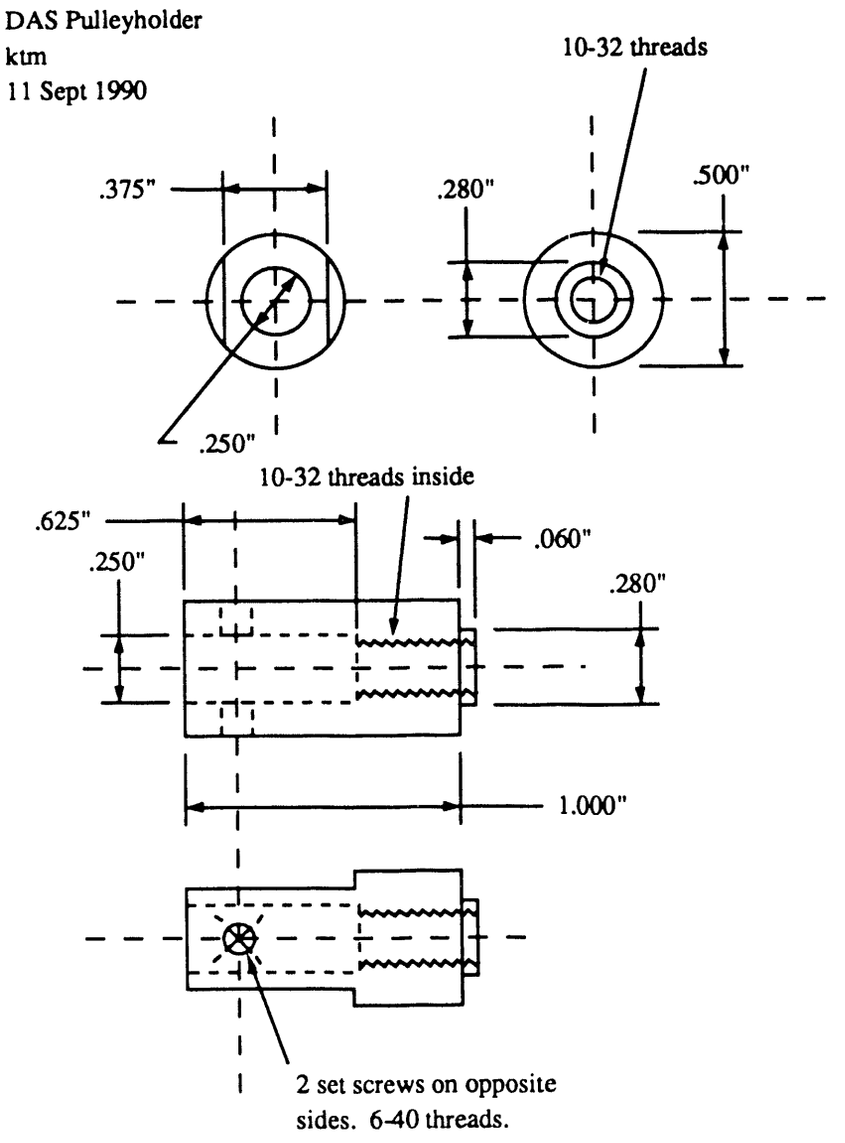

Figure A.11: Pulley holder for mounting the pulley on the motor.

Appendix B

Reorientation of a Spinning Body

We consider the torques arising from the reorientation of a rotor spinning at an angular velocity ω and supported by air bearings a fixed distance B from the rotor center. The rotor with mass M has height H and radius R. We assume that the reorientation axis is along the x-axis such that the sample rotation axis is always in the yz-plane: the angle θ describes the angle which the spinning axis makes with the z-direction.

If the angular velocity of the spinning axis reorientation is $\Omega = \mathrm{d}\theta/\mathrm{dt}$ then the angular momentum $\mathbf{L}$ at any instant is

$$\mathbf{L} = \omega I_0(\hat{\mathbf{e}}_z \cos\theta + \hat{\mathbf{e}}_y \sin\theta) + \Omega I_1 \hat{\mathbf{e}}_x, \tag{B.1}$$

where $\mathrm{I_0}$ and $\mathrm{I_1}$ denote moments of inertia parallel and perpendicular to the cylindrical rotor axis respectively. Explicitly

$$I_0 = \frac{MR^2}{2} \tag{B.2}$$

and

$$I_1 = \frac{MR^2}{4}\left(1 + \frac{H^2}{3R^2}\right). \tag{B.3}$$

To obtain the torque, we differentiate Eq. B.1 with respect to time and obtain two additive terms:

$$\mathbf{N}_g = \omega\Omega I_0(-\hat{\mathbf{e}}_z \sin\theta + \hat{\mathbf{e}}_y \cos\theta) \tag{B.4}$$

and

$$\mathbf{N}_r = \alpha I_1 \hat{\mathbf{e}}_x. \tag{B.5}$$

where $\alpha = \mathrm{d}\Omega/\mathrm{dt}$ is the angular acceleration of the reorientation. Note that the torque $\mathbf{N}_r$ is identical to that generated by reorienting a non-spinning cylinder. The gyroscopic torque, $\mathbf{N}_g$, arises from the fact that a spinning object is being realigned: it depends on the product of the two angular velocities, ω and Ω. Since $\mathbf{N}_g$ is at all times orthogonal to the drive axis it will be borne completely by the bearings which hold the stator and the motor need only provide a torque equal to $\mathbf{N}_r$ to effect the motion. This leads to the first important conclusion: a spinning sample is no more difficult for the motor to reorient than one which is static. Of course, the air bearings between the stator sleeve and the rotor must provide sufficient forces to support both of these torques. Empirically, this bearing load may be significant, since rotor touchdown associated with reorientation is observed unless bearing pressures of 30 psi are maintained.

Consider the case where reorientation through an angle $\Delta\theta$ occurs in a time τ_r and consists of a uniform angular acceleration (α) from rest up to a maximum angular velocity (Ω_{max}) during the first half of the reorientation. Uniform deceleration back to rest results in an overall triangular velocity profile and Eq. B.4 shows that the peak gyroscopic torque occurs at the midpoint of the motion where the angular velocity is

$$\Omega_{max} = \frac{\alpha\tau_r}{2}. \tag{B.6}$$

Using Eq. 7.5 from the main text we may relate Ω_{max} to $\Delta\theta$ and τ_r, finding

$$\Omega_{max} = \frac{2\Delta\theta}{\tau_r}. \tag{B.7}$$

Equation B.5 indicates that the reorientation torque is constant during the acceleration and simply undergoes a sign change when the motion changes to deceleration. The ratio of the torques may then be calculated:

$$\frac{|\mathbf{N}_r|}{|\mathbf{N}_g(max)|} = \frac{\alpha}{2\omega\Omega_{max}}\left(1 + \frac{H^2}{3R^2}\right) = \frac{\left(1 + \frac{H^2}{3R^2}\right)}{\omega\tau_r}. \tag{B.8}$$

For typical cylinder aspect ratios (H/2R) between 2 and 5, the numerator of Eq. B.8 falls between 1 and 35. The denominator, on the other hand, is the number of radians the rotor turns while it is undergoing reorientation. For a 5 kHz spinning rate and reorientation times between 10 and 50 msec, this falls between 300 and 1500. The second important conclusion then is that the main air bearing load associated with reorientation is generated by gyroscopic reaction forces.

To estimate the magnitude of the load associated with hopping in more familiar terms, we will calculate how large a sample packing imbalance is required to generate a bearing load comparable to that expected during reorientation. We characterize rotor imbalance by the parameter $\eta = \Delta R/R$, where ΔR is the distance of the actual center of gravity from the spinning axis and R is again the rotor radius. For a symmetric imbalance, the force on each of a pair of bearings holding the rotor is

$$F_b = \frac{\eta\omega L}{R}, \tag{B.9}$$

where ω and L are the magnitudes of the rotor angular velocity and momenta as defined above.

On the other hand, if we move the spinner with an angular velocity of reorientation Ω about an axis perpendicular to the spinning axis, we require a peak force

per bearing

$$F_r = \frac{\Omega_{max} L}{2B}, \tag{B.10}$$

where B is the offset of the each bearing ring from the spinner center.

To obtain the equivalent imbalance η_{eq} required to generate a force equal to the reorientation load, we equate Eqs. B.9 and B.10, obtaining

$$\eta_{eq} = \left(\frac{R}{2B}\right)\left(\frac{\Omega_{max}}{\omega}\right). \tag{B.11}$$

To a first approximation, R/B = 1, $\Omega_{max} = \pi/(2\tau_r)$, and $\omega = 2\pi/\tau_s$, where τ_r and τ_s are the reorientation time and spinning period respectively. This leads to $\eta_{eq} = \tau_s/8\tau_r$. For $\tau_s = 0.2$ msec and $\tau_r = 30$ msec, we find the equivalent offset to be one part in 1200. This is a very small value and it is not expected to affect spinner stability. Therefore we expect stable behavior of the rotor during the hop.

This analysis has shown that the magnitudes of the reorientation torques are smaller or comparable to those occurring in steady state motion. On the other hand bearing failure is observed during reorientation if bearing pressures are too low. Such failure may then be due to more complex motions, possibly involving gyroscopic oscillations and air bearing compression. Whatever the mechanism for the bearing failure, it is possible to perform the necessary hopping of a spinning rotor to accomplish the DAS experiments as sufficient bearing pressures are easily maintained in this design.

Appendix C

Computer Code

This appendix contains the code for five *Mathematica*™ programs used for calculations within the main text.

wigner.m – code included in the following three programs defines the matrix elements of the reduced and full second–order Wigner rotations.

static.m – calculates the spatial dependence for the second–order quadrupolar interaction in a static sample.

vass.m – calculates the spatial dependence for the second–order quadrupolar interaction in a sample spinning at an arbitrary angle with respect to the magnetic field.

dor.m – calculates the spatial dependence for the second–order quadrupolar interaction in a sample undergoing double rotation defined by two arbitrary angles.

dasangles.m – calculates the DAS complementary angles for the range of k values. This program was used to generate Fig. 3.1.

wigner.m

```
(* Construct second-degree reduced Wigner Functions
   dr as functions of m1, m2, and theta and then full Wigner
   matrices d as functions of i, j, alpha, beta, and gamma *)

Clear[dr]

dr[2,2,theta_] := ((1+Cos[theta])/2)^2

dr[1,2,theta_] := (1+Cos[theta])/2 Sin[theta]

dr[0,2,theta_] := Sqrt[3/8] Sin[theta]^2

dr[-1,2,theta_] := (1-Cos[theta])/2 Sin[theta]

dr[-2,2,theta_] := ((1-Cos[theta])/2)^2

dr[2,1,theta_] := -(1+Cos[theta])/2 Sin[theta]

dr[1,1,theta_] := Cos[theta]^2 - ((1-Cos[theta])/2)

dr [0,1,theta_] := Sqrt[3/8] Sin[2 theta]

dr[-1,1,theta_] := -Cos[theta]^2 + ((1+Cos[theta])/2)

dr[-2,1,theta_] := (1-Cos[theta])/2 Sin[theta]

dr[2,0,theta_] := Sqrt[3/8] Sin[theta]^2

dr[1,0,theta_] := -Sqrt[3/8]Sin[2 theta]

dr[0,0,theta_] := (3 Cos[theta]^2 - 1)/2

dr[-1,0,theta_] := Sqrt[3/8]Sin[2 theta]

dr[-2,0,theta_] := Sqrt[3/8] Sin[theta]^2

dr[2,-1,theta_] := -(1-Cos[theta])/2 Sin[theta]

dr[1,-1,theta_] := -Cos[theta]^2 + ((1+Cos[theta])/2)

dr[0,-1,theta_] := -Sqrt[3/8]Sin[2 theta]

dr[-1,-1,theta_] := Cos[theta]^2 - ((1-Cos[theta])/2)

dr[-2,-1,theta_] := (1+Cos[theta])/2 Sin[theta]

dr[2,-2,theta_] := ((1-Cos[theta])/2)^2

dr[1,-2,theta_] := -(1-Cos[theta])/2 Sin[theta]

dr[0,-2,theta_] := Sqrt[3/8] Sin[theta]^2

dr[-1,-2,theta_] := -(1+Cos[theta])/2 Sin[theta]

dr[-2,-2,theta_] := ((1+Cos[theta])/2)^2

Clear[d]

d[i_,j_,alpha_,beta_,gamma_] :=
dr[i,j,beta] (Cos[i alpha] + I Sin[i alpha]) *
(Cos[j gamma] + I Sin[j gamma])
```

static.m

```
(* Read in the definitions of the Wigner matrices *)

<< wigner.m

(* Construct the second-rank tensors in the principal axis
system of the EFG: note that eq is factored out *)

Clear[r]

r[2,2] = 1/2 eta;

r[2,-2] = 1/2 eta;

r[2,0] = Sqrt[3/2];

r[2,1] = 0;

r[2,-1] = 0;

(* The rotation is performed through the angles alpha, beta,
and gamma (a,b,c) to the interaction frame tensor R *)

Clear[R]

R[2,m_] := Sum[d[mp,m,a,b,c] r[2,mp], {mp,-2,2}];

R22 = R[2,2];

R2m2 = R[2,-2];

Rprod2 = R22 R2m2;

R21 = R[2,1];

R2m1 = R[2,-1];

Rprod1 = R21 R2m1;

(* The factors for the equations used are obtained from
   8 times the sum of 2 Rprod1 and Rprod2 *)

total = Expand[16 Rprod1 + 8 Rprod2];

(* A set of trigonometric simplifications *)

Expand[total //. Cos[n_?Negative x_.]   -> Cos[-n x]];

Expand[% //. Sin[n_?Negative x_.]   -> -Sin[-n x]];

Expand[% //. Cos[b] Sin[b] -> (Sin[2 b])/2];

Expand[% //. Cos[a]^2 -> (1 + Cos[2 a])/2];

Expand[% //. Cos[b]^2 -> (1 + Cos[2 b])/2];

Expand[% //. Cos[c]^2 -> (1 + Cos[2 c])/2];

Expand[% //. Cos[a]^4 -> (1 + Cos[2 a])/2 (1 + Cos[2 a])/2];

Expand[% //. Cos[b]^4 -> (1 + Cos[2 b])/2 (1 + Cos[2 b])/2];

Expand[% //. Cos[c]^4 -> (1 + Cos[2 c])/2 (1 + Cos[2 c])/2];

Expand[% //. Sin[a]^2 -> (1 - Cos[2 a])/2];
```

```
Expand[% //. Sin[2a]^2 -> (1 - Cos[4 a])/2];
Expand[% //. Sin[b]^2 -> (1 - Cos[2 b])/2];
Expand[% //. Sin[2b]^2 -> (1 - Cos[4 b])/2];
Expand[% //. Sin[c]^2 -> (1 - Cos[2 c])/2];
Expand[% //. Sin[2 c]^2 -> (1 - Cos[4 c])/2];
Expand[% //. Sin[a]^4 -> (1 - Cos[2 a])/2 (1 - Cos[2 a])/2];
Expand[% //. Sin[b]^4 -> (1 - Cos[2 b])/2 (1 - Cos[2 b])/2];
Expand[% //. Sin[c]^4 -> (1 - Cos[2 c])/2 (1 - Cos[2 c])/2];
Expand[% //. Cos[2 a]^2 -> (1 + Cos[4 a])/2];
Expand[% //. Cos[2 b]^2 ->  (1 + Cos[4 b])/2];
ans = Expand[% //. Cos[2 c]^2 ->  (1 + Cos[4 c])/2];
(* Finally, the answer *)
ans
```

$$
\begin{aligned}
&-\frac{45}{16} - \frac{5\,\text{eta}^2}{32} + \frac{39\,\text{eta}\,\text{Cos}[2\,a]}{8} + \frac{27\,\text{eta}^2\,\text{Cos}[4\,a]}{32} - \frac{9\,\text{Cos}[2\,b]}{4} + \\
&\frac{15\,\text{eta}^2\,\text{Cos}[2\,b]}{8} - \frac{3\,\text{eta}\,\text{Cos}[2\,a]\,\text{Cos}[2\,b]}{2} - \\
&\frac{9\,\text{eta}^2\,\text{Cos}[4\,a]\,\text{Cos}[2\,b]}{8} + \frac{81\,\text{Cos}[4\,b]}{16} + \frac{9\,\text{eta}^2\,\text{Cos}[4\,b]}{32} - \\
&\frac{27\,\text{eta}\,\text{Cos}[2\,a]\,\text{Cos}[4\,b]}{8} + \frac{9\,\text{eta}^2\,\text{Cos}[4\,a]\,\text{Cos}[4\,b]}{32}
\end{aligned}
$$

vass.m

```
(* Read in the definitions of the Wigner matrices  *)

<< wigner.m

(* Construct the second-rank tensors in the principal axis
system of the EFG:  note that eq is factored out *)

Clear[r]

r[2,2] =  1/2 eta;

r[2,-2] = 1/2 eta;

r[2,0] = Sqrt[3/2];

r[2,1] = 0;

r[2,-1] = 0;

(* The rotations are performed through the angles alpha
   and beta (a,b) to the rotor frame and then theta to the
   interaction frame tensor R *)

Clear[R]

R[2,m_,mp_] := Sum[dr[mp,m,theta] dr[mpp,mp,b] r[2,mpp] *
(Cos[mpp a] - I Sin[mpp a]),{mpp,-2,2}];

(* The time-independent terms in the product of spherical
   tensors are calculated *)

Rprod2 = R[2,2,0] R[2,-2,0] +
      R[2,2,1] R[2,-2,-1] +
      R[2,2,2] R[2,-2,-2] +
      R[2,2,-1] R[2,-2,1] +
      R[2,2,-2] R[2,-2,2];

Expand[%];

Rprod2 = %;

Rprod1 = R[2,1,0] R[2,-1,0] +
      R[2,1,1] R[2,-1,-1] +
      R[2,1,2] R[2,-1,-2] +
      R[2,1,-1] R[2,-1,1] +
      R[2,1,-2] R[2,-1,2];

Expand[%];

Rprod1 = %;

(* The factors for the equations used are obtained from
   8 times the sum of 2 Rprod1 and Rprod2 *)

total =  Expand[16 Rprod1  + 8 Rprod2];

(*  A set of trigonometric simplifications *)

Expand[total //. Cos[n_?Negative x_.]    ->  Cos[-n x]];

Expand[% //. Sin[n_?Negative x_.]    ->  -Sin[-n x]];
```

```
Expand[% //. Sin[theta]^4 -> (1 - Cos[theta]^2)(1 - Cos[theta]^2)];

Expand[% //. Cos[b]^2 -> (1 + Cos[2 b])/2];

Expand[% //. Cos[b]^4 -> (1 + Cos[2 b])/2 (1 + Cos[2 b])/2];

Expand[% //. Sin[b]^2 -> (1 - Cos[2 b])/2];

Expand[% //. Cos[b] Sin[b] -> Sin[2 b] / 2];

Expand[% //. Sin[2 b]^2 -> (1 - Cos[4 b])/2];

Expand[% //. Sin[2 a]^2 -> (1 - Cos[4 a])/2];

Expand[% //. Sin[b]^4 -> (1 - Cos[2 b])/2 (1 - Cos[2 b])/2];

Expand[% //. Cos[2 a]^2 -> (1 + Cos[4 a])/2];

Expand[% //. Sin[2 theta]^2 -> 4 (Cos[theta]^2 - Cos[theta]^4)];

Expand[%];% //. Cos[2 b]^2 -> (1 + Cos[4 b])/2];

ans = Expand[% //. Sin[theta]^2 -> 1 - Cos[theta]^2];

(* The number of terms in the final expression is *)

Length[ans]

36

(* The coefficients for the expansion may be obtained
   as below and factored into Legendre Polynomials *)

p2 = LegendreP[2,Cos[theta]];

p4 = LegendreP[4,Cos[theta]];

ans44 = Coefficient[ans, Cos[4 a] Cos[4 b] ]

      2           2           2           2           4
27 eta    135 eta  Cos[theta]    315 eta  Cos[theta]
------- - ------------------- + --------------------
  256             128                    256

cop4 = Expand[8 / 35 Coefficient[ans44, Cos[theta]^4 ]];

rem1 = Expand[ans44 - cop4 * p4];

cop2 = Expand[ 2 / 3 Coefficient[rem1, Cos[theta]^2]];

rem2 = Expand[rem1 - cop2 * p2];

(* The remainder should be zero *)

rem2

0

cop4  (* the p4 coefficient *)

     2
9 eta
------
  32
```

cop2 (* the p2 coefficient *)

```
0
```

**(* The other terms are calculated similarly. Depending
on method of coefficient extraction, special
tricks may be needed when i = 0 or j = 0 in
expansion (some arguments must be set to zero) as below *)**

newans = ans//.{Cos[2a]-> 0, Cos[4a]-> 0};

ans02 = Coefficient[newans, Cos[2 b]]

```
             2                    2          2            2
117    51 eta     297 Cos[theta]     63 eta  Cos[theta]
--- - ------- - --------------- + ------------------ +
32       64             16                  32

                  4          2            4
  405 Cos[theta]     45 eta  Cos[theta]
  --------------- + ------------------
        32                   64
```

cop4 = Expand[8 / 35 Coefficient[ans02, Cos[theta]^4]];

rem1 = Expand[ans02 - cop4 * p4];

cop2 = Expand[2 / 3 Coefficient[rem1, Cos[theta]^2]];

rem2 = Expand[rem1 - cop2 * p2];

(* The remainder should be zero *)

rem2

```
0
```

cop4 (* the p4 coefficient *)

```
           2
81    9 eta
-- + ------
28      56
```

cop2 (* the p2 coefficient *)

```
                2
  36     12 eta
-(--) + -------
  7         7
```

dor.m

```
(* Read in the definitions of the Wigner matrices  *)

<< wigner.m

Clear[r]

r[2,2] =  1/2 eta;

r[2,-2] = 1/2 eta;

r[2,0] = Sqrt[3/2];

r[2,1] = 0;

r[2,-1] = 0;


(* R is defined as one component of the full rotated quantity, and multiplied in a
   reasonable manner to form the products R22R2-2 and R21R2-1 *)


Clear[R]

R[2,m_,mp_,mpp_] := Sum[dr[mp,m,theta1] dr[mpp,mp,theta2] *
dr[mppp,mpp,b] r[2,mppp] *
(Cos[mppp a] - I Sin[mppp a]),{mppp,-2,2}];


Rprod2 = R[2,2,0,0] R[2,-2,0,0] +
      R[2,2,0,1] R[2,-2,0,-1] +
      R[2,2,0,2] R[2,-2,0,-2] +
      R[2,2,0,-1] R[2,-2,0,1] +
      R[2,2,0,-2] R[2,-2,0,2] +
      R[2,2,1,0] R[2,-2,-1,0] +
      R[2,2,1,1] R[2,-2,-1,-1] +
      R[2,2,1,2] R[2,-2,-1,-2] +
      R[2,2,1,-1] R[2,-2,-1,1] +
      R[2,2,1,-2] R[2,-2,-1,2] +
      R[2,2,-1,0] R[2,-2,1,0] +
      R[2,2,-1,1] R[2,-2,1,-1] +
      R[2,2,-1,2] R[2,-2,1,-2] +
      R[2,2,-1,-1] R[2,-2,1,1] +
      R[2,2,-1,-2] R[2,-2,1,2] +
      R[2,2,2,0] R[2,-2,-2,0] +
      R[2,2,2,1] R[2,-2,-2,-1] +
      R[2,2,2,2] R[2,-2,-2,-2] +
      R[2,2,2,-1] R[2,-2,-2,1] +
      R[2,2,2,-2] R[2,-2,-2,2] +
      R[2,2,-2,0] R[2,-2,2,0] +
      R[2,2,-2,1] R[2,-2,2,-1] +
      R[2,2,-2,2] R[2,-2,2,-2] +
      R[2,2,-2,-1] R[2,-2,2,1] +
      R[2,2,-2,-2] R[2,-2,2,2] ;

Expand[%];

Rprod2 = %;
```

```
Rprod1 = R[2,1,0,0] R[2,-1,0,0] +
      R[2,1,0,1] R[2,-1,0,-1] +
      R[2,1,0,2] R[2,-1,0,-2] +
      R[2,1,0,-1] R[2,-1,0,1] +
      R[2,1,0,-2] R[2,-1,0,2] +
      R[2,1,1,0] R[2,-1,-1,0] +
      R[2,1,1,1] R[2,-1,-1,-1] +
      R[2,1,1,2] R[2,-1,-1,-2] +
      R[2,1,1,-1] R[2,-1,-1,1] +
      R[2,1,1,-2] R[2,-1,-1,2] +
      R[2,1,-1,0] R[2,-1,1,0] +
      R[2,1,-1,1] R[2,-1,1,-1] +
      R[2,1,-1,2] R[2,-1,1,-2] +
      R[2,1,-1,-1] R[2,-1,1,1] +
      R[2,1,-1,-2] R[2,-1,1,2] +
      R[2,1,2,0] R[2,-1,-2,0] +
      R[2,1,2,1] R[2,-1,-2,-1] +
      R[2,1,2,2] R[2,-1,-2,-2] +
      R[2,1,2,-1] R[2,-1,-2,1] +
      R[2,1,2,-2] R[2,-1,-2,2] +
      R[2,1,-2,0] R[2,-1,2,0] +
      R[2,1,-2,1] R[2,-1,2,-1] +
      R[2,1,-2,2] R[2,-1,2,-2] +
      R[2,1,-2,-1] R[2,-1,2,1] +
      R[2,1,-2,-2] R[2,-1,2,2];

Expand[%];

Rprod1 = %;

(* The total frequency in the proper units is obtained next *)

total = Expand[16 Rprod1 + 8 Rprod2];

Length[total]

2064

(* Trigonemtric identities simplify the long answer *)

Expand[total //. Cos[n_?Negative x_.] -> Cos[-n x]];

Expand[%//. Sin[n_?Negative x_.] -> -Sin[-n x]];

Expand[%//. Sin[theta1]^4 -> (1 - Cos[theta1]^2)(1 - Cos[theta1]^2)];

Expand[%//. Sin[theta2]^4 -> (1 - Cos[theta2]^2)(1 - Cos[theta2]^2)];

Expand[%//. Cos[b]^2 -> (1 + Cos[2 b])/2];

Expand[%//. Cos[b]^4 -> (1 + Cos[2 b])/2 (1 + Cos[2 b])/2];

Expand[%//. Sin[b]^2 -> (1 - Cos[2 b])/2];

Expand[%//. Cos[b] Sin[b] -> Sin[2 b] / 2];

Expand[%//. Sin[2 b]^2 -> (1 - Cos[4 b])/2];
```

```
Expand[%//. Sin[2 a]^2 -> (1 - Cos[4 a])/2];
Expand[%//. Sin[b]^4 -> (1 - Cos[2 b])/2 (1 - Cos[2 b])/2];
Expand[%//. Cos[2 a]^2 -> (1 + Cos[4 a])/2];
Expand[%//. Sin[2 theta1]^2 -> 4 (Cos[theta1]^2 - Cos[theta1]^4)];
Expand[%//. Sin[2 theta2]^2 -> 4 (Cos[theta2]^2 - Cos[theta2]^4)];
Expand[%//. Cos[2 b]^2 -> (1 + Cos[4 b])/2];
Expand[%//. Sin[theta1]^2 -> 1 - Cos[theta1]^2];
Expand[%//. Sin[theta2]^2 -> 1 - Cos[theta2]^2];
ans = %;

Length[ans]
108

(* The Legendre polynomials are defined here as well as their products *)

p21 = LegendreP[2,Cos[theta1]];
p22 = LegendreP[2,Cos[theta2]];
p41 = LegendreP[4,Cos[theta1]];
p42 = LegendreP[4,Cos[theta2]];
p41p42 = Expand[p41 p42];
p21p22 = Expand[p21 p22];


(* The cofficients in front of the p4p4 and p2p2 terms are calculated *)
cop4p4 = Expand[8 8 /35 /35 Coefficient[ans, Cos[theta1]^4 Cos[theta2]^4]];
rem1 = Expand[ans - cop4p4 * p41p42];
r = Coefficient[rem1,Cos[theta1]^4 Cos[theta2]^4];
cop2p2 = Expand[2 2 /3 /3 Coefficient[rem1, Cos[theta1]^2 Cos[theta2]^2]];
rem2 = Expand[rem1 - cop2p2 * p21p22];
r = Coefficient[rem2,Cos[theta1]^2 Cos[theta2]^2];
Length[rem2]
2
rem2

                2
  12     4 eta
-(--) - ------
  5        5
```

cop4p4

$$\frac{729}{560} + \frac{81\,\eta^2}{1120} + \frac{81\,\eta\,\cos[2a]}{56} + \frac{27\,\eta^2\,\cos[4a]}{32} + \frac{81\,\cos[2b]}{28} +$$

$$\frac{9\,\eta^2\,\cos[2b]}{56} + \frac{27\,\eta\,\cos[2a]\,\cos[2b]}{14} - \frac{9\,\eta^2\,\cos[4a]\,\cos[2b]}{8}$$

$$\frac{81\,\cos[4b]}{16} + \frac{9\,\eta^2\,\cos[4b]}{32} - \frac{27\,\eta\,\cos[2a]\,\cos[4b]}{8} +$$

$$\frac{9\,\eta^2\,\cos[4a]\,\cos[4b]}{32}$$

cop2p2

$$-\frac{12}{7} + \frac{4\,\eta^2}{7} + \frac{24\,\eta\,\cos[2a]}{7} - \frac{36\,\cos[2b]}{7} + \frac{12\,\eta^2\,\cos[2b]}{7} -$$

$$\frac{24\,\eta\,\cos[2a]\,\cos[2b]}{7}$$

(* The remainder should be the same as rem2, and this is the isotropic second-order shift *)

f = Expand[ans - cop4p4 p41p42 - cop2p2 p21p22]

$$-\frac{12}{5} - \frac{4\,\eta^2}{5}$$

dasangles.m

```
(* Definition of the Legendre Polynomials    *)

p2[theta1_] := LegendreP[2,Cos[theta1]]

p4[theta2_] := LegendreP[4,Cos[theta2]]

(* Do loop will calculate theta 1 and theta 2
   for eack value of k from 0.8 to 5 in steps
   of 0.025                          *)

Clear[k];kout = {}; xout = {}; yout = {};
Do[
rule = FindRoot[{p2[x]+k p2[y] == 0,
p4[x]+k p4[y] == 0}, {x, 15 Degree}, {y, 65 Degree}];
xrule = rule[[1]]; yrule = rule[[2]];
AppendTo[kout,k];
AppendTo[xout,{k,(x /. xrule) / Degree //N} ];
AppendTo[yout,{k,(y /. yrule) / Degree //N} ],
{k, 0.8, 5, 0.025}]

(* Commands to plot the data used to make Fig 3.1  *)

ListPlot[xout, PlotJoined->True,AxesLabel->{k,theta1},
PlotRange-> {0, 90}]

ListPlot[yout, PlotJoined->True,AxesLabel->{k,theta2},
PlotRange-> {0, 90}]
```

END

DATE FILMED

11/08/91